Energy-related nanomaterials

Edited by Paul Ziemann and Alexei R. Khokhlov

Imprint

Energy-related nanomaterials

Paul Ziemann[*1] and Alexei R. Khokhlov[*2]

The triple "generation, conversion and storage of energy" are the fundamental building blocks toward realizing the general aim of an energy supply on demand as unrestricted as possible. Meanwhile, however, it has become clear that this general aim leads to conflicting feedback loops on the ecological environment. Growing awareness of such deteriorating feedbacks has triggered worldwide activities to search for technical approaches in order to at least reduce the negative environmental consequences of energy consumption. At this point, materials science plays a central role. In most cases, rather than looking for completely novel solutions related to the energy triple "generation, conversion and storage" materials science contributes to stepwise improvements of functional efficiencies, which are based on optimizing energy-related materials.

A well-known topic related to the transport of people and goods – an important subsector of human energy consumption – is the effort aimed at the reduction of the weight of cars, trucks, planes and ships in order to save fuel. Improved materials such as novel compounds or composites should not only result in a reduction of weight but should also have mechanical properties that are at least comparable to those of the materials they are exchanged for. Mechanical properties strongly depend on the internal structure of a material such as grain size, grain orientation, defect densities, local chemical composition, and layer sequence and thickness in layered systems. At this point, the micro- and nanometer scales enter both experimental and theoretical simulation routes towards materials optimization. Another materials property worth of being optimized is friction, which, when trying to walk or drive on icy streets is highly welcome, but in many cases is a source of dissipated energy. The friction of an object moving on or through a supporting or surrounding medium, respectively, appears to be closely related to surface or interface roughness, so that, again, the micro- and nanoscales are of major importance. For instance, a reduction of the friction of cargo vessels by only a few percent leads to considerable energy savings and a significant decrease of the worldwide CO_2 emission [1]. It is noteworthy that the nanopatterning of surfaces and interfaces to reduce friction by tailoring their wettability and anti-fouling behavior is often guided by mimicking nature [2,3]. Contributions of advanced materials science to energy savings are numerous even when restricting one's view just on personal surroundings: Intelligent housing with controlled energy delivery, distribution and consumption, including smart heat production and insulation as well as smart windows complemented by exploiting residual heat.

Besides energy savings to extend finite resources, negative ecological feedbacks demand alternatives to oil-derived fuels. As we have already outlined previously [4], this demand is particularly important in the context of mobility with its significant subsector of short and medium range transport of people and products. Despite the increasing efforts to implement public transit and public transportation systems, cars and trucks with conventional combustion engines are still the predominant means of transport causing a considerable contribution to the global CO_2 emission. Electrically powered vehicles can at least contribute to attenuate this emission problem.

Electrically powered vehicles strongly rely on fuel cell (FC) or, most importantly, lithium-ion battery (LIB) technology, which is well-known and is already used on a large scale. However, the efficiency and average lifetime of these devices is suboptimal, and new materials are needed to fulfill these requirements. The development of such materials is a challenging task for experimental and theoretical materials science, which can only be met by joint interdisciplinary efforts between physicists, chemists and engineers. In addition, energy storage poses an even greater challenge, requiring contributions from the fields of electrochemistry, catalysis and simulations on all length scales.

Therefore, the cooperation of research facilities with a long-established experience in materials-oriented chemistry including catalysis and electrochemistry is a logical step, enabling the participating scientists to join their complementary knowledge and experience. The gains of such a multidisciplinary team play was the driving force for the initiation of joint projects between Ulm University, Moscow State (Lomonosov) University, and the Russian Academy of Sciences, financially supported by a recently completed BMBF-i program that supports the installation of a joint research infrastructure between German and Russian partners [4].

The contributions to the Thematic Series "Energy-related nano-materials" exemplify the scientific outcome of this cooperation and are complemented by related work outside of this network. Emphasis is put on a balanced presentation of experimental and theoretical work as well as physics- and chemistry-oriented views and approaches. The contributions cover a plethora of research fields from materials-related problems that concern fuel cells, Li-based batteries, and organic solar cells, to energy-related applications of nanographite and silicon nanotubes as well as the optimization of thermoelectric materials and electro-chemistry-based microscopy.

We would like to thank all colleagues for their valuable contributions and are convinced that this Thematic Series will find many readers. The engaged editorial support by the Production Team of the Beilstein-Institut is greatly acknowledged.

Paul Ziemann and Alexei R. Khokhlov

Ulm, Moscow, September 2013

References

1. Corbett, J. J.; Koehler, H. W. *J. Geophys. Res.: Atmos.* **2003,** *108,* 4650. doi:10.1029/2003JD003751
2. Barthlott, W.; Koch, K., Eds. Biomimetic materials, *Beilstein J. Nanotechnol.* http://www.beilstein-journals.org/bjnano/browse/singleSeries.htm?sn=3.
3. Barthlott, W.; Koch, K. *Beilstein J. Nanotechnol.* **2011,** *2,* 135–136. doi:10.3762/bjnano.2.16
4. ITP Infoservice 01/2012 - 5. Schwerpunktausgabe: *Russland – Modernisierung durch Innovation und Forschung.* http://www.kooperation-international.de/fileadmin/public/downloads/itb/info_12_01_24_SAG.pdf.

Influence of the solvent on the stability of bis(terpyridine) structures on graphite

Daniela Künzel and Axel Groß[*]

Full Research Paper

Address:
Institute of Theoretical Chemistry, Ulm University, D-89069 Ulm,
Germany

Email:
Axel Groß[*] - axel.gross@uni-ulm.de

* Corresponding author

Abstract

The effect of solvation on the adsorption of organic molecules on graphite at room temperature has been addressed with force-field molecular dynamics simulations. As a model system, the solvation of a bis(terpyridine) isomer in water and 1,2,4-trichlorobenzene was studied with an explicit solvation model. The inclusion of solvation has a noticeable effect on adsorption energies. Although the results of the various considered force fields differ quite significantly, they all agree that the adsorption of BTP from the TCB solvent is almost thermoneutral. The substrate simply acts as a template to allow a planar arrangement of the network, which is stabilized by the intermolecular interaction. Using an atomic thermodynamics approach, the order of the stability of various network structures as a function of the chemical potential is derived yielding a sequence in agreement with the experiment.

Introduction

The controlled formation of structured surfaces by the formation of hydrogen-bonded organic networks is of technological interest for future applications such as molecular electronics, organic photovoltaics [1] or functionalized host–guest systems [2] that may be used in heterogeneous catalysis. As a model system for ordered organic adlayers, bis(terpyridines) (BTPs) have been studied intensively in recent years [2-10]. They are known to adsorb in a flat configuration on various surfaces and to form self-organized ordered surface structures. In previous publications, we were able to show that combined DFT and force-field simulations can help to explain experimental obser-

vations in the adsorption behavior of BTPs on graphite [11,12]. One example is the observation of blurred STM images of phthalocyanine molecules adsorbed as guest molecules in a BTP host network, which is due to the fact that rotations of the host molecules are hardly hindered by barriers [6,11].

Recently it was shown by scanning tunneling microscopy (STM) experiments that 3,3′-BTP exhibits a variety of adlayer structures at the interface between highly oriented pyrolytic graphite (HOPG) and the liquid as a function of the concentration in solution [6]. The resulting structures, i.e., one hexagonal,

two closely related linear, and one densely packed linear structure, were ordered according to their packing density as a function of the concentration. Furthermore, it was found that the presence of the liquid has a decisive influence on the structure formation: whereas at the liquid/HOPG interface three closely related linear patterns and one hexagonal two-dimensional pattern were identified, at the gas/HOPG interface only one of the linear patterns and the hexagonal structure were found. The concentration dependence of the different surface structures was rationalized within a thermodynamic model [13]. However, in the calculations of the adsorption energies the solvent was entirely neglected, as is typically done in calculations addressing the adsorption of organic molecules [14], even if experimentally they are deposited from a solution.

Hence, we here address the adsorption of BTP on graphite in the presence of a liquid phase in order to assess the explicit influence of the solvent on the molecular adsorption at the solid/liquid interface. Note that the modeling of a liquid requires the determination of free energies instead of just total energies, which means that computationally expensive statistical averages have to be performed in order to evaluate free-energy differences. Although electronic structure calculations based on density functional theory can reproduce the properties of planar arrangements of aromatic molecules satisfactorily [15-18], the large size of the considered systems and the requirement to perform thermal averages make first-principles electronic-structure calculations computationally prohibitively expensive. Therefore we employed classical force fields as included in the Forcite module of the Accelrys' Materials Studio package to describe the interaction between adsorbate, substrate and solvent. It is true that the force fields in this package tend to overestimate BTP adsorption energies on graphite [12]. Still, trends in the stability of BTP stuctures on graphite as a function of the environment should still be reproduced.

As a solvent, we have taken into account 1,2,4-trichlorobenzene (TCB), which was used in the experimental work [6]. Additionally, we have also considered water as a reference since many organic molecules are deposited from aqueous solutions. In this work, we show that the molecule–solvent interaction has an important influence on the stability range of the considered structures. Still, the order of the stability as a function of the chemical potential is not modified by the inclusion of the solvent effects. Because of the strong TCB–BTP interaction, the adsorption of a single BTP molecule on graphite out of a TCB solution is almost thermoneutral. Hence, it is the intermolecular interaction in the hydrogen-bonded networks on graphite that stabilizes the molecular layers; the surface just acts as a template to allow a planar arrangement of the hydrogen-bonded network.

Computational details

In this study, force-field molecular dynamics are used in order to describe the adsorption properties of solvated BTP molecules on graphite. The structure of 3,3′-BTP, which is known for its high versatility in surface structures is shown in Figure 1. There are of course force fields that reproduce structural properties of water quite satisfactorily [19,20]. However, here we need general-purpose force fields that are able to describe different solvents, solvent–molecule and molecule–surface interactions equally well. Hence, we use the Universal (UFF) [21], Compass (condensed-phase optimized molecular potentials for atomistic simulation studies) [22], Dreiding [23] and Consistent Valence (CVFF) [24] force fields included in the Forcite module of the Accelrys' Materials Studio package.

Figure 1: Structure of the 3,3′-BTP molecule.

The graphite surface is modeled by a five-layer graphite (0001) slab. Convergence criteria are chosen according to the ultrafine settings of the program. Partial charges of the atoms are assigned with the Gasteiger [25] and QEq [26] methods for UFF and Dreiding, whereas charging methods are already included in the CVFF and Compass force fields.

As mentioned in the introduction, the theoretical treatment of liquids requires a consideration of the free energies and free-energy differences. Typically, free energy differences are determined by performing constrained MD simulations using either umbrella sampling schemes [27,28], free-energy perturbation methods [29] or some other appropriate thermodynamic integration scheme, such as the recently developed enveloping distribution sampling (EDS) method [30].

However, using one of these schemes often requires a series of molecular dynamics simulations. In order to derive the adsorption energy of the BTP molecules from solution at finite temperatures, we rather take advantage of the fact that BTP molecules on the surface and in solution replace approximately the same amount of solvent molecules. Hence, we determine the free enthalpy of adsorption ΔE_{ads}^{free} from the solvent according to

Figure 2: Structural models used to derive the free enthalpy of adsorption of a dissolved molecule: (a) adsorbed molecule at the substrate/solvent interface and (b) dissolved molecule above the substrate/solvent interface.

the scheme illustrated in Figure 2, i.e., it is evaluated as the difference of the free enthalpy of the molecule adsorbed at the substrate/solvent interface minus the free enthalpy of the molecule dissolved above the substrate/solvent interface:

$$\Delta E_{\text{ads}}^{\text{free}} = E_{\text{ads}}^{\text{free}} - E_{\text{diss}}^{\text{free}} . \qquad (1)$$

We also determine free enthalpies instead of free energies, in order to remain consistent with our previous thermodynamics calculations that we want to improve by using the solvent model. The free enthalpies are derived as the energy average through the molecular dynamics simulations, which were performed within the NPT ensemble at 298 K (Nosé thermostat) and at 0.0001 GPa (Berendsen barostat) after initial geometry optimization steps of the randomly chosen starting configuration according to [31]. The first 50 ps of the simulations with a time step of 1 fs were considered as the equilibration time; all averages were performed by using the subsequent 100–150 ps of simulation time.

The free enthalpies of adsorption in the presence of the solvent will be contrasted with the adsorption energies at the solid/gas interface, which were calculated as usual according to [32]

$$E_{\text{ads}} = E_{\text{mol/surf}} - \left(E_{\text{mol}} + E_{\text{surf}} \right). \qquad (2)$$

where $E_{\text{mol/surf}}$ is the total energy of the molecule/surface system, and E_{mol} and E_{surf} are the total energies of the isolated molecule and the surface alone, respectively.

In order to validate the reliability of the force fields used in this study, we have considered liquid densities and the solvation

energies in water and TCB. In order to be consistent with our scheme to determine the free enthalpies of adsorption, we estimated the solvation energy E_{solv} from the free enthalpy of the dissolved molecule $E_{\text{mol-solv}}^{\text{free}}$, the free enthalpy of the solvent alone $E_{\text{solvent}}^{\text{free}}$, and the enthalpy of the isolated molecule E_{mol} according to

$$E_{\text{solv}} = E_{\text{mol-solv}}^{\text{free}} - \left(E_{\text{solvent}}^{\text{free}} + E_{\text{mol}} \right). \qquad (3)$$

This procedure neglects effects due to the volume change of the solvent when the molecule is dissolved. However, due to the large number of solvent molecules included in the simulations, the influence of these effects should be negligible.

Results and Discussion
Validation step 1: liquid densities
As a first test case, the densities of liquid water and 1,2,4-trichlorobenzene (TCB) are considered, yielding an indication as to whether the intermolecular interactions within the solvent phase can be reproduced correctly by a force field. The calculated results are compared with the corresponding experimental values for water [33] and TCB [34].

For water, a strong variation between the different force-field results is observed (Figure 3). The average densities of the molecular dynamics trajectory range from 0.07 g/cm³ for UFF with Gasteiger charging, up to 1.01 g/cm³ for Dreiding with QEq charges. A value of 0.997 g/cm³ would have been expected [33]. With UFF, the deviation from the experiment is particularly high with both charging methods. Dreiding performs well with QEq charging, but not with Gasteiger
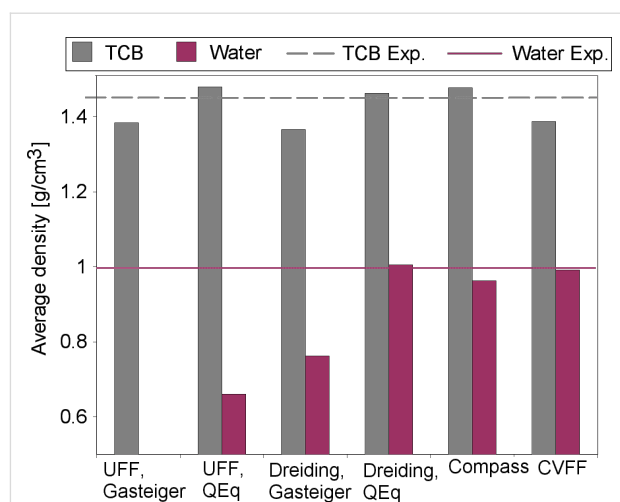

Figure 3: Force-field molecular dynamics densities of water and TCB at 298 K. Experimental values for water are taken from [33] and for TCB from [34].
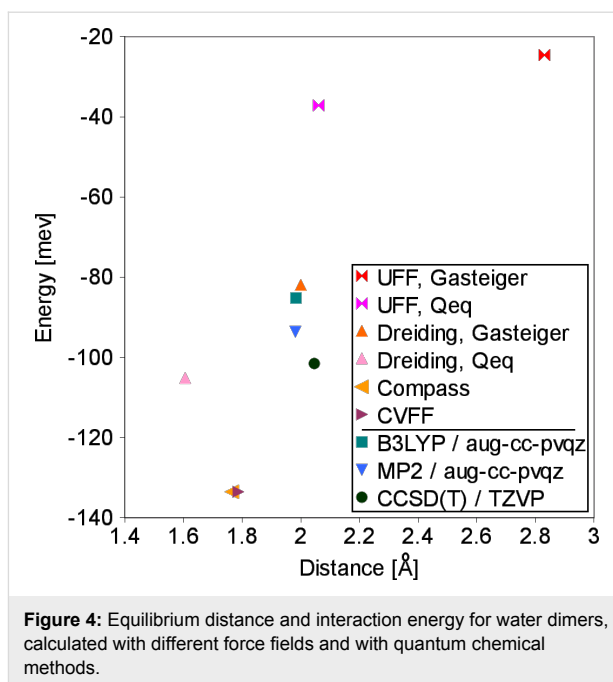
charges. Compass and CVFF also show a deviation from experimental values of less than 5%. Further Compass calculations with varying system size could show that the solvent density does not change noticeably over a wide range of system sizes. Starting from a system of 30 water molecules, the density remains at 0.96 g/cm^3. Using fewer water molecules leads to higher densities. But even when only three molecules are used, the density only increases by 8% to 1.04 g/cm^3.

The energy difference between an isolated molecule and a molecule in the condensed phase, the cohesive energy, is also relatively independent of the system size. In systems of 10 to 700 water molecules, the cohesive energy remains at −365 to −369 meV. With smaller systems, the cohesive energy decreases: With five molecules representing liquid water, it drops to −404 meV. We also checked the influence of the runtime of the trajectories on the average values. Total runtimes of 150 ps are used in order to evaluate the influence of the length of equilibration phase and actual trajectory. For the larger systems, the extreme cases of 20 ps equilibration time and 130 ps runtime on the one hand, and of 100 ps equilibration and only 50 ps runtime on the other hand differ in average potential energy by only a few millielectronvolts. The standard deviation in the potential energy remains below 10 meV per molecule for cell sizes above ten molecules.

In order to understand the reason for the discrepancy between calculated water densities and the experimental value, we determined the equilibrium O–H distance and interaction energy for a water dimer with different force fields and additionally also with quantum chemical methods. The corresponding results are plotted in Figure 4. The considered quantum chemical methods agree with an equilibrium distance of 1.98 to 2.05 Å, with interaction energies ranging from −85 to −102 meV. Interestingly enough, Dreiding with Gasteiger charging reaches a very similar result of 2.00 Å and −82 meV, but still the Dreiding/Gasteiger density is much too low. Dreiding/QEq, Compass and CVFF have stronger hydrogen bonds of 105 to 137 meV. Although they yield water–water distances that are too small, their densities agree very well with the experimental result. With less than 40 meV, UFF greatly underestimates the hydrogen bonds, resulting in particularly low densities.

TCB on the other hand is more accurately described by force fields. The force field densities vary between 1.37 g/cm^3 (Dreiding/Gasteiger) and 1.48 g/cm^3 (UFF/QEq). The deviation from the experimental density of 1.45 g/cm^3 [34] is less than 6% for all force fields.

In conclusion of this section, it is important to note that liquid water is only poorly reproduced by the force fields considered

Figure 4: Equilibrium distance and interaction energy for water dimers, calculated with different force fields and with quantum chemical methods.

in this study due to problems with the reliable description of intermolecular hydrogen bonds and liquid densities. For TCB on the other hand, the force-field results are reasonably accurate, possibly because hydrogen bonds are less important in the TCB bonding.

Validation step 2: solvation energies

As a further validation, we addressed the interaction between solvent and dissolved organic molecule, which should be reproduced accurately for a meaningful description of the system. As test systems, we considered the solvation of pyridine and benzene as small-but-similar models for the larger BTP molecule, which consists of pyridine and benzene rings. The resulting solvation energies evaluated according to Equation 3 are collected in Figure 5 and compared with the experimental solvation energies of −517 meV for pyridine and −329 meV for benzene in water [35].

Quantitatively, most of the force field results do not agree very well with the experiment. Dreiding/QEq reproduces 88% of the pyridine solvation energy. CVFF describes the benzene solvation rather well: it overestimates the energy by only 16%. UFF/Gasteiger is correct in a qualitative sense, pyridine has a higher gain in solvation energy than benzene. This is not achieved by any of the other force fields. Still, UFF/Gasteiger underestimates the solvation energies.

Both UFF/QEq and Dreiding/QEq calculations fail for benzene solvation, they overestimate the solvation energy by a factor of 3 to 4. On the other hand, pyridine solvation energies are too
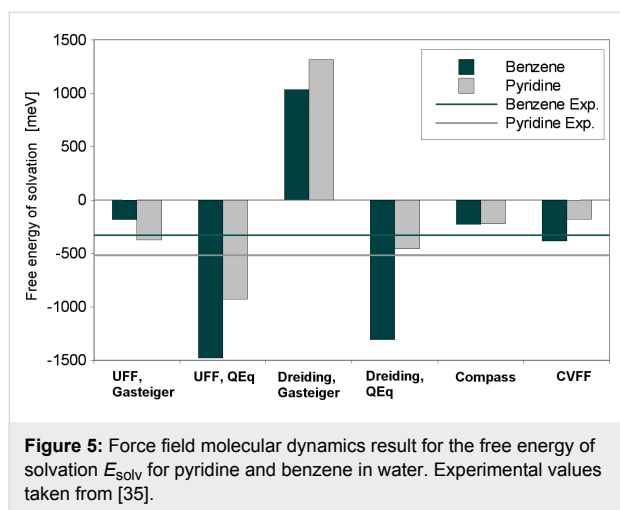
Figure 5: Force field molecular dynamics result for the free energy of solvation E_{solv} for pyridine and benzene in water. Experimental values taken from [35].

Figure 6: Force-field molecular dynamics result for the free energy of solvation E_{solv} for 3,3′-BTP in water and TCB.

small by a factor of 2 to 3 with CVFF and Compass. Dreiding/ Gasteiger calculations result in positive solvation energies, whereas negative values would be expected.

These results are certainly not satisfactory in a quantitative way. Obviously the problem with the description of the intermolecular hydrogen bonds directly translates to inaccurate solvation energies in water. Still, most of the force fields are able to show that pyridine and benzene have small negative solvation energies in water, so the method might still be useful for a more qualitative analysis of the BTP adsorption process.

Another problem might be the rather crude model we use that neglects the changes of volume in the system. However, if the number of water molecules is large enough, this volume change becomes smaller than the natural fluctuations in the volume throughout the trajectory. For the benzene in water case, with 300 water molecules the volume changes by 6% when a benzene molecule is added to the system whereas the standard deviation amounts to 8% of the average volume for the benzene–water solvated system. With a further increase of the
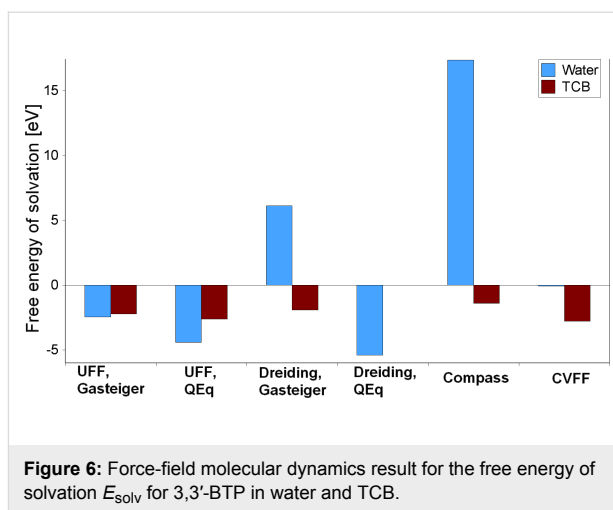
system size to 600 water molecules, the volume change amounts to less than 3%. Using more than 1200 water molecules brings about only small changes: For system sizes between 1200 and 2100 atoms, the volume change stays close to 1%, similar to the standard deviation.

Additionally, the BTP solvation process has been addressed. Note that due to the approximate nature of the determination of the solvation energy according to Equation 3 the results that are collected in Figure 6 and Table 1 can only be of a qualitative manner. However, to the best of our knowledge, there are no experimental values for the BTP solvation energies available. It is simply known that BTP molecules dissolve easily in TCB but are not soluble in water [4].

For the molecular dynamics simulations of the solvated BTP molecule, rather large unit cells containing 395 to 400 water molecules or 106 to 143 TCB molecules were used. This is a compromise between cells being large enough for minimal volume effects and being small enough for an efficient computational treatment.

Table 1: Solvation (E_{solv}) and adsorption (E_{ads}) energies of 3,3′-BTP in eV calculated using different force fields.

| | E_{solv} | | E_{ads} | | |
	Water	TCB	Water	TCB	Vacuum
UFF, Gasteiger	−2.459	−2.225	−4.270	0.137	−4.560
UFF, QEq	−4.413	−2.625			
Dreiding, Gasteiger	6.112	−1.925	−2.696	−0.142	−3.941
Dreiding, QEq	−5.404	−0.016			
Compass	17.349	−1.406	−1.409	0.072	−4.027
CVFF	−0.068	−2.787	−3.569	−0.052	−7.312
Experiment				−0.340 [2]	−2.54 [12]

The solvation energies of BTP in water and in TCB again vary strongly with the force field used. Not all force fields can reproduce the experimental findings at least in a qualitative way. Both UFF calculations and Dreiding/QEq result in a higher energy gain for the dissolution in water. With about 200 meV, the difference between solvation in water and TCB is only small for UFF/Gasteiger. It is more significant in the UFF/QEq and the Dreiding/QEq calculations with nearly 2 eV and more than 5 eV, respectively. Thus QEq charging is not used any more for the subsequent calculations.

Only with Compass, CVFF and Dreiding/Gasteiger, do the force field results show that it is energetically more favorable to dissolve the BTP molecule in TCB than in water. The Compass result is probably closest to the experimental observations. Here, the solvation in water is clearly not favorable, and the difference from the TCB solvation is more than 18 eV. Dreiding/Gasteiger show a similar trend, but with 8 eV, the energy difference is considerably smaller. In the CVFF calculation, the difference is only about 3 eV and the solvation in water is not decidedly unfavorable from an energetic point of view.

Adsorption of a dissolved BTP molecule

Finally, we consider the adsorption energy of 3,3′-BTP on graphite under different conditions, namely for the BTP adsorption under vacuum conditions, at the solid/liquid interface with TCB as a solvent, as in the experiment, and additionally the case of adsorption of a BTP molecule from water. These numbers are listed in Table 1. Furthermore, in Figure 7 they are compared to the adsorption energy under vacuum conditions derived both from experiment and from DFT-D3 [36] calculations [12] with semi-empirical corrections for the van der Waals attraction. Obviously force fields significantly overestimate the

interaction between graphite and the BTP molecule, as can be seen from the vacuum results [12]. Yet, as we will see below, for the adsorption from solution, results in semi-quantitative agreement with the experiment are still obtained.

The free enthalpies of adsorption were derived as illustrated in Figure 2: MD simulations were performed for a BTP molecule adsorbed on the surface with a solvent atmosphere at 298 K and for a dissolved molecule that is not yet adsorbed. The comparison of the average potential energies for the two different cases then yields the free enthalpy of adsorption of a dissolved molecule. The adsorption energies obtained following this procedure show surprising results: Even though the solvation and adsorption energies strongly vary with the force field, the general trend is the same in each case. While the adsorption from water leads to a high gain in energy, the adsorption from TCB is rather neutral in its energy balance. With UFF, adsorption from water yields over 90% of the energy that is obtained under vacuum conditions. Dreiding still reaches nearly 70%. With Compass and CVFF, this ratio drops to 35 and 49%, respectively. The adsorption energy from TCB is much smaller with all force fields, it ranges from 137 meV with UFF to −142 meV with Dreiding. This agrees qualitatively rather well with experimental findings, where the analysis of Langmuir adsorption isotherms has resulted in a 3,3′-BTP adsorption enthalpy of −340 meV at the solid/liquid interface [2]. In contrast to the observations under vacuum conditions, it might be that force fields tend to underestimate the interaction energy.

These findings can be rationalized fairly easily. BTP interacts strongly with the graphite surface via van der Waals interaction [12], thus the adsorption under vacuum conditions leads to a relatively high gain in energy. BTP also interacts strongly with the TCB solvent, which is why it can be dissolved in TCB. When it adsorbs on the surface, it gains the adsorption energy, but at the same time it loses part of the interaction with the solvent. In total, both contributions seem to balance out. The interaction between BTP and water, on the other hand, is rather weak. So in the hypothetical case of BTP adsorption from water, the system would gain a large adsorption energy, but the loss of BTP-water interaction is rather small, such that in total, an energy gain is associated with the adsorption.

Phase stability

Experimentally, it was observed that BTP on graphite in TCB solution exhibits a series of different structures, one hexagonal, two closely related linear, and one densely packed linear structure, that were ordered according to their packing density as a function of the concentration [6]. These structures are illustrated in Figure 8. Also the coexistence of different structures was found.
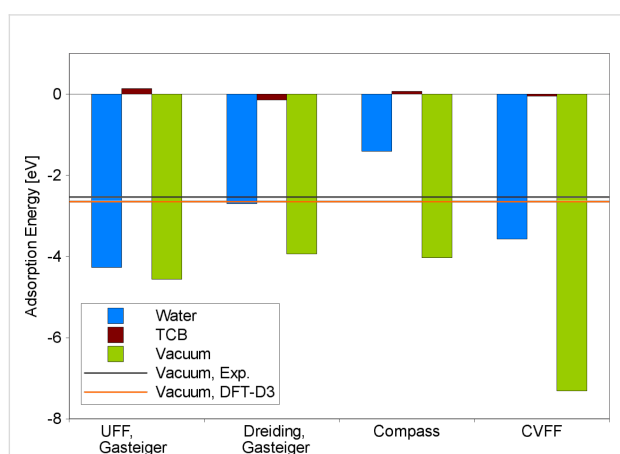

Figure 7: Adsorption energy of a 3,3′-BTP molecule on graphite: under vacuum conditions and at the solid/liquid interface from water or TCB, respectively. Experimental value and DFT-D3 result from [12].
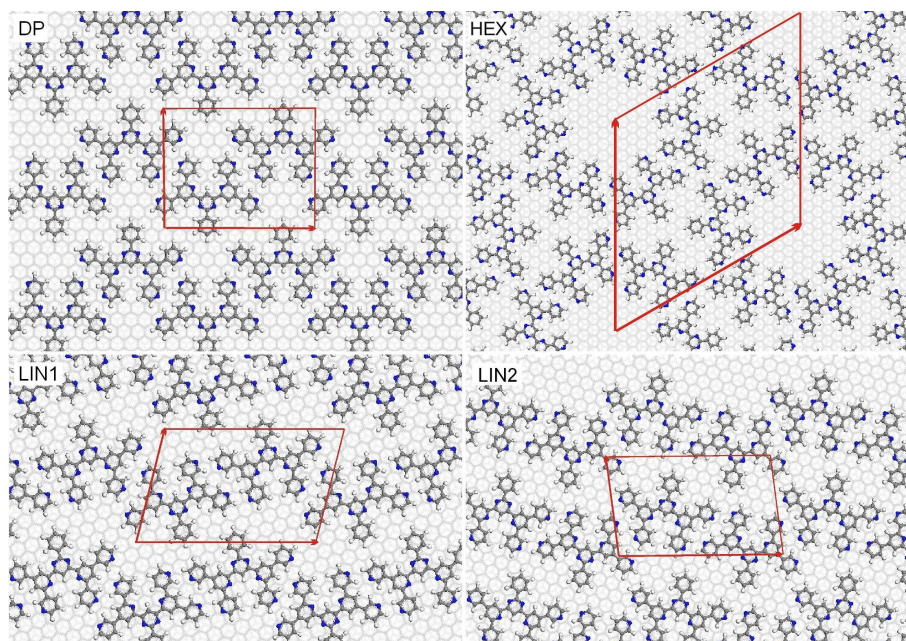
Figure 8: Structural models of the different 3,3′-BTP surface structures that have been observed at the liquid/solid interface.

Thermodynamically, the stability of the adsorbate structures is governed by the free energy. Neglecting entropic effects, the free energy of adsorption can be expressed as [13,32]

$$\Delta G = \rho \left(E_{ads} - \mu \right), \qquad (4)$$

where E_{ads} is the adsorption energy per molecule in a given structure and ρ is the density of molecules per surface area in this structure. μ is the chemical potential, which depends monotonically on the concentration. A plot of the free energy of adsorption ΔG versus the chemical potential μ shows which phase is lowest in free energy at a given potential range. Using the experimentally derived adsorption enthalpy [2] of a single molecule and estimated values for the hydrogen bonding between the molecules, the sequence of observed structures as a function of concentration could be reproduced [2]. This sequence could also be reproduced based on adsorption energies obtained from force-field calculations at the gas/solid interface, but at an entirely different range of chemical potentials because of the rather different energy reference related to molecules in the gas phase.

The calculations presented so far have already shown that the inclusion of TCB into the model has a drastic effect. It may well also be that the solvent affects the strength of the intermolecular interactions. We have therefore estimated ΔG at 298 K taking the presence of the solvent into account.

MD runs with the full surface structures including graphite, BTP and TCB were carried out corresponding to an explicit solvation model. Due to the computational effort of these very large cells, some simplifications were necessary. Only three carbon layers could be used in order to represent the graphite surface. MD runs covered 150 ps, with the initial 50 ps as equilibration time. For each phase, one trajectory run for the adsorbed ordered surface structure in the presence of the solvent and another trajectory run for the BTP molecules in solution, as illustrated in Figure 2 using the same unit cell, were performed. Ideally, no interaction between a BTP molecule and the surface or another BTP molecule should occur in the latter simulations. These simulations were done by using the Compass force field, which provided the most reliable results.

As a result, the adsorption energies in Table 2 are obtained. These adsorption energies combine the BTP/graphite interaction with intermolecular interactions and solvent effects. The

Table 2: Compass adsorption energy of 3,3′-BTP per molecule in different surface structures in electronvolts (eV) at the gas/solid interface and free enthalpy of adsorption at the liquid/solid interface at 298 K.

	DP	LIN1	LIN2	HEX
Vacuum conditions	−4.029	−4.173	−4.475	−4.491
Full solvation	0.203	−0.0775	−0.339	−0.0564

adsorption enthalpies range from 0.203 eV for the DP structure to −0.339 eV for the LIN2 structure. The Compass force field adsorption energy of a single BTP molecule amounts to 0.072 eV (see Table 1). This indicates that for the LIN1, LIN2 and HEX structures, whose adsorption enthalpies are negative, the intermolecular interaction is attractive, whereas for the DP structure the packing is so dense that the intermolecular interaction is already repulsive. The range of adsorption enthalpies is 80 meV larger than the range of adsorption energies of the corresponding structures at the gas/solid interface. Furthermore, at the gas/solid interface all structures are energetically more favorable per adsorbed molecule than the isolated adsorbed 3,3′-BTP molecule whose adsorption energy is −4.027 eV. This indicates that the intermolecular interaction is weakened by the presence of the solvent.

The phases in Figure 9 are ordered according to their packing densities, in agreement with the experiment. The broader range of adsorption energies now translates to a broad range of chemical potential values over which the phase transitions occur. In agreement with the semiempirical results, the transition between the LIN1 and LIN2 phases is found at a slightly positive chemical potential. However, compared to the semiempirical results, the HEX–LIN2 and LIN1–DP transitions occur at noticeably lower and higher chemical potentials, respectively. According to Figure 9, the HEX phase should not be observed since the free energy of adsorption is positive which means that the BTP-uncovered substrate is more stable. However, it is also apparent how close the two curves of the HEX and the LIN2 phases, on the one hand, and of the LIN1 and DP phases on the other hand are. Given the uncertainty of the force-field calculations, it may well be that the stability range of the LIN1 and LIN2 phases are smaller. It should also be noted that the stability ranges shown

in Figure 9 are based on the assumption of thermal equilibrium. Kinetic effects in the structure formation are not taken into account, which may lead to the formation of metastable structures.

Conclusion

The adsorption of 3,3′-BTP on graphite in the presence of water and TCB as solvents has been studied by molecular dynamics simulations at room temperature using various force fields. Whereas the results concerning water as a solvent show a wide spread between the different force fields, the results for TCB as a solvent are more consistent among the considered force fields. They all yield the result, in agreement with the experiment, that the adsorption of a single BTP molecule out of the TCB solvent is almost thermoneutral, i.e., it is not associated with a significant energy gain. Consequently, the formation of ordered hydrogen-bonded network structures of the BTP molecules in the presence of TCB as a solvent is mainly stabilized through the intermolecular interactions. The substrate basically only acts as a template allowing the planar arrangement of the BTP molecules. Finally, the stability of ordered BTP network structures on graphite at room temperature has been addressed within an atomic thermodynamics approach. In agreement with the experiment, four different phases are found to be ordered according to their packing densities as a function of the concentration of the BTP molecules in the solvent. However, the stability ranges of the linear phases seem to be too broad, caused probably by uncertainties in the force-field calculations.

Acknowledgements

Figure 9: Plot of the free adsorption enthalpy of different 3,3′-BTP phases against the chemical potential obtained with fully solvated surface structures by using the Compass force field.

References

1. Ma, C.-Q.; Mena-Osteritz, E.; Debaerdemaeker, T.; Wienk, M. M.; Janssen, R. A. J.; Bäuerle, P. *Angew. Chem., Int. Ed.* **2007,** *46,* 1679–1683. doi:10.1002/anie.200602653

2. Meier, C.; Landfester, K.; Künzel, D.; Markert, T.; Groß, A.; Ziener, U. *Angew. Chem., Int. Ed.* **2008,** *47,* 3821–3825. doi:10.1002/anie.200705527

3. Ziener, U.; Lehn, J.-M.; Mourran, A.; Möller, M. *Chem.–Eur. J.* **2002,** *8,* 951–957. doi:10.1002/1521-3765(20020215)8:4<951::AID-CHEM951>3.0.CO;2-9

4. Meier, C.; Ziener, U.; Landfester, K.; Weihrich, P. *J. Phys. Chem. B* **2005,** *109,* 21015–21027. doi:10.1021/jp054271d

5. Ziener, U. *J. Phys. Chem. B* **2008,** *112,* 14698–14717. doi:10.1021/jp805846d
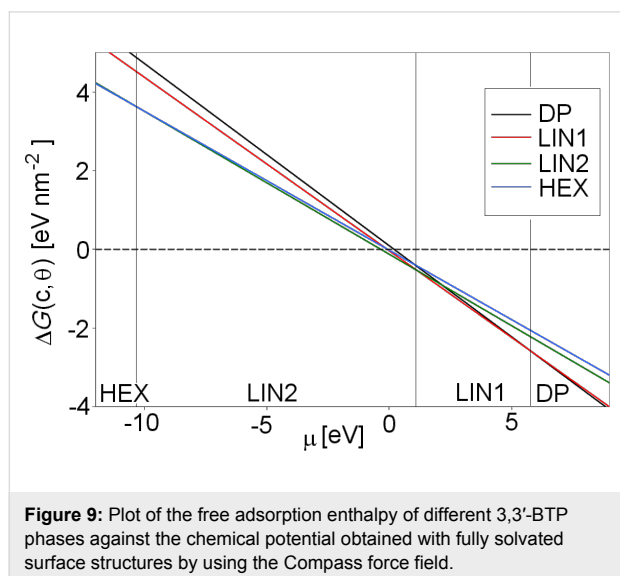
6. Meier, C.; Roos, M.; Künzel, D.; Breitruck, A.; Hoster, H. E.; Landfester, K.; Groß, A.; Behm, R. J.; Ziener, U. *J. Phys. Chem. C* **2010,** *114,* 1268–1277. doi:10.1021/jp910029z

7. Caterbow, D.; Künzel, D.; Mavros, M. G.; Groß, A.; Landfester, K.; Ziener, U. *Beilstein J. Nanotechnol.* **2011,** *2,* 405–415. doi:10.3762/bjnano.2.46

8. Roos, M.; Künzel, D.; Uhl, B.; Huang, H.-H.; Alves, O. B.; Hoster, H. E.; Groß, A.; Behm, R. J. *J. Am. Chem. Soc.* **2011,** *133,* 9208–9211. doi:10.1021/ja2025855

9. Roos, M.; Uhl, B.; Künzel, D.; Hoster, H. E.; Groß, A.; Behm, R. J. *Beilstein J. Nanotechnol.* **2011,** *2,* 365–373. doi:10.3762/bjnano.2.42

10. Waldmann, T.; Künzel, D.; Hoster, H. E.; Groß, A.; Behm, R. J. *J. Am. Chem. Soc.* **2012,** *134,* 8817–8822. doi:10.1021/ja302593v

11. Künzel, D.; Markert, T.; Groß, A.; Benoit, D. M. *Phys. Chem. Chem. Phys.* **2009,** *11,* 8867–8878. doi:10.1039/b907443k

12. Künzel, D.; Tonigold, K.; Kučera, J.; Roos, M.; Hoster, H. E.; Behm, R. J.; Groß, A. *ChemPhysChem* **2011,** *12,* 2242–2245. doi:10.1002/cphc.201100240

13. Reuter, K.; Scheffler, M. *Phys. Rev. B* **2001,** *65,* 035406. doi:10.1103/PhysRevB.65.035406

14. Kučera, J.; Groß, A. *Langmuir* **2008,** *24,* 13985–13992. doi:10.1021/la802368j

15. Yu, M.; Wang, J.; Mura, M.; Meng, Q.-Q.; Xu, W.; Gersen, H.; Lægsgaard, E.; Stensgaard, I.; Kelly, R. E. A.; Kjems, J.; Linderoth, T. R.; Kantorovich, L. N.; Besenbacher, F. *ACS Nano* **2011,** *5,* 6651–6660. doi:10.1021/nn202157m

16. Patra, A.; Wijsboom, Y. H.; Leitus, G.; Bendikov, M. *Chem. Mater.* **2011,** *23,* 896–906. doi:10.1021/cm102395v

17. Waldmann, T.; Nenon, C.; Tonigold, K.; Hoster, H. E.; Groß, A.; Behm, R. J. *Phys. Chem. Chem. Phys.* **2012,** *14,* 10726–10731. doi:10.1039/C2CP40800G

18. Rittmeyer, S. P.; Groß, A. *Beilstein J. Nanotechnol.* **2012,** *3,* 909–919. doi:10.3762/bjnano.3.101

19. Crozier, P. S.; Rowley, R. L.; Henderson, D. *J. Chem. Phys.* **2000,** *113,* 9202. doi:10.1063/1.1320825

20. Bukowski, R.; Szalewicz, K.; Groenenboom, G. C.; van der Avoird, A. *Science* **2007,** *315,* 1249–1252. doi:10.1126/science.1136371

21. Rappé, A. K.; Casewit, C. J.; Colwell, K. S.; Goddard, W. A., III; Skiff, W. M. *J. Am. Chem. Soc.* **1992,** *114,* 10024–10035. doi:10.1021/ja00051a040

22. Sun, H. *J. Phys. Chem. B* **1998,** *102,* 7338–7364. doi:10.1021/jp980939v

23. Mayo, S. L.; Olafson, B. D.; Goddard, W. A., III. *J. Phys. Chem.* **1990,** *94,* 8897–8909. doi:10.1021/j100389a010

24. Dauber-Osguthorpe, P.; Roberts, V. A.; Osguthorpe, D. J.; Wolff, J.; Genest, M.; Hagler, A. T. *Proteins: Struct., Funct., Genet.* **1988,** *4,* 31–47. doi:10.1002/prot.340040106

25. Gasteiger, J.; Marsili, M. *Tetrahedron* **1980,** *36,* 3219–3228. doi:10.1016/0040-4020(80)80168-2

26. Rappé, A. K.; Goddard, W. A., III. *J. Phys. Chem.* **1991,** *95,* 3358–3363. doi:10.1021/j100161a070

27. Torrie, G. M.; Valleau, J. P. *J. Comput. Phys.* **1977,** *23,* 187–199. doi:10.1016/0021-9991(77)90121-8

28. Hartnig, C.; Koper, M. T. M. *J. Chem. Phys.* **2001,** *115,* 8540. doi:10.1063/1.1408295

29. Zwanzig, R. W. *J. Chem. Phys.* **1954,** *22,* 1420–1426. doi:10.1063/1.1740409

30. Christ, C. D.; van Gunsteren, W. F. *J. Chem. Phys.* **2007,** *126,* 184110. doi:10.1063/1.2730508

31. Hashem, Y.; Auffinger, P. *Methods* **2009,** *47,* 187–197. doi:10.1016/j.ymeth.2008.09.020

32. Groß, A. *J. Comput. Theor. Nanosci.* **2008,** *5,* 894.

33. Gardas, R. L.; Dagade, D. H.; Coutinho, J. A. P.; Patil, K. J. *J. Phys. Chem. B* **2008,** *112,* 3380–3389. doi:10.1021/jp710351q

34. Kohler, F.; Rott, E. *Monatsh. Chem.* **1954,** *85,* 703–718. doi:10.1007/BF00902321

35. Abraham, M. H.; Whiting, G. S.; Fuchs, R.; Chambers, E. J. *J. Chem. Soc., Perkin Trans. 2* **1990,** 291–300. doi:10.1039/p29900000291

36. Grimme, S.; Antony, J.; Ehrlich, S.; Krieg, H. *J. Chem. Phys.* **2010,** *132,* 154104. doi:10.1063/1.3382344

Synthesis and thermoelectric properties of Re$_3$As$_{6.6}$In$_{0.4}$ with Ir$_3$Ge$_7$ crystal structure

Valeriy Y. Verchenko[1], Anton S. Vasiliev[1], Alexander A. Tsirlin[2],
Vladimir A. Kulbachinskii[3], Vladimir G. Kytin[3] and Andrei V. Shevelkov[*1,§]

Address:
[1]Department of Chemistry, Lomonosov Moscow State University,
Moscow 119991, Russia, [2]National Institute of Chemical Physics and
Biophysics, 12618 Tallinn, Estonia and [3]Faculty of Physics,
Lomonosov Moscow State University, Moscow 119991, Russia

Email:
Andrei V. Shevelkov[*] - shev@inorg.chem.msu.ru

* Corresponding author
§ Fax: +7 495 939 4788.

Abstract

The Re$_3$As$_{7-x}$In$_x$ solid solution was prepared for $x \leq 0.5$ by heating the elements in stoichiometric ratios in evacuated silica tubes at 1073 K. It crystallizes with the Ir$_3$Ge$_7$ crystal structure, space group $Im\bar{3}m$, with a unit-cell parameter a ranging from 8.716 to 8.747 Å. The crystal structure and properties were investigated for a composition with $x = 0.4$. It is shown that indium substitutes arsenic exclusively at one crystallographic site, such that the As–As dumbbells with $d_{As–As} = 2.54$ Å remain intact. Re$_3$As$_{6.6}$In$_{0.4}$ behaves as a bad metal or heavily doped semiconductor, with electrons being the dominant charge carriers. It possesses high values of Seebeck coefficient and low thermal conductivity, but relatively low electrical conductivity, which leads to rather low values of the thermoelectric figure of merit.

Introduction

Thermoelectric materials with good efficiency are highly awaited by modern power engineering. Utilizing either the Seebeck or Peltier effects, it is possible to produce electricity from waste heat (e.g., that stemming from combustion in car engines) or to cool an environment under an external power supply. However, the efficiency of these processes depends on the efficiency of the thermoelectric material in question, which is defined by the value of the figure of merit $ZT = TS^2\sigma / \kappa$, where T is the absolute temperature, S the Seebeck coefficient, σ the electrical conductivity, and κ the thermal conductivity. It is shown in the literature [1] that the best thermoelectric materials are to be sought among narrow-gap semiconductors

composed of heavy elements, in which structural features favor low thermal conductivity [2]. Attempts to improve the *ZT* value have led to the investigation of various types of thermoelectrics beyond the long-known lead and bismuth tellurides [3,4]. Among new candidates are the filled skutterudites [5,6], semiconducting clathrates [7], disordered materials such as Zn_4Sb_3 [8], and various inorganic and intermetallic compounds with complex crystal structures [9,10]. Compounds with the Ir_3Ge_7 structure type, namely $Mo_3Sb_{5+\delta}Te_{2-\delta}$ [11], $Nb_3Sb_2Te_5$ [12] and $Re_3As_{7-x}Ge_x$ [13], belong to the latter type of potential thermoelectric materials and have recently shown promising *ZT* values.

All members of the Ir_3Ge_7 family crystallize in the cubic space group *Im−3m* and feature the M–M dumbbells inside the Archimedean antiprism of the non-transition-element atoms. The strong hybridization of the transition-metal d-orbitals with the p-orbitals of a non-transition element may lead to the opening of a band gap near the Fermi level [14]. As a result, compounds with 55 valence electrons per formula unit (f.u.) exhibit semiconductor-like behavior. The number of valence electrons can be tuned through the solid-solution formation. For instance, $Mo_3Sb_5Te_2$ and Re_3As_6Ge adopt 55 e^- per f.u. and should be semiconductors according to the band structure calculations. Their doped analogues, $Mo_3Sb_{5.4}Te_{1.6}$ and $Re_3As_{6.4}Ge_{0.6}$, display minor deviation from 55 e^- per formula. They behave as heavily doped semiconductors and possess the *ZT* values of 0.8 at 1050 K and 0.3 at 700 K, respectively [13]. To expand the Ir_3Ge_7 family and search for new promising thermoelectrics, we investigated different ways of obtaining new solid solutions based on Re_3As_7 or Mo_3Sb_7 compounds. In this paper, we report on the synthesis of the $Re_3As_{7-x}In_x$ solid solution ($x \leq 0.5$), its crystal and electronic structures, and its thermoelectric properties.

Experimental
Synthesis and analysis
Rhenium (−325 mesh, 99.99%, Alfa Aesar) and arsenic (−70 mesh, 99.99%, Alfa Aesar) powders and indium ingots (99.95%, Sigma Aldrich) were used as received. Phase purity of the starting materials was checked by using the standard X-ray diffraction technique, and in all cases no impurity phases were found. To synthesize the title solid solution, stoichiometric quantities of the starting elements were heated in evacuated silica tubes at 1073 K for 7 days with further cooling to room temperature in a shut off furnace. Firstly, the samples were analyzed by means of X-ray powder diffraction using a Stoe STADI-IP diffractometer with Cu Kα₁ radiation (Ge monochromator, λ = 1.540598 Å). To evaluate the lattice constants of the $Re_3As_{7-x}In_x$ solid solution, all X-ray diffraction patterns were recorded with Ge as an internal standard (*a* = 5.6576 Å). The data were treated with the program package Stoe WinXPOW. Secondly, the obtained samples were analyzed with a JSM JEOL scanning electron microscope operated at 20 kV and equipped with an EDX detection system INCA x-Sight. Both point-spectra acquisition and element mapping were used to investigate the elemental and phase composition of the samples.

Structure determination
The crystal structure was determined by the Rietveld method from the X-ray powder diffraction data. For the sample with the nominal composition $Re_3As_{6.6}In_{0.4}$, hereafter sample **S1**, the data were recorded with the Bruker D8 Advance diffractometer, Cu Kα₁ radiation (Ge monochromator, λ = 1.540598 Å). For the Rietveld refinements we used the TOPAS software (version 4.2, Bruker-AXS). The refinement enabled us to determine minor quantities of three impurity phases (Table 1) that were taken into account during the subsequent refinement. The atomic parameters taken from the crystal structure of Re_3As_7 [15] were

Table 1: Crystallographic data from the powder diffraction experiment for **S1**.

refined composition	$Re_3As_{6.70(3)}In_{0.30(3)}$
formula weight (g·mol⁻¹)	1095.041
T (K)	300
wavelength (Å)	1.540598
space group	*Im−3m* (No. 229)
cell dimensions, *a* (Å)	8.74231(6)
V (Å³)	668.157(14)
no. of formula units per cell	4
calculated density (g·cm⁻³)	10.88
2θ range (°)	17.00–85.01
R_p, R_{wp}, GOF	0.056, 0.077, 1.4
impurity phases (weight %)	Re 2.0%, InAs 2.3%, In_2O_3 1.0%

Table 2: Atomic coordinates and displacement parameters for **S1**.

site	Wyck.	x	y	z	B_{iso} (Å^2)	occupancy
Re	12e	0.3396(2)	0	0	0.60(3)	1Re
E1	12d	1/4	0	1/2	0.82(11)	0.90(1)As + 0.10(1)In
As2	16f	0.1662(2)	0.1662(2)	0.1662(2)	0.82(5)	1As

used as the starting model. The refinement showed that the unique position of the rhenium atom was fully occupied. One of the two positions of the arsenic atoms, namely, the 12d site, showed a remarkably low atomic displacement parameter and was subsequently refined as jointly occupied by indium and arsenic. The refinement led to the composition $Re_3As_{6.70(3)}In_{0.30(3)}$ in reasonable agreement with the starting (synthetic) composition. Crystallographic details of the refinement are shown in Table 1, and the atomic parameters are shown in Table 2. Selected interatomic distances are listed in Table 3.

Table 3: Selected interatomic distances for **S1**.

bond	distance (Å)
Re–E1 × 4	2.597(1)
Re–As2 × 4	2.553(1)
Re–Re × 1	2.805(3)
As2–As2 × 1	2.539(5)
As2–As2 × 3	2.905(3)

Electronic-structure calculations

The FPLO (full potential local orbitals) code was utilized for the electronic-structure calculations [16]. FPLO performs density functional calculations with the local density approximation (LDA) for the exchange–correlation potential [17]. The crystallographic data presented in Table 4 were used for the calculations [15]. The integrations in the k space were performed by an improved tetrahedron method [18] on a grid of $16 \times 16 \times 16$ k points evenly spread in the first Brillouin zone.

Table 4: Re_3As_7 crystallographic data used for electronic-structure calculations [15].

Space group *Im*−3*m* (No. 229), *a* = 8.7162(7) Å

site	Wyck.	x	y	z
Re	12e	0.3406(9)	0	0
As1	12d	1/4	0	1/2
As2	16f	0.1687(20)	0.1687(20)	0.1687(20)

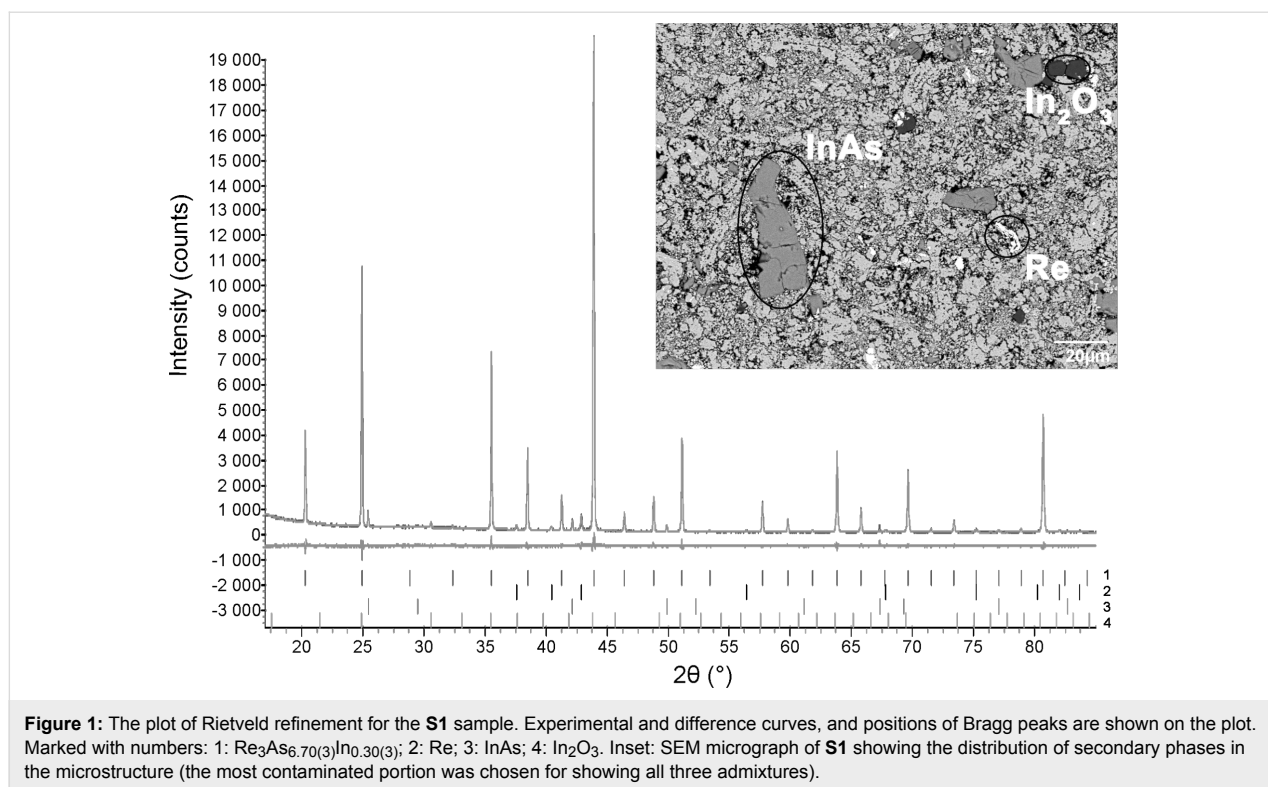## Physical property measurements

For thermal transport measurements, the sample **S1** was thoroughly ground and pressed at room temperature into a rectangular pellet of dimensions $8 \times 3 \times 2$ mm^3. The density of **S1** was estimated from the linear sizes of the pellet to be about 70% of the theoretical density. This pellet was used to measure the electrical conductivity (σ), the Seebeck coefficient (S), and the thermal conductivity (κ) in the temperature range of 77–300 K in a home-built setup. Resistance was determined from the voltage drops by applying a four-probe method in accordance with Ohm's law, i.e., $R = \Delta V/I$. The current (I) was scanned in the range between 2.5 µA and 16 mA, and subsequently σ was calculated after measuring the length between the contacts (L) according to $\sigma = L/(AR)$, with the area $A = 3 \times 2$ mm^2. The Seebeck coefficient and thermal conductivity were measured by using an internal standard to determine the temperature difference in a custom-designed sample puck that was plugged into the cold finger of a closed-cycle refrigerator. All measurements were performed under dynamic vacuum.

For the magnetization measurements, powder samples of Re_3As_7 and **S1** were loaded into plastic capsules. Measurements were performed with the VSM setup of Quantum Design PPMS in external fields of 0.1, 0.5, 1, 2, and 5 T. To estimate the diamagnetic contribution from the sample holder, an empty capsule was measured under the same conditions.

Results and Discussion
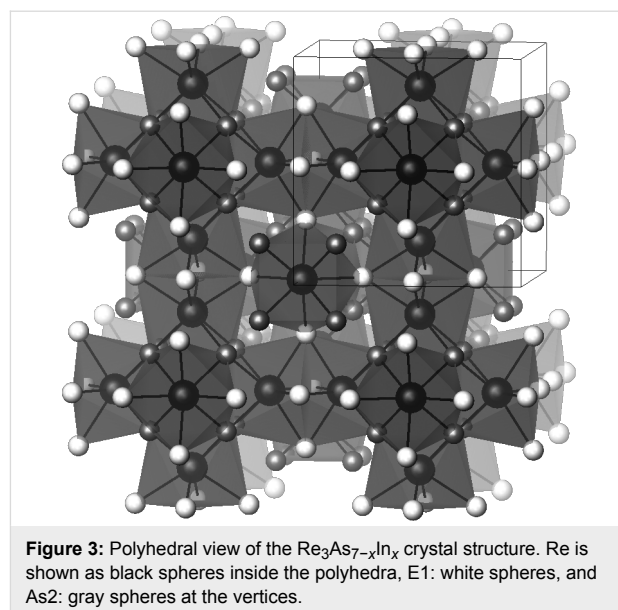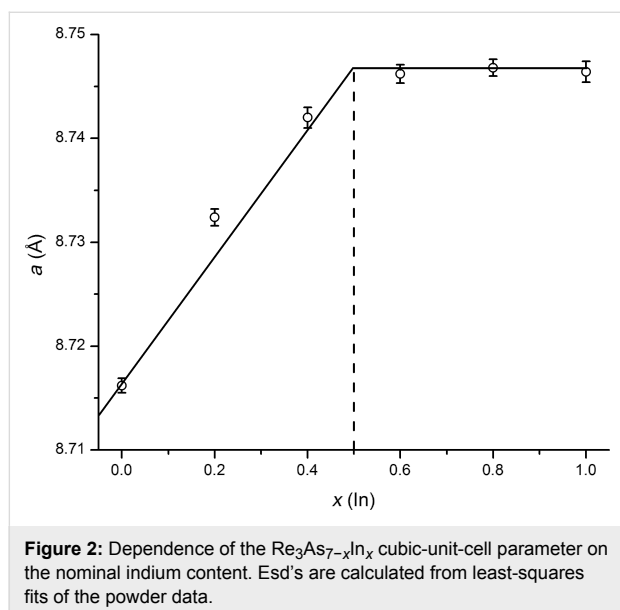## Synthesis, sample characterization and crystal structure

The synthesis of the $Re_3As_{7-x}In_x$ series with $x = 0$, 0.2, 0.4, 0.6, 0.8, and 1 from pure elements resulted in black powders that were stable in air. The obtained samples were analyzed by X-ray powder diffraction. All samples showed reflections of the main phase of the Re_3As_7 type (space group *Im*−3*m*), together with minor reflections of Re, InAs, and In_2O_3 admixtures, the presence of which was also confirmed with EPMA (Figure 1). In order to obtain single-phase samples, we tried to improve the synthetic procedure, but neither increasing the annealing time nor pressing the reactants into pellets led to phase-pure samples. Some general trends should be noted. For the samples with $0 \le x \le 0.4$, absolute intensities and, thus, quantities of admixtures remain constant, while for $x > 0.5$, quantities of Re and

Figure 1: The plot of Rietveld refinement for the **S1** sample. Experimental and difference curves, and positions of Bragg peaks are shown on the plot. Marked with numbers: 1: $Re_3As_{6.70(3)}In_{0.30(3)}$; 2: Re; 3: InAs; 4: In_2O_3. Inset: SEM micrograph of **S1** showing the distribution of secondary phases in the microstructure (the most contaminated portion was chosen for showing all three admixtures).

InAs start to increase. Additionally, we found by a linear interpolation that the unit cell parameter of the $Re_3As_{7-x}In_x$ solid solution increases up to $x = 0.5$, and then remains constant at higher x (Figure 2). All these facts suggest that the solid solution in question exists only for $x \leq 0.5$. The outermost composition $Re_3As_{6.5}In_{0.5}$ possesses exactly 55 valence electrons per formula unit. As mentioned above, this electron concentration should yield the semiconducting behavior for compounds with

the Ir_3Ge_7 structure type. Thus, the indium substitution for arsenic in Re_3As_7 could be used as a chemical modification to control transport properties of this system.

The crystal structure of the solid solution was studied for the **S1** sample by the Rietveld method from X-ray powder diffraction data (Figure 1, Table 1 and Table 2). The title compound crystallizes with the Ir_3Ge_7 crystal structure (Figure 3). This struc-

Figure 2: Dependence of the $Re_3As_{7-x}In_x$ cubic-unit-cell parameter on the nominal indium content. Esd's are calculated from least-squares fits of the powder data.

Figure 3: Polyhedral view of the $Re_3As_{7-x}In_x$ crystal structure. Re is shown as black spheres inside the polyhedra, E1: white spheres, and As2: gray spheres at the vertices.

ture can be described as being composed of rhenium-centered square antiprisms of E atoms, ReE$_8$ (E = As/In). Two square antiprisms are linked by sharing a square face. These pairs form the so-called Re$_2$E$_{12}$ barrels, the main building blocks of the crystal structure. The barrels, oriented along the main crystallographic directions, form two interpenetrating 3D networks in accordance with the body-centering and, thus, build up the entire crystal structure.

The formation of the solid solution may be associated with a chemical substitution on different crystallographic sites. There are two sites forming the coordination polyhedra of E atoms in the Ir$_3$Ge$_7$ structure type (Figure 4), and the substitution is possible for both sites depending on the chemical nature of the E elements. It is known from the literature that in the case of the Ge for As substitution in the parent compound Re$_3$As$_7$, all Ge atoms enter the As2 (16f) site [13]. In contrast, we have found that when indium substitutes for arsenic in Re$_3$As$_7$, all indium atoms are on the E1 (12d) site. The preference for the certain As position depends on different aspects, including size, nuclear charge, and number of valence electrons of the heteroatom. In particular, there is an E–E single bond between atoms occupying the 16f site, with a bond distance of 2.538(5) Å. Clearly, indium does not favor such a short bond to arsenic and, therefore, avoids the occupation of this site.
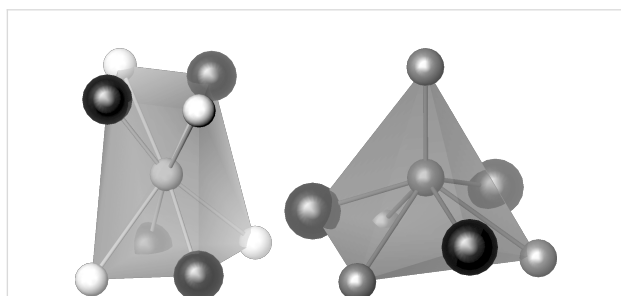

Figure 4: Coordination polyhedra of E1 (left) and As2 (right) sites in the crystal structure of Re$_3$As$_{7-x}$In$_x$.

Electronic structure, magnetic and thermo-electric properties

The computed density of states for Re$_3$As$_7$ is shown in Figure 5. The Fermi level lies slightly above the gap of 0.8 eV that separates the conduction band from the valence band. The nonzero DOS at E_F implies metallic behavior for the undoped Re$_3$As$_7$. Additionally, the steep slope of the DOS curve near E_F should lead to a high Seebeck coefficient according to $S \sim 1/N \cdot \partial N(E_F)/\partial E$ [19], provided that the system is made semiconducting by doping. Indeed, the absolute values of S for Re$_3$As$_{6.4}$Ge$_{0.6}$ exceed 150 µV·K^{-1} at high temperatures, thus leading to high values of ZT [13].
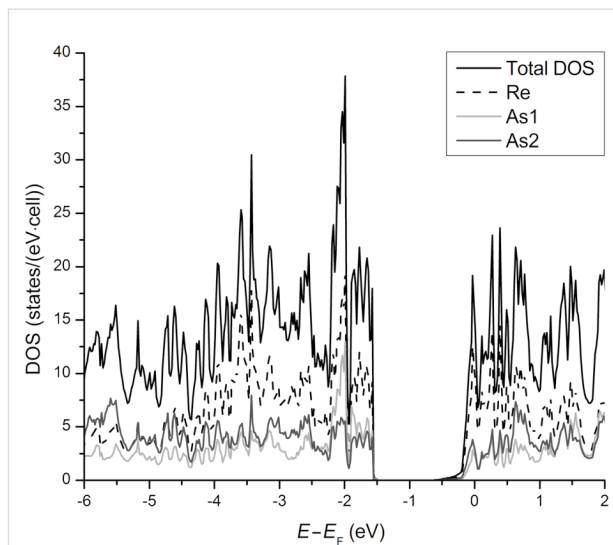

Figure 5: Density-of-states curve for Re$_3$As$_7$. Re contribution: dashed line, As1 and As2: light and dark gray lines, respectively.

In Re$_3$As$_7$, the calculated density of states at $E = E_F$ is 8.3 states/(eV·f.u.). For the solid solution Re$_3$As$_{6.7}$In$_{0.3}$ (the composition obtained from the Rietveld refinement of the X-ray powder diffraction data, see Table 1), the DOS is reduced to 5.15 states/(eV·f.u.), given the rigid-band shift with the assumption that Re$_3$As$_7$ possesses 56 valence electrons per f.u. and Re$_3$As$_{6.7}$In$_{0.3}$ 55.4 electrons. Therefore, both compounds should be metallic with a Pauli paramagnetic contribution to the total susceptibility $\chi = \chi_{dia} + \chi_P$, where χ_{dia} is core diamagnetism, and $\chi_P = \mu_B^2 \cdot N(E_F)$, with μ_B being the Bohr magneton [20]. The formula yields $\chi_P = 9 \times 10^{-5}$ and 5.5×10^{-5} emu/mol for Re$_3$As$_7$ and **S1**, respectively.

Experimentally, both Re$_3$As$_7$ and **S1** show substantial diamagnetism in the examined temperature range. However, the susceptibility curves, Figure 6, lie above the level of core diamagnetism $\chi_{dia} = -3.37 \times 10^{-4}$ emu/mol, computed for a combination of Re^{7+} and As(V) [21]. Therefore, both pure and In-doped Re$_3$As$_7$ feature an additional paramagnetic contribution to the susceptibility. The experimental value of $\chi_P = \chi - \chi_{dia} = 1.20(7) \times 10^{-4}$ emu/mol for Re$_3$As$_7$ is reasonably close to the one expected from the DOS at E_F. However, the calculation of χ_P substantially depends on the estimation method of χ_{dia}, especially for a compound that cannot be considered as ionic. For this reason, the calculated value of χ_P may differ from the experimental one. The susceptibility of the **S1** slightly decreases upon cooling but starts increasing below 80 K. While the low-temperature upturn could be due to a small number of paramagnetic impurities, the conspicuous increase in χ above 80 K does not conform to the Pauli paramagnetism and reflects deviations of **S1** from a simple metal.
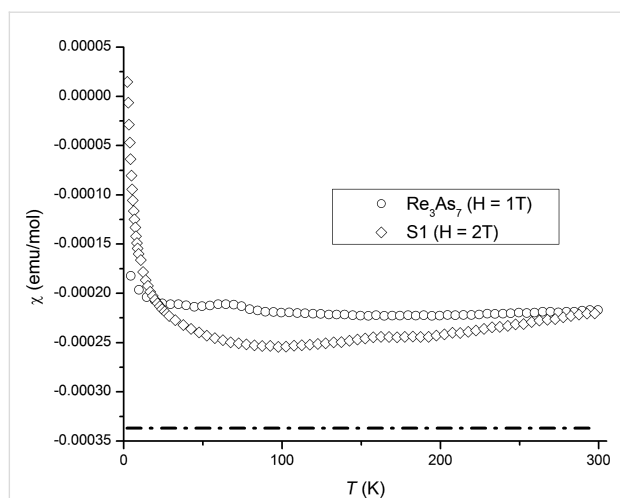
Figure 6: Magnetic susceptibility-versus-temperature plots for the Re$_3$As$_7$ and **S1** samples. The contribution of core diamagnetism is shown as a dash-dotted line.

Figure 7 compiles the plots of the electric conductivity (σ), Seebeck coefficient (S), thermal conductivity (κ), and ZT in the temperature range of 77–300 K for **S1**. S is negative in this temperature range, evidencing that the **S1** is an n-type conductor. However, the σ-versus-T behavior for the **S1** sample is neither metallic nor classically semiconducting, because σ increases almost linearly with temperature. Thus, **S1** can be regarded as a bad metal or degenerate semiconductor, consid-

ering the possible presence of defects, such as vacancies in its crystal structure, which was proposed earlier for Re$_3$As$_7$ [15]. In the Ir$_3$Ge$_7$ family, Re$_3$As$_{7-x}$Ge$_x$ exhibits n-type conductivity [13], while Mo$_3$Sb$_{5+\delta}$Te$_{2-\delta}$ is a p-type conductor [11]. The obtained values of S for **S1** are comparable with those for Re$_3$As$_{6.4}$Ge$_{0.6}$ and Mo$_3$Sb$_{5.4}$Te$_{1.6}$: -49, -72, and $+55$ μV·K^{-1} at 300 K, respectively [11,13]. Moreover, the extent of the substitution x in the Re$_3$As$_{7-x}$In$_x$ solid solution can be further optimized, and possibly lead to larger values of S. Unfortunately, the **S1** displays considerably lower values of the electrical conductivity compared to both Re$_3$As$_{7-x}$Ge$_x$ and Re$_3$As$_{7-x}$Sn$_x$ ($0.1 \leq x \leq 0.6$) [22]. For instance, the room-temperature value of 1090 Ω^{-1}·cm^{-1} for Re$_3$As$_{6.4}$Ge$_{0.6}$ [13] is about 3000 times larger than the observed value of 3.8 Ω^{-1}·cm^{-1} for **S1**.

The thermal conductivity of the sample **S1** is quite low. Its room-temperature value is 0.3 W·m^{-1}·K^{-1}, which is an order of magnitude lower than for the Ge- and Sn-substituted compounds. This may be caused by two factors: Firstly, it could be attributed to the preference of indium atoms for only one position within the crystal structure (increased structural complexity); secondly, relatively low density of the sample (about 70%) may diminish the thermal conductivity due to the sample porosity. The total thermal conductivity is a sum of the electronic (κ_e) and lattice (κ_L) parts. Taking into account the rather low electrical conductivity and applying the
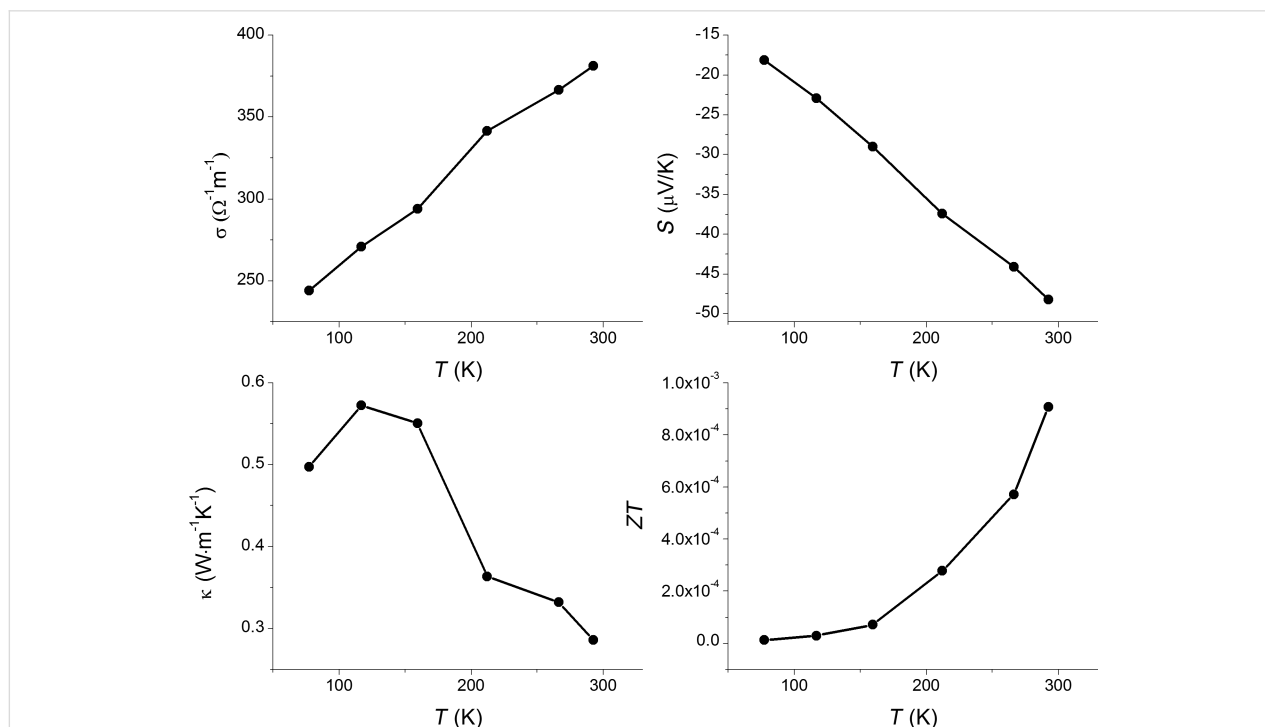

Figure 7: Thermoelectric properties of the **S1** sample as a function of temperature. Solid lines are drawn to guide the eye.

Wiedemann–Franz relation $\kappa_e = \sigma L T$, where L is the ideal Lorentz number, we estimate that the electronic part of the total thermal conductivity is negligibly small, and the observed value is essentially the lattice contribution to the thermal conductivity.

Combining the electrical conductivity, Seebeck coefficient and thermal conductivity, we calculate the temperature dependence of ZT shown in Figure 7. ZT increases with temperature, and reaches $ZT = 0.0008$ at room temperature, which is 30 times lower than for $Re_3As_{7-x}Ge_x$ [13]. Given the compositional width of the $Re_3As_{7-x}In_x$ solid solution and the low thermal conductivity of the investigated sample, we note that the optimum combination of S and σ for $Re_3As_{7-x}In_x$ is still to be found.

Conclusion

Chemical modification of Re_3As_7 resulted in the formation of the new Re_3As_7-based solid solution $Re_3As_{7-x}In_x$ ($x \leq 0.5$) with an Ir_3Ge_7 type of crystal structure. The indium for arsenic substitution occurs exclusively on the 12d site, thus keeping intact the As–As dumbbells with $d_{As-As} = 2.538(5)$ Å. While Re_3As_7 shows a Pauli paramagnetic contribution to the magnetic susceptibility in line with the results of band-structure calculations, the **S1** sample behaves as a bad metal or heavily doped semiconductor, with electrons being the dominant charge carriers. This compound combines low thermal conductivity with a relatively low electrical conductivity, and therefore, its thermoelectric figure of merit ZT reaches only 0.0008 at room temperature. Further optimization of the thermoelectric properties by varying the chemical composition of $Re_3As_{7-x}In_x$ is proposed.

Acknowledgements

References

1. Shevelkov, A. V. *Russ. Chem. Rev.* **2008,** *77,* 3–21. doi:10.1070/RC2008v077n01ABEH003746
2. Rowe, D. M. *CRC Handbook of Thermoelectrics;* CRC Press: Boca Raton, FL, 1995. doi:10.1201/9781420049718
3. Heremans, J. P.; Jovovic, V.; Toberer, E. S.; Saramat, A.; Kurosaki, K.; Charoenphakdee, A.; Yamanaka, S.; Snyder, G. J. *Science* **2008,** *321,* 554–557. doi:10.1126/science.1159725
4. Venkatasubramanian, R.; Colpitts, T.; Watko, E.; Lamvik, M.; El-Masry, N. *J. Cryst. Growth* **1997,** *170,* 817–821. doi:10.1016/S0022-0248(96)00656-2
5. Shi, X.; Yang, J.; Salvador, J.; Chi, M.; Cho, J.; Wang, H.; Bai, S.; Yang, J.; Zhang, W.; Chen, L. *J. Am. Chem. Soc.* **2011,** *133,* 7837–7846. doi:10.1021/ja111199y
6. Rogl, G.; Grytsiv, A.; Rogl, P.; Bauer, E.; Zehetbauer, M. *Intermetallics* **2011,** *19,* 546–555. doi:10.1016/j.intermet.2010.12.001
7. Shevelkov, A. V.; Kovnir, K. Zintl Clathrates. In *Zintl Phases;* Fässler, T. F., Ed.; Structure and Bonding, Vol. 139; Springer-Verlag: Berlin Heidelberg, 2011; pp 97–142. doi:10.1007/430_2010_25
8. Iverson, B. B. *J. Mater. Chem.* **2010,** *20,* 10778–10787. doi:10.1039/c0jm02000a
9. Zaikina, J. V.; Mori, T.; Kovnir, K. A.; Teschner, D.; Senyshin, A.; Schwarz, U.; Grin, Y.; Shevelkov, A. V. *Chem.–Eur. J.* **2010,** *16,* 12582–12589. doi:10.1002/chem.201001990
10. Gougeon, P.; Gall, P.; Al Orabi, R. A. R.; Fontaine, B.; Gautier, R.; Potel, M.; Zhou, T.; Lenoir, B.; Colin, M.; Candolfi, C.; Dauscher, A. *Chem. Mater.* **2012,** *24,* 2899–2908. doi:10.1021/cm3009557
11. Gascoin, F.; Rasmussen, J.; Snyder, G. J. *J. Alloys Compd.* **2007,** *427,* 324–329. doi:10.1016/j.jallcom.2006.03.030
12. Soheilnia, N.; Giraldi, J.; Assoud, A.; Zhang, H.; Tritt, T. M.; Kleinke, H. *J. Alloys Compd.* **2008,** *448,* 148–152. doi:10.1016/j.jallcom.2006.10.056
13. Soheilnia, N.; Xu, H.; Zhang, H.; Tritt, T. M.; Swainson, I.; Kleinke, H. *Chem. Mater.* **2007,** *19,* 4063–4068. doi:10.1021/cm0708517
14. Häussermann, U.; Elding-Pontén, M.; Svensson, C.; Lidin, S. *Chem.–Eur. J.* **1998,** *4,* 1007–1015. doi:10.1002/(SICI)1521-3765(19980615)4:6<1007::AID-CHEM1007>3.3.CO;2-Z
15. Jensen, P.; Kjekshus, A.; Skansen, T. *J. Less-Common Met.* **1969,** *17,* 455–458. doi:10.1016/0022-5088(69)90073-3
16. Koepernik, K.; Eschrig, H. *Phys. Rev. B* **1999,** *59,* 1743–1757. doi:10.1103/PhysRevB.59.1743
17. Perdew, J. P.; Wang, Y. *Phys. Rev. B* **1992,** *45,* 13244–13249. doi:10.1103/PhysRevB.45.13244
18. Blöchl, P. E.; Jepsen, O.; Andersen, O. K. *Phys. Rev. B* **1994,** *49,* 16223–16233. doi:10.1103/PhysRevB.49.16223
19. Kleinke, H. *Chem. Mater.* **2010,** *22,* 604–611. doi:10.1021/cm901591d
20. Ashcroft, N. W.; Mermin, N. D. *CRC Solid State Physics;* Brooks/Cole: Belmont, CA, 1976.
21. Bain, G. A.; Berry, J. F. *J. Chem. Educ.* **2008,** *85,* 532–536. doi:10.1021/ed085p532
22. Xu, H.; Holgate, T.; He, J.; Su, Z.; Tritt, T. M.; Kleinke, H. *J. Electron. Mater.* **2009,** *38,* 1030–1036. doi:10.1007/s11664-008-0623-0

Structural and thermoelectric properties of TMGa$_3$ (TM = Fe, Co) thin films

Sebastian Schnurr[*1], Ulf Wiedwald[1], Paul Ziemann[1], Valeriy Y. Verchenko[2] and Andrei V. Shevelkov[2]

Full Research Paper

Address:
[1]Institute of Solid State Physics, Ulm University, D-89081 Ulm, Germany and [2]Department of Chemistry, Lomonosov Moscow State University, Moscow 119991, Russia

Email:
Sebastian Schnurr[*] - sebastian.schnurr@uni-ulm.de

* Corresponding author

Abstract

Based on chemically synthesized powders of FeGa$_3$, CoGa$_3$, as well as of a Fe$_{0.75}$Co$_{0.25}$Ga$_3$ solid solution, thin films (typical thickness 40 nm) were fabricated by flash evaporation onto various substrates held at ambient temperature. In this way, the chemical composition of the powders could be transferred one-to-one to the films as demonstrated by Rutherford backscattering experiments. The relatively low deposition temperature necessary for conserving the composition leads, however, to 'X-ray amorphous' film structures with immediate consequences on their transport properties: A practically temperature-independent electrical resistivity of ρ = 200 μΩ·cm for CoGa$_3$ and an electrical resistivity of about 600 μΩ·cm with a small negative temperature dependence for FeGa$_3$. The observed values and temperature dependencies are typical of high-resistivity metallic glasses. This is especially surprising in the case of FeGa$_3$, which as crystalline bulk material exhibits a semiconducting behavior, though with a small gap of 0.3 eV. Also the thermoelectric performance complies with that of metallic glasses: Small negative Seebeck coefficients of the order of −6 μV/K at 300 K with almost linear temperature dependence in the range 10 K ≤ T ≤ 300 K.

Introduction

Intermetallic compounds usually behave as metals. In some cases, however, when a compound contains both, d- and p-block metals, semiconducting behavior may emerge. The number of such semiconducting intermetallic compounds is quite limited. For instance, RuAl$_2$ and RuGa$_2$ with TiSi$_2$ struc-

ture type [1], some Heusler alloys such as Fe$_2$VAl [2], and several intermetallics of FeGa$_3$ structure type [3,4] are known to be semiconductors, at least as bulk samples. The formation of the band gap in the isostructural compounds FeGa$_3$, RuGa$_3$ and RuIn$_3$ originates from the hybridization of the narrow d-bands

of the transition metal (TM) with rather broad p-bands of the group-III elements. In particular, such a hybridization also produces sharp features in the electronic density of states (DOS) close to the Fermi level, which are expected to be quite beneficial for an enhanced thermoelectric response [5,6]; large Seebeck coefficients of −350 µV/K [7] or even −563 µV/K [8] at room temperature were reported for bulk FeGa$_3$.

Recently, we found the existence of an unlimited solid solution between the isostructural intermetallics FeGa$_3$ and CoGa$_3$ [9]. With an increasing cobalt content in the Fe$_{1−x}$Co$_x$Ga$_3$ solid solution, the Fermi level shifts up to the conduction band and crosses peaks of high electronic density of states, ultimately leading to metallic and non-magnetic properties for CoGa$_3$. Thus, the composition of the solid solution x was found to be a tool to control the number of electronic states at the Fermi level $N(E_F)$ when the variation of $N(E_F)$ for different x was established from the results of band structure calculations and the nuclear quadrupole resonance (NQR) investigations of the nuclear spin–lattice relaxation rate. In line with these results, the Fe$_{1−x}$Co$_x$Ga$_3$ solid solution was found to behave as a metal for $x > 0.025$. For smaller values of x the system remains non-metallic, while the density of states at the Fermi level for $0 < x \leq 0.025$ increases drastically in comparison with pure FeGa$_3$. Such a sharp feature of $N(E_F)$ should lead to an appreciable thermoelectric performance, which can be tuned by accurate adjustment of the Co content.

Thus, having Fe$_{1−x}$Co$_x$Ga$_3$ solid solutions with tunable electronic properties available, the prospect of applications related to miniaturized sensors or generators of electrical energy naturally motivates to try and prepare corresponding thin films as well. This aim, however, immediately poses the question as to the most appropriate preparational method. Starting in the present work with hot-pressed pellets of FeGa$_3$ and CoGa$_3$, as well as of an Fe$_{0.75}$Co$_{0.25}$Ga$_3$ solid solution, one faces the main problem of picking a deposition technique which conserves these starting chemical compositions. Previous experience suggested applying pulsed laser deposition (PLD) for that purpose. However, it turned out that the pressed targets were not sufficiently stable but rather mechanically disintegrated during the ablation process. Thus, alternatively, thermal grain-by-grain evaporation from a powder source was applied leading to an averaging of the chemical composition over the thickness of the resulting films. In this way, stoichiometry changes due to fractional evaporation can be avoided as will be discussed below. Fractional evaporation and film disintegration is also a critical topic in the context of the preparation at elevated substrate temperatures or subsequent sample annealing in order to improve film crystallinity. In the present study with its emphasis on thermoelectric properties of the (TM)Ga$_3$ films,

the related figure of merit [10] ZT = $S^2\sigma T/\lambda$ (S: Seebeck coefficient, σ: electrical conductivity, λ: thermal conductivity, T: Kelvin temperature) indicates that low thermal conductivities may be of advantage in combination with reasonable high electrical conductivities. While the Seebeck coefficient is mostly dominated by asymmetric features of the electronic density of states $N(E)$ around E_F, σ and λ are influenced by both, electronic properties like $N(E_F)$ and the crystalline disorder effecting the corresponding transport mean-free-paths. As a consequence, in the present work focus is put on strongly disordered (TM)Ga$_3$ films relaxing the above mentioned fractional evaporation problem at elevated temperatures. Indeed, all (TM)Ga$_3$ films were evaporated onto substrates held at room temperature without subsequent annealing delivering nanocrystalline or even amorphous samples.

Experimental
Synthesis of bulk specimens
Powders of iron (Acros Organics, 99%) and cobalt (Alfa Aesar, 99.8%), and gallium rods (Aldrich, 99.999%) were used as received. Three specimens with chemical compositions FeGa$_3$, Fe$_{0.75}$Co$_{0.25}$Ga$_3$, and CoGa$_3$ were prepared by a standard ampoule technique. For that, the starting materials with total mass of 4 g in each case were sealed in quartz ampoules under a vacuum of $10^{−2}$ torr. Ampoules were annealed in a programmable furnace at 500 °C for seven days. Thereafter, the obtained powders were thoroughly ground in an agate mortar, sealed in quartz ampoules and annealed in a furnace at 600 °C for another seven days. The phase composition of the specimens was analyzed through a standard X-ray technique using a Stoe STADI-IP diffractometer with Cu Kα_1 radiation (Ge monochromator, λ_{Cu} = 1.540598 Å). In all cases powder diffraction patterns confirmed that single phase specimens were obtained (not shown). Calculated lattice parameters for the FeGa$_3$, Fe$_{0.75}$Co$_{0.25}$Ga$_3$, and CoGa$_3$ are in good agreement with previously reported values [8]. Resulting powders were pressed into cylindrical pellets with a diameter of 10 mm and a height of ca. 5–6 mm. These pellets and powders served as the starting materials for the thin-film preparation.

Preparation of thin films
The films were prepared by flash evaporation [11] of the corresponding FeGa$_3$, Fe$_{0.75}$Co$_{0.25}$Ga$_3$, or CoGa$_3$ powder. For that purpose, a rotating tube (inner diameter 3.5 mm) with an internal thread transports the powder towards its end, where the powder falls grain-by-grain onto an electrically heated tungsten boat and evaporates. Each grain (typical diameter 10 µm) contributes significantly less than a monolayer to the growing film. Due to the statistically varying composition of the grains, the resulting film stoichiometry is averaged over the film thickness with the mean value corresponding to the composition of

the starting powder. Film thicknesses in the range of 30–40 nm were realized at small rates of typically 1 nm/min as indicated by a quartz crystal monitor at a background pressure of 10^{-8} mbar with a cooling shield filled with liquid N_2. For the lateral patterning of the films evaporation was performed through masks in contact with the substrates (c-cut sapphire or glass) held at ambient temperature in all cases. In this way, film stripes of 500 μm width and 1.6 mm length were obtained. In the case of four-point resistance measurements performed within a ^{4}He-cryostat (in the range from 7 to 300 K by applying a current of 10 μA), the films were deposited on previously prepared gold contacts.

Structural and compositional characterization of thin films

To extract structural information of the thin films deposited onto sapphire substrates, X-ray diffraction measurements were performed with a Panalytical X'Pert diffractometer (Cu Kα) equipped with a silicon-based position-sensitive X'Celerator detector. Information about the chemical composition of the $(TM)Ga_3$ films was obtained by Rutherford backscattering spectroscopy (RBS) with 700 keV He^{2+} ions backscattered by 170° from samples deposited on silicon substrates. Simulating the experimental RBS spectra by the freely accessible software RUMP [12] delivers both, the chemical composition and the thickness of the films. Surface-roughness data of the $(TM)Ga_3$ films were obtained by applying height profilometry (Veeco Dektak 150) and averaging along 200 μm long traces (needle curvature 2.5 μm, contact force 50 mN).

Determination of thin film Seebeck coefficients

To determine the temperature-dependent Seebeck coefficients $S(T)$ of $(TM)Ga_3$ films, in a first step the films were complemented by strips of Pb to form $(TM)Ga_3$/Pb-thermocouples arranged on a thin (140 μm) glass substrate. Since $S(T)$ values for Pb are well documented in the literature [13], the corresponding values for $(TM)Ga_3$ films can be extracted from such thermocouples. The glass substrate is bridging the gap between the two parts of a split Cu sample holder, each half of which is equipped with a heater and thermometer allowing the temperature to be controlled independently. Thus, while ramping up the temperature of one half, the temperature of the other one is kept constant. When the resulting temperature difference ΔT reaches its maximum value ΔT_{max}, heating is reversed until, after crossing $\Delta T = 0$, the opposite maximum $-\Delta T_{max}$ is obtained. By periodically repeating this cycle, the average temperature $<T>$ linearly increases while ΔT exhibits a sawtooth-like behavior, which is closely followed by the corresponding sawtooth-curve for the thermoelectric voltage signal ΔU. The slope $\Delta U/\Delta T$ then delivers the Seebeck coefficient $S(<T>)$ assigned to the average

temperature. Performing these measurements within a ^{4}He cryostat allows the determination of $S(T)$ values in the temperature range between 7 K and 300 K. More experimental details about the above procedure can be found in [14].

Results and Discussion

The first aim was to confirm the expectation that flash evaporation of powders consisting of grains with chemical compositions statistically fluctuating around an average value leads to thin films with a stoichiometry reflecting this average. For this purpose RBS experiments were performed and two examples of $FeGa_3$ (42 nm) and $CoGa_3$ (47 nm) films on Si substrates, respectively, are presented in Figure 1. The film thicknesses given in brackets were determined by an in situ quartz crystal balance during evaporation. The experimental data in Figure 1a and Figure 1b are supplemented by RUMP simulations indicating a composition $FeGa_{3.2}$ with a film thickness of 40 nm and a composition $CoGa_3$ with a film thickness of 43 nm. Given the
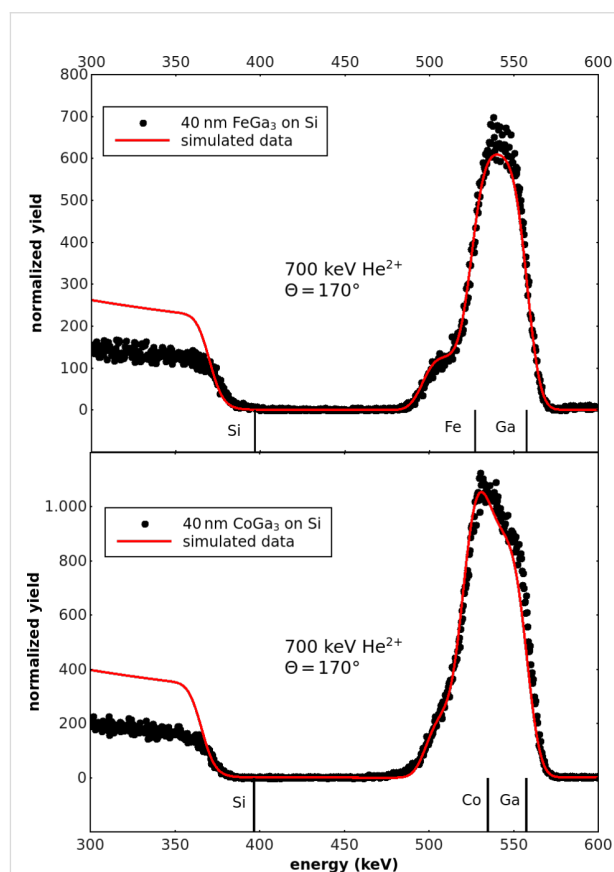

Figure 1: RBS spectra of $FeGa_3$ (a) and $CoGa_3$ (b) films deposited onto Si substrates. RUMP simulations (solid lines) deliver a composition of $FeGa_{3.2}$ with a thickness of 40 nm and a composition $CoGa_3$ with a thickness of 43 nm. Backscattering energies of Co, Ga and Si at the sample surface are indicated by vertical marks. The displacement of the Si edge of the substrate toward lower backscattering energies is caused by the film thickness.

typical RBS accuracy of 10%, in both cases the compositions are close to the expected ones of the starting material. Similarly, the thicknesses agree with those obtained from the quartz balance within an error of 9%. Thus, the RBS data confirm that flash evaporation of powders is an appropriate method to fabricate thin films reflecting closely the average chemical composition of the starting material. On the other hand, since Fe and Co are neighbors in the periodic table of the elements, their scattering contrast is too small to allow their thorough distinction in RBS. Thus, for $Fe_{1-x}Co_xGa_3$ solid solutions a determination of x by RBS was not possible.

Next, films prepared under identical conditions as those characterized by RBS were analyzed by XRD. Quite surprisingly, neither for $FeGa_3$ nor $CoGa_3$ any indication of Bragg peaks could be detected. Even the careful comparison of the film spectra to data of blank sapphire substrates tilted by 2° (to suppress the Bragg peaks of the single crystal) in order to provide a reference background did not reveal any significant differences. Thus, one can conclude that the film structure either is nanocrystalline with an average grain size below 4 nm or it is even amorphous. The conjecture of extremely small grains is supported by scanning electron microscopy (SEM) images taken with a high resolution Hitachi S5200 system (30 keV). Here, for all films completely featureless images were obtained suggesting flat amorphous or nanocrystalline samples with grains below the lateral SEM resolution of about 5 nm. Flatness could be corroborated by stylus measurements revealing a typical RMS averaged film roughness of 0.5 nm.

Thus, without explicitly distinguishing between nanocrystalline and amorphous, it is clear that all films are highly disordered with respect to their structure. This immediately poses the question as to how such strong disorder affects electrical transport properties like resistivity, ρ, and Seebeck coefficient, *S*. For amorphous metals, often addressed also as metallic glasses, this question has been analyzed experimentally as well as theoretically for quite some time revealing general trends as well as an improved principal understanding [15-17]. Such a general trend can be expressed by the empirical Mooij's rule [18] stating that there is a sign change of the temperature-coefficient of resistivity (TCR) of metallic glasses from positive to negative values around a resistivity of 150 $\mu\Omega\cdot$cm. Thus, around this value, resistivities of metallic glasses are expected to be almost temperature independent. The corresponding experimental data for our present films are presented in Figure 2 for the temperature range 7 K $\leq$ *T* $\leq$ 300 K. Three features of these resistivity results are immediately notable: 1) The absolute values for all three films, $CoGa_3$, $Fe_{0.75}Co_{0.25}Ga_3$, and $FeGa_3$, are extraordinarily high $\rho \geq 200$ $\mu\Omega\cdot$cm. 2) The sequence of these high ρ-values from 200 $\mu\Omega\cdot$cm for $CoGa_3$ to more than 600 $\mu\Omega\cdot$cm

for $FeGa_3$ with $Fe_{0.75}Co_{0.25}Ga_3$ in between, but closer to $FeGa_3$, reflects the expectation from the corresponding behavior of crystalline samples as mentioned in the introduction: A metallic behavior for $CoGa_3$ as opposed to a semiconducting one for $FeGa_3$, though with a small band-gap on the order of 0.25 eV [8]. 3) The TCR of the $CoGa_3$ films is indeed practically zero while the samples with even higher resistivities exhibit negative TCRs.

Figure 2: Electrical resistivity of $FeGa_3$, $CoGa_3$ and $Fe_{0.75}Co_{0.25}Ga_3$ films as a function of temperature. The inset gives a magnified view of the framed $FeGa_3$ low temperature behavior together with a fit to $\rho = \rho_0 + AT^2$ (A = −0.007 K^{-2}).

All three features may help to distinguish between amorphous/ nanocrystalline metallic and semiconducting behavior. Most importantly, in the case of $FeGa_3$, a gap of 0.3 eV leads to a resistivity of around $3\cdot10^{-3}$ $\Omega\cdot$m at 300 K as corroborated experimentally with crystalline bulk samples [8]. This value, however, is larger by a factor of 500 than what is found for our $FeGa_3$ films. Furthermore, the observed negative TCR shows a linear temperature-dependence rather than the Arrhenius behavior expected for a semiconductor. Although at low temperatures this may be masked by uncontrolled doping effects. But even in such a case, the pronounced linear temperature-dependence would appear as fortuitous. On the other hand, for the family of high resistivity metallic glasses such a linear behavior is characteristic: A more-or-less linear temperature dependence is observed above about 150 K in all metallic glasses in this family [19]. Even the T^2-behavior $\rho = \rho_0 + AT^2$ (A < 0) at low temperatures as it is additionally typical for this family of metallic glasses [15] can be found here at T < 40 K (cf. inset of Figure 2). Taken together, the data strongly suggest an interpretation in terms of metallic glasses for all three types of films. In case of $FeGa_3$, however, such a conclusion demands that amorphization due to the applied film preparation method results in a

higher average density leading to metallic rather than semiconducting properties. The electronic density of states at the Fermi level $N(E_F)$ for amorphous FeGa$_3$, on the other hand, should be still well below the corresponding value for CoGa$_3$ to account for its higher resistivity.

The conclusion on the amorphous state of the presently discussed films has immediate implications on their thermoelectric behavior. First of all, the scattering of electrons is dominated by the static disorder rather than by phonons. As a consequence, phonon drag effects, which usually are responsible for strong non-linear temperature dependence of the Seebeck coefficients $S(T)$ below typically 100 K in crystalline samples, are expected to be absent. Furthermore, with any 'sharp' features in the electronic density of states smeared out by structural disorder, the logarithmic derivative of electric conductivity σ with respect to energy E taken at the Fermi energy E_F, $(d\ln\sigma(E)/d\ln E)_{EF}$, should also lead to a smooth temperature behavior. Thus, referring to the Mott formula for $S(T)$ [16],

$$S(T) = -\left(\pi^2 k_B{}^2 T / 3eE_F\right)\left(d\ln\sigma(E)/d\ln E\right)_{E_F}$$

one expects an almost linear T-dependence of the second term delivering the sign of $S(T)$. Indeed, these expectations are mostly confirmed by experiments including metallic glasses containing transition metals with both signs being reported [16,20]. In Figure 3 the $S(T)$ results for our presently studied films are presented. Again, the data comply with the above expectations for amorphous metals: Smooth, almost linear temperature behavior with no indication for phonon drag peaks in the lower temperature range. Also the magnitude of the $S(300\,\text{K})$-values ranging between 4 and 8 µV/K are typical of high-resistance metallic glasses [16]. This clearly confirms the idea of amorphous rather than nanocrystalline structures for the films, especially when comparing these values with corresponding data of crystalline bulk FeGa$_3$ samples for which much larger Seebeck coefficients of −350 µV/K [7] or even −563 µV/K [8] at ambient temperature have been reported. Two more details are interesting to note: 1) The negative signs of $S(T)$ within the observed temperature range of bulk and film samples coincide, indicating a predominant electron transport and 2) according to [20], substituting Fe by a concentration of 5 atom % Co in crystalline bulk samples leads to a transition into a metallic state. Similarly, while 1 atom % Co was found to enhance the magnitude of $S(300\,\text{K})$ by a factor of two, this enhancement is completely reduced down to the starting value of FeGa$_3$ by increasing the Co concentration to either 5 or even 10 atom % [21]. On the other hand, comparison to the present film data shows that at 25 atom % Co the thermoelectric behavior is already very close to that of pure CoGa$_3$ supporting the

idea of a metallic glass in that case. Unfortunately, $S(T)$ results for crystalline bulk CoGa$_3$ samples are not available to the best of our knowledge, although because of the expected metallic behavior of that system [9] small $S(300\,\text{K})$-values of only some µV/K are likely. However, in crystalline samples a possibly present phonon drag may give rise to more pronounced nonlinearities in the temperature dependence of the Seebeck coefficient. Thus, at this point we conclude that the thermoelectric behavior of our films as presented in Figure 3 indicates an electron-dominated transport and that the data are consistent with the assumption of a highly disordered glassy metallic structure.
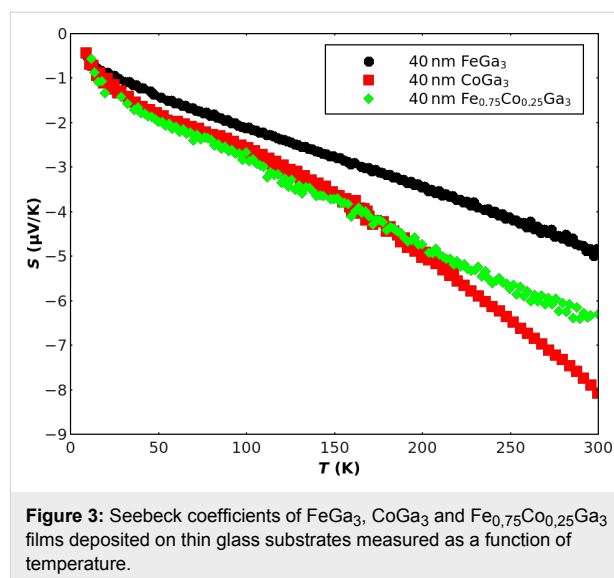

Figure 3: Seebeck coefficients of FeGa$_3$, CoGa$_3$ and Fe$_{0.75}$Co$_{0.25}$Ga$_3$ films deposited on thin glass substrates measured as a function of temperature.

Conclusion

Based on a recently developed powder synthesis of FeGa$_3$ and CoGa$_3$ as well as an intermediate solid solution (Fe$_{0.75}$Co$_{0.25}$)Ga$_3$, flash evaporation onto various substrates held at ambient temperature was applied for fabricating the corresponding thin films. This method proved successful in reliably transferring the powder stoichiometry one-to-one into the film. Such a conservation of chemical composition, however, can be obtained only at relatively low deposition temperatures. As a consequence, films of all the above compositions were found to be X-ray amorphous with no indications for the presence of crystallites larger than 5 nm. These new metallic glasses displayed transport properties quite distinct from their crystalline counterparts. The most pronounced difference in this respect is observed for FeGa$_3$, which, in its crystalline state, exhibits a semiconducting behavior, though with a small gap of about 0.3 eV. Guided by the performance of standard group-IV semiconductors like Si, which easily can be transformed into an amorphous structure with still semiconducting properties, one would expect amorphous FeGa$_3$ to be semiconducting as well. In marked contrast with that expectation, however, one finds in

that case the behavior of a typical metallic glass: Much smaller resistivity than what would be expected for a semiconductor with a 0.3 eV gap and a linear rather than exponential temperature-dependence of the resistivity. Correspondingly, the Seebeck coefficient S(300 K) is much lower than what is expected for a semiconductor but well within the range typical for metallic glasses. Thus, it appears that for semiconducting intermetallic compounds formed due to the specific hybridization effects between narrow d- and broad sp-bands, rather than due to the formation of strong covalent bonds, structural disorder completely removes the gap. Besides smearing out small features in the electronic density of states, structural disorder may also result in enhanced densities of samples with an accompanying tendency towards the metallic state. As a consequence, the possibility of tuning the electronic properties by substituting Fe by Co in crystalline $FeGa_3$ samples and, in this way, shifting the Fermi energy into and out of peaked features in the electronic density of states, is no longer available in the corresponding amorphous films. In the case of $CoGa_3$, however, we recently succeeded in transforming an amorphous into a polycrystalline film by annealing at 300 °C for one hour. Comparison to XRD powder data for crystalline $CoGa_3$ allowed to identify all significant Bragg peaks (13) in the 2θ-range between 10 and 80° for the annealed sample, although different intensity ratios indicate a preferential growth in the (400)-direction. This recent result not only corroborates the amorphous structure of the as-prepared $CoGa_3$ films, but also fosters hope that electronic fine tuning will be possible in future.

Acknowledgements

References

1. Evers, J.; Oehlinger, G. *Mater. Res. Bull.* **1984,** *19,* 1177–1180. doi:10.1016/0025-5408(84)90068-0
2. Graf, T.; Felser, C.; Parkin, S. S. P. *Prog. Solid State Chem.* **2011,** *39,* 1–50. doi:10.1016/j.progsolidstchem.2011.02.001
3. Häussermann, U.; Boström, M.; Viklund, P.; Rapp, Ö.; Björnängen, T. *J. Solid State Chem.* **2002,** *165,* 94–99. doi:10.1006/jssc.2001.9503
4. Bogdanov, D.; Winzer, K.; Nekrasov, I. A.; Pruschke, T. *J. Phys.: Condens. Matter* **2007,** *19,* 232202. doi:10.1088/0953-8984/19/23/232202
5. Freericks, J. K.; Demchenko, D. O.; Joura, A. V.; Zlatić, V. *Phys. Rev. B* **2003,** *68,* 195120. doi:10.1103/PhysRevB.68.195120
6. Shevelkov, A. V.; Kovnir, K. Zintl Clathrates. In *Zintl Phases – Principles and recent developments;* Fassler, T. F., Ed.; Structure and Bonding, Vol. 139; Springer: Heidelberg New York Dordrecht London, 2011; pp 97–142. doi:10.1007/430_2010_25
7. Hadano, Y.; Narazu, S.; Avila, M. A.; Onimaru, T.; Takabatake, T. *J. Phys. Soc. Jpn.* **2009,** *78,* 013702. doi:10.1143/JPSJ.78.013702
8. Amagai, Y.; Yamamoto, A.; Iida, T.; Takanashi, Y. *J. Appl. Phys.* **2004,** *96,* 5644. doi:10.1063/1.1803947
9. Verchenko, V. Yu.; Likhanov, M. S.; Kirsanova, M. A.; Gippius, A. A.; Tkachev, A. V.; Gervits, N. E.; Galeeva, A. V.; Büttgen, N.; Krätschmer, W.; Lue, C. S.; Okhotnikov, K. S.; Shevelkov, A. V. *J. Solid State Chem.* **2012,** *194,* 361–368. doi:10.1016/j.jssc.2012.05.041
10. Rowe, D. M. *Thermoelectrics Handbook: Macro to Nano;* CRC/Taylor & Francis: Boca Raton, FL, USA, 2006.
11. Pulker, H. K. *Vak. Forsch. Prax.* **2000,** *12,* 197–198. doi:10.1002/1522-2454(200006)12:3<197::AID-VIPR197>3.0.CO;2-N
12. Rutherford Backscattering Data Analysis Plotting and Simulation Package - Computer Graphic Service. http://www.genplot.com (accessed May 15, 2013).
13. Roberts, R. B. *Philos. Mag.* **1977,** *36,* 91–107. doi:10.1080/00318087708244450
14. Reiff, S.; Huber, R.; Ziemann, P.; Kaiser, A. B. *J. Phys.: Condens. Matter* **1989,** *1,* 10107. doi:10.1088/0953-8984/1/50/012
15. Mizutani, U.; Yoshino, K. *J. Phys. F: Met. Phys.* **1984,** *14,* 1179. doi:10.1088/0305-4608/14/5/014
16. Gallagher, B. L.; Greig, D. *J. Phys. F: Met. Phys.* **1982,** *12,* 1721. doi:10.1088/0305-4608/12/8/016
17. Siebold, T.; Ziemann, P. *Solid State Commun.* **1993,** *87,* 269–271. doi:10.1016/0038-1098(93)90640-9
18. Mooij, J. H. *Phys. Status Solidi A* **1973,** *17,* 521–530. doi:10.1002/pssa.2210170217
19. Mizutani, U. *Prog. Mater. Sci.* **1983,** *28,* 97–228. doi:10.1016/0079-6425(83)90001-4
20. Bittar, E. M.; Capan, C.; Seyfarth, G.; Pagliuso, P. G.; Fisk, Z. *J. Phys.: Conf. Ser.* **2010,** *200,* 012014. doi:10.1088/1742-6596/200/1/012014
21. Haldolaarachchige, N.; Karki, A. B.; Phelan, W. A.; Xiong, Y. M.; Jin, R.; Chan, J. Y.; Stadler, S.; Young, D. P. *J. Appl. Phys.* **2011,** *109,* 103712. doi:10.1063/1.3585843

License and Terms

Novel composite Zr/PBI-O-PhT membranes for HT-PEFC applications

Mikhail S. Kondratenko[*1,§], Igor I. Ponomarev[2], Marat O. Gallyamov[1,2],
Dmitry Y. Razorenov[2], Yulia A. Volkova[2], Elena P. Kharitonova[1]
and Alexei R. Khokhlov[1,2]

Abstract

Novel composite membranes for high temperature polymer-electrolyte fuel cells (HT-PEFC) based on a poly[oxy-3,3-bis(4′-benz-imidazol-2″-ylphenyl)phtalide-5″(6″)-diyl] (PBI-O-PhT) polymer with small amounts of added Zr were prepared. It was shown in a model reaction between zirconium acetylacetonate ($Zr(acac)_4$) and benzimidazole (BI) that Zr-atoms are capable to form chemical bonds with BI. Thus, Zr may be used as a crosslinking agent for PBI membranes. The obtained Zr/PBI-O-PhT composite membranes were examined by means of SAXS, thermomechanical analysis (TMA), and were tested in operating fuel cells by means of stationary voltammetry and impedance spectroscopy. The new membranes showed excellent stability in a 2000-hour fuel cell (FC) durability test. The modification of the PBI-O-PhT films with Zr facilitated an increase of the phosphoric acid (PA) uptake by the membranes, which resulted in an up to 2.5 times increased proton conductivity. The existence of an optimal amount of Zr content in the modified PBI-O-PhT film was shown. Larger amounts of Zr lead to a lower PA doping level and a reduced conductivity due to an excessively high degree of crosslinking.

Introduction

Polymer-electrolyte fuel cells (PEFC) based on polybenzimi-dazole (PBI) membranes doped with phosphoric acid (PA) as an electrolyte can be operated without any humidification of reactant gases at an elevated temperature range, in which the CO tolerance of the Pt catalyst becomes higher. This allows the use of cheap hydrogen fuel, which was not thoroughly purified, such as hydrogen produced by natural gas reforming, at the place of consumption. On the way to commercialization, how-

ever, this promising type of PEFC still faces several problems concerning its long term stability and the overall efficiency of electrode and membrane materials. These properties should be further improved in order to make HT-PEFC economically reasonable.

The proton conductivity of PBI membranes generally increases with the PA doping level [1]. At the same time, higher PA doping levels usually result in decreased mechanical strength, which may lead to an increased crossover of reactant gases. The design of an advanced membrane for HT-PEFC applications necessitates the finding of an appropriate compromise between proton conductivity on the one hand and good mechanical properties as well as low gas permeability on the other hand.

Various PBI-based composites have been proposed in order to achieve an optimal balance of these properties. In order to enhance the mechanical strength, various polymers, such as PTFE [2,3] or polymer sulfonic acids, which can form ionic bonds with basic PBI (Nafion [4], SPEEK [5,6]), were proposed as functional fillers for PBI membranes. Even carbon nanotubes were impregnated into PBI matrices for a higher durability [7,8]. In order to improve the conductivity, proton conductors such as heteropolyacids ($H_3SiW_{12}O_{40}$ (SiWA) [9-12], $H_3PW_{12}O_{40}$ (PWA) [12], $Cs_{2.5}H_{0.5}PMo_{12}O_{40}$ (CsPMoA) [13]), lithium hydraziniumsulfate, $LiN_2H_5SO_4$, (LiHzS) [14] and Zr-containing compounds (zirconium pyrophosphate [15], zirconium tricarboxybutylphosphonate [16,17]) were introduced into PBI membranes. According to the literature, researchers generally use quite high amounts (10–50%) of modifying agents when producing composite membranes. Such high amounts are required to achieve an optimal structure of the functional filler inside the PBI matrix, i.e., a well-developed proton-conducting channel system if solid proton conductors are added, or a durable polymer frame, e.g., for ionic crosslinking by polymer sulfonic acids.

In the present work we propose an alternative approach to the design of composite membranes based on PBI. We propose adding a rather small number of zirconium atoms into PBI matrices by means of Zr precursors (zirconium tetraacetate ($Zr(OAc)_4$) or zirconium acetylacetonate ($Zr(acac)_4$)). Zirconium atoms, which have a valence of four, exhibit coordination numbers of up to nine and may form crosslinks between PBI chains. In this way, they can improve the chemical and thermal stability as well as the mechanical strength of a membrane. At the same time, zirconium is able to form acidic phosphates with intrinsic proton conductivity, and acts as a coordination centre for PA, which improves the electrolyte binding in the matrix. This should result in increased proton conductivity, and a more

effective transport and better acid retention in a membrane during long-time operation. For the present paper we examined the properties of composite membranes based on poly[oxy-3,3-bis(4′-benzimidazol-2″-ylphenyl)phtalide-5″(6″)-diyl] (PBI-O-PhT, chemical structure is shown in Figure 1) [18,19] with the addition of small amounts of zirconium. Additionally, the performance of HT-PEFC based on these composite membranes is studied.
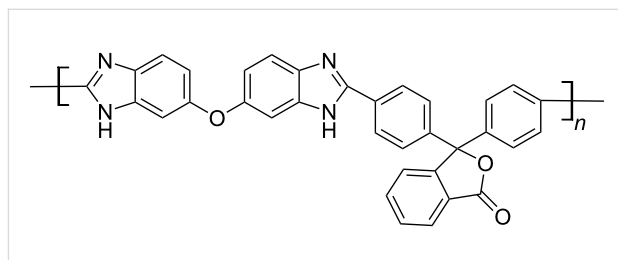

Figure 1: Chemical structure of poly[oxy-3,3-bis(4′-benzimidazol-2″-ylphenyl)phtalide-5″(6″)-diyl] (PBI-O-PhT).

Experimental
Membrane preparation
PBI-O-PhT synthesis

Initially, 3,3',4,4'-tetraaminodiphenyl ether (0.461 g, 2 mmol) and 4,4′-diphenylphtalidedicarboxylic acid (0.749 g, 2 mmol) were mixed under dry argon flow with 3.8 mL of Eaton's reagent (P_2O_5:$MeSO_3H$ 9:1 wt.) in a three-neck flask equipped with a mechanical stirrer and a heater with temperature control. The mixture was stirred for 2 h at 80 °C, then for 1 h at 100 °C, and finally 1 h at 120 °C. Then 0.57 g (4 mmol) of P_2O_5 was added, and the reaction continued for a further 2 h at 120 °C. Then the temperature was raised to 145–150 °C, and the reaction continued for 2–5 h, until a dramatic increase in the viscosity of the mixture was observed. After that, the mixture was diluted with an equal volume of 85% H_3PO_4 and stirred to obtain a homogenous solution. The latter was slowly poured into water and dispersed, then filtered, washed with water until pH 7, treated with methanol for extraction of residuals in a Soxhlet extractor, and dried in vacuum for 5 h at 100 °C. The chemical structure of the product was confirmed by ^{1}H NMR and IR spectra, and elemental analysis. The intrinsic viscosity, [η], measured in *N*-methylpyrrolidone (NMP) at 25 °C was 2.02 dL/g.

Film casting and crosslinking

Standard procedure: Polymer films were cast from a 10% polymer solution in NMP on glass plates heated at 60–80 °C. After solvent evaporation (8–12 h), the films were heated in vacuum at 160 °C for 2 h for additional drying, put in hot water to extract any residuals, then placed in 2% H_2SO_4 for 24 h at room temperature, and then heated in an oven with air circula-

tion for 1 h at 350 °C for the three-dimensional crosslinking of polymer chains.

Zr-procedure: Zr(IV) acetylacetonate ($Zr(acac)_4$) or Zr(IV) tetraacetate ($Zr(OAc)_4$) were dissolved in NMP and added to the polymer solution in corresponding quantities before casting. The subsequent procedure was the same as the standard one except for the step of immersing the films in 2% H_2SO_4.

Doping with PA: In order to obtain the membrane material, the cross-linked films were doped with 77% PA at 60 °C for three days. The resulting membrane thickness was about 50 μm. Before assembling the fuel cells, the membranes were stored in 85% PA at room temperature. In total, four series of membranes were prepared and tested: (1) Non modified PBI-O-PhT standard (reference membrane), (2) PBI-O-PhT modified by adding 0.75 wt % $Zr(acac)_4$, (3) PBI-O-PhT modified by adding 2 wt % $Zr(acac)_4$, and (4) PBI-O-PhT modified by adding 0.75 wt % $Zr(OAc)_4$.

SAXS

High resolution small-angle diffraction patterns of PBI-O-PhT and Zr/PBI-O-PhT composite membranes doped with PA were recorded with a SAXS- and WAXS camera S3-Micropix, manufactured by Hecus (Cu Kα, λ = 1.542 Å). Two detectors were used: a two-dimensional Pilatus 100K and a linear position-sensitive-detector PSD 50M operating at a pressure of 8 bar Ar/Me. A Xenocs Genix generator supplied the high-voltage (50 kV) and the current (1mA) for the detectors. Fox 3D vacuum optics were used to shape the X-ray beam, and the slits in the Kratky collimator were set to 0.1 and 0.2 mm, respectively. The angular scale was between 0.003 $Å^{-1}$ and 1.9 $Å^{-1}$. In order to eliminate the influence of air, the X-ray optics system and the camera were evacuated to a pressure of $(2–3) \times 10^{-2}$ mmHg. The exposition time was varied from 600 to 5000 s.

FT-IR

Because the loading of Zr precursors in the composite membranes is very low, no noticeable changes in the FT-IR spectra of composite and reference samples could be observed. Hence, in order to confirm the active role of zirconium in the PBI-O-PhT crosslinking process we studied a model reaction of benzimidazole (BI) with $Zr(acac)_4$ in a melt in the temperature range of 320–350 °C, which was also applied for heating the films. As a result of this interaction, a dark brown non-melting insoluble product of polymeric nature is formed. A mixture of BI with $Zr(acac)_4$ (4:1 molar ratio) and the reaction product, which occurred after heating this mixture up to 320–350 °C, were pressed into KBr pellets, and FT-IR spectra were taken by using a Nicolet Magna-IR-750 spectrometer.

TMA

Thermomechanical analysis of the composite membranes doped with PA was conducted by using a Netzsch TMA 202 instrument. Five heating/cooling cycles from 40 to 190 °C in air and under a constant load of 0.05 N were performed for each membrane sample.

Fuel cell testing
Fuel cell assembly

Cells with an active area of 5 cm^2 were assembled. Gas diffusion electrodes containing 1 $mg \cdot cm^{-2}$ Pt (Pt/C ratio = 40%) were taken from a commercial membrane–electrode assembly (MEA) Celtec P1000 (BASF). In our experience, they have a rather reproducible performance. Therefore, we used them in order to ensure the most reliable comparison of different membranes in operating fuel cells. Membranes were prepared according to the procedure described above. The membrane–electrode assemblies (MEAs) were assembled with fuel cell hardware units (Arbin Instruments) including bipolar graphite plates with a reagent supply system and current collectors.

Break-in

After assembly the fuel cells were heated up to 160 °C and operated at a constant current density of 0.4 $A \cdot cm^{-2}$ for a 50 hour break-in. Pure hydrogen and air were supplied separately to the anode and cathode electrodes, respectively, without any humidification or excessive pressure. The gas flows were controlled by Bronkhorst El-Flow mass-flow controllers, which used an RS-232 interface. During the electrochemical measurements the air flow on the cathode was kept at a rather high value of 200 $mL \cdot min^{-1}$ (corresponding to a stoichiometry of about 6 for a current density j = 0.4 $A \cdot cm^{-2}$) to minimize the oxygen-transport limitations [19].

Steady state polarization curves

All electrochemical measurements were performed by the use of an Autolab PGSTAT 302 (Eco Chemie) potentiostat/galvanostat with a built-in frequency response analyser module FRA 2. Steady state galvanostatic polarization curves were measured in a current density range from 0 to 0.4 $A \cdot cm^{-2}$ at 160 °C. The current step was 2 $mA \cdot cm^{-2}$. After setting each current value the system was allowed to reach a steady state for about 10 s before measuring the voltage.

Impedance measurements

The impedance of the fuel cells with membranes of different types was measured in a galvanostatic mode at frequencies from 100 kHz to 0.1 Hz for ten different current density values (from 0.04 to 0.40 $A \cdot cm^{-2}$). The magnitude of the current perturbation was 2 $mA \cdot cm^{-2}$. After setting each direct-current density

value, the system was allowed to reach a steady state for 10 min before taking the frequency scan. An equivalent circuit with a transmission line of n repeating units (Figure 2) was used for fitting the impedance data. Such an approach allows accounting for a distributed structure of active layers (AL) and is described in detail in our previous paper [19]. Each repeating unit with index i stands for a thin sublayer of the AL and models the following processes: charge-transfer during the oxygen reduction reaction, double layer charging and ohmic losses due to finite proton conductivity of the AL. The following parameters were obtained as a result of the impedance spectra approximation: the undistributed ohmic resistance of a cell, R_m, (mainly membrane resistance); the distributed resistance of proton transport in the cathode AL, R_{el}; the charge transfer resistance, R_{ct}; and the double layer capacitance, C (Figure 2). Fitting of the impedance spectra was performed by means of the Zview modelling software using the DX-6 distributed element for the transmission line with n repeating units. In order to define the membrane resistances more accurately, the resistance of the test cell itself (including the resistance of current collecting plates, contacts and wires) was subtracted from the undistributed ohmic resistance, R_m, obtained from the impedance data. In order to determine the resistance of the test cell we measured the resistance of the cell assembled without a membrane and with direct contact between the electrodes. The value of this resistance was 4.7 mΩ.

Hydrogen crossover-current measurements

For hydrogen crossover-current measurements, the cathode was fed with pure nitrogen, and pure hydrogen was supplied to the anode. The dry gases were supplied at an ambient pressure at flow rates of 50 mL·min^{-1}. After several minutes the open-circuit voltage reached its steady-state value of about 120 mV. Then the voltage was swept slowly (1 mV·s^{-1}) to 500 mV and the resulting current of hydrogen oxidation was recorded. A similar technique of hydrogen crossover-current measurements is described in [20,21].

2000 hour durability test

PBI-O-PhT modified by adding 0.75 wt % Zr(acac)$_4$ and a non-modified PBI-O-PhT reference membrane were tested in fuel cells operating at 160 °C at a constant current density of 0.4 A·cm^{-2} for 2000 h. Hydrogen and air flows were the same as described above.
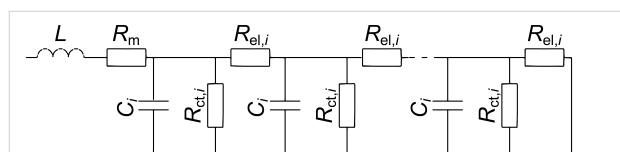
Results and Discussion

X-ray scattering data presented in Figure 3 indicate that the composite membranes have a uniform amorphous structure. Compared to the non-composite reference sample there are no noticeable differences. Similar SAXS patterns for PBI films have also been reported by Kannan et al. [8]. Only an amorphous halo without any scattering peaks is observed in the region
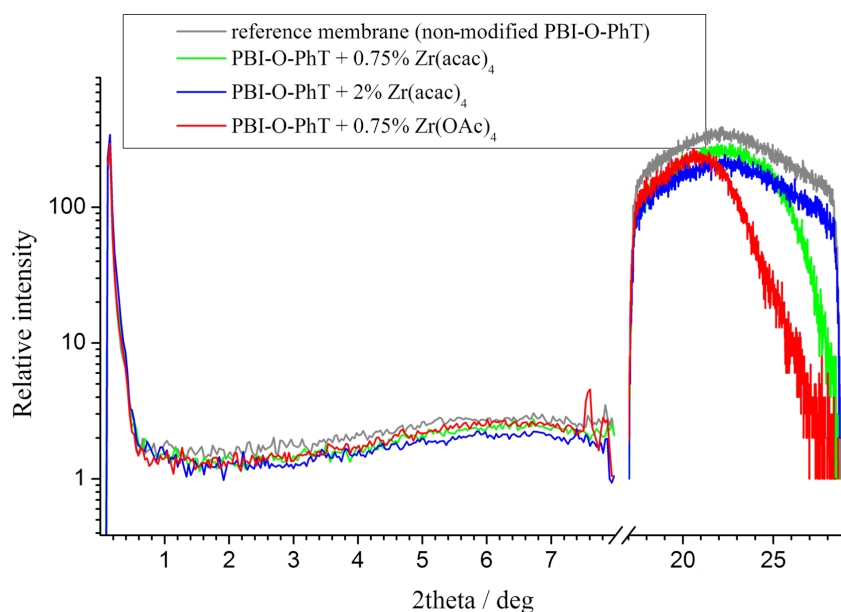

Figure 2: Equivalent circuit with a transmission line for modelling the impedance response of the active layers.

Figure 3: Small angle X-ray scattering results for the different types of composites and the reference membrane.

between 20 and 30° (2θ) for all samples of the series. The absence of any noticeable structural changes in the composite membranes is quite expectable since we added only very small amounts of Zr compounds. According to the obtained data, Zr-based crystallites are not formed (the samples are amorphous), so that Zr atoms should be uniformly distributed inside the PBI-O-PhT films. Slight differences of the intensity of the scattered radiation above 25° are observed for membranes with different amounts of the Zr precursor. Membranes with higher Zr amounts (2 wt % $Zr(acac)_4$) and the reference membrane have stronger structure correlations with a characteristic length of approximately 7 Å in comparison to membranes with lower Zr amounts (0.75 wt % $Zr(acac)_4$ or $Zr(OAc)_4$). This is probably explained by the different number of crosslinks, which is higher between polymer chains of the reference membrane and the membranes with 2 % $Zr(acac)4$ loadings than between polymer chains of the membranes with 0.75 % Zr precursors loadings.

In order to prove the active role of zirconium compounds in the PBI-O-PhT crosslinking process we studied a model reaction of benzimidazole (BI) with $Zr(acac)_4$. FT-IR spectra of a mixture of BI with $Zr(acac)_4$, and of the product of the reaction occurring after heating this mixture to 320–350 °C, are presented in Figure 4. The spectrum of the mixture after heating dramatically differs from the initial one. One can observe a noticeable shift and widening of the absorption peaks of the BI aromatic

system at 1590, 1530, 1409, 1246 cm^{-1}, and an appearance of several new strong broad peaks at 1561, 1452, 617, 473 cm^{-1}, which can be attributed to the formation of both chemical and coordination bonds of zirconium with BI. According to this data one can conclude that the PBI-O-PhT macromolecules inside the membranes, which have been modified by adding $Zr(acac)_4$ or $Zr(OAc)_4$ and subsequent heating, are crosslinked by zirconium. It is noteworthy, that pristine non-crosslinked PBI-O-PhT films dissolve in PA. Adding small amounts of Zr makes the films stable and insoluble in PA even at 180 °C.

A possible mechanism of the crosslinking process of PBI by $Zr(acac)_4$ and further doping with PA is shown in Figure 5. Due to lability of the N–Zr bonds in the excess of PA, one can expect a dynamical behaviour of the Zr-crosslinks. We suggest that zirconium is forming chemical bonds not only with PBI-O-PhT macromolecules but also with PA molecules after the doping procedure, as shown in the right part of Figure 5. Since the coordination number of zirconium ranges from six to nine, one can also expect coordination bonds of Zr atoms with several PA molecules (not shown in Figure 5). Due to the dynamic nature of the Zr-crosslinks and the coordination bonds of Zr with PA, the composite Zr/PBI-O-PhT membranes should show higher PA doping levels in comparison to the reference PBI-O-PhT membrane with stiff sulfuric crosslinks [18,19]. This increased acid uptake of the composite membranes is observed experimentally, and the results are presented in Table 1.
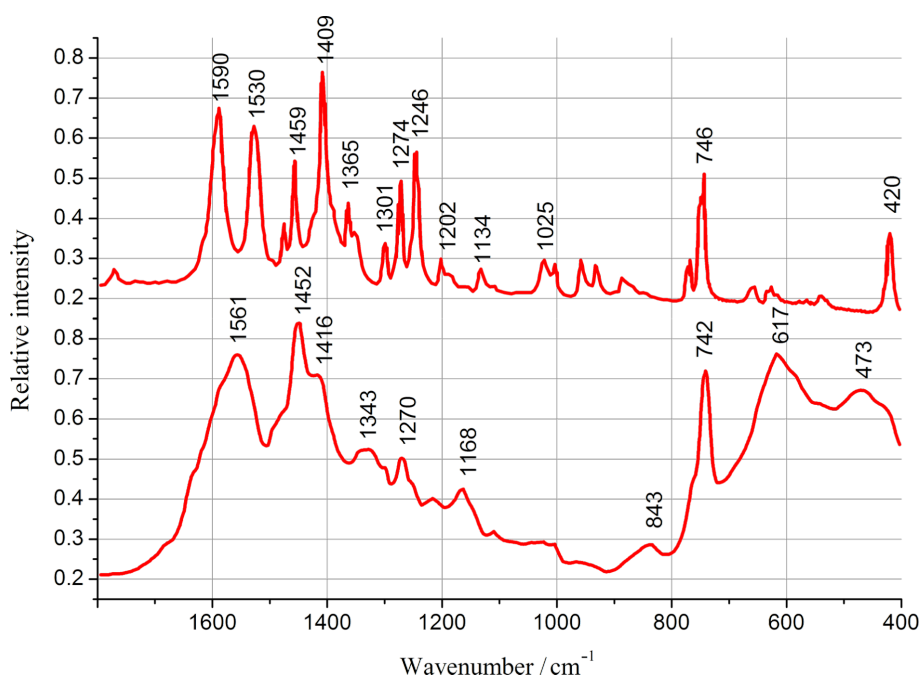

Figure 4: FT-IR spectra of a mixture of BI with $Zr(acac)_4$ (4:1 molar ratio, upper spectrum) and of the product of the reaction occurring after heating of this mixture to 320–350 °C (lower spectrum).
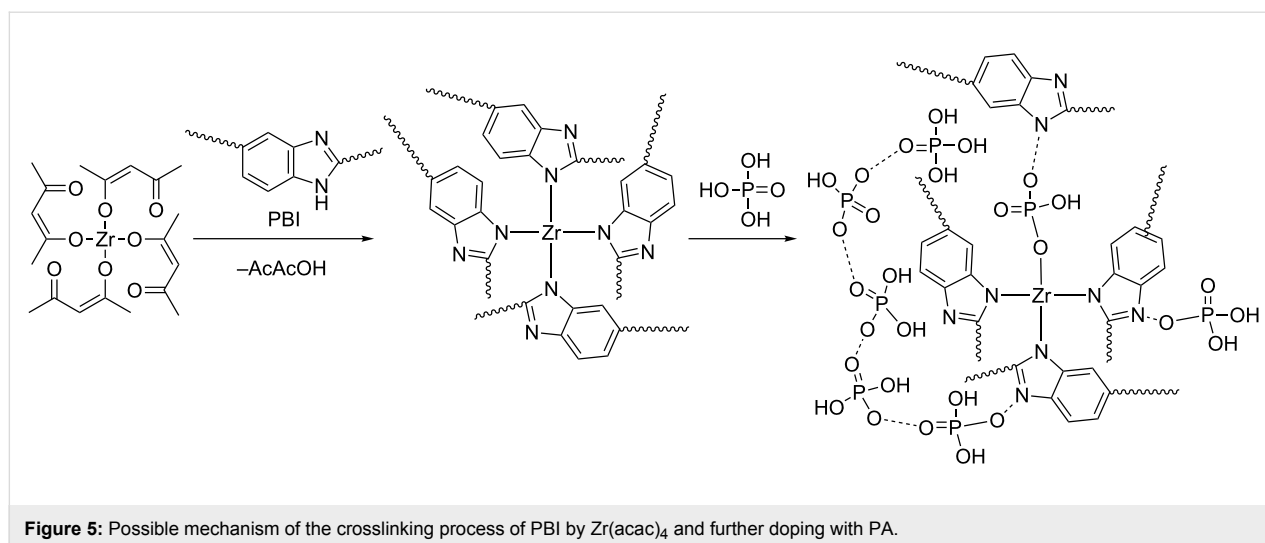
Figure 5: Possible mechanism of the crosslinking process of PBI by Zr(acac)$_4$ and further doping with PA.

Table 1: Equilibrium phosphoric acid (PA) doping levels for composite PBI-O-PhT membranes.

membrane type	equilibrium PA doping level
reference membrane (pristine sulfuric-crosslinked PBI-O-PhT)	380%
PBI-O-PhT + 0.75 wt % Zr(acac)$_4$	430%
PBI-O-PhT + 0.75 wt % Zr(OAc)$_4$	430%
PBI-O-PhT + 2 wt % Zr(acac)$_4$	400%

From Table 1 one can see that the transition from stiff sulfuric crosslinks in the reference PBI-O-PhT membrane (for comparison here we used pristine PBI-O-PhT membranes, thermally crosslinked in the presence of sulfuric acid as described in [18]) to dynamic crosslinks of PBI-O-PhT chains by zirconium resulted in a raise of acid uptake from 380 to 430% for samples with 0.75 wt % Zr precursor loading. An increase of this loading to 2 wt % leads to a lower acid uptake of 400% which can be explained by an excessive degree of crosslinking.

The strong tendency of Zr-atoms to coordinate atoms of both PBI chains and PA is rather fortunate not only from the viewpoint of enhanced mechanical properties of the composite, but also due to the expected improved ability to retain the liquid electrolyte. Indeed, in a typical PBI material suitable proton conductivity is achieved only at a doping level of several phosphoric acid molecules per PBI monomer unit. Only one PA molecule is really bound to the protonated N-atom, the other molecules are retained by hydrogen bonds. This acid–base bonding requires an immobilized proton to be excluded from the proton transport. In contrast, the direct coordination bonding between Zr and the O-atom of a PA molecule spares the corresponding proton for proton transport, but the additional contribu-

tion to hydrogen bonding for electrolyte molecules in the matrix is still achieved.

Composite membranes with Zr-crosslinks show a high acid uptake and, at the same time, demonstrate excellent mechanical stability in a temperature range of 20–190 °C, which is confirmed by TMA results presented in Figure 6 and Figure 7. The thermal expansion under constant load is smooth and can be reproduced well for several repeated heating/cooling cycles for all samples (Figure 6). The thermal expansion coefficient calculated from TMA data as presented in Figure 7 is positive and has similar values for the reference samples and the composites with 0.75 wt % loading of Zr precursors. Composite membranes with 2 wt % Zr(acac)$_4$ have a higher crosslinking degree resulting in a higher stiffness and a higher thermal expansion coefficient (Figure 7).

Fuel cells with all types of the Zr/PBI-O-PhT composite membranes demonstrate an enhanced performance in comparison to the pristine reference PBI-O-PhT membrane (Figure 8). High open-circuit voltages of about 900–930 mV indicate a low hydrogen permeability. Indeed, the measured hydrogen crossover-currents (Figure 9) are about 3 mA·cm^{-2} for all samples of the membranes. This is lower than the 4–5 mA·cm^{-2} reported by Neyerlin et al. [20] for PBI membranes from a commercial Celtec P-1000 MEA (BASF). Polarisation curves of fuel cells with different composite membranes demonstrate a similar behaviour. More detailed analysis has been performed by means of EIS by using an equivalent circuit with a transmission line for the approximation of impedance spectra.

According to the impedance data, using zirconium as a crosslinking agent allows to achieve a significantly reduced membrane resistance in comparison to the non-modified reference
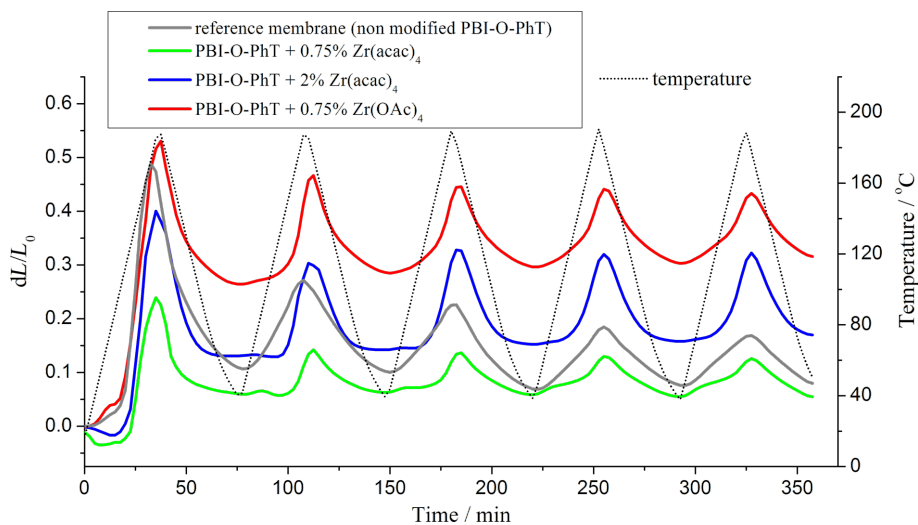
Figure 6: Change of the relative membrane thickness in a series of five consecutive heating/cooling cycles. The temperature change is given by the dotted line.
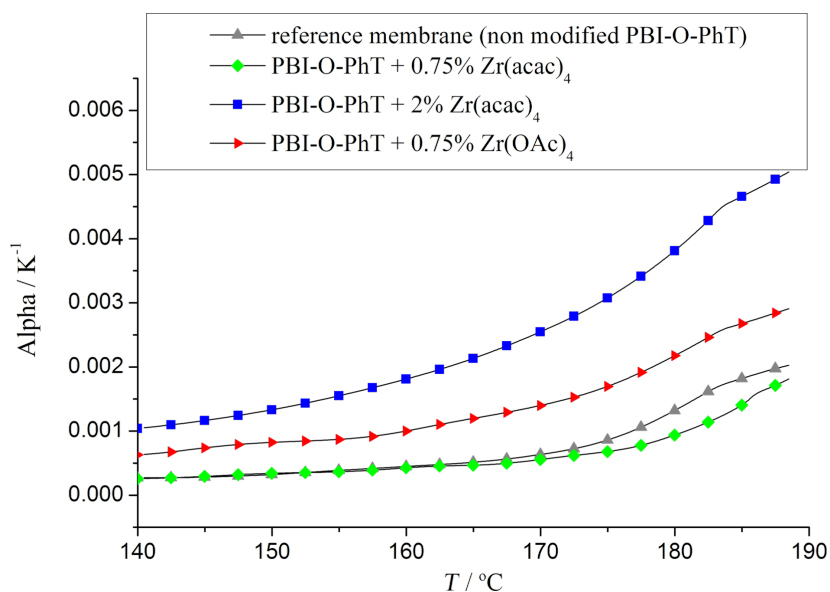

Figure 7: Thermal expansion coefficients of the composite membranes.

sample (Figure 10). The membrane thickness is virtually identical for all samples (about 50 μm). That means that the conductivity of the composite membranes is noticeably higher (about 0.04 S·cm^{-1}, 0.07 S·cm^{-1}, and 0.1 S·cm^{-1} at 160 °C for the pristine crosslinked PBI-O-PhT reference membrane, for PBI-O-PhT with 2 wt % Zr(acac)$_4$ and for PBI-O-PhT with 0.75 wt % Zr(acac)$_4$ or Zr(OAc)$_4$ loading, respectively). The increase of the conductivity is because of the higher uptake of PA by the composite Zr/PBI-O-PhT film. It can be explained by the dynamic nature of the zirconium crosslinks between the

macromolecules and the ability of zirconium to form acidic phosphates and act as a coordination centre for PA. As shown in Table 1, the PA uptake of a membrane decreases with an increasing degree of crosslinking, so the observed resistance of membranes with 2 wt % Zr precursor loading is higher than for membranes with 0.75 wt % loading.

According to data presented in Figure 11, the distributed resistances of the cathode AL are also lower in fuel cells with composite membranes containing Zr. This beahvior is expected.
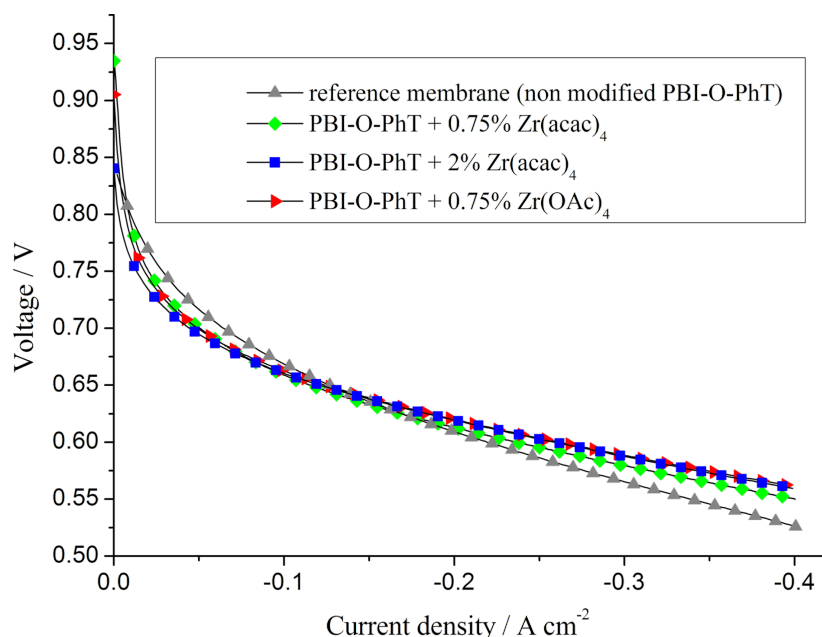
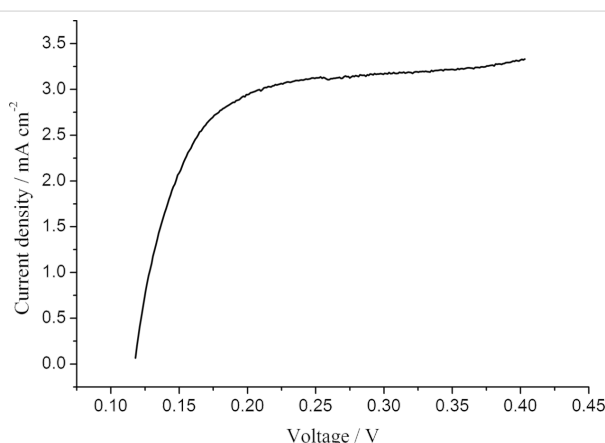**Figure 8:** Performance of fuel cells based on PBI membranes of different types. Air is used as an oxidant, *T* = 160 °C.

Figure 9: Oxidation current of hydrogen diffusing through the membrane for PBI-O-PhT with 0.75 wt % $Zr(OAc)_4$. H_2/N_2 operation, *T* = 160 °C.

Since the composite films take up more PA they should release more PA into the AL of the electrodes during the break-in of the fuel cell. According to our previous study [19] the amount of acid inside the AL has a significant influence on the distributed resistance: the higher the content of PA electrolyte in the electrode AL, the lower their resistance. This way the observed active-layer resistance values correlate with the equilibrium acid-doping level of the membranes presented in Table 1.

The dependence of the acid content in the electrode AL on the equilibrium doping-level of the membranes is also confirmed by the double-layer capacitance data presented in Figure 12. The

capacitance values, which can be measured by means of impedance spectroscopy, depend on the boundary area between the proton- (PA) and electron- (Pt and carbon support) conducting phases and serve as a good indicator of the acid content in the AL [22,23]. The data in Figure 12 indicate that membranes with 0.75 wt % $Zr(acac)_4$ release the highest amount of acid into the AL. The lowest amount of PA is in the AL of cells with the pristine reference membranes, which is in good agreement with AL resistance data (Figure 11). It is interesting that the cells with composite membranes modified by adding 0.75 wt % $Zr(OAc)_4$ have lower double layer capacitance values in comparison to the cells with PBI-O-PhT membranes modified by adding the same amount (0.75 wt %) of $Zr(acac)_4$. That means that membranes for which $Zr(OAc)_4$ was used as a Zr precursor release less PA into the electrodes than membranes with the same loading of $Zr(acac)_4$. At the same time, these membranes contain the same quite high amount of PA (430%, see Table 1). The enhanced acid-retaining properties of PBI-O-PhT + $Zr(OAc)_4$-membranes may be explained by the hydrolysis of $Zr(OAc)_4$ by water vapour present in the air during the film-casting process. This could result in the formation of a Zr oxide film at the surface of the membrane, and the oxide film may prevent acid from leaching out of the membrane. The fact that the acid retention properties of the PBI membranes depend on the type of Zr precursor is unexpected and needs further investigation.

According to [23] one cannot distinguish charge- and mass-transfer processes from a single impedance spectrum of

Figure 10: Membrane resistances as functions of the current density for fuel cells with different PBI membranes. *T* = 160 °C.

Figure 11: Distributed cathode active layer resistances as functions of current density for fuel cells with different PBI membranes. *T* = 160 °C.

HT-PEFC since they have similar relaxation times. Thus, the polarization resistances presented in Figure 13 account for both charge- and mass-transfer contributions. Since the electrodes in all FC tests are the same, the differences of the polarization resistance are mainly due to the redistribution of PA inside the

MEA and the variation of the PA amount inside the electrode AL. An increase of this amount leads to a flooding of the AL pores and a less effective oxygen transport, which results in higher polarization-resistance values. Thus, the highest resistance is observed for FC with PBI-O-PhT membranes modified

489

Figure 12: The double layer capacitance as a function of the current density for fuel cells with different PBI membranes (T = 160 °C). A higher capacitance indicates a higher area of interphase boundary (PA/Pt and C), which depends on the amount of PA in the active layer.

Figure 13: Polarization resistance (the sum of charge-transfer and mass-transfer resistances) as a function of the current density for fuel cells with different PBI membranes (T = 160 °C). Higher resistances indicate a lower oxygen transport in the active layer because of a higher acid content in AL.

with 0.75 wt % $Zr(acac)_4$, which release large amounts of acid in the AL. The PBI-O-PhT films with 0.75 wt % $Zr(OAc)_4$ release lower amounts of PA, and so the polarization resistance for FC based on these membranes is lower. Yet the lowest polarization resistance is observed for FC with the pristine reference membrane since it contains and releases the lowest amount of liquid electrolyte. It is noteworthy, that the comparative analysis of the acid content of the AL by using polarization-resistance measurements is in good agreement with AL-resistance and double-layer capacitance data.

According to the impedance data, PBI-O-PhT membranes modified by adding an amont of 0.75 wt % Zr precursor are good candidates for FC applications. In order to check their durability and overall chemical and thermal stability the membranes were tested in operating fuel cells for 2000 h (Figure 14). An increase in performance of about 15–20 mV due to the redistribution of PA inside the MEA and the formation of the effective boundary between the three phases (electron and proton conducting phases and gas phase) is observed during the first 1000 h. This relaxation time is noticeably higher than the typical time of about 100 hours reported in the literature as a suitable break-in period of HT-PEFC [24]. This may be attributed to the high PA amount in the composite membrane. The characteristic 1000 h may be the time needed to remove excessive acid from the AL of the electrodes. It is worth noticing that after the first thousand hours of operation, the performance of the FC with composite membranes is stable and at the same time higher than that of the pristine-membrane reference sample.

Conclusion

Adding small amounts (0.5–2.0 wt %) of zirconium precursors (Zr(acac)$_4$ or Zr(OAc)$_4$) into PBI-O-PhT films and subsequent heating allows to produce composite membranes with thermally and chemically stable zirconium crosslinks. The membranes become insoluble in PA and may be used in fuel cells without any additional crosslinking. After PA doping, due to the expected dynamic nature of Zr-crosslinks, these novel composite membranes demonstrate an enhanced PA uptake providing improved proton conductivity and at the same time exhibit a favourable thermal and mechanical stability. The acid-retention

ability of the composite membranes is also improved but depends on the type of the Zr precursor. The films modified with Zr(OAc)$_4$ keep acid more strongly than films modified with the same amounts of Zr(acac)$_4$. It is possible to manage the acid redistribution inside the MEA by varying the amount of the Zr precursor: the higher the Zr content, the better the acid-retention properties. The existence of an optimal Zr content in a PBI-O-PhT film was shown. Larger amounts of Zr lead to a lowering of the PA doping level and a lower conductivity due to a higher degree of crosslinking.

Acknowledgements

References

1. Ma, Y.-L.; Wainright, J. S.; Litt, M. H.; Savinell, R. F. *J. Electrochem. Soc.* **2004,** *151,* A8–A16. doi:10.1149/1.1630037
2. Lin, H.-L.; Yu, T. L.; Chang, W.-K.; Cheng, C.-P.; Hu, C.-R.; Jung, G.-B. *J. Power Sources* **2007,** *164,* 481–487. doi:10.1016/j.jpowsour.2006.11.036
3. Lin, H. L.; Hsieh, Y. S.; Chiu, C. W.; Yu, T. L.; Chen, L. C. *J. Power Sources* **2009,** *193,* 170–174. doi:10.1016/j.jpowsour.2009.01.062
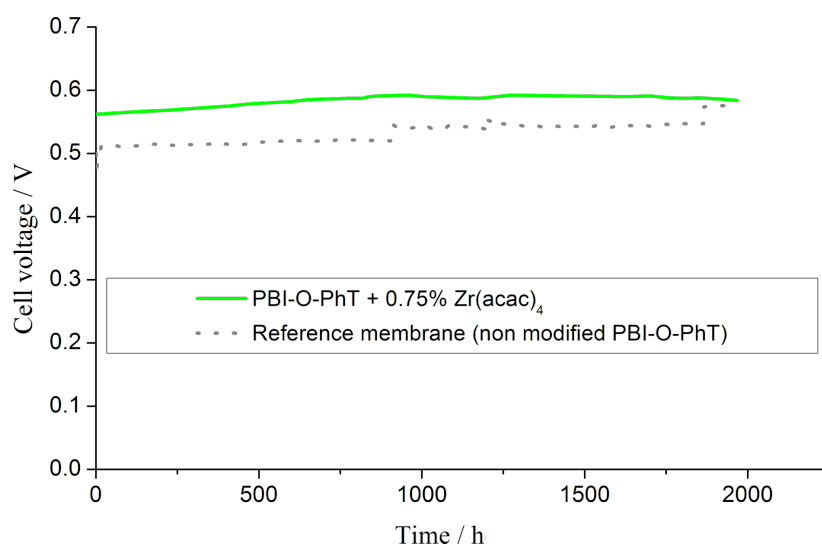

Figure 14: 2000-hour stability test of a composite PBI-O-PhT + 0.75 wt % Zr(acac)$_4$ membrane and the reference membrane in an operating fuel cell. H$_2$/air, *T* = 160 °C, current density 0.4 A·cm^{-2}.

4. Zhai, Y.; Zhang, H.; Zhang, Y.; Xing, D. *J. Power Sources* **2007,** *169,* 259–264. doi:10.1016/j.jpowsour.2007.03.004

5. Zaidi, S. M. J. *Electrochim. Acta* **2005,** *50,* 4771–4777. doi:10.1016/j.electacta.2005.02.027

6. Silva, V. S.; Ruffmann, B.; Vetter, S.; Mendes, A.; Madeira, L. M.; Nunes, S. P. *Catal. Today* **2005,** *104,* 205–212. doi:10.1016/j.cattod.2005.03.051

7. Kannan, R.; Aher, P. P.; Palaniselvam, T.; Kurungot, S.; Kharul, U. K.; Pillai, V. K. *J. Phys. Chem. Lett.* **2010,** *1,* 2109–2113. doi:10.1021/jz1007005

8. Kannan, R.; Kagalwala, H. N.; Chaudhari, H. D.; Kharul, U. K.; Kurungot, S.; Pillai, V. K. *J. Mater. Chem.* **2011,** *21,* 7223–7231. doi:10.1039/c0jm04265j

9. Staiti, P.; Minutoli, M.; Hocevar, S. *J. Power Sources* **2000,** *90,* 231–235. doi:10.1016/S0378-7753(00)00401-8

10. Staiti, P.; Minutoli, M. *J. Power Sources* **2001,** *94,* 9–13. doi:10.1016/S0378-7753(00)00597-8

11. Staiti, P. *Mater. Lett.* **2001,** *47,* 241–246. doi:10.1016/S0167-577X(00)00241-X

12. Verma, A.; Scott, K. *J. Solid State Electrochem.* **2010,** *14,* 213–219. doi:10.1007/s10008-008-0678-0

13. Li, M.-Q.; Shaob, Z.-G.; Scott, K. *J. Power Sources* **2008,** *183,* 69–75. doi:10.1016/j.jpowsour.2008.04.093

14. Jung, J.-W.; Kim, S.-K.; Lee, J.-C. *Macromol. Chem. Phys.* **2010,** *211,* 1322–1329. doi:10.1002/macp.200900712

15. Kim, T.-H.; Lim, T.-W.; Park, Y.-S.; Shin, K.; Lee, J.-C. *Macromol. Chem. Phys.* **2007,** *208,* 2293–2302. doi:10.1002/macp.200700261

16. Jang, M. Y.; Yamazaki, Y. *Solid State Ionics* **2004,** *167,* 107–112. doi:10.1016/j.ssi.2003.12.003

17. Jang, M. Y.; Yamazaki, Y. *J. Power Sources* **2005,** *139,* 2–8. doi:10.1016/j.jpowsour.2004.03.080

18. Ponomarev, I. I.; Chalykh, A. E.; Aliev, A. D.; Gerasimov, V. K.; Razorenov, D. Yu.; Stadnichuk, V. I.; Ponomarev, Iv. I.; Volkova, Yu. A.; Khokhlov, A. R. *Dokl. Phys. Chem.* **2009,** *429,* 237–241. doi:10.1134/S0012501609110062

19. Kondratenko, M. S.; Gallyamov, M. O.; Khokhlov, A. R. *Int. J. Hydrogen Energy* **2012,** *37,* 2596–3602. doi:10.1016/j.ijhydene.2011.10.087

20. Neyerlin, K. C.; Singh, A.; Chu, D. *J. Power Sources* **2008,** *176,* 112–117. doi:10.1016/j.jpowsour.2007.10.030

21. Inaba, M.; Kinumoto, T.; Kiriake, M.; Umebayashi, R.; Tasaka, A.; Ogumi, Z. *Electrochim. Acta* **2006,** *51,* 5746–5753. doi:10.1016/j.electacta.2006.03.008

22. Oono, Y.; Sounai, A.; Hori, M. *J. Power Sources* **2009,** *189,* 943–949. doi:10.1016/j.jpowsour.2008.12.115

23. Mamlouk, M.; Scott, K. *Electrochim. Acta* **2011,** *56,* 5493–5512. doi:10.1016/j.electacta.2011.03.056

24. Modestov, A. D.; Tarasevich, M. R.; Filimonov, V. Ya.; Zagudaeva, N. M. *Electrochim. Acta* **2009,** *54,* 7121–7127. doi:10.1016/j.electacta.2009.07.031

A nano-graphite cold cathode for an energy-efficient cathodoluminescent light source

Alexander N. Obraztsov[*1,2], Victor I. Kleshch[1] and Elena A. Smolnikova[1]

Full Research Paper

Address:
[1]Department of Physics, M.V. Lomonosov Moscow State University, Moscow 119991, Russia and [2]Department of Physics and Mathematics, University of Eastern Finland, Joensuu 80101, Finland

Email:
Alexander N. Obraztsov[*] - obraz@polly.phys.msu.ru

* Corresponding author

Abstract

The development of new types of light sources is necessary in order to meet the growing demands of consumers and to ensure an efficient use of energy. The cathodoluminescence process is still under-exploited for light generation because of the lack of cathodes suitable for the energy-efficient production of electron beams and appropriate phosphor materials. In this paper we propose a nano-graphite film material as a highly efficient cold cathode, which is able to produce high intensity electron beams without energy consumption. The nano-graphite film material was produced by using chemical vapor deposition techniques. Prototypes of cathodoluminescent lamp devices with a construction optimized for the usage of nano-graphite cold cathodes were developed, manufactured and tested. The results indicate prospective advantages of this type of lamp and the possibility to provide advanced power efficiency as well as enhanced spectral and other characteristics.

Introduction

The fundamental importance of light in our lives cannot be overstated. The sun is the only natural source of light emission with appropriate intensity. This is the driving force for the elaboration of artificial light sources. The demand on artificial lighting increases constantly and will continue to increase in the future. The conversion of electric energy is the most practical way for light generation and it is currently used in incandescent bulbs, gas discharge, and electroluminescent lamps of various designs, shapes, input and output power. Additionally, a photoluminescent process is used to convert blue or ultraviolet radia-

tion, produced by gas discharge or by electroluminescence, to white light. Unfortunately, because of the fundamental principles of nature, the energy efficient generation of light requires the usage of extremely toxic materials (mercury, heavy metals and others). This leads to the necessity of expensive and laborious efforts to dispose of the mercury-based fluorescent devices and the semiconductor-based light emitting diode (LED) lamps (see, e.g., [1,2]). Moreover, the spectral characteristics of the light produced by these fluorescent and LED lamps are often not perceived as pleasing in contrast to incandescent

lamps. But incandescent bulbs convert only 5% of the consumed energy into light and are thus considered as ineffective. The other 95% of the energy are transformed into heat, which cannot be considered as waste in many countries where electricity is used for house heating practically every day. In the "energy efficient" fluorescent and LED lamps the energy conversion ratio is about 10%, so that there is a decrease of energy loss on heating only from 95 to 90%. At the same time, production costs for these lamps, i.e. consumption and waste of energy at the production plant, are many times higher compared to the production costs of incandescent bulbs.
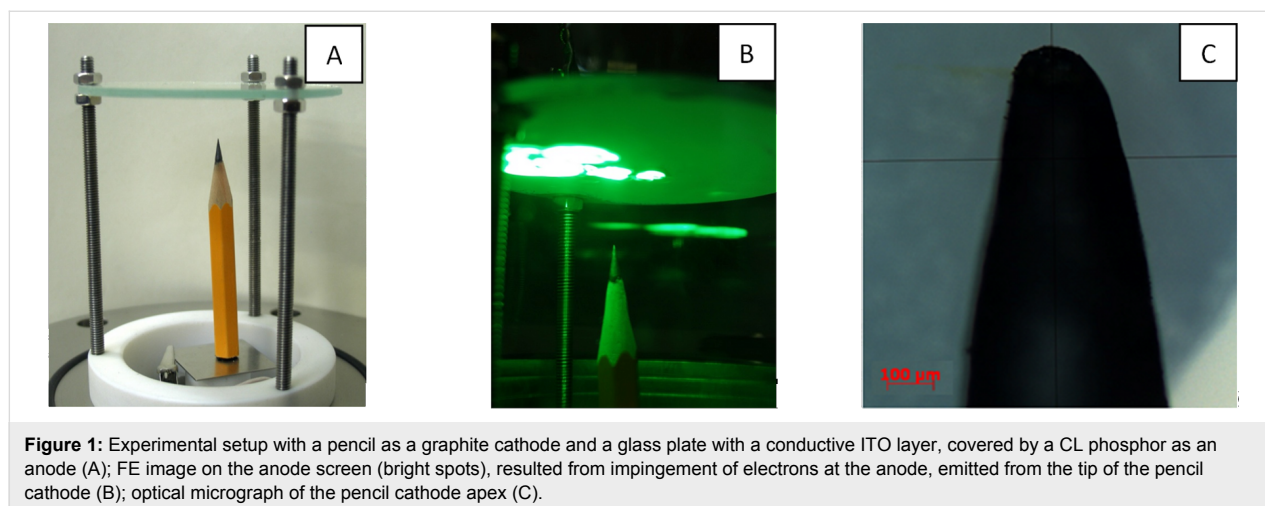
Thus, the development of new types of light sources is necessary to provide better energy efficiency, spectral characteristics, and other properties desired by the consumer. The process of cathodoluminescence (CL), which is potentially able to provide a conversion of up to 35% [3] (or more for nanostructured phosphors [4]) of the energy of the excited electron into radiation, is therefore attractive for light generation [5]. The most suitable source of electrons is the field emission (FE) cathode [5], allowing to exploit the FE effect for the creation of CL light emitting lamps. Cathodes of this type (also called "cold cathodes") are capable of generating intense electron beams virtually without any energy consumption because of the quantum tunneling nature of the FE effect [6]. Individual field emitters are required to have a needle- or blade-shape with a high aspect ratio in order to provide a sufficient intensity of the electric field at moderate voltages. Multi-emitter cathodes are necessary to achieve a reasonable total intensity of electron beams, because the current from a single emitter is limited due to its small emission surface area. To prevent field shielding the individual emitters, composing flat multi-emitter FE cathodes, must be separated from each other by a distance a few times larger than the height of the emitters [7,8]. To survive under the action of the extremely strong electric field, FE cathodes must be made from rather strong materials – hard metals, or selected semiconductors. From this point of view graphite-like materials, having the strongest interatomic interaction, are attractive for the FE cathode production. In this paper we describe the production technique and the electron field emission (FE) characteristics of nano-graphite films (NGF) and prototypes of CL lamps with NGF cold cathodes.

Results and Discussion

A simple demonstration of the FE abilities of graphite is presented in the experimental setup shown in Figure 1A, with the cathode made of a usual pencil (see details about the experimental techniques below). The field emission of electrons was observed from the apex of the pencil at a voltage in the range of 2 to 5 kV, applied between the pencil core and the transparent anode. The anode was constructed of a glass plate with a conductive indium tin oxide (ITO) layer and covered by a CL phosphor. The bright spots in Figure 1B indicate the impingement of emitted electrons with the CL anode and demonstrate the presence of a few emission sites on the pencil tip. Figure 1C shows an optical micrograph of the tip. A typical field emission current vs voltage dependence is presented in Figure 2. It demonstrates a rather high density of the obtained electron beam (up to 400 mA/cm^2) according to our estimation. However, the observed emission was very unstable in time with blinking and moving spots in the FE image and with a variation of the FE current. The averaged total value of the field emission current at constant applied voltage significantly decreased with time within a few minutes. Black traces were observed on the anode screen after these measurements. This demonstrates the process of the deposition of material from the pencil core, degraded under the action of the electric field.

These results are quite similar to other materials with a graphitic type of atomic bonding: carbon fibers [9], glassy carbon [10],

Figure 1: Experimental setup with a pencil as a graphite cathode and a glass plate with a conductive ITO layer, covered by a CL phosphor as an anode (A); FE image on the anode screen (bright spots), resulted from impingement of electrons at the anode, emitted from the tip of the pencil cathode (B); optical micrograph of the pencil cathode apex (C).

Figure 4: HRTEM image of the top-edge fragment of the graphite flake extracted from NGF material.

graphite [11], and carbon nanotubes [12]. The low threshold voltage and the intensive emission properties, which are usually observed for these materials, result from the high aspect ratio of emission sites, which are located on the edges of the graphene monoatomic layers. The low stability of the FE process is stems from the weak interaction between these atomic layers, which lead to their splitting and detachment under the action of the strong electric field. This problem is essentially eliminated in mesoporous nano-graphite film (NGF) material obtained by chemical vapor deposition (CVD) [13,14]. Scanning electron microscopy (SEM) demonstrates that this type of film material consists of tiny graphite flakes (see Figure 3). Transparency of these flakes for secondary electrons in the SEM observations indicates that their thickness is just a few nanometers (see Figure 3B). High resolution imaging with transmission electron microscopy (HRTEM) and electron diffraction analysis [15] confirm this conclusion and indicate that these flakes consist of a few graphene layers (of 5 to 50) oriented predominantly perpendicular to the substrate surface (see Figure 4). The thick-

ness of only a few nanometers results in the high aspect ratio (of 500 to 1000) of these flakes, while the distance between them (in the range of 1 to 4 μm) is close to the estimated optimal value [8].

A significant advantage of this flaky material is its atomic structure at the top edges where adjacent graphene layers are connected with each other. In HRTEM images these connections look like arced structures at the top ends of the graphene layers (see Figure 4). This specific structure results from the material formation process in the plasma activated gaseous environment [13-15]. It is noteworthy that HRTEM images (Figure 4) clearly demonstrate the atomic structure for only a small range of depth in the focal plane. Consequently, we suppose that the pairing for each layer switches from one side to

Figure 3: Typical SEM images of NGF material taken with different magnifications: overview of the mesoporous structure of the film (A) and a fragment of a flake transparent for secondary electrons taken with a higher resolution (B).

the other, preventing the mutual shift of the atomic layers. This greatly increases the mechanical stability of these flakes. The arced atomic structures formed on the edges of the graphite nanocrystals lead to a local modification of the electronic properties of the material and the formation of a double potential barrier structure. This increases the quantum tunneling probability and the electron field emission intensity [13]. Starting to grow immediately on the Si substrate, these graphite crystallites have an excellent adhesion and electrical contact with the substrate. The mechanical strength and the excellent electrical conductivity at the contact between the nano-graphite flakes and the substrate also provide an improved stability of the NGF cold cathodes. Taking into account that an electron emission from the nano-graphite flakes only occurs from small areas located on their edges, aspect ratios for emission sites are similar to that for CNT emitters. However, cross sections of the flakes are much larger than for nanotubes or nanowires. This circumstance also provides an increased stability of the NGF emitters because o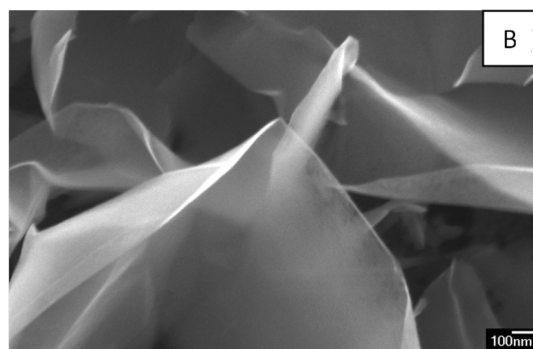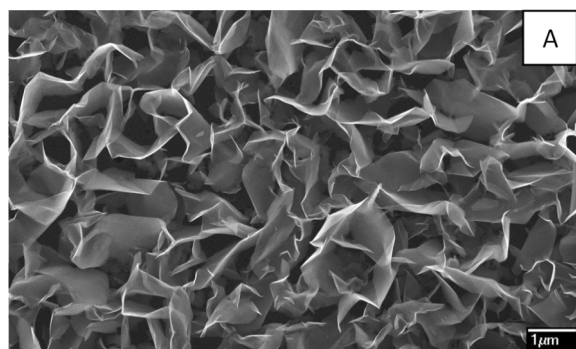f the reduction of the resistivity for individual emitters and the consequent lowering of the Joule heating effect. All together these factors greatly improve the performance of NGF cold cathodes in comparison with other types of cold cathodes. The typical threshold electric field value for NGF cathodes is from 1 to 1.5 V/μm (at emission current density of 1 μA/cm^2), the emission sites density is up to 10^6 cm^{-2} (at a current density of about 100 mA/cm^2), and the maximal emission current is about 1 A/cm^2 (at applied fields about 2.5 V/μm) [16,17]. The maximal achievable current value requires special attention because of its importance for many practical applications in vacuum electronics.

The local emission current density for an individual emitter is expressed by the Fowler–Nordheim equation [6]

$$j_{\text{FN}} = \frac{A}{\phi t(y)} F^2 \exp[-B \frac{\phi^{3/2}}{F} \Theta(y)] \qquad (1)$$

where j_{FN} is the current density, F is the strength of the local electric field, φ is the work function, $t(y)$ and $\Theta(y)$ are tabular functions of $y = e(eF)^{1/2}/\varphi$; $A = e^3/(8\pi h)$; $B = 8\pi(2m)^{1/2}/(3he)$ are constants, e is the electron charge, m the electron mass, and h is the Planck constant. The maximal value of this local current density (j_{max}) may be estimated by assuming a potential barrier transparency equal to 1:

$$j_{max} = \pi em E_{\text{F}}^2 / h^3 \cong 4.3 \times 10^9 E_{\text{F}}^2 \cong 1.1 \times 10^{11} \text{A/cm}^2 \quad (2)$$

where $E_{\text{F}} = p_{\text{F}}^2/2m \cong 5$ eV is the estimated Fermi energy for metals. However, the stable emission current density, experi-

mentally observed at room temperature for a single metallic needle, does not exceed 10^5 A/cm^2 [18]. The total value of the emission current density for a multiemitter cathode (J) may be estimated as

$$J = j_{\text{FN}} sn \approx j_{\text{FN}} s \frac{1}{L^2} \approx j_{\text{FN}} \pi r^2 \frac{1}{h^2} \approx j_{\text{FN}} \pi \beta^{-2} \qquad (3)$$

where s is the average emitting surface area of the individual emitters, n is the density of the emission sites with the geometrical parameters height h, radius of emission area r, L is the distance between two emission sites which is supposed to be in the same order as the height h, and β is the so-called field enhancement factor which may be estimated as the aspect ratio r/h. Thus, the expected range for the averaged emission current density of a multiemitter cold cathode, with aspect ratios of an individual emitter between 100 and 1000, is in the range of 10 to 10^{-1} A/cm^2 for materials with 'metallic' conductivity and work functions about 5 eV. In the particular case of NGF cathodes with aspect ratios of flaky emitters about 500 to 1000, the maximal current density should be about 1 A/cm^2. This estimation perfectly corresponds to our experimental measurements [19]. A cathode exploitation in an appropriate vacuum environment (on the order of 10^{-6} Torr) with a current value of about 100 mA/cm^2 provides its long life (more than 10 thousand hours), while current densities higher than 1 A/cm^2 or a vacuum level reduction lead to its fast degradation within a few minutes [20].

Taking into account that the normal operation of a CL phosphor requires current densities in the range of 1 to 10 mA/cm^2 [3,5], the efficient application of NGF cathodes is possible in CL lamps with a total anode area which is 10 to 100 times larger than the cathode emitting surface. A variant of such a kind of CL lamp has been disclosed in [21] and is presented by a photograph in Figure 5. The FE cathode of this lamp is made of a Ni cylindrical rod (1 mm diameter) with an NGF film covering its end, while the anode is made of an Al thin film deposited over the CL phosphor layer covering the inner semispherical (5 mm diameter) surface of the lamp bulb. The emitting end of the Ni rod is located at the center of the semispherical anode surface and voltage applied between the cathode and the anode is in the range of 5 to 10 kV at a vacuum inside the sealed bulb of about 10^{-6} Torr. Applied with a pulsed voltage (pulse duration of about 15 μs, repetition rate of about 1 kHz) this lamp produces a bright light radiation (see Figure 5).

The light emission of this lamp originates from the cathodoluminescence of the phosphor layer which is located directly under the Al film. This construction is not optimal, similar to other ones reported previously [23-25], because of the energy
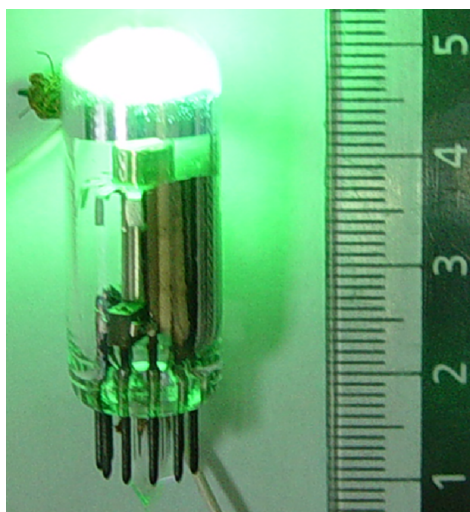
Figure 5: Photograph of the CL diode lamp with an NGF cathode with an emitting surface (of about 1 mm diameter) located at the center of the semispherical surface of the CL anode (of about 5 mm diameter). Applied voltage: pulses of about 15 µs, repetition rate of about 1 kHz with 8 kV amplitude. The image is an adapted version of a previously published graphic in [22] with permission from *J. Nanoelectron. Optoelectron.* © 2009.

loss of electrons in the Al film and the loss of light radiation during its propagation through the CL phosphor layer to the output. These disadvantages have been eliminated in a lamp made in accord with the design disclosed in [26]. This type of lamp has a cylindrical diode structure similar to [23] with an anode made of a reflecting Al layer deposited onto half the inner surface of the cylindrical glass bulb and the CL layer deposited over the Al layer. This structure allows direct excitation of the CL phosphor by the electrons emitted from the wire cathode (1 mm Ni wire covered by NGF film) located on the axis of the lamp. The absence of the intermediate material (Al) between the cathode and the CL layer reduces the loss of electron energy and, thus, increases the overall energy efficiency of the lamp. The light generated in the CL phosphor radiates directly from the lamp through the transparent glass surface. An example of such a kind of lamp is presented by the photograph in Figure 6. In this particular prototype three cylindrical diode segments have been placed in one rectangular vacuum envelope. Each segment has its own NGF cathode (40 mm long, 1 mm in diameter) and its own anode (the Al layer is deposited onto inner side of the semicylindrical glass of 8 mm diameter) covered by different phosphor materials to provide red, green and blue colors of radiation.

The spectral characteristics of the emitted light are determined by the composition of the CL phosphor materials. For the prototype of the CL lamp presented in Figure 6 the following phosphors were used: ZnS CdS:CuAl for green, Y_2O_2S:Eu for red, and ZnS:Ag for blue. Measured emission spectra and color coordinates (marked by white circle) for each segment are shown in Figure 7.

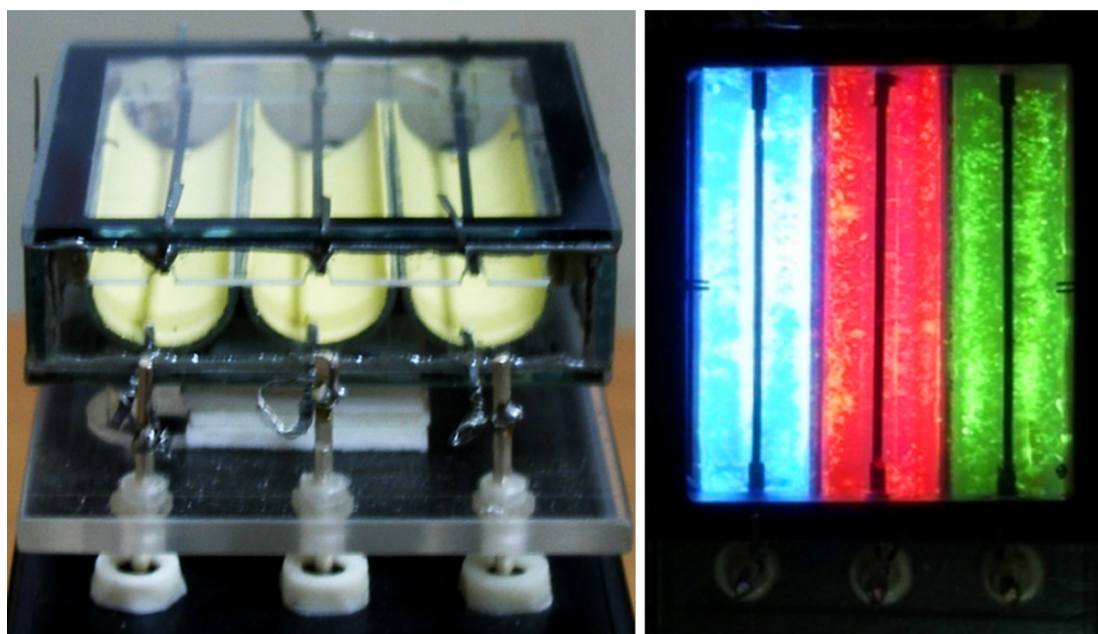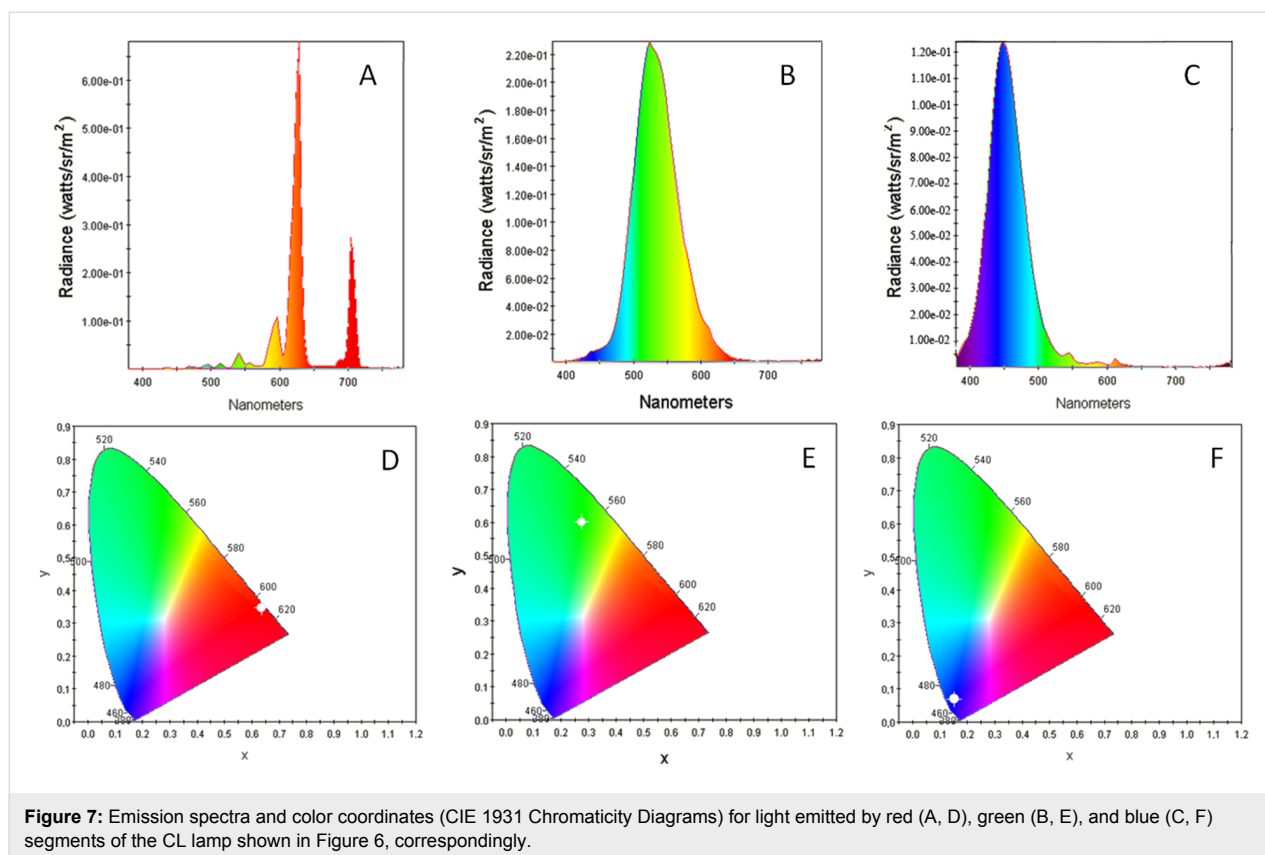**Figure 6:** Photographs showing the general design of the CL lamp (left side) and the light emission from RGB segments (right side) with the application of a pulsed voltage (pulse duration 15 µs, repetition rate 1 kHz, amplitude 8 kV) and with a total current per segment of about 0.25 mA. The image is an adapted version of a previously published graphic in [22] with permission from *J. Nanoelectron. Optoelectron.* © 2009.

Figure 7: Emission spectra and color coordinates (CIE 1931 Chromaticity Diagrams) for light emitted by red (A, D), green (B, E), and blue (C, F) segments of the CL lamp shown in Figure 6, correspondingly.

With a total power consumption of about 2 W per segment, light intensities correspond to an energy efficiency of about 10% for green light, about 4% for red, and about 3% for blue. These values are the ratios of the total output energy of light and the total input energy of electric current. An inhomogeneity of the light emission over the anode surface (see Figure 6) is owing to the usage of experimental laboratory-level technologies for the cathode and lamp manufacturing, and we believe that it may be eliminated with the application of more advanced industrial methods. This inhomogeneity almost completely disappears with an increase of the input power due to the corresponding increase of radiation brightness. However, the energy efficiency, estimated as the ratio of the energy of the electron beam produced by the NGF cathode to the energy of emitted light, decreases with the rising of consumed power. This is because of the increasing temperature of the phosphor due to the heat generated by the electron bombardment [3]. The use of materials and special designs, allowing more efficient heat dissipation, may reduce the temperature and increase the energy efficiency of the lamps with NGF cold cathodes up to the values predicted from a general consideration of the CL process [3-5]. Standard RGB phosphors used in the present study were designed for an application in cathode-ray tubes (CRT), and their properties were adapted to high accelerating voltages (more than 10 kV) and low currents (1 mA range) of the electron beam. This determines the electrical characteristics of the CL lamp prototypes, including a pulsed operation mode with high voltage short pulses which is necessary to limit the total current. The development of special phosphors, adapted for the application at higher currents and lower voltages, will improve the characteristics of CL lamps and lead to record values of power efficiency.

Conclusion

Prototypes of CL lamps were manufactured by using cold nano-graphite cathodes. NGF films produced by plasma enhanced CVD consist of a mesoporous graphite flaky material. Each flake is a well ordered graphite crystallite of nanometer thickness, composed of graphene atomic layers, oriented predominantly in the direction perpendicular to the substrate surface. The top edge of the nano-graphite crystallites has a special atomic arrangement providing connections between neighboring graphene layers. This arrangement is responsible for the significant improvement of the mechanical stability of the nano-graphite crystallites as well as for modifications of their electronic properties. Moreover, the special atomic arrangement of the nano-graphite crystallites also results in the formation of a heterogeneous structure with a double potential barrier for the electrons which escape from the graphite to the vacuum under the influence of a strong electric field during the cold emission.

The quantum tunneling character of the electron field emission process is responsible for the extremely low energy consumption of the electron beam production. Together with an appropriate lamp design, the cold electron emission from NGF provides an excellent total power efficiency of the CL light source, which is about 10% (for green light) at current laboratory stage. Another advantage of this technology is the potential ability to provide light sources with any colors by simply mixing the phosphor materials.

Experimental

NGF materials were obtained by chemical vapor deposition (CVD) from a hydrogen/methane gas mixture activated by a direct current discharge. The details of the used home-made CVD system and the corresponding process are described in [13,14]. For the cathode production pieces of Ni wire with 1 mm diameter were placed in a CVD reactor to deposit NGF film material on one of their ends (in case of the lamp presented in Figure 5) or on a cylindrical lateral surface (in case of the lamp presented in Figure 6). The cathodes were used for the lamp production "as grown" without any special post treatments. The as-grown films were inspected with scanning electron microscopy (SEM) by using a Zeiss Leo 1550 instrument and with transmission electron microscopy (TEM) by using a JEOL 3000f instrument.

Field emission tests were performed as described in details in [15-17,19-21] in a vacuum chamber with a basic pressure of about 10^{-6} Torr. The used experimental set-up allows the registration of FE current–voltage dependencies and the distribution of emission sites over the cathode surface in direct current and pulsed regimes corresponding to the device applications. The CL lamp manufacturing was made with the use of standard vacuum electronic technologies, including outgasing with thermal annealing at about 400 °C and porous Ti getter insertion into the sealed device. Commercially available CL phosphor materials with the chemical composition ZnS CdS:CuAl for green lamps, Y_2O_2S:Eu for red lamps, and ZnS:Ag for blue lamps were used for the lamp manufacturing. Spectral and luminosity characteristics of CL lamp prototypes were measured by using a HR4000-UV-NIR (Ocean Optics) spectrometer and a LS-110 Luminance Meter (Minolta).

Acknowledgments

References

1. Eckelman, M. J.; Anastas, P. T.; Zimmerman, J. B. *Environ. Sci. Technol.* **2008,** *42,* 8564–8570. doi:10.1021/es800117h
2. Lim, S.-R.; Kang, D.; Ogunseitan, O. A.; Schoenung, J. M. *Environ. Sci. Technol.* **2011,** *45,* 320–327. doi:10.1021/es101052q
3. Ozawa, L. *Cathodoluminescence and Photoluminescence: Theories and Practical Applications;* CRC Press, Taylor and Francis Group: Boca Raton, FL, USA, 2010.
4. Liu, H.; Hu, L.; Watanabe, K.; Hu, X.; Dierre, B.; Kim, B.; Sekiguchi, T.; Fang, X. *Adv. Funct. Mater.* **2013,** *23,* 3701–3709. doi:10.1002/adfm.201203711
5. Chubun, N. N.; Chakhovskoi, A. G.; Hunt, C. E. J. *J. Vac. Sci. Technol., B: Microelectron. Nanometer Struct.–Process., Meas., Phenom.* **2003,** *21,* 1618–1621. doi:10.1116/1.1587134
6. Gomer, R. *Field Emission and Field Ionization;* AIP: New York, NY, USA, 1993.
7. Nilsson, L.; Groening, O.; Emmenegger, C.; Kuettel, O.; Schaller, E.; Schlapbach, L.; Kind, H.; Bonard, J.-M.; Kern, K. *Appl. Phys. Lett.* **2000,** *76,* 2071–2073. doi:10.1063/1.126258
8. Kleshch, V. I.; Obraztsov, A. N.; Obraztsova, E. D. *Fullerenes, Nanotubes, Carbon Nanostruct.* **2008,** *16,* 384–388. doi:10.1080/15363830802269356
9. Sheshin, E. P.; Baturin, A. S.; Nikolskiy, K. N.; Tchesov, R. G.; Sharov, V. B. *Appl. Surf. Sci.* **2005,** *251,* 196–200. doi:10.1016/j.apsusc.2005.03.193
10. Chakhovskoi, A. G.; Hunt, C. E.; Forsberg, G.; Nilsson, T.; Persson, P. *J. Vac. Sci. Technol., B: Microelectron. Nanometer Struct.–Process., Meas., Phenom.* **2003,** *21,* 571–575. doi:10.1116/1.1527956
11. Dharmadhikari, C. V.; Khairnar, R. S.; Joag, D. S. *J. Phys. D: Appl. Phys.* **1992,** *25,* 125–130. doi:10.1088/0022-3727/25/1/018
12. Bonard, J.-M.; Croci, M.; Klinke, C.; Kurt, R.; Noury, O.; Weiss, N. *Carbon* **2002,** *40,* 1715–1728. doi:10.1016/S0008-6223(02)00011-8
13. Obraztsov, A. N.; Volkov, A. P.; Nagovitsyn, K. S.; Nishimura, K.; Morisawa, K.; Nakano, Y.; Hiraki, A. *J. Phys. D: Appl. Phys.* **2002,** *35,* 357–362. doi:10.1088/0022-3727/35/4/311
14. Obraztsov, A. N.; Zolotukhin, A. A.; Ustinov, A. O.; Volkov, A. P.; Svirko, Yu. P. *Carbon* **2003,** *41,* 836–839. doi:10.1016/S0008-6223(02)00402-5
15. Kleshch, V. I.; Vasilyeva, E. A.; Lyashenko, S. A.; Obronov, I. V.; Tyurnina, A. V.; Obraztsov, A. N. *Phys. Status Solidi B* **2011,** *248,* 2623–2626. doi:10.1002/pssb.201100111
16. Kleshch, V. I.; Rackauskas, S.; Nasibulin, A. G.; Kauppinen, E. I.; Obraztsova, E. D.; Obraztsov, A. N. *J. Nanoelectron. Optoelectron.* **2012,** *7,* 35–40. doi:10.1166/jno.2012.1212
17. Kleshch, V. I.; Susi, T.; Nasibulin, A. G.; Obraztsova, E. D.; Obraztsov, A. N.; Kauppinen, E. I. *Phys. Status Solidi B* **2010,** *247,* 3051–3054. doi:10.1002/pssb.201000212
18. Fursey, G. N. *Field Emission in Vaccum Microelectronics;* Kluwer Academic / Plenum Publishers: New York, NY, USA, 2005.
19. Lyashenko, S. A.; Volkov, A. P.; Obraztsov, A. N. *Tech. Phys.* **2012,** *57,* 251–255. doi:10.1134/S1063784212020168
20. Vasil'eva, E. A.; Kleshch, V. I.; Obraztsov, A. N. *Tech. Phys.* **2012,** *57,* 1003–1007. doi:10.1134/S1063784212070237
21. Obraztsov, A. N. Diode cathodoluminescent lamp. RU Patent 2382436, Oct 21, 2008.

22. Obraztsov, A. N.; Kleshch, V. I. *J. Nanoelectron. Optoelectron.* **2009,** *4,* 207–219. doi:10.1166/jno.2009.1023

23. Croci, M.; Arfaoui, I.; Stöckli, T.; Chatelain, A.; Bonard, J.-M. *Microelectron. J.* **2004,** *35,* 329–336. doi:10.1016/j.mejo.2003.07.003

24. Knapp, W.; Schleussner, D.; Baturin, A. S.; Yeskin, I. N.; Sheshin, E. P. *Vacuum* **2002,** *69,* 339–344. doi:10.1016/S0042-207X(02)00355-X

25. Fu, W.; Liu, P.; Tang, J.; Liu, L.; Fan, S. J. *J. Vac. Sci. Technol., B: Microelectron. Nanometer Struct.–Process., Meas., Phenom.* **2008,** *26,* 1404–1406. doi:10.1116/1.2958243

26. Obraztsov, A. N. Cathodoluminescent light source having an electron field emitter coated with nanocarbon film material. U.S. Patent 7683530, March 23, 2010.

Large-scale atomistic and quantum-mechanical simulations of a Nafion membrane: Morphology, proton solvation and charge transport

Pavel V. Komarov[1,2], Pavel G. Khalatur[*1,3] and Alexei R. Khokhlov[1,3,4]

Full Research Paper

Open Access

Address:
[1]Institute of Organoelement Compounds, RAS, Moscow 119991, Russia, [2]Department of Theoretical Physics, Tver State University, Tver 170002, Russia, [3]Institute for Advanced Energy Related Nanomaterials, Ulm University, Ulm D-89069, Germany and [4]Physics Department, Moscow State University, Moscow 119991, Russia

Email:
Pavel G. Khalatur[*] - khalatur@polly.phys.msu.ru

* Corresponding author

Keywords:
atomistic simulation; morphology; Nafion membrane; proton transport; quantum molecular dynamics

Abstract

Atomistic and first-principles molecular dynamics simulations are employed to investigate the structure formation in a hydrated Nafion membrane and the solvation and transport of protons in the water channel of the membrane. For the water/Nafion systems containing more than 4 million atoms, it is found that the observed microphase-segregated morphology can be classified as bicontinuous: both majority (hydrophobic) and minority (hydrophilic) subphases are 3D continuous and organized in an irregular ordered pattern, which is largely similar to that known for a bicontinuous double-diamond structure. The characteristic size of the connected hydrophilic channels is about 25–50 Å, depending on the water content. A thermodynamic decomposition of the potential of mean force and the calculated spectral densities of the hindered translational motions of cations reveal that ion association observed with decreasing temperature is largely an entropic effect related to the loss of low-frequency modes. Based on the results from the atomistic simulation of the morphology of Nafion, we developed a realistic model of ion-conducting hydrophilic channel within the Nafion membrane and studied it with quantum molecular dynamics. The extensive 120 ps-long density functional theory (DFT)-based simulations of charge migration in the 1200-atom model of the nanochannel consisting of Nafion chains and water molecules allowed us to observe the bimodality of the van Hove autocorrelation function, which provides the direct evidence of the Grotthuss bond-exchange (hopping) mechanism as a significant contributor to the proton conductivity.

Introduction

The hydrogen-based power engineering is one of the most important technologies of clean energy. The main problem here is to design efficient fuel cells (FC), electrochemical devices that transform hydrogen fuels into electric power avoiding combustion processes that proceed with large energy loss [1]. The earliest fuel cells based on proton exchange membrane

(PEM), consisting of a copolymer of sulfonated polystyrene and divinylbenzene, served as the power plants for the Gemini space missions in the early 1960s. Now, PEM fuel cells show the greatest, most immediate, and most widespread potential applications and are considered as a promising power source for portable devices, home power plants and vehicles.

Typically, PEM is a polymer material, which is a key component of polymer electrolyte fuel cells (PEFCs). The polymer membrane provides a conducting medium for transferring positively charged hydrogen ions (protons) from the anode to the cathode; also, it serves as a barrier to fuel gas cross-leaks and electrical insulation between the electrodes.

On the anode side, hydrogen fuel diffuses to the anode catalyst where it dissociates into electrons e^- and protons H^+: $H_2 \leftrightarrow 2H^+ + 2e^-$. The hydrated polymer membrane behaves as a solid electrolyte: it swells in the presence of water and passes through into cathode compartment only positively charged protons. On the cathode catalyst, they react exothermically with oxygen molecules and electrons (which have traveled through the external circuit) to form water, $4H^+ + O_2 + 4e^- \leftrightarrow 2H_2O$, while electrons travel through the external circuit to produce electric current. Because the overall reaction taking place in a PEFC is $2H_2 + O_2 \leftrightarrow 2H_2O$, the only waste product is water vapor. The structural organization of PEM determines to a large extent the process of proton transfer from anode to cathode, which is responsible for overall FC efficiency [1].

The membranes are manufactured from special polymers containing both nonpolar atom groups and a relatively small number of polar groups that can dissociate in the water environment to give ions. Such polymers are called ionomers (they are a variety of polyelectrolytes). Up to now, the perfluorosulfonic acid (PFSA) polymers, such as Nafion developed by DuPont in the late 1960s are the most successful PEM materials due to

their excellent mechanical properties, chemical stability, and high proton conductivity (5×10^{-2} S/cm at 23 °C) [2]. For a long time, Nafion is regarded as a benchmark material in PEFCs due to its excellent combination of conductivity and chemical stability [2-4].

Nafion is a copolymer composed of the fluorocarbon backbone with attached side chains terminated with sulfonic functional groups (Figure 1a).

The backbone of Nafion is similar to that of common Teflon [poly(tetrafluoroethylene)] showing pronounced hydrophobic properties. (Teflon is not only insoluble in water but even not wetting with water.) On the contrary, the polar sulfonic acid groups SO_3H are strongly hydrophilic and tend to attract water. In the presence of water, they dissociate and deliver protons that serve as charge carriers. Due to the competition of hydrophobic and hydrophilic interactions in a water environment, ionomers tend to separate into a hydrophobic polymer-rich matrix and water-rich nanochannels embedded in the matrix. The details of this process and the organization of the nanochannels are not well understood at the present time. It is assumed that the walls of the hydrophilic channels contain mainly dissociated sulfonic acid groups and their counter ions enabling proton conductivity of the PEM while the hydrophobic domains maintain its mechanical stability [2]. Owing to this specific microphase separated morphology, Nafion and similar nanostructured materials are widely used not only in fuel cell manufacture but also in organic batteries, for water purification by reverse osmosis, etc.

Although the microphase-separated morphology of water-containing PEMs is clearly evidenced by numerous experiments and widely accepted, the detailed information on the resulting nanostructure at molecular level and the mechanism of the proton transport are the subject of active discussions in the current literature (see, for example [5-12]). The importance of
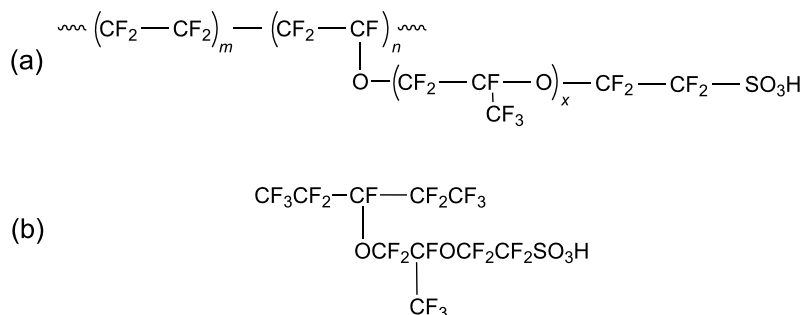

Figure 1: (a) Nafion chain. (b) Nafion sulfonated monomer.

optimizing the morphology becomes clear in the following example. In order to achieve high proton conductivity, the molecular structure should be such that the hydrated membrane contains wide interconnected water channels, but these might deteriorate the mechanical characteristics of the membrane. From a general point of view it is clear that the structural organization of the hydrated membrane under different physico-chemical conditions is determined by the balance between the elastic deformation of Nafion chains in hydrophobic phase and various intermolecular interactions. Equally important is the understanding of the molecular basis of electrochemical reactions and related to them degradation processes that occur at all stages of the PEFC operation. Many fundamental issues in these fields can be solved using multiscale computer simulations.

Computer simulations are the most consistent theoretical methods as a starting point in understanding such complex systems as PEMs. In principle, Nafion morphologies, which develop as a result of molecular interactions and processing conditions, and other functional properties of PEMs can be modeled on different levels. In particular, a large amount of simulation work has already been carried out over the past decade in an attempt to characterize the morphology of hydrated Nafion membranes at the atomistic scale [13-28]. The total number of atoms in these systems was limited to about two million because of computer memory and CPU limitations [28]. Significant efforts have been made to take into account quantum effects and chemical reactions within the molecular dynamics models. For this purpose, the so-called Reax force field (ReaxFF) [29,30] and empirical valence bond (EVB) methods [31-33] were applied to simulate Nafion. Explicit proton and charge delocalization of the excess proton transport were treated on the basis of the self-consistent multistate empirical valence bond (SC–MS–EVB) method [34-36]. In addition to the atomistic MD simulations mentioned above, there are also mesoscale models in the literature. They include coarse-grained particle-based models widely used in dissipative particle dynamics (DPD) simulations [37-47] and continuum field-theoretic models in which local density fields are employed as collective variables for simulating the structural evolution of phase-separation morphologies [11,48-53]. Several different quantum mechanics approaches have been used in attempts to understand electronic structure and proton conduction in PEFCs [54-59]. There are excellent reviews that cover this subject in considerable detail [5,12,60].

In this paper, the atomistic and first-principles molecular dynamics simulations are employed to investigate the structure formation in hydrated Nafion membrane and the solvation and transport of protons in the water channel of the membrane.

Results and Discussion
Atomistic molecular dynamics
Model and simulation technique

As an atomistic model of a hydrated Nafion membrane, we simulated a system consisting of n_c identical Nafion chains with $n_s = 10$ sulfonate groups (Figure 2) and n_w water molecules. These species were placed in a cubic box with periodic boundary conditions.

Figure 2: (a) Fragment of a Nafion chain with sulfonic acid groups in dissociated state. The side chains are periodically separated by 15 CF_2 groups ($m = 7$ in Figure 1a). This corresponds to an average equivalent weight (EW) of Nafion, which is about 1150 g/mol (EW is defined by the number of grams of dry Nafion per mole of sulfonic acid groups, when the material is in the acid form, and is given by the relation EW = 100m + 446). A 1100 EW holds for the standard commercialized Nafion 117. All sulfonic acid groups of Nafion are supposed to be in dissociated state. (b) Schematic representation of Nafion as a hydrophobic-hydrophilic copolymer with amphiphilic (A) units. Hydrophilic (P) sites are depicted in yellow and hydrophobic (H) chain sections are shown in gray. Connected H and P groups are considered as an amphiphilic HP "dipole".

All sulfonic acid groups of Nafion were supposed to be in dissociated state (Figure 2a) and hence they had negative charge, while released protons were bound to water molecules to give hydronium ions H_3O^+ responsible for charge transfer reactions.

The hydration level, $[H_2O]/[SO_3H]$, is defined as the ratio of the number of water molecules to the number of sulfonated groups: $\lambda = n_w/n_s n_c$. The value of λ was 5, 10, and 20. Note that the hydration level $\lambda = 5$ is close to the percolation threshold value for water molecules in a Nafion membrane [38,48], while $\lambda = 10$ and 20 is close to the operating regime. At these hydration levels, the membrane may function as a proton-conducting material [61-63]. One should keep in mind that the range of λ values corresponding to the specified hydration regime (low or high hydration conditions) depends on the ratio of hydrophobic/hydrophilic segments in a polymer chain [53]. That is why under certain conditions the state with $\lambda = 10$ and 20 can be referred to the high hydration level. For the systems under study, both λ values correspond to high acidities (pH<<1). Thus, the chosen λ values correspond to concentrated solutions of strong acids.

For atomistic molecular dynamics (AMD) simulations we used the LAMMPS software package [64] in its highly optimized form for hybrid CPU/GPU nodes so that the computations scaled almost linearly on a massively parallel supercomputer. The force field has a significant effect on the results of any atomistic MD simulation. In this work, a class II (second-generation) polymer-consistent force field (PCFF) [65] was employed. PCFF is an ab-initio based force field in which the total potential energy of an atomistic system is represented as a sum of the following terms: valence terms (the energy contributions for bond, bond angle, torsion, and out-of-plane angle coordinates as well as the energy contributions for diagonal and off-diagonal cross-coupling terms between internal coordinates) and intra- and intermolecular non-bonded interaction terms (a Lennard–Jones "9-6" potential for the van der Waals interactions and a Coulombic term for electrostatic interactions). We used the same force field both for the neutral and the charged species (hydronium cations and sulfonic acid anions SO_3^-). For the neutral species, Coulomb interactions in PCFF have been parameterized with charge increments or nonzero atom type charges. For positively/negatively charged ions, charge assignment was done by the charge equilibration method after specifying an overall net charge for the whole structure or the corresponding atomic groups.

Simulation details are identical to those described in our work [27]. Integration step was 1 fs. A 12 Å cut-off radius was applied for Coulomb and van der Waals interactions. The electrostatic interactions were treated by using the PPPM method with a precision of 10^{-6}. The dielectric constant was set to 1. All the simulations described in this study were performed in an isobaric-isothermal (NPT) ensemble at T = 300 K and P = 1 atm, using the Nose–Hoover coupling algorithm with relaxation constants of 0.1 and 0.5 ps for the thermostat and barostat, respectively.

It is well known that the accuracy of any atomistic simulation increases if the size of the material sample is sufficiently large. For hydrated ionomer materials capable of segregating under different conditions, this means that we should operate with the number of atoms about several millions in order to adequately reproduce the system morphology. Another crucial point in any MD study is fully equilibrating the simulated amorphous structure. Therefore our simulations were organized as follows. At the first step during 200 ns, a relatively small system was simulated with the total number of atoms N = 65,608 (64 Nafion chains). To avoid metastable structures due to local energy minima trapping, we generated several samples. Each initial configuration was created as a random distribution of Nafion chains, water molecules and hydronium ions. In the initial state we did not build our systems at a density equal to the experi-

mental one. Instead, not to start with strongly entangled chains, our initial configurations were generated randomly at a density far below the experimental reference. After the energy minimization, the final density of these configurations was subsequently refined during a long relaxation under NPT conditions. Next, the simulation box was replicated twice along three directions and the resultant system of N = 524,864 atoms (512 Nafion chains) was simulated during 200 ns after a long relaxation. The subsequent replication of the system led to the final system of N = 4,198,912 atoms (4096 chains, the initial box size 356^3 Å^3). The run of 200 ns was used to obtain the completely equilibrated system, which was also simulated within the time interval of 200 ns. The system density after equilibration ranged from 1.59 to 1.85 g/cm^3, depending on hydration level. As λ increases, the membrane "swells" more and its density decreases.

The computations reported in this study were performed on the massively parallel supercomputer "Lomonosov" (at Moscow State University) which is based on a hybrid blade system TB2/TB1.1/TB2-TL from T-Platforms equipped with 4,446 X86 compute nodes (Intel Xeon X5570/X5670 2.93 GHz CPUs, 35 568 processor cores), 1554 512-core Tesla X2070 GPUs from Nvidia, and Infiniband QDRinterconnect. Most of our MD simulations were carried out in parallel on 512 hybrid (CPU/GPU) nodes.

Morphology

As an example, Figure 3 shows typical snapshots obtained from the atomistic simulation of the three systems studied at λ = 10 and T = 298 K.

The MD simulations demonstrated that a hydrated Nafion membrane becomes phase segregated into hydrophobic and hydrophilic domains at all hydration levels investigated. There is a well pronounced network of hydrophilic nanochannels resulting from self-organization and formed by water, hydronium ions, and negatively charged SO_3^- groups. It is seen from Figure 3 that the channels show a tendency to a lamella-like arrangement within several nearest layers (a "curly" lamellar structure). However, the regular spatial arrangement of the channels disappears at the level of far removed layers (at length scales of several nanometers). The hydrophobic matrix permeated by ion-conducting hydrophilic channels is formed mainly by the nonpolar backbones of chains comprising carbon and fluorine atoms. Importantly, the formation of a continuous and percolated aqueous subphase was observed in our simulation even at λ = 5. This observation is confirmed by a number of other theoretical studies of hydrated Nafion. Using the formalism of pair-connectedness correlation functions within the framework of the self-consistent integral equation pRISM
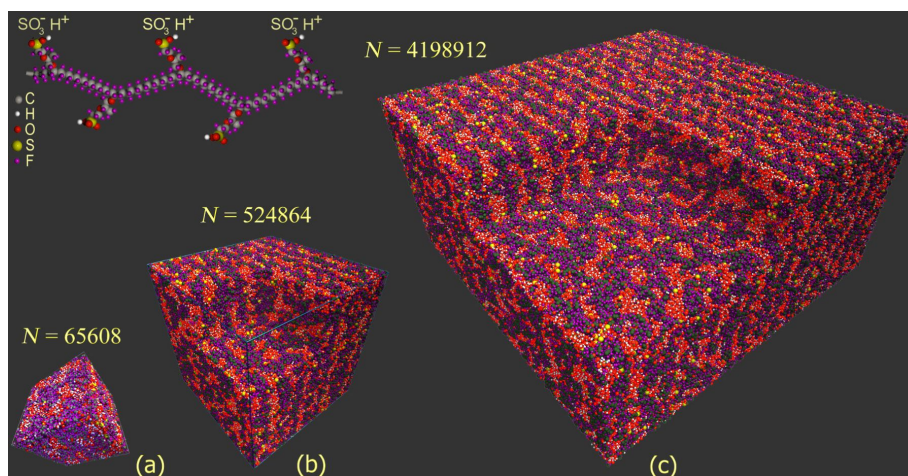
Figure 3: Typical structures predicted by fully atomistic molecular dynamics simulations for hydrated Nafion membrane (10 water molecules per SO$_3^-$ group) and a fragment of Nafion chain. In the systems studied at ambient temperature and under atmospheric pressure (NPT ensemble), all SO$_3$H groups are dissociated, while released protons are bound to water molecules to give hydronium ions H$_3$O$^+$. The total number of atoms N in a simulation box with periodic boundary conditions is specified for each system. A portion of materials is removed from the images of systems (b) and (c) for a better understanding of the structural organization. The evolution of each system was monitored for 200 ns after relaxation.

theory, we have previously shown that the percolation transition associated with the formation of a continuous water cluster through the entire system occurs near $\lambda \approx 3$ [48]. This is also in keeping with the MD results by Dupuis et al. [22] who found that a λ-value of 5–6 is close to the percolation threshold.

Additional information related to the formation of conductive channels and their topology was obtained from analysis of slices through the hydrophilic subphase (for more detail, see [27]). It was found that the hydrophilic subphase is organized like a sponge-like network and the global membrane morphology can be classified as bicontinuous: both the hydrophilic and the hydrophobic subphase are continuous in space. In other words, both for the hydrophobic-rich regions and hydrophilic-rich regions, one can trace a path from any side of the simulation box to any other side of the box, through one single phase. So both *majority* (hydrophobic) and *minority* (hydrophilic) phases have percolating network-like structures, although the spatial distribution of microdomains does not appear to visually conform to simple periodic shapes. The water network is, of course, not a static entity, but a dynamic system whose shape can change as the water molecules and the local hydrophobic environment diffuse.

In order to further characterize the predicted microphase-separated structure, we calculated for each simulated system the partial structure factors $S(q) = \int d\mathbf{r} \exp(-i\mathbf{q} \cdot \mathbf{r}) \rho(\mathbf{r})$ which are the Fourier transform of the partial densities ρ within the simulation box. Of particular interest is the structure factor of the water phase responsible for the formation of ion-conducting channels. These structure factors were compared to those

known for different "perfect" morphologies. Several perfect morphologies were considered as possible candidates. First, a simple lamellar (LAM) morphology and hexagonally perforated lamellae (HPL) were considered as candidate phases. The HPL structure consists of alternating minority and majority component layers (that is the hydrophilic and hydrophobic species in our case) in which hexagonally packed domains of majority components extend through the minority component [66]. Possible bicontinuous architectures are naturally associated with well known bicontinuous cubic phases (BCPs). Among many BCPs found in block copolymers and concentrated surfactant systems, the double-diamond (DD) structure with the space group $Pn\overline{3}m$, and the Schoen's double gyroid (DG structure with space group $Ia\overline{3}d$) are most common [67-69]. These structures are the most probable candidates and were used for comparison. The results are shown in Figure 4, where we compare the partial structure factors $S(q)$ calculated for the water phase with those known for HPL, DD and DG morphologies [66-69].

First of all, we would like to draw attention to the fact that the positions of the main harmonics predicted for the three systems with different total number of atoms practically coincide. From inspection of Figure 4, we see that the partial structure factor $S(q)$ has several distinct peaks. This means that the microphase separation leads to the development of an ordered or partly ordered structure. Next, we analyze the positions of these peaks which correspond to the various harmonics.

One can conclude that the spatial organization of hydrated Nafion is drastically different from that expected for the LAM
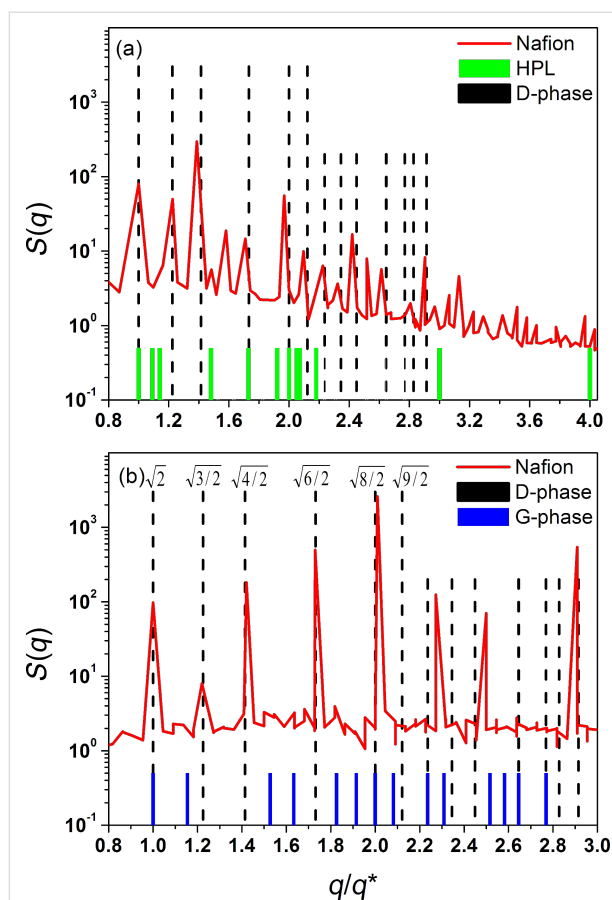
Figure 4: Partial structure factors, $S(q)$, of the water phase (red line) calculated for (a) the 524,864-atom system and (b) the 4,198,912-atom system at $\lambda = 10$ and $T = 298$ K. These functions are compared to those known for a perfect structure, including hexagonally perforated lamellae (HPL), double diamond (DD) and double gyroid (DG). The vertical lines correspond to the expected peaks for these structures [66-69]. The $S(q)$ functions are plotted versus q/q^*, where q is the wave number and q^* is the position of the first, most intensive maximum of the $S(q)$. The peaks are shown at each magnitude of the scattering vector $|\mathbf{q}| = \sqrt{h^2 + k^2 + l^2}$, where h, k, and l are the Miller indices associated with the allowable reflections. (a) The solid (green) and dashed (black) vertical lines correspond to the expected harmonics for $P6_3/mmc$ (consistent with the HPL structure) and $Pn\overline{3}m$ (consistent with DD structure) crystallographic symmetries. (b) The vertical lines correspond to the expected harmonics for $Pn\overline{3}m$ (consistent with DD structure) and $Ia\overline{3}d$ (consistent with DG structure) crystallographic symmetries.

and HPL mesophases for which the main harmonics are spaced at a ratio of 1:2:3:4… There are also significant differences between the simulated structure and the DG morphology. On the other hand, except for several very weak peaks, most of the intense peaks observed for the 4,198,912-atom system closely resemble the ones expected for $Pn\overline{3}m$ crystallographic symmetry. Indeed, the Bragg reflections of a perfect structure with $Pn\overline{3}m$ symmetry are characterized by scattering intensities in the relative (scattering vector) positions $\sqrt{2}$, $\sqrt{3}$, $\sqrt{4}$, $\sqrt{6}$, $\sqrt{8}$, $\sqrt{10}$, $\sqrt{12}$, and $\sqrt{19}$, while the eight main harmonics predicted in our simulation are spaced at a q/q^* ratio of

1.0:1.22:1.42:1.73:2.01:2.25:2.49:2.90 (cf. Figure 4b). As seen, there is a fairly good agreement between the positions of these peaks. However, the peaks at the relative positions $\sqrt{9}$, $\sqrt{11}$, $\sqrt{14}$, $\sqrt{16}$, and $\sqrt{17}$ expected for a structure with $Pn\overline{3}m$ space group are absent or almost invisible. Taking this into account, one has to conclude that microphase-separated Nafion does not form a perfect DD phase, indicating the large amount of various defects present in the simulated structure. These structural defects include a considerable number of undulations and perforations, as can be seen from the examination of numerous snapshots similar to those shown in Figure 3. Nevertheless, the overall organization averaged over many configurations is best described by a pattern, which is consistent with bicontinuous DD morphology. Note that the DD-like mesophases are rather typical for both triblock copolymer melts and amphiphile/water systems [70,71]. In particular, bicontinuous cubic phases (e.g., DD and DG) and transitions between them are often observed for mixtures of water with surfactants or lipids [71].

The observed specific structural organization of hydrated Nafion can be understood by reference to simple models of amphiphilic copolymers [72-75]. Indeed, Nafion is a typical polyamphiphile: its perfluorosulfonic acid macromolecule contains a strongly hydrophobic backbone and less hydrophobic side chains having strongly polar end group. Furthermore, it is known that the association of the hydrated proton with Nafion also suggests its amphiphile-like behavior [35]. From this viewpoint, a hydrophobic-amphiphilic (HA) model of Nafion can schematically be depicted like that shown in Figure 2b. In this model, each amphiphilic unit is a hydrophobic-polar (HP) "dipole" that corresponds to the short side chain of Nafion. The two antagonistic groups, H and P, in the HP "dipole" are repelling each other, but they have to "get along" with each other due to the chemical connectivity, so that the amphiphilic unit prefers to be localized at the H/P boundary, rather than in H- or P-bulk phase. This means that the HP unit possesses a significant surface activity and behaves as an interface modifier (surfactant). This behavior should be seen particularly clearly in the presence of one more polar component, namely water. The tendency to form interfaces between different domains is the key to understand the phase behavior of polyamphiphiles. It has been demonstrated that this feature can lead to fairly specific scenarios of self-organization in the system of amphiphilic-nonpolar copolymers [74-76]. In particular, an amphiphilic component with very incompatible H and P units can form thin channels and slits permeating through a matrix of a majority hydrophobic component [76]. The origin of such morphologies has been discussed for these materials and the physical forces responsible are well recognized. Essentially interfacial tension controls their morphologies. The interfacial tension tends to decrease interfacial stretching, thereby leading

to the formation of highly curved monolayers consisting of amphiphilic units with their polar groups in contact with water and hydrophobic groups shielded from contacting the water. When the concentration of these units is not too high, the monolayers are folded in such a way as to form a pattern of connected water channels. Such a behavior is typical for surfactants, lipids, polymeric foams, and assemblies of soap bubbles. In principle, the same percolating structures we observe for our model membrane. In this respect, the structure of hydrated Nafion closely resembles the bicontinuous cubic phase well-known for lyotropic mesophases. The bicontinuous morphology is an especially attractive one for many applications requiring a high interfacial area, such as fuel cell membranes, organic solar cells, etc. In particular, it is clear that such a morphology of the microphase-separated system should be favorable for ionic conductivity.

From the partial structure factor $S(q)$ we can estimate the characteristic size of water-containing channels and pores in which ion transfer occurs in a Nafion polymeric membrane. The position of the first peak in the structure factor, q^*, provides a measure of the average size of water channels, $d = 2\pi/q^*$. For $\lambda = 5$, 10 and 20, this measure gives $d = 25.5$, 39.6, and 50.1 Å, respectively, in reasonable agreement with the available experimental data for hydrated Nafion [8]. As seen, our simulation predicts that the effect of the water content on d is well pronounced: the micro-size of channels drastically increases with hydration level, the behavior commonly observed in experimental studies.

Finally, we should explain why the snapshots of the simulated systems clearly demonstrate a layered structure (Figure 3),

while the analysis of structure factors reveals a bicontinuous DD-like morphology (Figure 4). The answer is surprisingly simple. In Figure 5 we present the density distribution in a bicomponent system corresponding to a geometrically perfect DD structure (the OBDD microdomain morphology). It is seen that at any slice, the DD structure looks like a regular layered pattern, in a manner similar to that seen in Figure 3.

The convenient approach to visualize the spatially complex internal structure within the simulated volume is the use of a surface of constant atomic density (isodensity surface) instead of atomistic representation. As an example, we show in Figure 6 the isodensity surface that demonstrates the distribution of water oxygens in the 524,864-atom system at $\lambda = 10$. The isodensity surface was defined as $\rho_O/\overline{\rho}_0 = 1/2$, where $\overline{\rho}_0$ is the average density of water oxygens in the system. As seen, the 3D distribution of the hydrophilic subphase most closely resembles that which is typical for DD structure (Figure 5).

The main result of our large-scale atomistic simulations is the observation that virtually all hydrophilic channels are connected to each other even at relatively low water content in the system. In fact, these channels represent conductive nano-wires which should be responsible for the ionic transport during the operation of a fuel cell. From a global point of view, the channels can be considered as a spatial continuous network organized in an irregular ordered pattern, which is largely similar to that formed by the minority phase of the double-diamond structure. The existence of such a specific structural organization can explain in part the surprisingly high ionic conductivity of the hydrated Nafion membrane.

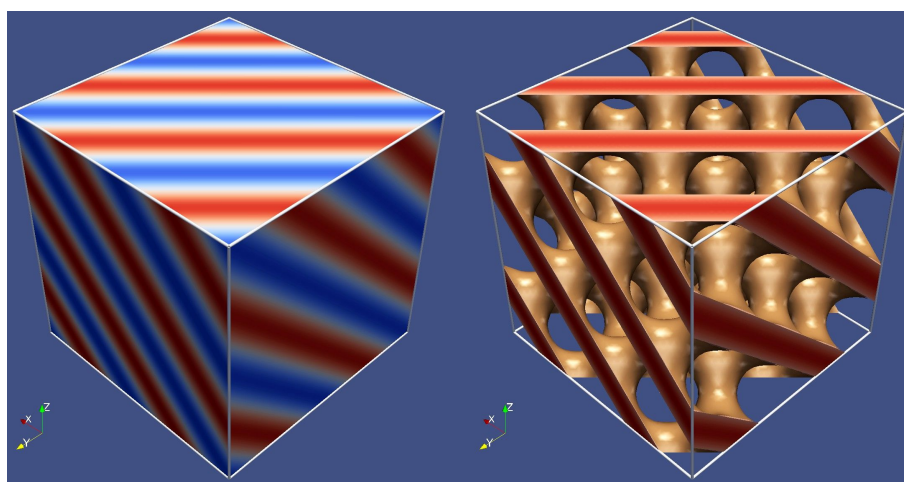**Figure 5:** Ordered bicontinuous double diamond structure (space group 224), which contains two separate, connected, triply periodic, tetrahedrally coordinated networks comprised of the minority (A, "red") component in a matrix of the majority (B, "blue") component. Both the red and blue domains are three-dimensionally continuous. The right part of the figure shows the minority component bound by the isodensity surface.
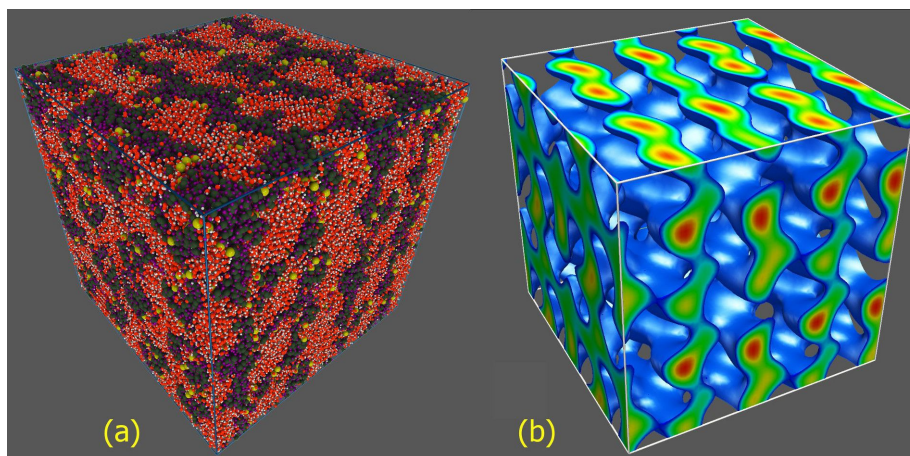
Figure 6: (a) Atomistic representation of the 524,864-atom system and (b) the isodensity surface that demonstrates the distribution of water oxygen atoms in the same system.

Ion pairing

The ionic conductivity is to a large extent determined by electrostatic interactions and directly related to ion pairing. The accepted mechanism of the ionic conductivity involves the mobile ions moving from one polymer chain to another by a chain-flexing process called segmental motion [77]. To clarify the issue of whether the driving force for dissociation (association) of positively/negatively charged ions, H_3O^+ and SO_3^-, is dominantly of energetic or entropic nature, we examined the temperature dependence of pair correlation functions (PCFs) $g_{+-}(r)$ and the corresponding potential of mean force $W_{+-}(r) = -k_B T \ln g_{+-}(r)$. The value of $W_{+-}(r)$ is identified with the free energy F as a function of interionic separation r at a given temperature T. The results discussed in this subsection were obtained from the simulations of our smallest (65,608-atom) system at a hydration level of 10, and the temperature ranged from 200 K to 500 K.

From the analysis of PCFs we concluded that the ion association is seen to decrease with increasing temperature but a quite strong ion pairing is observed even at $T = 500$ K. On the other hand, no complete clustering is visible even at the lowest temperature considered. It was found that the $W_{+-}(r)$ function demonstrates a rather typical behavior well known for electrolyte solutions: there are one or two deep minima at the distance corresponding to associated sulfonate/hydronium ion pairs $SO_3^-\cdot H_3O^+$ and solvent-separated ion pairs as well as a shallow third minimum at longer distances, probably due to a second solvation shell for the ions (Figure 7). As the temperature is subsequently increased, the minimum for the contact ion pairs and solvent-separated ion pairs becomes deeper. More importantly, the main contribution to the free energy of contact ion pairs seems to be dominated by the entropy gain, not the poten-

Figure 7: The potential of mean force, $W_{+-}(r)$, and the energetic and entropic contributions, ΔU and $-T\Delta S$, to $W_{+-}(r)$ as a function of the SO_3^-–H_3O^+ separation at $T = 300$ K.

tial energy contribution. To demonstrate this, we performed a thermodynamic decomposition of the potential of mean force.

If the standard state for free energy is defined as that for the infinitely separated cation and anion, $r \to \infty$, then one can write

$$W_{+-}(r) - W_{+-}(\infty) \equiv \Delta F = \Delta U - T\Delta S \qquad (1)$$

where $W_{+-}(\infty) = 0$ and $\Delta S = -\partial W_{+-}(r)/\partial T$. The entropic part ΔS of free energy for different distances and temperatures was calculated numerically using B-splines constructed for the set of the PCFs. Having ΔS, one can find ΔU from Equation 1. An

example demonstrating the behavior of the energetic and entropic contributions, ΔU and $-T\Delta S$, is presented in Figure 7 for $T = 300$ K. Figure 8 shows the surfaces $\Delta U(r,T)$ and $-T\Delta S(r,T)$ calculated for the regions $2.2 < r < 6$ Å via the separation of the potential of mean force.

As seen, the behavior of the contributions to $W_{+-}(r)$ is rather complex, depending on the regions of r and T. The energetic contribution acts against squeezing charged groups together below the Lennard–Jones contact distance, as expected. On the other hand, in the region of short interionic distances, including the region of the first minimum of $W_{+-}(r)$, the entropic contribution to the free energy is negative. As the distance increases, the energy appears to weakly prevent the formation of ion pairs, while the entropy gain remains to be the main driving force for contact pairs.

It is instructive to trace the temperature dependence of the energetic and entropic contributions for some specific interion separations, in particular, for those corresponding to the main minimum of $W_{+-}(r)$. For associated ion states (at $r \approx 2.28$ Å), we see from Figure 8 that the entropic part of free energy demonstrates a general tendency to increase and thus leads to a decrease in ΔF as the temperature is increased, while the energetic contribution changes weakly with temperature (except the region located between about 300 and about 400 K, where both ΔU and $-T\Delta S$ display oppositely directed oscillations). The superposition of ΔU and $-T\Delta S$ results in a monotonous decrease in ΔF which appears to be a nearly linear function of temperature.

From the data presented above we can conclude that the change in ion association observed in the system is largely an entropic effect. Ion pairing, which takes place with decreasing temperature, leads to a decrease in entropy and to a corresponding increase in free energy for the entire system. One part of the explanation of this effect follows from loss of low-frequency modes due to ion association. Because these modes are mainly responsible for transport processes, we can expect that the entropic effects would play an important role in the interpretation of the features related to ionic conductivity. Also, it should be noted that an increase in temperature favors the disruption of water-ion contacts, thus leading to an additional increase in the total system entropy.

It is worthwhile to compare the effects of ion pairing observed for polyelectrolytes and for electrolyte solutions, including polymer electrolytes, in which both cations and anions are mobile. A particularly interesting feature of this phenomenon in the case of electrolyte solutions is evidence that pairing increases with increasing temperature [78,79]. It has been suggested (e.g., [80,81]) and shown by computer simulation [82,83] that this effect might occur because more entropy is available to ion pairs than to dissociated ions, leading to an entropically driven temperature dependent contribution to the binding free energy. For the ionomeric system studied here we observe an opposite effect of the temperature, the ion pairing decreases with increasing temperature, although the entropic effect is dominant. Presumably, the different behavior of these systems arises from the mobility of anions in polyelectrolytes, including hydrated Nafion, is strongly restricted.

In addition to the thermodynamic properties, it is instructive to discuss spectral densities of the hindered translational motions of cations. The spectral density is defined by the Fourier transform of the velocity autocorrelation function (VACF)

$$f(\mathbf{v}, \omega) = \frac{m}{3\pi k_B T} \int\limits_0^\infty \langle \mathbf{v}(t) \cdot \mathbf{v}(0) \rangle e^{i\omega t} dt \qquad (2)$$
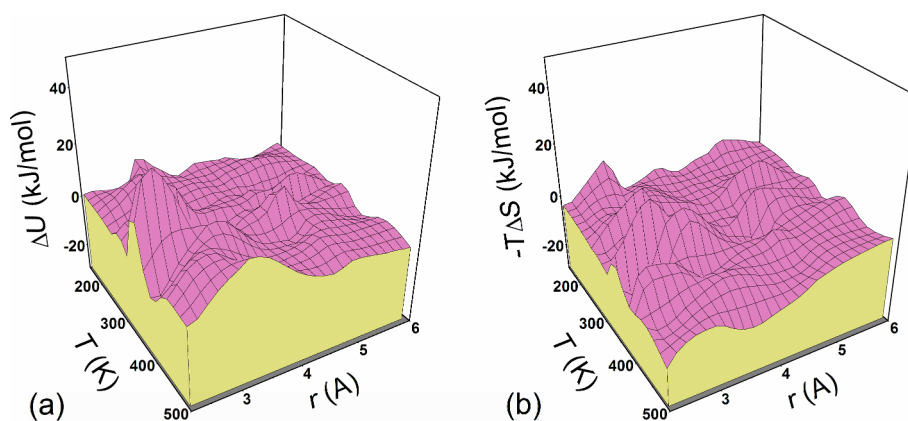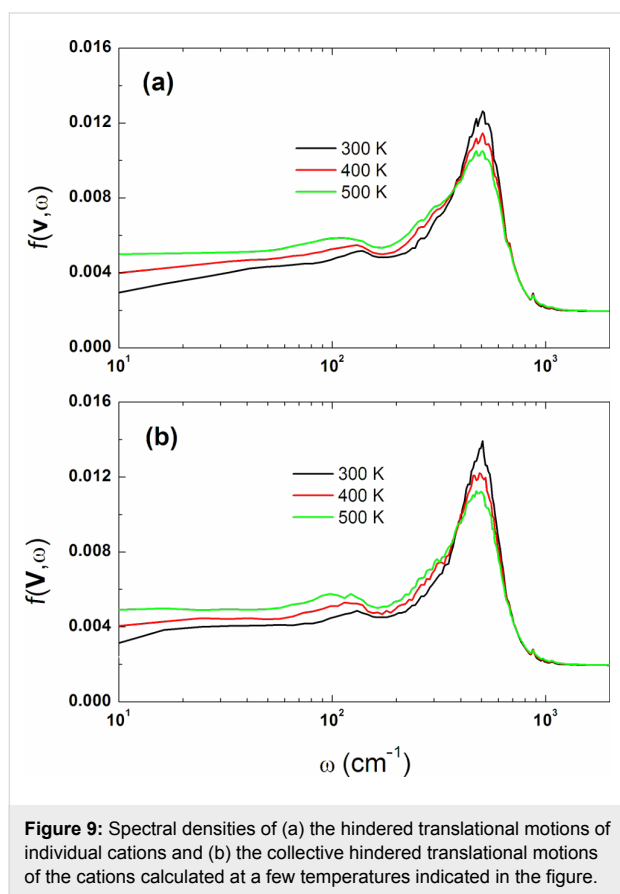

Figure 8: The surfaces (a) $\Delta U(r,T)$ and (b) $-T\Delta S(r,T)$ calculated for the region $2.2 < r < 6$ Å via the separation of the potential of mean force $W_{+-}(r)$.

where m is the mass of the cation, ω is the frequency, and the factor before the integration sign is chosen so that $\int_0^\infty f(\mathbf{v},\omega)d\omega = 1$. Also, using the collective VACF $\langle \mathbf{V}_i(t) \cdot \mathbf{V}_i(0) \rangle$, where $\mathbf{V}(t) = \sum_i \mathbf{v}_i(t)$ and $\mathbf{v}_i(t)$ is the center-of-mass velocity of an individual cation at time t, we calculated the spectral density of the collective hindered translational motions, $f(\mathbf{V},\omega)$, which is directly related to the frequency-dependent ionic conductivity. These functions are presented in Figure 9 for frequencies ω up to 2000 cm^{-1} at three different temperatures.

Figure 9: Spectral densities of (a) the hindered translational motions of individual cations and (b) the collective hindered translational motions of the cations calculated at a few temperatures indicated in the figure.

The results show similar but not identical behavior for $f(\mathbf{v},\omega)$ and $f(\mathbf{V},\omega)$. First, we note that any vibratory component present in the particle motions would appear in spectral densities as a peak away from the origin. These features clearly manifest themselves in the simulated results, which indicate that the motion of the cations has both a vibratory and a diffusive component (Figure 9). In general, such behavior is essentially the same for both spectral densities. Of special interest is the peak located in the region between 490 and 510 cm^{-1}, which is believed to indicate the fast vibration of the cation due to the formation of ionic bonds between oxygens of the sulfonate groups and the cation. As the temperature is increased, the vibration intensity at this frequency, ω_o, becomes lower and this is accompanied by broadening the peak toward lower frequen-

cies and by a weak "red shift" in the main peak. As a result, the diffusive component of motion increases. The same is true for the direct-current (dc) conductivity, which is proportional to $f(\mathbf{V},0)$. From the power spectra shown in Figure 9 we can conclude that, although significant ion association does exist, the cations are still mobile and would contribute to ionic conductivity even at low temperatures. As has been pointed out above, the loss of low-frequency modes due to ion association is largely an entropic effect.

Quantum molecular dynamics
Models and simulation technique
In the simulation of the structure and dynamics of materials at nanoscale, the electron subsystem (in many cases) should be taken into account in an explicit form. Naturally, this requires the solution of the Schrödinger equation to describe the quantum evolution of the system of many nuclei and electrons. This approach is accomplished in quantum molecular dynamics (QMD), which considers in combination the motion of classical (atomic nuclei) and quantum (electrons) particles [84]. The model treats simultaneously the alteration of wave function defining electron density redistribution and the change of coordinates of classical atoms, i.e., the Schrödinger and Newton equations are solved in combination at each time step. The approach consists in the determination of forces affecting atoms "on the fly" from electronic structure calculations based on the first (ab initio) quantum-mechanical principles rather than on empirical potentials. This provides a possibility to observe not only structural properties of materials at classical level but also electronic effects responsible for chemical transformations. However, the QMD method requires computer resources by orders of magnitude larger than those sufficient for typical atomistic MD simulations. In this work, we describe for the first time the results of QMD modeling of microphase separation and ion-conducting channels in a Nafion membrane. To that end, two models were developed.

Model I. First of all, we tested whether it is possible to predict the microphase separation of water and Nafion using QMD. For this purpose, a relatively small system consisting of six identical sulfonated Nafion monomers (Figure 1b) and 30 or 60 water molecules (corresponding to a hydration level of 5 or 10) was studied in a cubic box with periodic boundary conditions. The initial distribution of molecules in the box was random.

Model II. The model of an ion-conducting channel was based on the data obtained from our classical MD simulation at $\lambda = 10$ and $T = 298$ K. The channel was modeled as a slit whose two opposite walls separated by a distance of 37.21 Å along the Z-axis were built of eight Nafion strands oriented along the X-axis of a unit simulation cell with periodic boundary condi-

tions (Figure 10). The lateral distance between the neighboring Nafion strands was extracted from atomistic MD simulations and refined later by QMD. The chains are virtually infinite in the periodic cell. Each periodic strand contains two sulfonic acid groups, resulting in sixteen SO_3H groups per unit cell. The interior of the channel is filled with water molecules, resulting in a 1200-atom system. The dimensions of the rectangular unit cell are $20.46 \times 19.91 \times 37.21$ Å along the X-, Y-, Z-axes, respectively. The thickness of the slit (37.21 Å) adopted in the model corresponds to the average size of the hydrophilic channel estimated from the atomistic MD.

We employed the CP2k package [85] and the so-called "Car–Parrinello-like approach to Born–Oppenheimer MD" recently developed by Kühne et al. [86]. This hybrid quantum mechanical simulation scheme combines Born–Oppenheimer quantum molecular dynamics (BOMD) [84] and Car–Parrinello molecular dynamics (CPMD) [87] within Kohn–Sham electron density functional theory (DFT) [88]. As in the original CPMD, the electronic wave functions are not self-consistently optimized here during the evolution of electrons and ions. However, the fictitious Newtonian dynamics is substituted by a similarly coupled electron-ion MD. Importantly, this computational scheme does not require the use of a fictitious mass parameter, but similar to BOMD, the electrons are kept on the Born–Oppenheimer surface, corresponding to their instantaneous electronic ground state, by means of explicit electronic structure optimization after each MD step [89]. This implies that the time step can be chosen to be as large as the particular ionic resonance limit. The main advantage of this hybrid approach is that the best aspects of both conventional QMD methods, CPMD and BOMD, are exploited simultaneously.

From a computational viewpoint, the hybrid CPMD/BOMD scheme proved to be much more efficient than BOMD and CPMD separately, thereby allowing one to increase the size of simulated systems and use rather complex variants of DFT.

We used a recently modified version of the code CP2K/Quickstep [85], which is a numerical implementation of the Gaussian and plane waves (GPW) method [90] based on the Kohn–Sham formulation of DFT. The electronic charge density was expanded in an auxiliary plane-wave basis at the Γ-point up to a kinetic energy cutoff of 280 Ry. The high-precision "molecular-optimized" (MOLOPT) triple basis set with a supplementary set of polarization functions (TZVP-MOLOPT-GTH) [91] was employed. This basis set was specifically optimized to perform accurate DFT-based molecular calculations for a wide range of chemical environments, including gas phase, interfaces, and condensed phase [91]. The Kohn–Sham orbitals were expanded in contracted Gaussian basis sets. Core electrons were removed by the introduction of norm conserving pseudopotentials developed by Goedecker, Teter and Hutter (GTH) [92]. The exchange–correlation potential was approximated by the PBE-D functional supplemented by a damped interatomic potential to account for van der Waals interactions [93]. This approach turned out to be reasonably accurate yet computationally affordable for our systems, which are very large. The dispersion correction term was used because it is known that the inclusion of van der Waals interactions systematically improves the density of liquid water [94]. All the technical parameters (γ_D, K, etc.) of the hybrid CPMD/BOMD method were selected as recommended in [95], where static and dynamical properties of liquid water were studied. The QMD computations were performed on 1024 nodes of the supercomputer "Lomonosov".
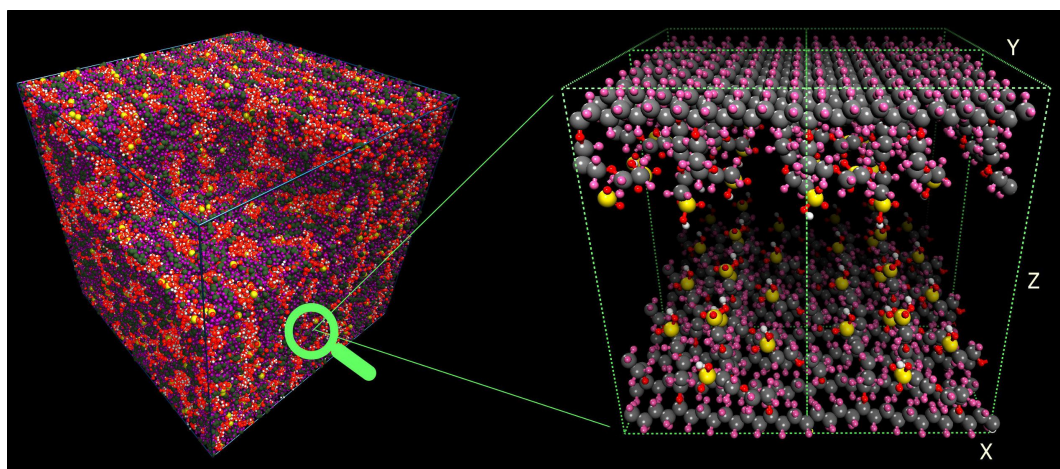

Figure 10: Model of the ion-conducting channel studied by quantum molecular dynamics. The initial configuration is shown. Channel walls are formed by Nafion chains oriented along the *X*-axis. The chains are infinite in the periodic cell. The total number of atoms in the system is 1200. Water molecules filling the channel are omitted for visual clarity. Conventional atom colors are used.

Given the high computational cost of a QMD simulation, the initial configuration of the ion-conducting channel (Figure 10) was first pre-equilibrated for 10 ns using a classical PCFF force field, followed by a 50-ps equilibration with QMD in the canonical (NVT) ensemble. The integration of the equations of motions for ions was performed using the velocity-Verlet algorithm coupled to a Nose–Hoover chain thermostat on each nuclear degree of freedom. The target temperature for the equilibration was set to 400 K. The temperature was then reduced to 298 K and the simulation was continued for additional 110 ps. After that the productive QMD run was performed for 120 ps at 298 K. This time window is sufficient for studying the charge-transport processes in a system where low energy barriers are effectively washed out by zero-point motion. Because the initial configuration for the QMD simulations of the nanochannel was taken from the classical MD trajectory, it was important to

check the stability of the model channel. No strong drift of the structure was observed over most of the 120-ps QMD simulation and therefore the system remains stable.

In the QMD simulations of Model I, the same methodology and protocol as described above were applied, except that the simulation time was 200 ps (after 100 ps of equilibration). Note that a rather long equilibration time (at least 100 ps) is required to achieve an equilibrium content of water–proton complexes (especially Eigen cations) in the system.

Segregation of water and perfluorosulfonic acid molecules

The final molecular configuration obtained for Model I at $\lambda = 10$ is presented in Figure 11. As seen, the Teflon backbone and hydrophobic side chains are pushed out of the aqueous

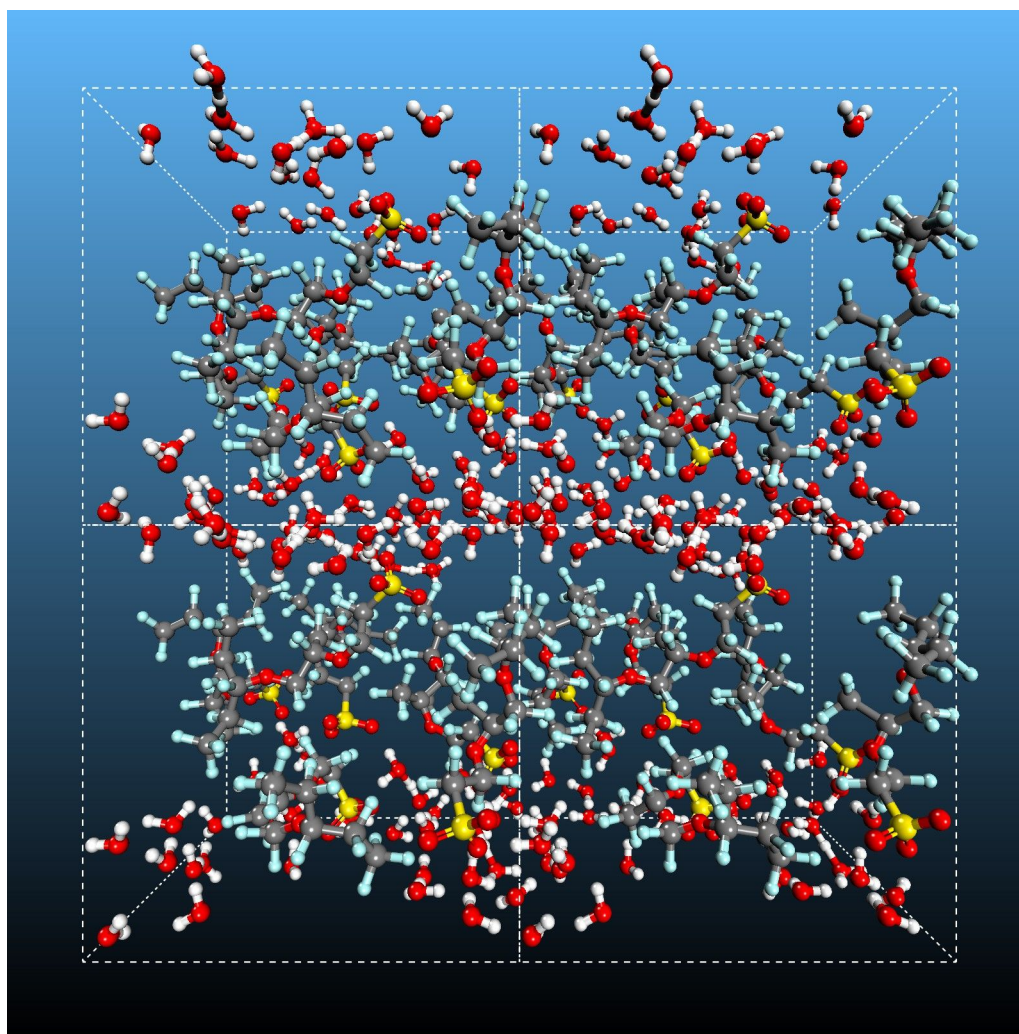**Figure 11:** Snapshot of the water-containing Nafion structure obtained after the 200 ps QMD simulation at 298 K and λ = 10. The simulation box is replicated two times along the X- and Z-directions. For clarity, some of the equivalent atoms (not all) across the periodic boundaries are also depicted. Oxygen is shown in red, carbon in gray, fluorine in light blue, hydrogen in white, and sulfur in yellow.

medium by the water molecules, while the strongly polar SO_3^- groups bound to the side chains favor contact with water and, as a result, they tend to localize at the interface between the hydrophobic units and water. From examination of various snapshots, it is evident that a lamella-like microphase-separated structure is formed in this small system. Thus we can conclude that even though the system is not large enough to investigate the nanoscale morphology, a hydrophilic/hydrophobic segregation indeed occurs in the hydrated Nafion. Of course, the system size is also too small to develop more complex micro-segregated morphologies like bicontinuous superstructure. Actually, we observe the formation of a hydrophilic channel in the system. Also, the formation of both hydronium ions and more complex hydrated proton clusters is clearly seen (Figure 11). This issue is discussed in more detail in the next subsection.

Additionally we analyzed pair correlation functions (PCFs). Figure 12a shows PCF $g_{OH}(r)$, where O indicates the oxygen atom belonging to the SO_3 groups and H denotes any hydrogen. At the hydration level $\lambda = 5$, the first sharp peak located at $r \approx 1.01$ Å corresponds to the O–H bond distance in non-dissociated SO_3H. This means that at low water loading, not all SO_3H groups are ionized. At the same time, it should be stressed that perfluorosulfonic acids require only three water molecules to exhibit spontaneous proton dissociation [57]. At the higher hydration level, $\lambda = 10$, practically all protons are dissociated and this "valence" peak is not visible. The main peak in $g_{OH}(r)$ is associated with the first coordination shell formed by water molecules and positively charged ions around the SO_3 groups, giving an average first solvation shell size of approximately 3.5 water molecules.

In Figure 12b we show the $g_{OO}(r)$ function calculated for the oxygen atoms of water and the oxygen atoms of charged water-

proton complexes $H^+(H_2O)_n$ (for the definition of $H^+(H_2O)_n$, see the next section). It has the first sharp peak around 2.5 Å, which is associated with the formation of hydrated proton complexes. The remarkable intensity of this peak is an indication that water molecules are considerably localized near these complexes. The area under the first peak corresponds to a coordination number of about 3. The differences in $g_{OO}(r)$ between the systems at $\lambda = 5$ and 10 are comparatively minor: no significant difference on the peak positions of the PCFs occurs. Nevertheless, the second and third coordination spheres become more pronounced when λ is increased.

Proton solvation in hydrophilic channel

In simulating the model of an ion conducting nanochannel (Model II), our main goal was to reveal the details of the structural and dynamic mechanism of charge transfer. The statistical analysis of the 120-ps trajectories obtained from ab initio MD simulations allows us to establish some general features of the mechanism responsible for proton solvation and transport inside the hydrophilic channels of PEMs.

The sulfonic acid groups of Nafion in aqueous surrounding release protons, which bind to water molecules to give hydronium ions. Once hydronium ions are formed, they do not stay alone, because they develop more complex hydrated proton forms with nearby water molecules in continuously exchanging configurations. These configurations include, e.g., the Zundel cation $H_5O_2^+$, the Eigen cation (a triply solvated hydronium ion $(H_2O)_4H^+$ or $H_3O^+\cdot(H_2O)_3$), and other more complex solvation structures $H^+(H_2O)_n$ with $n > 4$ [96-100]. In the Zundel cation, the proton mainly resides in between two water molecules, $H_2O\cdots H^+\cdots OH_2$. The Eigen cation consists of a hydronium core symmetrically solvated by three additional water molecules [96-100]. In liquid water or other hydrogen bonded liquids, the
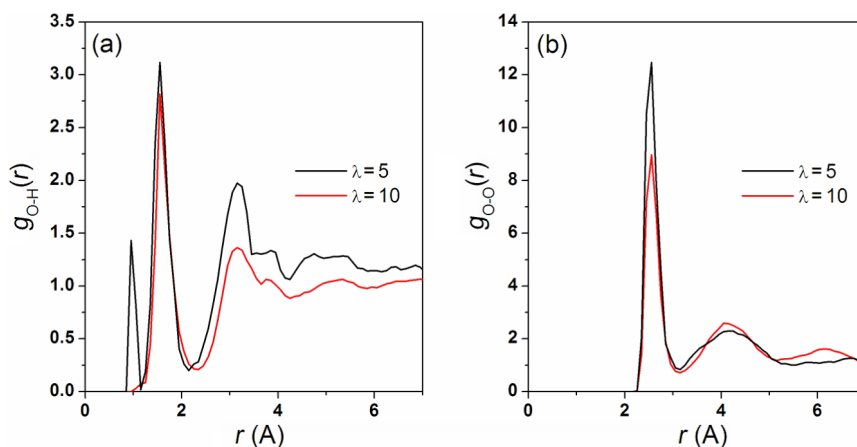

Figure 12: (a) Pair correlation functions, $g_{OH}(r)$, for the oxygen atoms of the SO_3 groups and any proton, at $\lambda = 5$ and 10. (b) Pair correlation functions, $g_{OO}(r)$, for the oxygen atoms of H_2O and proton–water complexes, at $\lambda = 5$ and 10.

description of the proton solvation is usually limited by the Zundel cation and the Eigen cation. The difference between potential energy of these cations is very small (ca. 2–3 kcal/mol); as a result, these two solvation forms can interconvert on the femto- to picosecond time scale [97]. While the proton transport mechanism is believed to involve the inter-conversion between these cations [97], the details of the solvation process and aqueous proton transfer are still unknown for ionomer membranes.

In order to identify water–proton complexes $H^+(H_2O)_n$ with $n = 1$–4, the hydronium oxygens were first selected as those closest to the centre of excess positive charges. After that their three hydrogens were found by a shortest-distance criterion. Finally, the complexes were completed by adding the closest water molecules. At each time step the hydrated proton forms were constructed anew. Snapshots of the simulated system clearly demonstrate the formation of various proton complexes (Figure 13).

The QMD simulations showed that the presence of water in the model nanochannel causes dissociation of $-SO_3H$ units resulting in the formation of the $SO_3^- \cdot H_3O^+$ ion pairs. The dissociation and transfer of the hydrogen ion to the aqueous medium occur very fast, typically within 0.1–0.2 ps. Due to the further solvation, the ion pairs transform into shared proton complexes $SO_3^- \cdot H_3O^+ \cdot (H_2O)$. The Zundel cations are then formed via the proton transfer reaction $H_3O^+ + H_2O \rightarrow H_5O_2^+$. At the next step, the topological defects in the hydrogen bond network occur in the form of Zundel–Zundel transformations.

Also, the solvated hydronium complexes in the form of the Eigen cations exist as an intermediate state in Zundel–Eigen–Zundel proton exchange.

The hydronium and the nearest water molecules constantly interchange the proton within a very short time. In this way, the excess proton rattles between the oxygen atoms of two neighboring water molecules. In other words, the proton is transferred temporarily from a water molecule to its neighboring molecule by hopping, but then returns to its original location. It is clear that this process will not contribute significantly to the actual diffusion of protons in water phase. This picture is in agreement with both experimental observation [101] and theoretical work [102] which predicts that proton transfer along the hydrogen bond network should be essentially barrierless. Also, the proton may rattle between water molecules and the SO_3^- units similar to the rapid hopping between H_3O^+ and H_2O.

We calculated the average relative content (per SO_3^- group) of different hydrated proton complexes $[A]/[SO_3^-]$, where $[A]$ denotes the concentration of the species $H^+(H_2O)_n$ and $[SO_3^-]$ is the concentration of SO_3^- groups. The results are shown in Table 1.

Table 1: Average relative content of different hydrated proton complexes.

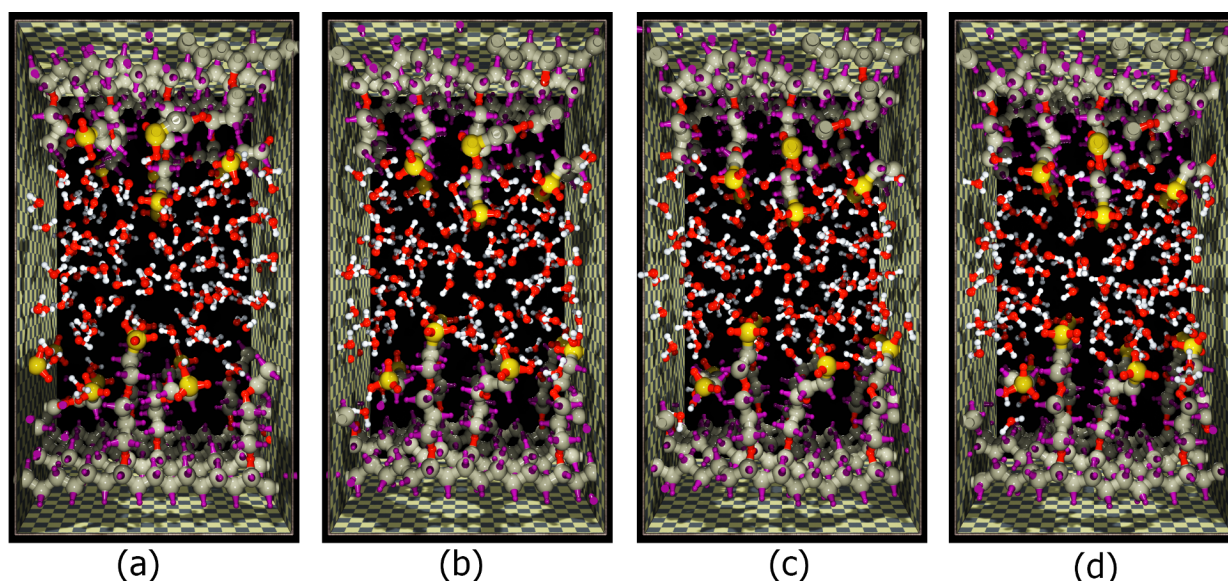| ion	H_3O^+	$H_5O_2^+$	$H_7O_3^+$	$H_9O_4^+$	$H_3O^+ \cdot (H_2O)_3$
$[ion]/[SO_3^-]$	0.664	0.294	0.004	0.000	0.438

(a)   (b)   (c)   (d)

Figure 13: Sequence of snapshots from the QMD simulation of the ion-conducting nanochannel at different time points, starting with the initial configuration (a).

It is seen that the hydronium, Zundel and Eigen ions dominate in the system, while the $H_7O_3^+$ and $H_9O_4^+$ complexes are very rare.

In Figure 14 we present the relative content of hydrated proton complexes [A], A = H_3O^+, $H_5O_2^+$, $H_3O^+\cdot(H_2O)_3$, as a function of simulation time. The time autocorrelation functions, $C(A;t)$, calculated for these processes and the time-dependent cross-correlation functions, $C(A,B;t)$, characterizing the correlation between three different pairs of the same complexes are shown in Figure 15. It is notable that the $C(A;t)$ correlation functions exhibit an exponential decay at very short time ($\approx$10 fs). The estimated relaxation time τ_h associated with the formation of hydronium ions is greater than the relaxation time τ_Z found for Zundel ions, but is considerably less than the relaxation time τ_E found for Eigen ions. This result suggests that the proton exchange between hydronium and water molecules is a relatively fast process as compared to the formation of both hydronium and Eigen ions. An analogous conclusion can be drawn from the data shown in Figure 15b for the cross-correlation functions. The reversible transition $H_3O^+ + 3H_2O \leftrightarrow H_3O^+\cdot(H_2O)_3$ is a strongly correlated process, as can be expected, while the mutual transformations of hydronioum/Zundel ions (reversible transition $H_3O^+ + H_2O \leftrightarrow H_5O_2^+$) and Zundel/Eigen ions (reversible transition $H_5O_2^+ + 2H_2O \leftrightarrow H_3O^+\cdot(H_2O)_3$) are less correlated. Note that proton transmission becomes possible only when the surrounding water molecules rearrange at particular points in time to enable the Zundel cation and at other times the Eigen cation configuration.

The widely accepted view is that the proton transfer process can generally be described as the sequential transformation hydronium–Zundel–hydronium (h–Z–h) [5,6]. This mechanism is highly analogous to the Eigen–Zundel–Eigen (E–Z–E) transformation model of proton transfer in water [97,102]. For hydrated polymeric membranes, however, the situation may in principle be different. In this case, one may wonder what influence the presence of SO_3^- groups has on the proton hydration and transfer. The key difference between bulk water and the membrane is that in membrane, there is a high surface density of SO_3^- groups which are located at the water/Nafion interface (cf. Figure 11 and Figure 13). Thus, the nanochannels can be understood as high surface charge density pores where the passage of charge should be affected by Donnan exclusion effects, whose exact role and mechanism, however, is still being debated (for more details, see [103]). Due to the fact that protons may be trapped by negatively charged SO_3^- groups, they remain for a relatively long time at the interface instead of being released into the bulk. Hydronium cations formed in this interfacial region are closer to the surface than water molecules

Figure 14: A 5-ps section of a QMD trajectory showing the change in the relative content of different hydrated proton complexes at λ = 10. This short time section is chosen for visibility, but the behavior shown here is typical of any time section from the same trajectory.

Figure 15: (a) Normalized time autocorrelation functions for the processes [A](*t*), where A denotes H_3O^+, $H_5O_2^+$, and $H_3O^+\cdot(H_2O)_3$, at λ = 10. (b) Time-dependent cross-correlation functions (in arbitrary units) characterizing the formation of different pairs of hydrated proton complexes at λ = 10.

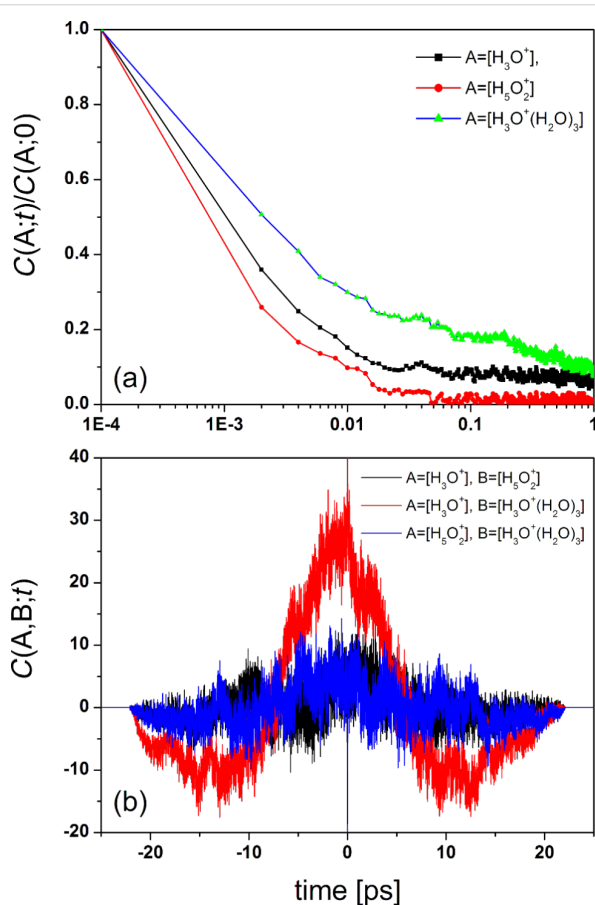so that they can more or less easily be transformed into Zundel ions at the hydronium/water interface, but not into Eigen ions. The results shown in Figure 15b directly confirm this behavior.

It follows from the analysis of PCFs and snapshots that the configuration in which a hydronium ion is hydrogen bonded to oxygens of two SO_3^- groups is frequently found in the system. Due to steric hindrance, the accessibility of the hydronium with respect to the surrounding water molecules decreases in this configuration. Such a steric hindrance makes it difficult to form a hydrogen bond between the hydronium and neighboring water molecules. As a result, a proton is detached from a SO_3H group, transferred temporarily from this group to its neighboring deprotonated group SO_3^- by hopping (assisted or not assisted by surrounding water molecules), but then can return to its original location. In a sense, this behavior is reminiscent of the "cage effect" in classical liquids, where a particle can be trapped inside a virtual cage formed by its neighbors for some time, before it can escape from this cage and then diffuse in the bulk liquid. It may well be that this is one of the reasons why the relaxation time τ_h is greater than τ_Z (cf. Figure 15).

Since the SO_3^- groups are close to each other in the water channel, free protons can reside in between these groups, thereby decreasing the effective degree of dissociation. We call this dissociation mechanism "abnormal dissociation". Schematically, the process can be represented as follows: $SO_3H + SO_3^- \leftrightarrow SO_3^- + SO_3H$. It is clear that the "abnormal dissociation" will reduce the number of proton participating in the protonation of water. Naturally, in these circumstances, we should speak about an "effective dissociation" that generally is lower as compared to an expected 100% dissociation. In practice, however, a significant decrease in the degree of dissociation can be expected only for a very narrow channel, at low water loading.

Thus, from the results of the QMD simulations, one can expect that for our model nanochannel, proton transfer through Zundel–Eigen–Zundel (Z–E–Z) transformations, which feature importantly in the transfer of the protons at high water content [97,104], should dominate over the transfer through Zundel–Zundel (Z–Z) transformations. On the other hand, in agreement with the scenario proposed by Paddison et al. [105] and Idupulapati et al. [106], the dominant transport mechanism consisting of sequences Z–Z transformations can be favorable at very low water content when the channel diameter is very small, comparable to the size of the Eigen cation.

Proton transport and the Grotthuss mechanism

There are several hypothetical models that describe proton transport in aqueous media. The most known and widely

discussed model that explains the reasons of abnormally fast diffusion of the proton in water was formulated by Grotthuss more than 200 years ago [107-110]. This model implies that chains of dipoles can explain the transport of charge in water. For a long time, the Grotthuss mechanism (also called the *hop-and-turn* or *relay* mechanism) was no more than an elegant hypothesis. In 2005, Nibbering and colleagues [109] found that hydrogen ions are indeed transmitted very efficiently through water, as predicted by the Grotthuss model [107]. It should be noted that this experimental study become possible by using a unique technique based on ultrashort laser flashes, that enabled the determination of the jump-like proton transmission from acids via water to bases in time steps of 150 femtoseconds. Very recently, Kulig and Agmon also presented the experimental evidence of the Grotthuss mechanism, using a "clusters-in-liquid" approach for calculating the infrared spectrum from any set of charges in bulk water and water clusters [100]. It should be borne in mind that in general, the mobility of protons in aqueous environments is determined by a combination of the two contributions: a fast Grotthuss-type proton hopping and the much more slow hydrodynamic diffusion of protonated water clusters [110]. It cannot be said, however, that the problem related to the Grotthuss mechanism has found a unified solution. The subject has given rise to renewed interest particularly in view of the growing role played by ab-initio molecular dynamics methods applied to the transport of excess protons in water and water solutions (see, e.g., [102,111-118]).

The Grotthuss proton-transfer process implies that an excess proton moves through the hydrogen bond network of water molecules through the formation/cleavage of O–H bonds when the Zundel or Eigen cation can form. From the chemical viewpoint, such process corresponds to heterolytically dissociating and reforming individual H_2O molecules. Of course, all molecules in liquid phase are also involved in normal thermal motion. Therefore the resulting charge migration should be a superposition of two alternating motion motifs: (i) usual "slow" (vehicle or Stokes) diffusion of a proton within the hydronium ion, which behaves as a transport container and (ii) the fast proton hopping far along the network of hydrogen bonds between neighboring water molecules. This means that the dynamics of charge transfer should involve at least two distinctive characteristic times and corresponding to them two characteristic spatial scales related to one or another motion motif.

To verify this hypothesis, we calculated the autocorrelation portion $G_s(\mathbf{r},t)$ of the van Hove space–time correlation function $G(\mathbf{r},t)$ [119], which is a fundamental property of liquid structure and in practice results from the Fourier transform of the so-called intermediate scattering function obtained experimentally from incoherent neutron scattering. The $G_s(\mathbf{r},t)$ function
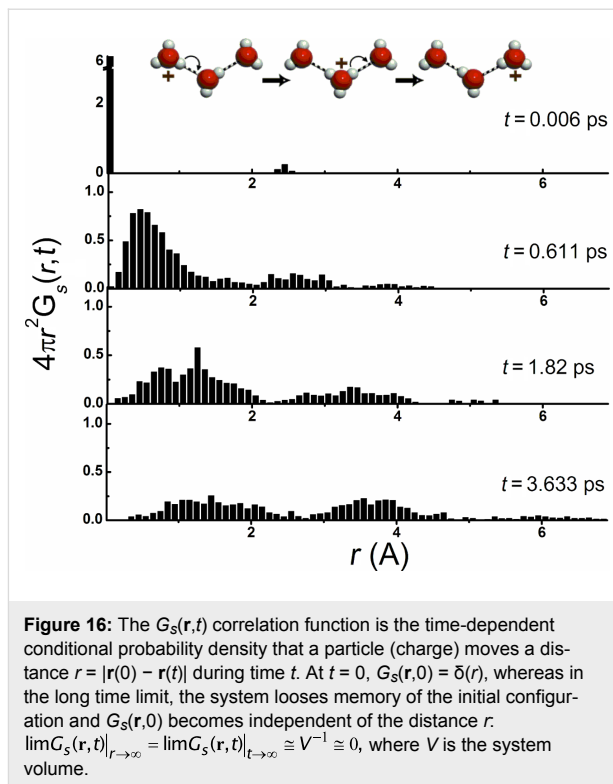
provides a probability to detect a particle at moment t in a space point **r** on condition that it was in the origin of coordinates at $t = 0$. However, unlike common computations, we monitored positive charge movement rather than particle position. This methodology is similar to an "identity concept" proposed by Agmon and coworkers [120]. Also, like this work, we did not differentiate between "unproductive" and "productive" (successful) proton transfer. The $G_s(\mathbf{r},t)$ function defined in this way is relevant for characterizing the heterogeneous dynamics related to proton transfer.

The results are shown in Figure 16 for four different time intervals. The sufficiently large extent of generated QMD trajectories and obtained statistics allow one to observe the bimodality of the $G_s(\mathbf{r},t)$ function, which provides the direct evidence of the Grotthuss mechanism. Over very short times (in femtosecond time scale), the proton moves at small distance within hydronium so that $G_s(\mathbf{r},t)$ shows only one maximum. This motion can mainly be attributed to "unproductive" proton transfers, including fast "proton rattling", i.e., recurrent proton-transfer events that occur within the non-transfer intervals [121]. At longer monitoring time (in picosecond time scale), the first maximum of $G_s(\mathbf{r},t)$ is gradually shifted to longer distances and then splits into two maxima (Figure 16). The position of the second maximum roughly corresponds to the size of the first hydration shell and changes little over time. However, the intensity of both maxima naturally decreases with time: in the long time limit, the system looses memory of the initial configuration and $G_s(\mathbf{r},t)$ becomes independent of the distance. It is natural to assume that the well-pronounced second maximum on the van Hove autocorrelation function is associated with the proton hopping along the network of hydrogen bonds, as schematically illustrated by the insert in Figure 16.

From the above discussion, it is reasonable to conclude that we obtained a direct confirmation that the charge transfer in the hydrophilic channel of the ionomeric membrane indeed proceeds via the Grotthuss mechanism. Of course, analysis of $G_s(\mathbf{r},t)$ provides information on the time and length scales of dynamic processes but not on different molecular structures that participate in the charge mobility process.

Conclusion

Due to up-to-date demands on the polymer proton-exchange membranes with excellent mechanical characteristics, chemical stability, high proton conductivity, in-depth understanding the polymer microstructure and its connection with physical properties and fuel cell operating conditions is needed. Because the charge mobility can hardly become higher than in water or aqueous hydrochloric acid solution, the key challenge is to increase the charge mobility by optimizing the morphology of

Figure 16: The $G_s(\mathbf{r},t)$ correlation function is the time-dependent conditional probability density that a particle (charge) moves a distance $r = |\mathbf{r}(0) - \mathbf{r}(t)|$ during time t. At $t = 0$, $G_s(\mathbf{r},0) = \delta(r)$, whereas in the long time limit, the system looses memory of the initial configuration and $G_s(\mathbf{r},0)$ becomes independent of the distance r: $\lim G_s(\mathbf{r},t)\big|_{r\to\infty} = \lim G_s(\mathbf{r},t)\big|_{t\to\infty} \cong V^{-1} \cong 0$, where V is the system volume.

the membrane. Although a considerable experimental effort has been undertaken to study the morphology of hydrated Nafion, the microsegregated structure of this complex material is not well understood until now. This is primarily due to the ambiguous interpretation of experimental data. In this regard the role of computer modeling is particularly significant. Of course, it is impossible to solve this problem without using different mutually supplementary computational methods (quantum mechanical, atomistic, and mesoscopic) and the wide application of high-performance computing. This is a fundamentally multiscale materials science problem. In the present work, large-scale atomistic and first-principles molecular dynamics simulations were employed to investigate the structure formation in a hydrated Nafion membrane and the solvation and transport of protons in the water channel of the membrane. The most important findings from the research can be summarized as follows.

1. We have carried out atomistic force field-based simulations for water/Nafion systems, containing more than 4 million atoms, which are large enough to observe several hydrophilic domains. At water loading levels corresponding to the operating conditions, the predicted microphase-separated morphology can be classified as bicontinuous: both *majority* (hydrophobic) and *minority* (hydrophilic) subphases are three-dimensionally continuous and organized in an irregular ordered pattern, which is largely similar to that known for bicontinuous

double-diamond structures. This behavior is due to the fact that Nafion is a typical amphiphilic polymer: it combines, in one macromolecule, strongly hydrophobic and strongly hydrophilic groups, which gives rise to a constrained hydrophobic/hydrophilic nanoseparation in the presence of physisorbed water. As a result, the developed morphology is generally close to the partly ordered mesophases or microemulsions characteristic of low-molecular-weight surfactant systems in a non-polar solvent. The existence of the well pronounced two-phase structural organization can explain in part the surprisingly high ionic conductivity of hydrated Nafion membranes even at relatively low water content. The characteristic size of the hydrophilic channels estimated from Bragg's equation for water phase is about 25–50 Å, depending on water content. This is in reasonable agreement with the available experimental data for hydrated Nafion.

2. To clarify the issue of whether the driving force for ion dissociation (association) is dominantly of energetic or entropic nature, we have calculated the potential of mean force (PMF), which characterizes the interaction between hydronium cations and oppositely charged sulfonate groups of Nafion, and examined its temperature dependence. The energetic and entropic contributions were found using a thermodynamic decomposition of PMF. It was shown that ion association observed with decreasing temperature is largely an entropic effect related to the loss of low-frequency modes. Because these modes are mainly responsible for transport processes, one can expect that the entropic effects would play an important role in ionic conductivity. Although at temperatures substantially below room temperature, significant ion association does exist, the cations are still mobile and contribute to ionic conductivity.

3. For a relatively small system consisting of sulfonated Nafion monomers and water molecules, it was shown that quantum molecular dynamics simulations are able to predict the microsegregation of water and Nafion: water molecules, hydrated proton complexes, and sulfonic groups are arranged in the hydrophilic regions surrounded by the hydrophobic sections of Nafion and thus the two-phase structure is maintained.

4. Based on the results from our atomistic simulation, a realistic model of an ion-conducting channel containing Nafion chains and water molecules was designed and studied using quantum molecular dynamics. Proton solvation is only fairly understood in bulk water, but has not been comprehended in the ion-conducting channels of proton conducting ionomer membrane. This contrasts with the importance of this process for membrane transport. We have found that the proton exchange between hydronium and water molecules is a relatively fast process as compared to the formation of both hydronium and Eigen ions. The formation processes of hydronium and Eigen ions are strongly correlated, while the mutual transformations of hydronium/Zundel ions and Zundel/Eigen ions are less correlated processes. From the results of the QMD simulations, one can expect that for our model of the ion-conducting nanochannel, proton transfer through Zundel–Eigen–Zundel transformations should dominate.

5. Our extensive 120 ps-long density functional theory (DFT)-based simulations of charge migration in the 1200-atom model of the hydrophilic Nafion nanochannel allowed us to observe the bimodality of the van Hove autocorrelation function $G_s(\mathbf{r},t)$, which provides the direct evidence of the Grotthuss bond-exchange (hopping) mechanism as a significant contributor to the proton conductivity. Over very short times (in femtosecond time scale), the proton moves at small distance within the hydronium so that $G_s(\mathbf{r},t)$ shows only one maximum. At longer monitoring times (in picosecond time scale), this maximum gradually shifts to longer distances and then splits into two maxima, the second of which indicates the proton hopping along the network of hydrogen bonds.

Acknowledgements

References

1. Behling, N. H. *Fuel Cells: Current Technology Challenges and Future Research Needs;* Elsevier Academic Press: New York, NY, USA, 2012.
2. Mauritz, K. A.; Moore, R. B. *Chem. Rev.* **2004,** *104,* 4535–4586. doi:10.1021/cr0207123
3. Wilson, M. S.; Gottesfeld, S. *J. Electrochem. Soc.* **1992,** *139,* L28–L30. doi:10.1149/1.2069277
4. Morris, D. R.; Sun, X. *J. Appl. Polym. Sci.* **1993,** *50,* 1445–1452. doi:10.1002/app.1993.070500816
5. Paddison, S. J. *Annu. Rev. Mater. Res.* **2003,** *33,* 289–319. doi:10.1146/annurev.matsci.33.022702.155102
6. Kreuer, K.-D.; Paddison, S. J.; Spohr, E.; Schuster, M. *Chem. Rev.* **2004,** *104,* 4637–4678. doi:10.1021/cr020715f
7. Weber, A. Z.; Newman, J. *Chem. Rev.* **2004,** *104,* 4679–4726. doi:10.1021/cr020729l
8. Schmidt-Rohr, K.; Chen, Q. *Nat. Mater.* **2008,** *7,* 75–83. doi:10.1038/nmat2074
9. Devanathan, R. *Energy Environ. Sci.* **2008,** *1,* 101–119. doi:10.1039/B808149M
10. Elliott, J. A. Atomistic Structural Modelling of Ionomer Membrane Morphology. In *Device and Materials Modeling in PEM Fuel Cells;* Paddison, S. J.; Promislow, K. S., Eds.; Topics in Applied Physics, Vol. 113; Springer Science: Berlin-Heidelberg, Germany, 2009; pp 413–436. doi:10.1007/978-0-387-78691-9_15
11. Galperin, D.; Khalatur, P. G.; Khokhlov, A. R. Morphology of Nafion Membranes: Microscopic and Mesoscopic Modeling. *Device and Materials Modeling in PEM Fuel Cells;* Topics in Applied Physics, Vol. 113; Springer Science: Berlin-Heidelberg, Germany, 2009; pp 453–483. doi:10.1007/978-0-387-78691-9_17

12. Jorn, R.; Savage, J.; Voth, G. A. *Acc. Chem. Res.* **2012,** *45,* 2002–2010. doi:10.1021/ar200323q

13. Elliott, J. A.; Hanna, S.; Elliott, A. M. S.; Cooley, G. E. *Phys. Chem. Chem. Phys.* **1999,** *1,* 4855–4863. doi:10.1039/A905267D

14. Ennari, J.; Elomaa, M.; Sundholm, F. *Polymer* **1999,** *40,* 5035–5041. doi:10.1016/S0032-3861(98)00731-9

15. Vishnyakov, A.; Neimark, A. V. *J. Phys. Chem. B* **2000,** *104,* 4471–4478. doi:10.1021/jp993625w

16. Vishnyakov, A.; Neimark, A. V. *J. Phys. Chem. B* **2001,** *105,* 7830–7834. doi:10.1021/jp004082p

17. Vishnyakov, A.; Neimark, A. V. *J. Phys. Chem. B* **2001,** *105,* 9586–9594. doi:10.1021/jp0102567

18. Urata, S.; Irisawa, J.; Takada, A.; Shinoda, W.; Tsuzuki, S.; Mikami, M. *J. Phys. Chem. B* **2005,** *109,* 4269–4278. doi:10.1021/jp046434o

19. Jang, S. S.; Molinero, V.; Çağın, T.; Goddard, W. A., III. *J. Phys. Chem. B* **2004,** *108,* 3149–3157. doi:10.1021/jp036842c

20. Jang, S. S.; Molinero, V.; Çağın, T.; Goddard, W. A., III. *Solid State Ionics* **2004,** *175,* 805–808. doi:10.1016/j.ssi.2004.08.039

21. Brandell, D.; Karo, J.; Liivat, A.; Thomas, J. O. *J. Mol. Model.* **2007,** *13,* 1039–1046. doi:10.1007/s00894-007-0230-7

22. Venkatnathan, A.; Devanathan, R.; Dupuis, M. *J. Phys. Chem. B* **2007,** *111,* 7234–7244. doi:10.1021/jp0700276

23. Devanathan, R.; Venkatnathan, A.; Dupuis, M. *J. Phys. Chem. B* **2007,** *111,* 8069–8079. doi:10.1021/jp0726992

24. Devanathan, R.; Venkatnathan, A.; Dupuis, M. *J. Phys. Chem. B* **2007,** *111,* 13006–13013. doi:10.1021/jp0761057

25. Chen, P. Y.; Chiu, C. P.; Hong, C. W. *J. Electrochem. Soc.* **2008,** *155,* B1255–B1263. doi:10.1149/1.2987878

26. Chertovich, A.; Khalatur, P. G.; Khokhlov, A. R. *Compos. Interfaces* **2009,** *16,* 547–577. doi:10.1163/156855409X450936

27. Komarov, P. V.; Veselov, I. N.; Chu, P. P.; Khalatur, P. G.; Khokhlov, A. R. *Chem. Phys. Lett.* **2010,** *487,* 291–296. doi:10.1016/j.cplett.2010.01.049

28. Knox, C. K.; Voth, G. A. *J. Phys. Chem. B* **2010,** *114,* 3205–3218. doi:10.1021/jp9112409

29. Jang, S. S.; Blanco, M.; Goddard, W. A., III; Caldwell, G.; Ross, R. B. *Macromolecules* **2003,** *36,* 5331–5341. doi:10.1021/ma025645t

30. Goddard, W., III; Merinov, B.; van Duin, A.; Jacob, T.; Blanco, M.; Molinero, V.; Jang, S. S.; Jang, Y. H. *Mol. Simul.* **2006,** *32,* 251–268. doi:10.1080/08927020600599709

31. Walbran, S.; Kornyshev, A. A. *J. Chem. Phys.* **2001,** *114,* 10039–10048. doi:10.1063/1.1370393

32. Spohr, E.; Commer, P.; Kornyshev, A. A. *J. Phys. Chem. B* **2002,** *106,* 10560–10569. doi:10.1021/jp020209u

33. Kornyshev, A. A.; Spohr, E. Proton Transport in Polymer Electrolyte Membranes Using Theory and Classical Molecular Dynamics. In *Device and Materials Modeling in PEM Fuel Cells;* Paddison, S. J.; Promislow, K. S., Eds.; Topics in Applied Physics, Vol. 113; Springer Science: Berlin-Heidelberg, Germany, 2009; pp 349–363. doi:10.1007/978-0-387-78691-9_12

34. Petersen, M. K.; Wang, F.; Blake, N. P.; Metiu, H.; Voth, G. A. *J. Phys. Chem. B* **2005,** *109,* 3727–3730. doi:10.1021/jp044535g

35. Petersen, M. K.; Voth, G. A. *J. Phys. Chem. B* **2006,** *110,* 18594–18600. doi:10.1021/jp062719k

36. Tse, Y.-L. S.; Herring, A. M.; Kim, K.; Voth, G. A. *J. Phys. Chem. C* **2013,** *117,* 8079–8091. doi:10.1021/jp400693g

37. Shirvanyanz, D. G.; Pavlov, A. S.; Khalatur, P. G.; Khokhlov, A. R. *J. Chem. Phys.* **2000,** *112,* 11069–11079. doi:10.1063/1.481747

38. Mologin, D. A.; Khalatur, P. G.; Khokhlov, A. R. *Macromol. Theory Simul.* **2002,** *11,* 587–607. doi:10.1002/1521-3919(20020601)11:5<587::AID-MATS587>3.0.CO;2-P

39. Yamamoto, S.; Hyodo, S. *Polym. J.* **2003,** *35,* 519–527.

40. Hyodo, S.-A. *Mol. Simul.* **2004,** *30,* 887–893. doi:10.1080/08927020412331298694

41. Mologin, D. A.; Khalatur, P. G.; Khokhlov, A. R. *Novel Approaches to the Structure and Dynamics of Liquids. Experiments, Theories and Simulations;* Kluwer Academic Publishers: Dordrecht, The Netherlands, 2004; pp 397–416.

42. Allahyarov, E.; Taylor, P. L. *Phys. Rev. E* **2009,** *80,* No. 020801(R). doi:10.1103/PhysRevE.80.020801

43. Allahyarov, E.; Taylor, P. L. *J. Phys. Chem. B* **2009,** *113,* 610–617. doi:10.1021/jp8047746

44. Dorenbos, G.; Morohoshi, K. *Energy Environ. Sci.* **2010,** *3,* 1326–1338. doi:10.1039/B924171J

45. Elliott, J. A.; Wu, D.; Paddison, S. J.; Moore, R. B. *Soft Matter* **2011,** *7,* 6820–6827. doi:10.1039/C1SM00002K

46. Morohoshi, K.; Hayashi, T. *Polymers (Basel, Switz.)* **2013,** *5,* 56–76. doi:10.3390/polym5010056

47. Jorn, R.; Voth, G. A. *J. Phys. Chem. C* **2012,** *116,* 10476–10489. doi:10.1021/jp300040w

48. Khalatur, P. G.; Talitskikh, S. K.; Khokhlov, A. R. *Macromol. Theory Simul.* **2002,** *11,* 566–586. doi:10.1002/1521-3919(20020601)11:5<566::AID-MATS566>3.0.CO;2-0

49. Galperin, D. Y.; Khokhlov, A. R. *Macromol. Theory Simul.* **2006,** *15,* 137–146. doi:10.1002/mats.200500059

50. Wescott, J. T.; Qi, Y.; Subramanian, L.; Capehart, T. W. *J. Chem. Phys.* **2006,** *124,* 134702. doi:10.1063/1.2177649

51. Komarov, P. V.; Veselov, I. N.; Pavlov, A. S.; Khalatur, P. G. *Russ. J. Phys. Chem. A* **2009,** *83,* 984–989. doi:10.1134/S003602440906020X

52. Komarov, P. V.; Veselov, I. N.; Khalatur, P. G. *Polym. Sci., Ser. A* **2010,** *52,* 191–208. doi:10.1134/S0965545X10020136

53. Komarov, P. V.; Veselov, I. N.; Chu, P. P.; Khalatur, P. G. *Soft Matter* **2010,** *6,* 3939–3956. doi:10.1039/B921369D

54. Tuckerman, M. E.; Laasonen, K.; Sprik, M.; Parrinello, M. *J. Phys.: Condens. Matter* **1994,** *6,* A93. doi:10.1088/0953-8984/6/23A/010

55. Tuckerman, M.; Laasonen, K.; Sprik, M.; Parrinello, M. *Chem. Phys.* **1995,** *103,* 150. doi:10.1063/1.469654

56. Paddison, S. J.; Pratt, L. R.; Zawodzinski, T.; Reagor, D. W. *Fluid Phase Equilib.* **1998,** *150-151,* 235–243. doi:10.1016/S0378-3812(98)00323-9

57. Paddison, S. J. *J. New Mater. Electrochem. Syst.* **2001,** *4,* 197–207.

58. Paddison, S. J.; Elliott, J. A. *Solid State Ionics* **2007,** *178,* 561–567. doi:10.1016/j.ssi.2007.01.007

59. Elliott, J. A.; Paddison, S. J. *Phys. Chem. Chem. Phys.* **2007,** *9,* 2602–2618. doi:10.1039/b701234a

60. Paddison, S. J. Proton Conduction in PEMs: Complexity, Cooperativity and Connectivity. In *Device and Materials Modeling in PEM Fuel Cells;* Paddison, S. J.; Promislow, K. S., Eds.; Topics in Applied Physics, Vol. 113; Springer Science: Berlin-Heidelberg, Germany, 2009; pp 385–412. doi:10.1007/978-0-387-78691-9_14

61. Devanathan, R.; Venkatnathan, A.; Rousseau, R.; Dupuis, M.; Frigato, T.; Gu, W.; Helms, V. *J. Phys. Chem. B* **2010,** *114,* 13681–13690. doi:10.1021/jp103398b

62. Laporta, M.; Pegoraro, M.; Zanderighi, L. *Phys. Chem. Chem. Phys.* **1999,** *1,* 4619–4628. doi:10.1039/A904460D

63. Malek, K.; Eikerling, M.; Wang, Q.; Liu, Z.; Otsuka, S.; Akizuki, K.; Abe, M. *J. Chem. Phys.* **2008,** *129,* 204702. doi:10.1063/1.3000641

64. LAMMPS (Large-scale Atomic/Molecular Massively Parallel Simulator). http://lammps.sandia.gov (accessed June 26, 2013).

65. Sun, H. *J. Comput. Chem.* **1994,** *15,* 752–768. doi:10.1002/jcc.540150708

66. Ahn, J.-H.; Zin, W.-C. *Macromolecules* **2000,** *33,* 641–644. doi:10.1021/ma9912812

67. Garstecki, P.; Hołyst, R. *J. Chem. Phys.* **2001,** *115,* 1095. doi:10.1063/1.1379326

68. Vigild, M. E.; Almdal, K.; Mortensen, K.; Hamley, I. W.; Fairclough, J. P. A.; Ryan, A. J. *Macromolecules* **1998,** *31,* 5702–5716. doi:10.1021/ma9716746

69. Enlow, J. D.; Enlow, R. L.; McGrath, K. M.; Tate, M. W. *J. Chem. Phys.* **2004,** *120,* 1981. doi:10.1063/1.1635811

70. Faul, C. F. J.; Antonietti, M. *Adv. Mater.* **2003,** *15,* 673–683. doi:10.1002/adma.200300379

71. Hyde, S. T.; Schröder, G. E. *Curr. Opin. Colloid Interface Sci.* **2003,** *8,* 5. doi:10.1016/S1359-0294(03)00014-1

72. Vasilevskaya, V. V.; Khalatur, P. G.; Khokhlov, A. R. *Macromolecules* **2003,** *36,* 10103–10111. doi:10.1021/ma0350563

73. Vasilevskaya, V. V.; Klochkov, A. A.; Lazutin, A. A.; Khalatur, P. G.; Khokhlov, A. R. *Macromolecules* **2004,** *37,* 5444–5460. doi:10.1021/ma0359741

74. Khalatur, P. G.; Khokhlov, A. R. *Adv. Polym. Sci.* **2006,** *195,* 1–100. doi:10.1007/12_049

75. Kriksin, Y. A.; Khalatur, P. G.; Erukhimovich, I. Yu.; ten Brinke, G.; Khokhlov, A. R. *Soft Matter* **2009,** *5,* 2896–2904. doi:10.1039/B905923G

76. Khokhlov, A. R.; Khalatur, P. G. *Chem. Phys. Lett.* **2008,** *461,* 58–63. doi:10.1016/j.cplett.2008.06.054

77. Pollock, D. W.; Williamson, K. J.; Weber, K. S.; Lyons, L. J.; Sharpe, L. R. *Chem. Mater.* **1994,** *6,* 1912–1914. doi:10.1021/cm00047a004

78. McBreen, J.; Lin, I.-C. *J. Electrochem. Soc.* **1992,** *139,* 960–966. doi:10.1149/1.2069375

79. McBreen, J.; Yang, X. Q.; Lee, H. S.; Okamoto, Y. *J. Electrochem. Soc.* **1996,** *143,* 3198–3203. doi:10.1149/1.1837187

80. Ratner, M. A.; Nitzan, A. *Faraday Discuss. Chem. Soc.* **1988,** *88,* 19–42. doi:10.1039/DC9898800019

81. Forsyth, M.; Payne, V. A.; Ratner, M. A.; de Leeuw, S. W.; Shriver, D. F. *Solid State Ionics* **1992,** *53-56,* 1011–1026. doi:10.1016/0167-2738(92)90285-W

82. Payne, V. A.; Forsyth, M.; Ratner, M. A.; Shriver, D. F.; de Leeuw, S. W. *J. Chem. Phys.* **1994,** *100,* 5201. doi:10.1063/1.467184

83. Halley, J. W.; Duan, Y.; Curtiss, L. A.; Baboul, A. G. *J. Chem. Phys.* **1999,** *111,* 3302. doi:10.1063/1.479609

84. Marx, D.; Hutter, J. *Ab Initio Molecular Dynamics: Basic Theory and Advanced Methods;* Cambridge University Press: New York, NY, USA, 2009.

85. VandeVondele, J.; Krack, M.; Mohamed, F.; Parrinello, M.; Chassaing, T.; Hutter, J. *Comput. Phys. Commun.* **2005,** *167,* 103–128. doi:10.1016/j.cpc.2004.12.014

86. Kühne, T. D.; Krack, M.; Mohamed, F. R.; Parrinello, M. *Phys. Rev. Lett.* **2007,** *98,* 066401. doi:10.1103/PhysRevLett.98.066401

87. Car, R.; Parrinello, M. *Phys. Rev. Lett.* **1985,** *55,* 2471–2474. doi:10.1103/PhysRevLett.55.2471

88. Kohn, W.; Sham, L. J. *Phys. Rev.* **1965,** *140,* A1133–A1138. doi:10.1103/PhysRev.140.A1133

89. Kühne, T. D.; Tod, A.; Pascal, T. A.; Kaxiras, E.; Jung, Y. *J. Phys. Chem. Lett.* **2011,** *2,* 105–113. doi:10.1021/jz101391r

90. Lippert, G.; Hutter, J.; Parrinello, M. *Mol. Phys.* **1997,** *92,* 477–487. doi:10.1080/002689797170220

91. VandeVondele, J.; Hutter, J. *J. Chem. Phys.* **2007,** *127,* 114105. doi:10.1063/1.2770708

92. Goedecker, S.; Teter, M.; Hutter, J. *Phys. Rev. B* **1996,** *54,* 1703–1710. doi:10.1103/PhysRevB.54.1703

93. Grimme, S. *J. Comput. Chem.* **2006,** *27,* 1787–1799. doi:10.1002/jcc.20495

94. Schmidt, J.; VandeVondele, J.; Kuo, I.-F. W.; Sebastiani, D.; Siepmann, J. I.; Hutter, J.; Mundy, C. J. *J. Phys. Chem. B* **2009,** *113,* 11959–11964. doi:10.1021/jp901990u

95. Kühne, T. D.; Krack, M.; Parrinello, M. *J. Chem. Theory Comput.* **2009,** *5,* 235–241. doi:10.1021/ct800417q

96. Wicke, E.; Eigen, M.; Ackermann, T. *Z. Phys. Chem.* **1954,** *1,* 340–364. doi:10.1524/ZPCH.1954.1.5_6.340

97. Markovitch, O.; Agmon, N. *J. Phys. Chem. A* **2007,** *111,* 2253–2256. doi:10.1021/jp068960g

98. Zundel, G. *Angew. Chem., Int. Ed. Engl.* **1969,** *8,* 499–509. doi:10.1002/anie.196904991

99. Zundel, G. In *The Hydrogen Bond, Recent Developments in Theory and Experiments;* Schuster, P.; Zundel, G.; Sandorfy, C., Eds.; North Holland, 1976; pp 687–766.

100. Kulig, W.; Agmon, N. *Nat. Chem.* **2013,** *5,* 29–35. doi:10.1038/nchem.1503

101. Woutersen, S.; Bakker, H. J. *Phys. Rev. Lett.* **2006,** *96,* 138305. doi:10.1103/PhysRevLett.96.138305

102. Tuckerman, M. E.; Marx, D.; Klein, M. L.; Parrinello, M. *Science* **1997,** *275,* 817–820. doi:10.1126/science.275.5301.817

103. Samulski, E. T. *Nat. Mater.* **2011,** *10,* 486–487. doi:10.1038/nmat3059

104. Kim, E.; Weck, P. F.; Balakrishnan, N.; Bae, C. *J. Phys. Chem. B* **2008,** *112,* 3283–3286. doi:10.1021/jp711568f

105. Paddison, S. J.; Elliott, J. A. *Phys. Chem. Chem. Phys.* **2006,** *8,* 2193–2203. doi:10.1039/B602188C

106. Idupulapati, N.; Devanathan, R.; Dupuis, M. *J. Phys. Chem. A* **2010,** *114,* 6904–6912. doi:10.1021/jp1027178

107. de Grotthuss, C. J. T. *Ann. Chim. (Cachan, Fr.)* **1806,** *58,* 54–74.

108. Agmon, N. *Chem. Phys. Lett.* **1995,** *244,* 456–462. doi:10.1016/0009-2614(95)00905-J

109. Mohammed, O. F.; Pines, D.; Dreyer, J.; Pines, E.; Nibbering, E. T. J. *Science* **2005,** *310,* 83–86. doi:10.1126/science.1117756

110. Cukierman, S. *Biochim. Biophys. Acta* **2006,** *1757,* 876–885. doi:10.1016/j.bbabio.2005.12.001

111. Marx, D.; Tuckerman, M. E.; Hutter, J.; Parrinello, M. *Nature* **1999,** *397,* 601–604. doi:10.1038/17579

112. Geissler, P.; Dellago, C.; Chandler, D.; Hutter, J.; Parrinello, M. *Science* **2001,** *291,* 2121–2124. doi:10.1126/science.1056991

113. Tuckerman, M. E.; Marx, D.; Parrinello, M. *Nature* **2002,** *417,* 925–929. doi:10.1038/nature00797

114. Marx, D. *ChemPhysChem* **2006,** *7,* 1848–1870. doi:10.1002/cphc.200600128

115. Berkelbach, T. C.; Lee, H.-S.; Tuckerman, M. E. *Phys. Rev. Lett.* **2009,** *103,* 238302. doi:10.1103/PhysRevLett.103.238302

116. Hayes, R. L.; Paddison, S. J.; Tuckerman, M. E. *J. Phys. Chem. B* **2009,** *113,* 16574–16589. doi:10.1021/jp907853p

117. Hassanali, A.; Prakash, M. K.; Eshet, H.; Parrinello, M.
Proc. Natl. Acad. Sci. U. S. A. **2011,** *108,* 20410–20415.
doi:10.1073/pnas.1112486108
118. Vilčiauskas, L.; Tuckerman, M. E.; Bester, G.; Paddison, S. J.;
Kreuer, K.-D. *Nat. Chem.* **2012,** *4,* 461–466.
doi:10.1038/NCHEM.1329
119. van Hove, L. *Phys. Rev.* **1954,** *95,* 249–262.
doi:10.1103/PhysRev.95.249
120. Markovitch, O.; Chen, H.; Izvekov, S.; Paesani, F.; Voth, G. A.;
Agmon, N. *J. Phys. Chem. B* **2008,** *112,* 9456–9466.
doi:10.1021/jp804018y
121. Chandra, A.; Tuckerman, M. E.; Marx, D. *Phys. Rev. Lett.* **2007,** *99,*
145901. doi:10.1103/PhysRevLett.99.145901

License and Terms

Ultramicrosensors based on transition metal hexacyanoferrates for scanning electrochemical microscopy

Maria A. Komkova[1], Angelika Holzinger[2], Andreas Hartmann[2],
Alexei R. Khokhlov[3], Christine Kranz[2], Arkady A. Karyakin[1]
and Oleg G. Voronin[*1,§]

Full Research Paper

Address:
[1]Faculty of Chemistry, M.V. Lomonosov Moscow State University, Moscow, Russia, [2]Institute of Analytical and Bioanalytical Chemistry, University of Ulm, Ulm, Germany and [3]Faculty of Physics, M.V. Lomonosov Moscow State University, Moscow, Russia

Email:
Oleg G. Voronin[*] - ol.voronin@gmail.com

* Corresponding author
§ Phone: +7 495 939 46 05; Fax: +7 495 939 46 05

Abstract

We report here a way for improving the stability of ultramicroelectrodes (UME) based on hexacyanoferrate-modified metals for the detection of hydrogen peroxide. The most stable sensors were obtained by electrochemical deposition of six layers of hexacyanoferrates (HCF), more specifically, an alternating pattern of three layers of Prussian Blue and three layers of Ni–HCF. The microelectrodes modified with mixed layers were continuously monitored in 1 mM hydrogen peroxide and proved to be stable for more than 5 h under these conditions. The mixed layer microelectrodes exhibited a stability which is five times as high as the stability of conventional Prussian Blue-modified UMEs. The sensitivity of the mixed layer sensor was 0.32 $A \cdot M^{-1} \cdot cm^{-2}$, and the detection limit was 10 μM. The mixed layer-based UMEs were used as sensors in scanning electrochemical microscopy (SECM) experiments for imaging of hydrogen peroxide evolution.

Introduction

The detection of hydrogen peroxide (H_2O_2) is of great importance in monitoring of food and the environment [1] as well as clinical [2], biological and chemical studies [3]. For example, hydrogen peroxide is a marker of inflammatory diseases [4].

Moreover, in fuel cells research, hydrogen peroxide is one of the key molecules as it is produced in the cathode chamber of the hydrogen–oxygen fuel cells causing degradation of the proton-exchange membranes [5]. Investigations of the local

distribution of hydrogen peroxide on the surface of living cells and electrode materials as well as the in vivo analysis requires sensors with a size of 25 μm and less. For such electrodes (ultramicroelectrodes, UME) the thickness of the diffusion layer is comparable to the diameter of the electrode resulting in enhanced mass transport in comparison to macroscopic electrodes and thus leading to improved sensitivity and detection limits [6].

There are a number of studies which demonstrate the detection of H_2O_2 in SECM experiments based on its oxidation at bare platinum electrodes at a potential of 600 mV vs SCE [7-13]. However, such a high oxidation potential is often disadvantageous for real-world applications as interfering compounds may be co-oxidized. Prussian Blue (PB) is the most advantageous hydrogen peroxide transducer [14-16] due to its higher activity in H_2O_2 reduction and oxidation reactions, higher selectivity for hydrogen peroxide reduction in the presence of oxygen, and insensitivity to the presence of reducing compounds (e.g., ascorbate, paracetamol, etc.) [17]. We have already demonstrated miniaturized PB based electrodes with diameters ranging from 10 μm [18] to 125 μm [19]. For the electrodes with diameters of 125 μm, a record sensitivity of approximately 9 A·M^{-1}·cm^{-2} in H_2O_2 detection was achieved. However, the stability of PB in neutral aqueous solutions is not sufficient in respect to the long-term continuous monitoring of high levels of H_2O_2 [20]. Moreover, different iron complexing agents (e.g., EDTA) are known to solubilize PB. This problem is particularly severe for PB-modified UME.

Operational stability of the PB can be improved by covering its surface with polymer films [21,22], by entrapment of the catalysts into sol–gel [23-25], and by conductive polymer matrixes [26,27]. In [20] we have demonstrated a novel approach for the stabilization of a sensor based on mixed iron-nickel hexacyanoferrates. Here, we report on the highly stable ultramicrosensors comprised of alternating films of iron and nickel hexacyanoferrates for the imaging of hydrogen peroxide distribution in SECM.

Results and Discussion

Hexacyanoferrates were deposited onto UMEs with a diameter of 10 μm and 25 μm, respectively. Three types of UME were used: (i) carbon, (ii) platinum and (iii) platinum covered with an ion beam induced deposition (IBID)-generated Pt/C composite material [28]. Deposition of PB was carried out by using cyclic voltammetry (CV) as described elsewhere in detail [29]. PB was deposited using 5 cycles. A further increase of cycles led to a decreased stability. In spite of the good selectivity, PB-based electrodes showed low operational stability in batch measurements (see Table 1).

Stabilized sensors were obtained by using a layer-by-layer deposition with mixed layers of PB and Ni–HCF. Ni^{2+} and $Fe(CN)_6^{3-}$ ions tend to form insoluble precipitate in pure aqueous solutions. Therefore an excessive amount of supporting electrolyte (0.5 M KCl) was used during the deposition of Ni–HCF films. Deposition of Ni–HCF was performed by using CV as described elsewhere [20]. Every two cycles of PB deposition were followed by 2 cycles of Ni–HCF deposition forming one "bilayer". AFM images of Prussian blue and Ni–HCF deposited on top are shown in Figure 1. After the last deposition step the electrodes were activated by CV as described in the Experimental section of this manuscript.
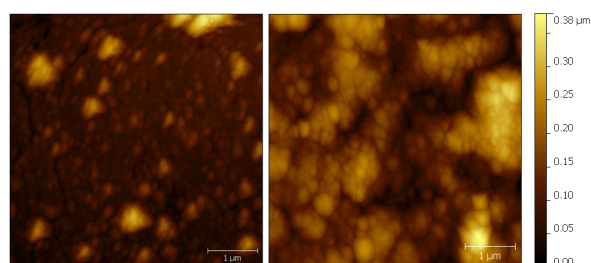

Figure 1: AFM topography images of Prussian blue layer (left) and Ni-HCF layer (right) deposited on top (contact mode images were recorded in air with 0.3 lines/s at a resolution of 512 × 512 lines/image).
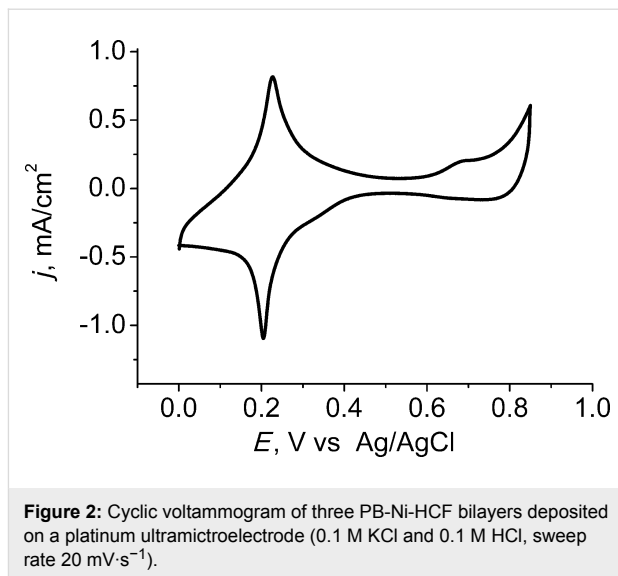
Table 1: Sensitivity and operational stability of the ultramicrosensors (pH 6, batch regime).

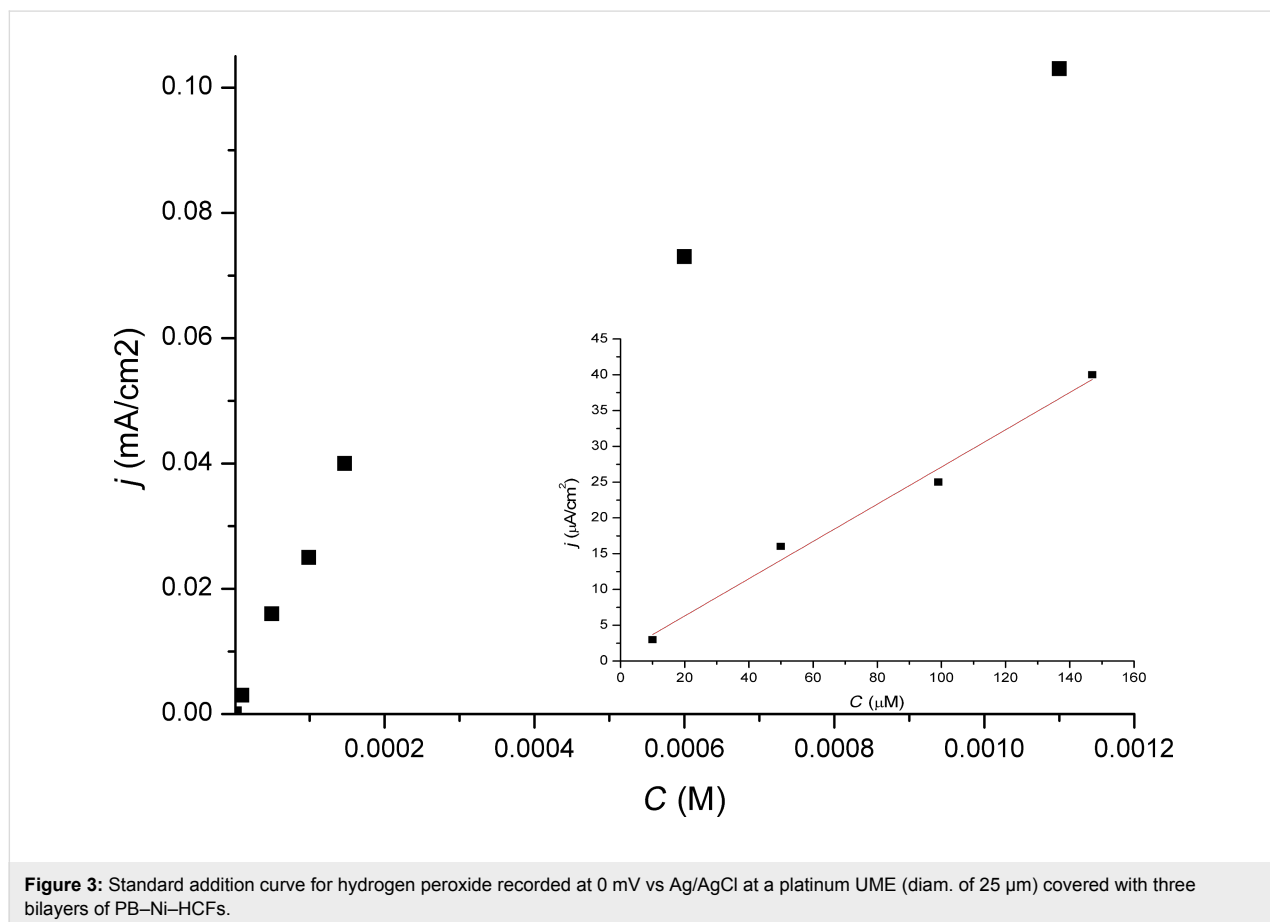| type of UME	type of film	sensitivity, mA/cm^2	stability in 1 mM of H_2O_2, min
glassy carbon	PB	1600	10
glassy carbon	PB–Ni–HCF	81	240
platinum	PB	1050	15
platinum	PB–Ni–HCF	320	240
ion deposited Pt–C composite	PB	760	60
ion deposited Pt–C composite	PB–Ni–HCF	100	300

Increasing the number of bilayers from one to three resulted in a higher sensitivity of the modified electrodes. A continued increase of the number of PB–Ni–HCF bilayers resulted in a loss of mechanical stability. Therefore, all further experiments were carried out with electrodes modified with three bilayers. A typical cyclic voltammogram of a 3-layer-modified microelectrode in supporting electrolyte solution is shown in Figure 2.

Table 1 summarizes the comparison of sensitivity and stability of PB–Ni–HCF-sensors using different electrode materials with data for UMEs only modified with PB. The measurements were carried out in a batch regime. The sensors with mixed layers showed a significantly improved stability and an expected decrease in sensitivity. Figure 3 shows an exemplary calibration curve for a microsensor based on PB–Ni–HCF mixed layers deposited on a platinum UME (diam. of 25 μm).

PB–Ni–HCF-modified platinum microelectrodes were also applied in SECM experiments to map hydrogen peroxide profiles in substrate-generation-tip-collection mode (see Figure 4). As clearly visible in the SECM image, the reduction current significantly increased when the PB–Ni-modified electrode was scanned towards the center of the H_2O_2-generating

Figure 2: Cyclic voltammogram of three PB-Ni-HCF bilayers deposited on a platinum ultramictroelectrode (0.1 M KCl and 0.1 M HCl, sweep rate 20 mV·s^{-1}).

gold electrode (Figure 4A). Control experiments were carried out by repeated SECM scans with three different scanning electrodes: (i) a blank platinum electrode (biased at 0 V vs Ag/AgCl), (ii) a platinum electrode modified only with Ni–HCF, and (iii) a PB–Ni–HCF-modified UME with no poten-
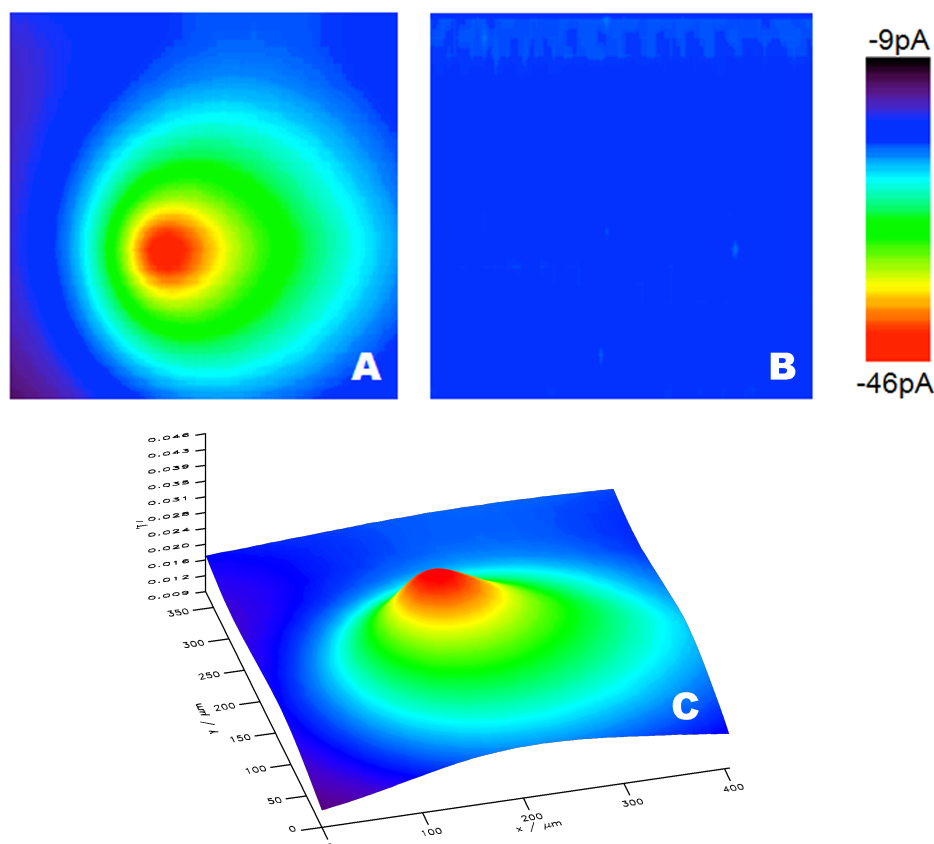

Figure 3: Standard addition curve for hydrogen peroxide recorded at 0 mV vs Ag/AgCl at a platinum UME (diam. of 25 μm) covered with three bilayers of PB–Ni–HCFs.

Figure 4: SECM image of an H_2O_2-generating gold electrode (diam. of 25 μm). A and B are 2D plots of images recorded with a platinum UME (diam. of 25 μm) covered with three layers of PB–Ni–HCF and with Ni–HCF, respectively. C illustrates a 3D plot of A.

tial applied to the H_2O_2 generating gold electrode. In all control experiments a significant signal was not recorded. After the imaging experiments, the integrity of the film was confirmed by CV recorded in 0.1 M HCl/KCl.

Conclusion

Ultramicrosensors for the detection of hydrogen peroxide with increased stability have been developed. It was shown that the electrodeposition of multiple PB–Ni–HCF bilayers on UME provides a significantly enhanced stability of the electrocatalytic films for different electrode materials. UMEs modified with PB–Ni–HCF films retained more than 95% of the initial catalytic activity during at least 5 hours continuous monitoring in 1 mM hydrogen peroxide.

Experimental

Experiments were carried out in solutions prepared with Millipore water (resistivity 18.2 MΩ). All inorganic salts, organic solvents, and hydrogen peroxide (30% solution) were obtained at the highest purity from Sigma-Aldrich. Polishing materials

were obtained from Leco Instruments GmbH and Allied High Tech Products Inc. Gold and platinum microwires were purchased from Goodfellow. The micro glassy carbon electrodes were obtained from ESA Biosciences Inc.

The electrochemical experiments were conducted in a three-electrode setup using either a CHI842B bipotentiostat or a μ-Autolab Type III (Eco Chemie) potentiostat as described in detail elsewhere [18]. An Ag/AgCl was used as a reference electrode and platinum was used as a counter electrode.

Microelectrodes were prepared as described elsewhere [30] by sealing platinum or gold wires (25 μm and 10 μm in diameter, respectively) under vacuum in borosilicate glass (Hilgenberg) or soda lime glass, respectively, followed by consecutive grinding, and polishing steps. Electrodes were then cleaned in an ultrasonic bath for 15 minutes. Circular Pt/C composite layers were deposited onto a microelectrode using a focused ion beam gas-assisted process (Quanta 3D FEG, FEI Eindhoven). The circular Pt/C composite were deposited on 10 μm Pt elec-

trodes and had a radius of approx. 6.5 µm and a thickness of approx. 150 nm (ion beam current: 300 pA and a dwell time of 200 ns) with a ratio of carbon to platinum in the range of 60 atom % C to 24 atom % Pt [28]. Cyclic voltammetry, optical microscopy, and AFM (5500 AFM, Agilent Technologies) imaging were performed for characterizing the fabricated microelectrodes.

The deposition of PB was carried out as described in detail elsewhere [18]. The electrodeposition of nickel hexacyanoferrate (NiHCF) was carried out in a non-colloid solution containing 1 mM $NiCl_2$ and 0.5 mM $K_3[Fe(CN)_6]$ with an excessive amount of supporting electrolyte (0.1 M HCl and 0.5 M KCl), while cycling the electrode potential between 0 and 0.85 V at a scan rate of 100 mV/s applying 20 scans. After the deposition of NiHCF, the electrodes were rinsed with MilliQ water (Millipore MilliQ system) and and tempered at 80 °C for 0.5 h.

The deposition of the mixed films was performed as follows. First, a layer of PB was deposited by cyclic voltammetry as described above applying 2 scans. The electrodes were rinsed with distilled water and dried at 80 °C for 15 min. Then, the deposition of NiHCF was carried out by cyclic voltammetry applying 2 cycles. All layers (except the first and the last ones) were synthesized without temperature treatment. The activation was carried out by CV applying 10 cycles in 0.1 M KCl and 0.1 M HCl solution within the limits of 0.00 to +0.85 V at a scan rate of 40 mV/s and was performed after electrosynthesis of the last layer. Then the electrodes were dried at 80 °C for 0.5 h.

SECM measurements were performed in generation–collection mode as described in detail elsewhere [18]. A gold microelectrode (25 µm in diameter) was used for generating hydrogen peroxide (bias: −0.4 V vs Ag/AgCl). Platinum microelectrodes covered with PB, PB/NiHCF and NiHCF were used to detect the reduction current of hydrogen peroxide at 0.00 V vs Ag/AgCl. The microelectrode modified by metal cyanoferrate was positioned in close proximity to the hydrogen peroxide generating UME in feedback mode recording the Faraday current of the Au microelectrode during the approach of the modified electrode. Prior to the approach curve, the electrodes were positioned centered to each other using an optical microscope. The non-biased modified UME was then approached to the Au microelectrode while the feedback current at the Au UME was recorded in 10 mM ferrocyanide/0.1 M KCl. A negative feedback signal was obtained due to the hindered diffusion of ferrocyanide towards the Au UME when the modified electrode is in the vicinity. The SECM image was then recorded in constant-height mode at a distance of 50 µm (determined by Mira software package, G. Wittstock, University of Oldenburg).

Acknowledgements

References

1. Anglada, J. M.; Aplincourt, P.; Bofill, J. M.; Cremer, D. *ChemPhysChem* **2002,** *3,* 215–221. doi:10.1002/1439-7641(20020215)3:2<215::AID-CPHC215>3.0.CO;2-3

2. Camci-Unal, G.; Alemdar, N.; Annabi, N.; Khademhosseini, A. *Polym. Int.* **2013,** *62,* 843–848. doi:10.1002/pi.4502

3. Gomes, M. P.; Garcia, Q. S. *Biologia (Warsaw, Pol.)* **2013,** *68,* 351–357. doi:10.2478/s11756-013-0161-y

4. Majewska, E.; Kasielski, M.; Luczynski, R.; Bartosz, G.; Bialasiewicz, P.; Nowak, D. *Respir. Med.* **2004,** *98,* 669–676. doi:10.1016/j.rmed.2003.08.015

5. Mu, S.; Xu, C.; Yuan, Q.; Gao, Y.; Xu, F.; Zhao, P. *J. Appl. Polym. Sci.* **2013,** *129,* 1586–1592. doi:10.1002/app.38785

6. Bard, A. J.; Faulkner, L. R. *Electrochemical Methods: Fundamentals and Applications,* 2nd ed.; John Wiley & Sons: New York, U.S., 2001.

7. Kranz, C.; Wittstock, G.; Wohlschläger, H.; Schuhmann, W. *Electrochim. Acta* **1997,** *42,* 3105–3111. doi:10.1016/S0013-4686(97)00158-8

8. Pierce, D. T.; Unwin, P. R.; Bard, A. J. *Anal. Chem.* **1992,** *64,* 1795–1804. doi:10.1021/ac00041a011

9. Wittstock, G.; Wilhelm, T.; Bahrs, S.; Steinrücke, P. *Electroanalysis* **2001,** *13,* 669–675. doi:10.1002/1521-4109(200105)13:8/9<669::AID-ELAN669>3.0.CO;2-S

10. Wittstock, G.; Schuhmann, W. *Anal. Chem.* **1997,** *69,* 5059–5066. doi:10.1021/ac970504o

11. Kishi, A.; Inoue, M.; Umeda, M. *J. Phys. Chem. C* **2009,** *114,* 1110–1116. doi:10.1021/jp909010q

12. Eckhard, K.; Schuhmann, W. *Electrochim. Acta* **2007,** *53,* 1164–1169. doi:10.1016/j.electacta.2007.02.028

13. Fernández, J. L.; Bard, A. *J. Anal. Chem.* **2003,** *75,* 2967–2974. doi:10.1021/ac0340354

14. Karyakin, A. A.; Gitelmacher, O. V.; Karyakina, E. E. *Anal. Chem.* **1995,** *67,* 2419–2423. doi:10.1021/ac00110a016

15. Karyakin, A. A.; Karyakina, E. E. *Sens. Actuators, B* **1999,** *57,* 268–273. doi:10.1016/S0925-4005(99)00154-9

16. Karyakin, A. A.; Karyakina, E. E.; Gorton, L. *Anal. Chem.* **2000,** *72,* 1720–1723. doi:10.1021/ac990801o

17. Kozlovskaja, S.; Baltrūnas, G.; Malinauskas, A. *Microchim. Acta* **2009,** *166,* 229–234. doi:10.1007/s00604-009-0185-8

18. Voronin, O. G.; Hartmann, A.; Steinbach, C.; Karyakin, A. A.; Khokhlov, A. R.; Kranz, C. *Electrochem. Commun.* **2012,** *23,* 102–105. doi:10.1016/j.elecom.2012.07.017

19. Mokrushina, A. V.; Heim, M.; Karyakina, E. E.; Kuhn, A.; Karyakin, A. A. *Electrochem. Commun.* **2013,** *29,* 78–80. doi:10.1016/j.elecom.2013.01.004

20. Sitnikova, N. A.; Borisova, A. V.; Komkova, M. A.; Karyakin, A. A. *Anal. Chem.* **2011,** *83,* 2359–2363. doi:10.1021/ac1033352

21. García-Jareño, J. J.; Navarro-Laboulais, J.; Vicente, F. *Electrochim. Acta* **1996,** *41,* 2675–2682. doi:10.1016/0013-4686(96)00121-1

22. Lukachova, L. V.; Kotel'nikova, E. A.; D'Ottavi, D.; Shkerin, E. A.; Karyakinia, E. E.; Moscone, D.; Palleschi, G.; Curulli, A.; Karyakin, A. A. *Bioelectrochemistry* **2002,** *55,* 145–148. doi:10.1016/S1567-5394(01)00146-3
23. Bharathi, S.; Lev, O. *Appl. Biochem. Biotechnol.* **2000,** *89,* 209–216. doi:10.1385/ABAB:89:2-3:209
24. Guo, Y. Z.; Guadalupe, A. R.; Resto, O.; Fonseca, L. F.; Weisz, S. Z. *Chem. Mater.* **1999,** *11,* 135–140. doi:10.1021/cm9806275
25. Salimi, A.; Abdi, K. *Talanta* **2004,** *63,* 475–483. doi:10.1016/j.talanta.2003.11.021
26. Borisova, A. V.; Karyakina, E. E.; Cosnier, S.; Karyakin, A. A. *Electroanalysis* **2009,** *21,* 409–414. doi:10.1002/elan.200804408
27. Koncki, R.; Wolfbeis, O. S. *Anal. Chem.* **1998,** *70,* 2544–2550. doi:10.1021/ac9712714
28. Wiedemair, J.; Menegazzo, N.; Pikarsky, J.; Booksh, K. S.; Mizaikoff, B.; Kranz, C. *Electrochim. Acta* **2010,** *55,* 5725–5732. doi:10.1016/j.electacta.2010.05.008
29. Karyakin, A. A.; Kuritsyna, E. A.; Karyakina, E. E.; Sukhanov, V. L. *Electrochim. Acta* **2009,** *54,* 5048–5052. doi:10.1016/j.electacta.2008.11.049
30. Rudolph, D.; Neuhuber, S.; Kranz, C.; Taillefert, M.; Mizaikoff, B. *Analyst* **2004,** *129,* 443–448. doi:10.1039/b400051j

License and Terms

Electrochemical and electron microscopic characterization of Super-P based cathodes for Li–O$_2$ batteries

Mario Marinaro[*1,§], Santhana K. Eswara Moorthy[*2,§], Jörg Bernhard[2], Ludwig Jörissen[1], Margret Wohlfahrt-Mehrens[1] and Ute Kaiser[2]

Full Research Paper

Address:
[1]Zentrum für Sonnenenergie- und Wasserstoff-Forschung Baden-Württemberg, 89081 Ulm, Germany and [2]Electron Microscopy Group of Materials Science, University of Ulm, Albert-Einstein-Allee 11, 89081 Ulm, Germany

Email:
Mario Marinaro[*] - mario.marinaro@zsw-bw.de;
Santhana K. Eswara Moorthy[*] - santhana.eswara@uni-ulm.de

* Corresponding author
§ These authors contributed equally to this work.

Abstract

Aprotic rechargeable Li–O$_2$ batteries are currently receiving considerable interest because they can possibly offer significantly higher energy densities than conventional Li-ion batteries. The electrochemical behavior of Li–O$_2$ batteries containing bis(trifluoromethane)sulfonimide lithium salt (LiTFSI)/tetraglyme electrolyte were investigated by galvanostatic cycling and electrochemical impedance spectroscopy measurements. Ex-situ X-ray diffraction and scanning electron microscopy were used to evaluate the formation/dissolution of Li$_2$O$_2$ particles at the cathode side during the operation of Li–O$_2$ cells.
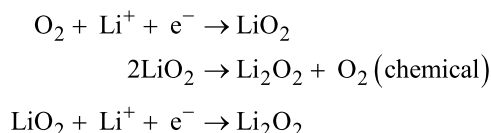
Introduction

The development of new types of electrochemical power sources is nowadays considered a key factor for further development of hybrid and fully electric vehicles. Indeed one of the major concerns for the practical use of fully electric vehicles is the limited mileage of such vehicles. Aprotic rechargeable Li–O$_2$ batteries may overcome this limitation since they can provide a much higher energy density than common Li-ion batteries. However, research about this new battery technology is still at an early stage. There are indeed still many open questions that need to be answered before proceeding for further development.

One of the main challenges is represented by the choice of a suitable electrolyte, which allows for the formation of the

desired products during the operation of a typical Li–O$_2$ battery. In this context, recently published literature [1-3] gives new insights about the mechanism through which the reduction and the oxidation of oxygen occur in aprotic environments. During discharge, the oxygen reduction reaction (ORR) proceeds in a stepwise fashion leading to the formation of LiO$_2$ and Li$_2$O$_2$ as shown in the chemical reactions below. Conversely, upon charging, the oxygen evolution reaction (OER) gives O$_2$ and Li$^+$ back via a 2-electrons reaction.

$$O_2 + Li^+ + e^- \rightarrow LiO_2$$
$$2LiO_2 \rightarrow Li_2O_2 + O_2 \,(\text{chemical})$$
$$LiO_2 + Li^+ + e^- \rightarrow Li_2O_2$$

The unsuitability of commonly used electrolytes for Li-ion batteries (e.g., electrolytes based on carbonates) in Li–O$_2$ cells has been demonstrated by several research groups [4-8]. Indeed, the main discharge product when using carbonates-based electrolytes is represented by the byproduct Li$_2$CO$_3$ rather than the desired Li$_2$O$_2$. On the other hand, ether-based electrolytes seem able to give the desired discharge products, even if their long-term stability is still questionable [9-15].

In view of this, we present an investigation of the lithium-oxide phases that are generated during the operation of Li–O$_2$ batteries, which use LiTFSI/tetraglyme as the electrolyte. The electrochemical behaviors of the batteries were investigated by galvanostatic cycling and electrochemical impedance spectroscopy. The physico–chemical investigation of the lithium-oxide phases that form and dissolve at the cathode side upon discharge and charge of Li–O$_2$ batteries has been carried out by using X-ray diffraction and SEM measurements.

Experimental
Electrolyte preparation
Tetraethylene glycol dimethyl ether (tetraglyme) purchased from Aldrich was dried over molecular sieves and under vacuum (at 80 °C) before being stored in an Ar-filled glovebox (MBrown), in which the levels of O$_2$ and H$_2$O were kept constantly below 0.1 ppm. Bis(trifluoromethane)sulfonimide lithium salt (LiTFSI) was also purchased from Aldrich and vaccum-dried before being used. The 1 M LiTFSI/tetraglyme electrolyte was prepared and stored in a glovebox.

Electrodes manufacturing
Carbon cathodes for Li–O$_2$ cells were prepared by airbrushing a suspension of Super-P (Timcal) and polyvinylidene fluoride (PvdF) in *N*-methyl-2-pyrrolidone (mass ratio Super-P/PvdF 8:2) on a gas diffusion layer (Toray paper). The obtained electrodes of 12 mm in diameter were first dried at 100 °C in order

to allow the evaporation of the solvent and then further dried at 130 °C under vacuum, thus minimizing the moisture content. The average loading for all the electrodes was about 1 mg·cm^{-2} based on the carbon content.

Electrochemical measurements
Electrochemical measurements were carried out using commercially available 3-electrode ECC–air cells (EL-cell GmbH, Germany) equipped with inlet and outlet for O$_2$ purging. Lithium disks acted as the counter and the reference electrode, 1 M LiTFSI/tetraglyme and Whatman glass fiber were the electrolyte and the separator, respectively, and the Super-P based electrode was set as the working electrode. The cells were assembled in an Ar-filled glovebox (MBraun) and sealed. The batteries were then taken outside the glovebox and pure O$_2$ was purged for 60 min before starting the electrochemical measurements. Galvanostatic cycles of the Li–O$_2$ cells have been collected at a current of 50 mA·(g carbon)$^{-1}$. Electrochemical impedance spectroscopy (EIS) measurements have been carried out in the frequency range between 200 kHz and 5 mHz superimposing a sinusoidal potential oscillation of ±2.5 mV. Electrochemical measurements have been carried out using a vmp 2/z (Bio-Logic, France). All potentials reported hereafter are given versus the Li$^+$/Li semi-couple.

X-ray measurements
X-ray diffraction patterns have been collected on a Siemens D5000 diffractometer equipped with a Cu Kα source and θ/2θ Bragg–Brentano geometry. For ex-situ measurements, cells were disassembled in an Ar-filled glovebox. Electrodes were first washed with tetraglyme and then vacuum dried. Finally the carbon cathodes were placed in an air-tight sample holder prior to run the measurements.

Scanning electron microscopy
A Zeiss dual-beam NVISION 40 was used for scanning electron microscopy. The operating voltage for imaging was 5 kV. The images were acquired using a secondary-electron detector with an in-lens configuration.

Results and Discussion
The first galvanostatic discharge/charge curve of a typical Li–O$_2$ battery that has a carbon-based cathode, a lithium metal anode and LiTFSI/tetraglyme electrolyte is reported in Figure 1. The cell was cycled following a time-limited constant-current protocol. A current of 50 mA·(g carbon)$^{-1}$ was applied for 10 h leading to a final specific capacity of 500 mAh·(g carbon)$^{-1}$. At the expense of some energy density, the use of such protocol ensures good cyclability (more than 30 charge–discharge cycles) of the Li–O$_2$ cells [10,15]. The shape of the galvanostatic curve is characterized by a flat discharge plateau at ≈2.7 V,

whereas upon charging the potential of the cell rapidly increases to 3.2 V, then proceeding up to 3.9 V in a sloped manner and finally approaching the end of the charge at ≈4.3 V.
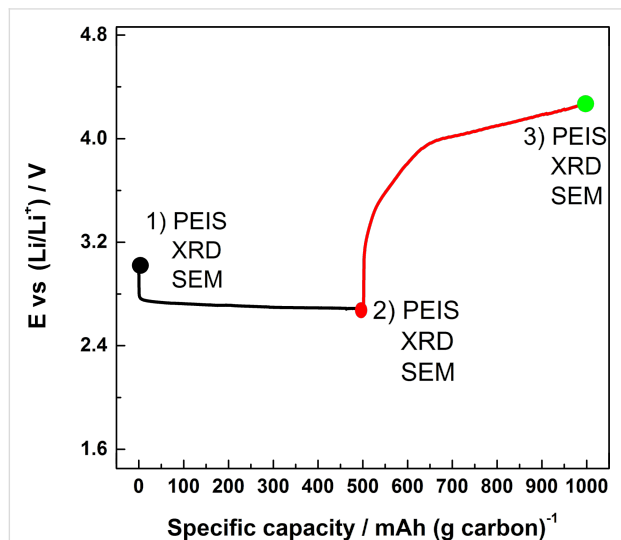

Figure 1: First galvanostatic discharge/charge curve of a typical Li–O_2 battery consisting of a carbon-based cathode, lithium metal anode and LiTFSI/tetraglyme as electrolyte.

In order to investigate the cathode/electrolyte interface, we examined the evolution of the cell impedance during the first cycle. Electrochemical impedance spectra have therefore been collected from fresh, once discharged and re-charged electrodes, as shown in Figure 2. The EIS results can be used to evaluate the formation of an insulating phase at the electrode. The 3-electrode configuration of the used cell allowed for isolating the only contribution of the cathode to the total impedance of the cell. The Nyquist dispersion of the fresh cathode reported in Figure 2 (black squares) displays a depressed semicircle from high to middle frequencies, which can be ascribed to the charge transfer resistance [16]. The impedance spectrum acquired at the end of the discharge (Figure 2, red circles) clearly shows an increased amplitude of the semicircle associated with an increased charge-transfer resistance. The observed behavior can be explained on the basis of a growing insulating phase at the cathode side and more specifically directly related to the formation of Li_2O_2 upon discharge, as demonstrated by the XRD results that will be discussed later on. After charging (Figure 2, green triangles) the impedance associated with the charge transfer decreases, which suggests that the formation/dissolution of Li_2O_2 is reversible in the system. The reasons for the different values of the charge-transfer resistances of the fresh and of the charged electrodes are still unclear. Although the XRD results (see Figure 3) do not show evidences of Li_2CO_3, we cannot exclude that traces of this compound, either in an amorphous state and/or below the detection

limit of the X-ray diffraction technique, forms during discharge as a consequence of the instability of the carbon-based electrode [17,18] or of the electrolyte [15] during cycling. The formation of the insulating Li_2CO_3 within the cathode structure would explain the different charge-transfer values found for the fresh and re-charged electrodes, respectively.
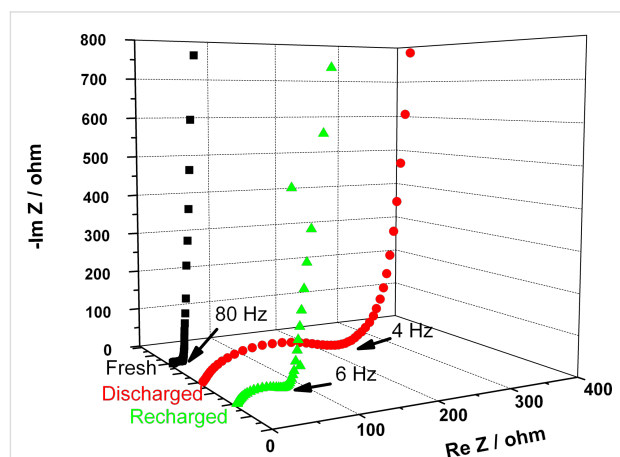

Figure 2: Electrochemical impedance spectra of pristine (black), once discharged (red) and re-charged (green) electrodes.

By means of X-ray diffraction we confirmed the reversible formation and dissolution of Li_2O_2. The comparison of the diffraction patterns of pristine, discharged and recharged electrodes is reported in Figure 3. The two X-ray patterns of the fresh and of the charged electrodes show the same peaks. In contrast, the
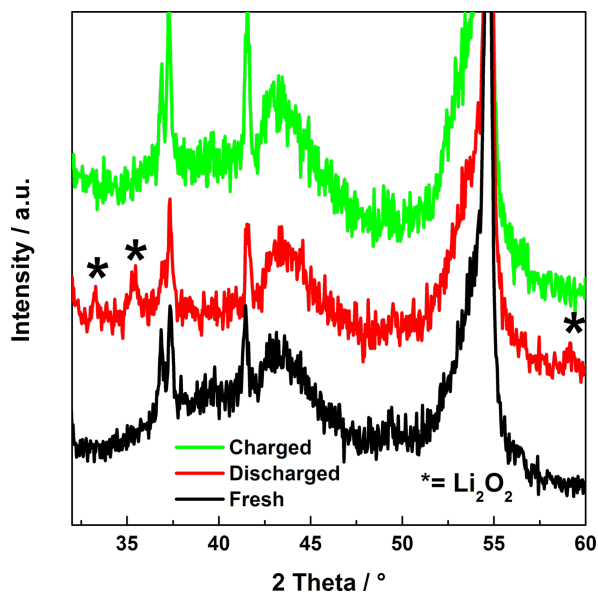

Figure 3: X-ray diffractograms of pristine, discharged and charged carbon cathodes. Note the additional peaks of Li_2O_2 (marked by asterisk) for the discharged state of the cathode.

diffractogram of the electrode in the discharged state shows three additional peaks, marked with asterisks, which belong to the crystal structure of Li_2O_2. Apart from the Li_2O_2 phase we could not identify any other peaks (such as those of Li_2O, Li_2CO_3 or LiF).

The SEM images of the electrode at pristine, discharged up to 500 mAh·(g carbon)$^{-1}$ and recharged states are shown in Figure 4. Discharging the battery forms lithium peroxide on the cathode as seen in Figure 4B. It can be noticed that the Li_2O_2 particles appear to have a hollow structure with a smooth surface and nodular morphology. The dimensions of the particles are typically in the range of 200 to 350 nm. From Figure 4C it is obvious that upon recharging the battery the

Li_2O_2 particles disappear in accordance with the expectation. Our SEM results are consistent with the XRD results shown in Figure 3, which show Li_2O_2 peaks in discharged case but not in the recharged case. These results are also consistent with the results from electrochemical impedance spectroscopy.

In order to comprehend the electrochemical and microstructural changes that occur when the depth of discharge of a Li–O_2 battery is further increased, Li–O_2 cells were cycled under a fixed capacity regime of 1000 mAh·(g carbon)$^{-1}$. The galvanostatic curve referred to the first cycle is shown in Figure 5. It can be seen that the general shape of this curve is similar to that of Figure 1 even though in the latter case the capacity was limited to 500 mAh·(g carbon)$^{-1}$.
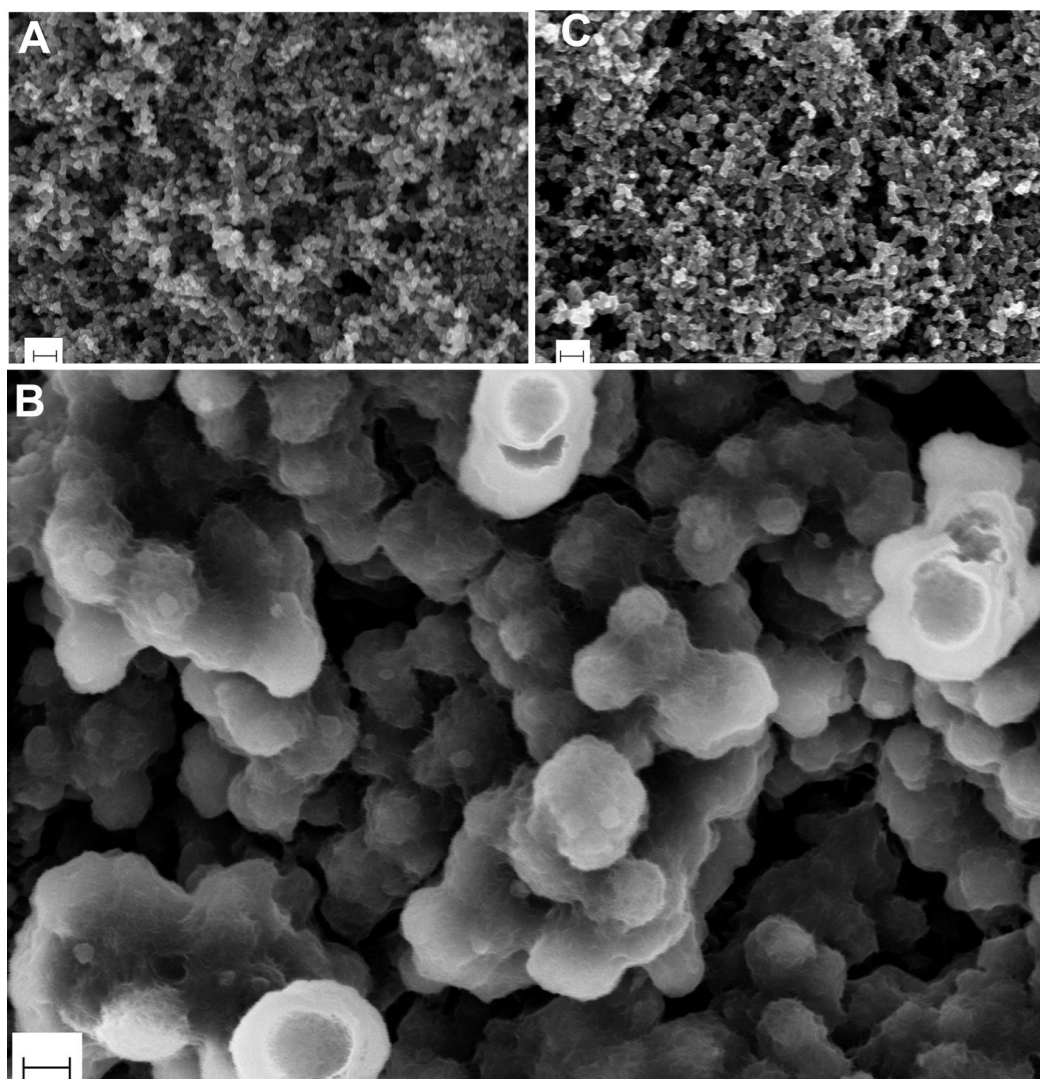

Figure 4: SEM micrographs of (A) pristine electrode, (B) discharged electrode for which the capacity was limited at 500 mAh·(g carbon)$^{-1}$ and (C) recharged electrode of Li–O_2 batteries. Note that the large Li_2O_2 particles in (B) appear to have a hollow structure with a smooth surface and nodular morphology. The scale bars correspond to 200 nm.
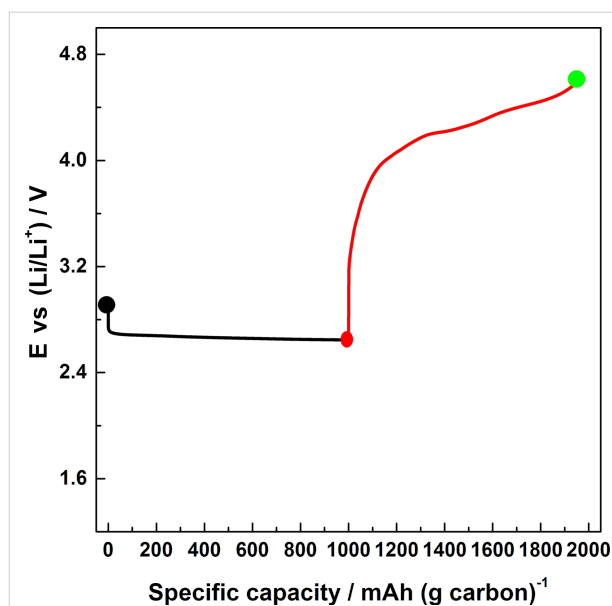
Figure 5: First galvanostatic curve of a Li–O$_2$ battery discharged up to 1000 mAh·(g carbon)$^{-1}$.

The corresponding SEM images of the discharged and recharged electrodes are shown in Figure 6. The formation and dissolution of lithium peroxide crystals upon discharging and recharging are evident from these images. By comparing Figure 6A with Figure 4B, the following three features are obvious: (a) the morphology of the particles is rather smooth in both the cases (b) the particles in Figure 6A are filled (not hollow) in contrast to the case of Figure 4B and (c) the size of the Li$_2$O$_2$ particles formed in the case of Figure 6A are in the range of 250–350 nm, which is somewhat larger than in the case of Figure 4B. From point (b) we can infer that the formation mechanism of the Li$_2$O$_2$ must involve a transformation from a

hollow to filled structure with the progression of the discharge. Moreover, the continuous coverage of Li$_2$O$_2$ on carbon seen in Figure 4B is starkly different from the discontinuous coverage shown in Figure 6A. This may be due to thermodynamic and kinetic factors at play during discharge which determines the overall morphology of the reaction products. Although the exact mechanism is unclear, it also explains the aforementioned transformation from hollow to filled structures. Finally, from points (b) and (c) together we can also qualitatively understand the excess mass deposited on the electrode due to a continued discharge up to 1000 mAh·(g carbon)$^{-1}$, as would be expected.

Conclusion

In conclusion, we demonstrated the reversibility of the oxygen electrochemical redox reaction during the operation of a Li–O$_2$ battery. The use of the LiTFSI/tetraglyme electrolyte allows for obtaining the desired discharge product that is identified as Li$_2$O$_2$. The combination of electrochemical techniques and ex-situ analysis, such as XRD and SEM, led us to ascribe the discharge plateau to the electrochemical reduction of O$_2$ which is subsequently re-oxidized upon charge. From the SEM images, it can be seen that with the progression of the discharge reaction, a hollow shell structure of Li$_2$O$_2$ particles forms initially which then transforms to a completely filled solid structure suggesting that the deposition mechanism must be responsible for this transformation.
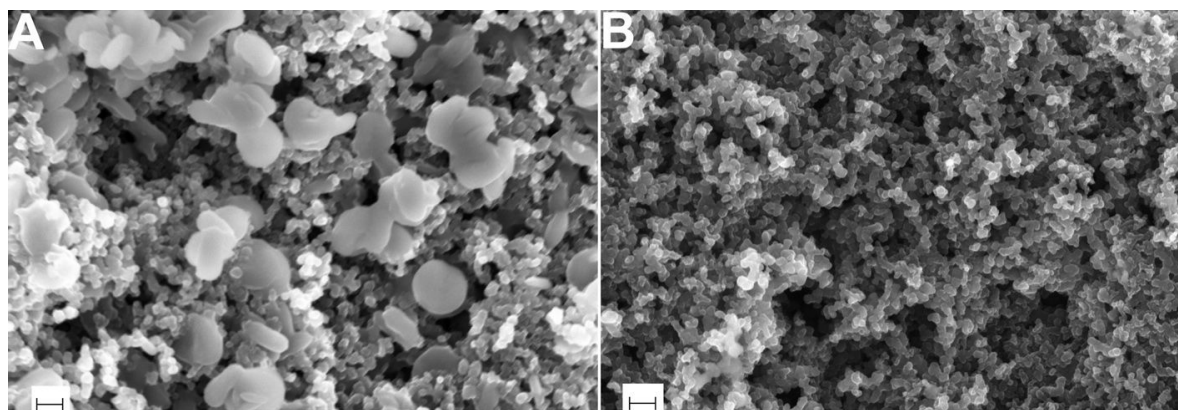
Acknowledgements

Figure 6: Microstructures of (A) discharged and (B) recharged electrodes. The formation of lithium peroxide crystals on the discharged electrode up to 1000 mAh·(g carbon)$^{-1}$ is clearly visible in (A). The scale bars correspond to 200 nm.

References

1. O'Laoire, C.; Mukerjee, S.; Abraham, K. M. *J. Phys. Chem. C* **2010,** *114,* 9178–9186. doi:10.1021/jp102019y
2. Peng, Z.; Freunberger, S. A.; Hardwick, L. J.; Chen, Y.; Giordani, V.; Bardé, F.; Novák, P.; Graham, D.; Tarascon, J.-M.; Bruce, P. G. *Angew. Chem., Int. Ed.* **2011,** *50,* 6351–6355. doi:10.1002/anie.201100879
3. Hassoun, J.; Croce, F.; Armand, M.; Scrosati, B. *Angew. Chem., Int. Ed.* **2011,** *50,* 2999–3002. doi:10.1002/anie.201006264
4. Bryantsev, V. S.; Blanco, M. *J. Phys. Chem. Lett.* **2011,** *2,* 379–383. doi:10.1021/jz1016526
5. Freunberger, S. A.; Chen, Y.; Peng, Z.; Griffin, J. M.; Hardwick, L. J.; Bardé, F.; Novák, P.; Bruce, P. G. *J. Am. Chem. Soc.* **2011,** *133,* 8040–8047. doi:10.1021/ja2021747
6. Xiao, J.; Hu, J.; Wang, D.; Hu, D.; Xu, W.; Graff, G. L.; Nie, Z.; Liu, J.; Zhang, J.-G. *J. Power Sources* **2011,** *196,* 5674–5678. doi:10.1016/j.jpowsour.2011.02.060
7. Xu, W.; Xu, K.; Viswanathan, V. V.; Towne, S. A.; Hardy, J. S.; Xiao, J.; Nie, Z.; Hu, D.; Wang, D.; Zhang, J.-G. *J. Power Sources* **2011,** *196,* 9631–9639. doi:10.1016/j.jpowsour.2011.06.099
8. Xu, W.; Viswanathan, V. V.; Wang, D.; Towne, S. A.; Xiao, J.; Nie, Z.; Hu, D.; Zhang, J.-G. *J. Power Sources* **2011,** *196,* 3894–3899. doi:10.1016/j.jpowsour.2010.12.065
9. Jung, H.-G.; Hassoun, J.; Park, J.-B.; Sun, Y.-K.; Scrosati, B. *Nat. Chem.* **2012,** *4,* 579–585. doi:10.1038/nchem.1376
10. Lim, H.-D.; Park, K.-Y.; Gwon, H.; Hong, J.; Kim, H.; Kang, K. *Chem. Commun.* **2012,** *48,* 8374–8376. doi:10.1039/c2cc32788k
11. Freunberger, S. A.; Chen, Y.; Drewett, N. E.; Hardwick, L. J.; Bardé, F.; Bruce, P. G. *Angew. Chem., Int. Ed.* **2011,** *50,* 8609–8613. doi:10.1002/anie.201102357
12. Ryan, K. R.; Trahey, L.; Ingram, B. J.; Burrell, A. K. *J. Phys. Chem. C* **2012,** *116,* 19724–19728. doi:10.1021/jp306797s
13. Peng, Z.; Freunberger, S. A.; Chen, Z.; Bruce, P. G. *Science* **2012,** *337,* 563–566. doi:10.1126/science.1223985
14. Meini, S.; Piana, M.; Beyer, H.; Schwämmlein, J.; Gasteiger, H. A. *J. Electrochem. Soc.* **2012,** *159,* A2135–A2142. doi:10.1149/2.011301jes
15. Marinaro, M.; Theil, S.; Jörissen, L.; Wohlfahrt-Mehrens, M. *Electrochim. Acta* **2013,** *108,* 795–800. doi:10.1016/j.electacta.2013.06.147
16. Cecchetto, L.; Salomon, M.; Scrosati, B.; Croce, F. *J. Power Sources* **2012,** *213,* 233–238. doi:10.1016/j.jpowsour.2012.04.038
17. Gallant, B. M.; Mitchell, R. R.; Kwabi, D. G.; Zhou, J.; Zuin, L.; Thompson, C. V.; Shao-Horn, Y. *J. Phys. Chem. C* **2012,** *116,* 20800–20805. doi:10.1021/jp308093b
18. McCloskey, B. D.; Speidel, A.; Scheffler, R.; Miller, D. C.; Viswanathan, V.; Hummelshøj, J. S.; Nørskov, J. K.; Luntz, A. C. *J. Phys. Chem. Lett.* **2012,** *3,* 997–1001. doi:10.1021/jz300243r

License and Terms

Optimization of solution-processed oligothiophene:fullerene based organic solar cells by using solvent additives

Gisela L. Schulz[*1], Marta Urdanpilleta[2], Roland Fitzner[1], Eduard Brier[1], Elena Mena-Osteritz[1], Egon Reinold[1] and Peter Bäuerle[*1,§]

Full Research Paper

Address:
[1]Institute of Organic Chemistry II and Advanced Materials, University of Ulm, Albert-Einstein-Allee 11, D-89081 Ulm, Germany and
[2]Department of Applied Physics, University of the Basque Country (UPV/EHU), Plaza de Europa, 1, 20018 Donostia - San Sebastián, Spain

Email:
Gisela L. Schulz[*] - gisela.schulz@uni-ulm.de;
Peter Bäuerle[*] - peter.baeuerle@uni-ulm.de

* Corresponding author
§ Fax: (+49) 731-50-22840

Abstract

The optimization of solution-processed organic bulk-heterojunction solar cells with the acceptor-substituted quinquethiophene **DCV5T-Bu$_4$** as donor in conjunction with PC$_{61}$BM as acceptor is described. Power conversion efficiencies up to 3.0% and external quantum efficiencies up to 40% were obtained through the use of 1-chloronaphthalene as solvent additive in the fabrication of the photovoltaic devices. Furthermore, atomic force microscopy investigations of the photoactive layer gave insight into the distribution of donor and acceptor within the blend. The unique combination of solubility and thermal stability of **DCV5T-Bu$_4$** also allows for fabrication of organic solar cells by vacuum deposition. Thus, we were able to perform a rare comparison of the device characteristics of the solution-processed **DCV5T-Bu$_4$**:PC$_{61}$BM solar cell with its vacuum-processed **DCV5T-Bu$_4$**:C$_{60}$ counterpart. Interestingly in this case, the efficiencies of the small-molecule organic solar cells prepared by using solution techniques are approaching those fabricated by using vacuum technology. This result is significant as vacuum-processed devices typically display much better performances in photovoltaic cells.

Introduction

The demand for the development of new materials for applications in organic bulk-heterojunction solar cells (BHJSCs) has been growing over the last decade [1-3]. In response, the field has been expanding rapidly with the number of new compounds being produced at an increasingly faster rate [3-5]. The photoactive layer in BHJSCs is fabricated by simultaneous deposition of both, the electron donor (D) as a p-type and the electron acceptor (A) as n-type semiconducting material. The field can be divided based on the type of donor material; polymer or oligomer/dye molecules. Oligomers or, as they are sometimes referred to, "small" molecules, have the advantage of possessing a defined molecular structure that is monodisperse in nature and allows for purification and characterization, which leads to the derivation of valuable structure–property relationships. Problems with respect to reproducibility of solar cell results due to batch to batch variations of the synthetic organic materials, such as in the case of polymers, are of less significance. On the other hand, the preparation of structurally defined oligomers sometimes requires costly multi-step syntheses.

Diketopyrrolopyrroles [4], oligothiophenes [5], merocyanines [6], phthalocyanines [7], and squarine dyes [8,9] have all been investigated as promising donor materials in efficient BHJSCs. Power conversion efficiencies (PCEs) up to 6.9% have been reported for oligomers based on vacuum-processed [10] and 8.2% for solution-processed single junction devices [11]. Among these prominent classes of compounds, in particular oligothiophenes end-capped with electron-withdrawing cyano groups proved to have excellent performance in BHJSCs. Oligothiophenes of various lengths (from 3 to 7 thiophene units), which contain various alkyl side chains (methyl to octyl) with different substitution patterns, have been incorporated in photoactive layers of BHJSCs. When using vacuum deposition, the highest efficiency for single-junction solar cells to date has been reported to be 6.9% for dicyanovinyl (DCV)-capped quinquethiophene with methyl substituents on the central thiophene unit blended with C_{60} in a ratio of 2:1 [10]. In the case of solution-processed BHJSCs, a septithiophene derivative incorporating regioregular octyl chains, capped with DCV groups, and blended with [6,6]-phenyl-C_{61}-butyric acid methyl ester (PC$_{61}$BM), displayed a PCE of 3.7% when spin-coated from a chloroform solution [12]. This efficiency was further increased to 5.1% upon replacement of the terminal DCV acceptors units with octyl cyanoacetate termini [13]. A further improvement to 6.1% was obtained by the use of an alkylated septithiophene that bears terminal rhodanine acceptor groups [13]. Through combination of the rhodanine acceptor with a benzodithiophene core unit, an additional increase in PCE to 8.1% was achieved [14,15]. Simultaneously, a series of dithienosiloles flanked with

two thiadiazolopyridine units were reported with efficiencies of up to 8.2% in combination with [6,6]-phenyl-C_{71}-butyric acid methyl ester (PC$_{71}$BM) [11,16,17].

We now report on the application of a DCV-capped quinquethiophene derivative, which contains four butyl chains along the oligomer backbone (**DCV5T-Bu$_4$**), as the p-type semiconducting material in solution-processed BHJSCs. Due to its thermal stability as well as its solubility, this material has the unique advantage of being processable in both vacuum and solution. This allows for a direct comparison of the two deposition techniques and the resulting solar cell performances. There have been several reports describing the photovoltaic characteristics of vacuum-deposited **DCV5T-Bu$_4$** [18-20], which in combination with C_{60} gave an efficiency of 3.4% in planar heterojunctions [18] and 3.5% in bulk heterojunctions [21]. Herein, the synthesis and characterization of the **DCV5T-Bu$_4$** is described, as well as the photovoltaic performance of solution-processed BHJSCs. To date, there have been many reports of polymer-based solar cells, which have demonstrated significant increases in efficiencies with the use of solvent additives [22-28], however, there are only a handful of examples in which oligomer-based donors were used [15-17,29]. This work further investigates the effect of a solvent additive on active layer film formation and relates the findings to the solar cell performance [30].

Experimental

Materials and methods: Tetrahydrofuran (THF, Merck) was dried under reflux over sodium/benzophenone (Merck) and distilled. Dimethylformamide (DMF, Merck) was first refluxed over P_4O_{10} and distilled, then refluxed over BaO and distilled again. 1-Chloronaphthalene (CN, Aldrich) was distilled prior to use. All synthetic steps were carried out under argon atmosphere. Malononitrile and β-alanine were purchased from Merck and 2-isopropoxy-4,4,5,5-tetramethyl[1,3,2]dioxaborolane and thiophene were purchased from Aldrich. Diiodoterthiophene **1** [31], bisstannylterthiophene **5** [21], and 2-[(5-bromothien-2-yl)methylene]malononitrile (**6**) [32] were synthesized according to known literature procedures. NMR spectra were recorded on a Bruker AMX 500 (^{1}H NMR: 500 MHz; ^{13}C NMR: 125 MHz) or a Bruker Avance 400 (^{1}H NMR: 400 MHz; ^{13}C NMR: 100 MHz) at 298 K. Chemical shift values (δ) are given in ppm and were calibrated on residual non-deuterated solvent peaks (CDCl$_3$: ^{1}H NMR: 7.26 ppm, ^{13}C NMR: 77.0 ppm; $C_2D_2Cl_4$: ^{1}H NMR: 6.00 ppm, ^{13}C NMR: 74.0 ppm; CD$_2$Cl$_2$: ^{1}H NMR: 5.32 ppm, ^{13}C NMR: 53.5 ppm; THF-d_8: ^{1}H NMR: 3.58 ppm, ^{13}C NMR: 67.7 ppm) as internal standard. EI and CI mass spectroscopy was performed on a Finnigan MAT SSQ-7000 or a Varian Saturn 2000 GCMS. MALDI-TOF spectra were

recorded on a Bruker Daltonics Reflex III using dithranol or DCTB (trans-2[3-4-*tert*-butylphenyl]-2-methyl-2-propenylidene)-malononitrile) as matrices. UV–vis absorption spectroscopy was carried out on a Perkin Elmer Lambda 19 using Merck Uvasol grade solvents. The maximum solubility of **DCV5T-Bu₄** was measured by using UV–vis absorption spectroscopy. After determination of the molar extinction coefficient, saturated solutions were made, stirred for 60 min at 60 °C then allowed to cool to room temperature. The saturated solution was then filtered and diluted for absorption spectroscopy, and the corresponding concentration could be determined. Cyclic voltammetry experiments were performed with a computer-controlled Autolab PGSTAT30 potentiostat and a three-electrode single-compartment cell with a platinum working electrode, a platinum wire counter electrode and an Ag/AgCl reference electrode. All potentials were internally referenced to the ferrocene/ferrocenyl couple (−5.1 eV). Melting points were determined using a Mettler Toledo DSC 823e and were not corrected. Elemental analyses were performed on an Elementar Vario EL. Plastic-sheets precoated with silica gel, Merck Si60 F254, were used for thin layer chromatography. Glass columns packed with Merck Silica 60, mesh 0.063–0.2 μm, were used for column chromatography. High performance liquid chromatography was performed on a Hitachi instrument equipped with a UV–vis detector L-7420, columns (Nucleosil 100-5 NO₂ with a pore size of 100 Å) from Machery-Nagel using a dichlormethane/*n*-hexane mixture (40:60) as eluent. Surface images were recorded with the help of a Bruker Nanoscope V AFM at ambient temperature in tapping mode.

Synthesis: 3',3''',4',4'''-Tetrabutyl-2,2':5',2'':5'',2''':5''',2''''-quinquethiophene (**3**): Diiodoterthiophene **1** (2.77 g, 3.80 mmol) and 2-(thien-2-yl)-4,4,5,5-tetramethyl-[1,3,2]-dioxaborolane **2** (1.76 g, 8.36 mmol) were combined with a 2 M aqueous solution of potassium phosphate (12.5 mL, 25 mmol) in dimethoxyethane (60 mL). Tris(dibenzylideneaceton)dipalladium (41 mg, 0.04 mmol) and tri-*tert*-butylphosphine (16 mg, 0.08 mmol) were added to the reaction mixture under argon and it was refluxed for 24 h. After evaporation of the solvent, the crude product was purified by column chromatography on silica gel with petrol ether as eluent to yield pentamer **3** (1.70 g, 2.67 mmol, 70%) as an orange solid. Mp 72–73 °C; ^{1}H NMR (CDCl₃) δ 7.31–7.30 (m, 2H, ThH), 7.15–7.14 (m, 2H, ThH), 7.08–7.05 (m, 4H, ThH), 2.77–2.69 (m, 8H), 1.58–1.42 (m, 16H), 0.98-0.93 (m, 12H); ^{13}C NMR (CDCl₃) 140.19, 136.19, 135.94, 129.77, 127.39, 125.96, 125.90, 125.34, 32.97, 32.95, 28.01, 27.83, 23.09, 23.03, 13.93, 13.89. EIMS *m/z*: M⁺ 636.8 (calcd for C₃₆H₄₄S₅: 636); Anal. calcd for C₃₆H₄₄S₅: C, 67.87; H, 6.96; S, 25.17; found: C, 67.95; H, 6.36; S, 25.01.

3',3''',4',4'''-Tetrabutyl-2,2':5',2'':5'',2''':5''',2''''-quinquethiophene-5,5''''-dicarbaldehyde (**4**): To a solution of quinquethiophene **3** (1.50 g, 2.4 mmol) in dichloromethane (18 mL), a mixture of phosphoryl chloride in DMF (26 mL, 22.4 mmol) was added. The reaction was refluxed for 16 h and subsequently stirred for 2 h at room temperature. A saturated aqueous solution of sodium bicarbonate (200 mL) was added and the organic phase was extracted and dried over sodium sulphate. The crude material was purified by column chromatography on silica gel with dichloromethane as eluent to give dicarbaldehyde **4** (1.30 g, 1.88 mmol, 80%) as a dark red solid. Mp 89–90 °C; ^{1}H NMR (CDCl₃) 9.91 (s, 2H, CHO), 7.73 (d, *J* = 4.0 Hz, 2H, ThH), 7.28 (d, *J* = 4.0 Hz, 2H, ThH), 7.16 (s, 2H, ThH), 2.83–2.76 (m, 8H), 1.60–1.50 (m, 16H), 1.02–0.98 (m, 12H); ^{13}C NMR (CDCl₃) 182.53, 146.27, 142.62, 142.26, 140.84, 136.74, 135.94, 131.86, 129.01, 126.62, 126.15, 32.84, 32.56, 28.11, 27.92, 23.01, 13.84; MALDI-TOF *m/z*: M⁺ 692.3 (calcd for C₃₈H₄₄O₂S₅: 692). Anal. calcd for C₃₈H₄₄O₂S₅: C, 65.85; H, 6.40; S, 23.19; found: C, 65.95; H, 6.63; S, 22.93.

2,2'-((3',3''',4',4'''-Tetrabutyl-2,2':5',2'':5'',2''':5''',2''''-quinquethiophene-5,5''''-diyl)bis(methanylylidene))dimalononitrile (**DCV5T-Bu₄**) by method (A): A suspension of dialdehyde **4** (0.80 g, 1.15 mmol), malononitrile (0.23 g, 3.45 mmol), and β-alanine (11 mg, 0.12 mmol) in THF/EtOH (1:3 mixture, 60 mL) was stirred for 20 h under reflux. The solvent was completely removed in vacuo and the resulting black solid was purified by column chromatography on silica gel with dichloromethane as eluent to yield **DCV5T-Bu₄** (0.83 g, 1.05 mmol, 91%) as a dark violet to black solid.

2,2'-((3',3''',4',4'''-Tetrabutyl-2,2':5',2'':5'',2''':5''',2''''-quinquethiophene-5,5''''-diyl)bis(methanylylidene))dimalononitrile **DCV5T-Bu₄** by method (B): A mixture of bisstannylterthiophene **5** (3.91 g, 4.90 mmol), 2-[(5-bromothien-2-yl)methylene]malononitrile **6** (2.46 g, 10.29 mmol) and tetrakis(triphenylphosphine)palladium(0) (283 mg, 0.245 mmol) was mixed in DMF (120 mL) and heated under argon at 80 °C for 72 h. After cooling, the resulting precipitate was filtered off and washed repeatedly with methanol and *n*-hexane. The DMF filtrate was then concentrated and stored at 7 °C and the resulting precipitate was filtered off and washed with methanol and *n*-hexane and combined with the previously isolated solid. Purification via column chromatography on silica gel was done using dichloromethane. After drying under vacuum **DCV5T-Bu₄** (1.7g, 2.15 mmol, 46%) was obtained as a dark violet to black solid. The purity of quinquethiophene **DCV5T-Bu₄** was confirmed by analytical high performance liquid chromatography (see Supporting Information File 1). Mp 204 °C (onset DSC). ^{1}H NMR, ^{13}C NMR, MALDI-TOF, and elemental analysis were all consistent with the previously reported values [20].

Device fabrication: Photovoltaic devices were made following a previously reported procedure [33], with a few exceptions. The active areas of the cells were 0.2 cm². The spectral response was measured under monochromatic light from a 300 W Xenon lamp in combination with a monochromator (Oriel, Cornerstone 260), modulated with a mechanical chopper. The response was recorded as the voltage over a 220 Ω resistor, using a lock-in amplifier (Merlin 70104). A calibrated Si cell was used as reference.

Results and Discussion

Two different synthetic strategies were employed to synthesize the DCV-capped quinquethiophene **DCV5T-Bu₄** (Scheme 1). In the first approach (A) we started with the preparation of quinquethiophene **3** by Pd(0)-catalyzed Suzuki-type cross-coupling reaction of butyl-substituted diiodoterthiophene **1** and boronic ester **2** in 70% yield. For the sequential introduction of the terminal DCV acceptor groups, pentamer **3** was formylated in both α-positions under Vilsmeier–Haack conditions to yield dialdehyde **4**, which was subsequently converted into the target compound by a Knoevenagel condensation with malononitrile using β-alanine as catalyst. We recently developed the more versatile synthetic route (B), in which the already DCV-functionalized terminal thiophene **6** was coupled with bis-stannylated butyl-substituted terthiophene **5** in a two-fold Pd(0)-

catalyzed Stille-type coupling reaction to obtain **DCV5T-Bu₄** on the gram scale in 46% yield. After purification by column chromatography, the high purity and thermal stability of oligomer **DCV5T-Bu₄** were confirmed by analytical high performance liquid chromatography (HPLC) and differential scanning calorimetry (DSC), respectively (see Supporting Information File 1).

The optical properties of **DCV5T-Bu₄** were investigated by using UV–vis absorption spectroscopy and are displayed in Figure 1a and summarized in Table 1. In dilute chloroform solutions, absorption was observed between 400 and 600 nm, which is assigned to a π–π* transition. The maximum absorption was located at 515 nm, with a molar extinction coefficient of 62 300 L mol⁻¹ cm⁻¹ [20]. In comparison to the measurements performed in solution, thin films of neat **DCV5T-Bu₄** showed a broader absorption profile that was shifted to the red with maxima at 590 and 630 nm. The onset of absorption was shifted for 87 nm, which reduces the band gap to 1.77 eV. The second maximum appearing at lower energy is attributed to the well-ordered packing of the **DCV5T-Bu₄** molecules in the solid state.

The electrochemical properties of **DCV5T-Bu₄** were probed by using cyclic voltammetry, the results of which are plotted in

Scheme 1: Alternative synthetic routes used to yield **DCV5T-Bu₄**.
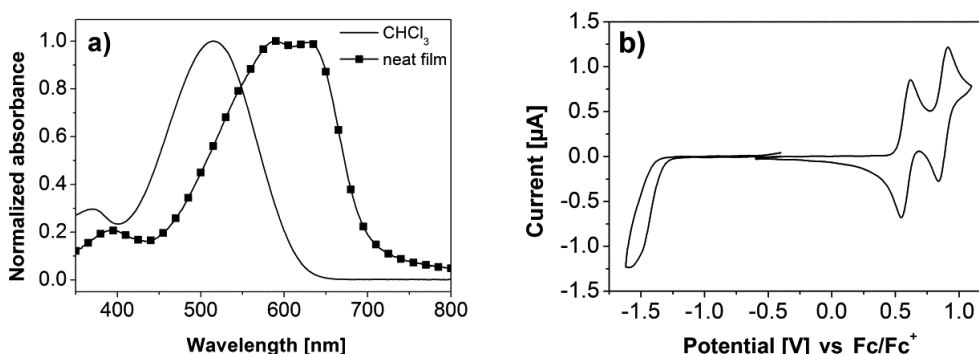
Figure 1: (a) Absorption spectrum of **DCV5T-Bu₄** measured in chloroform and as thin film, spin-coated from chlorobenzene at 80˚C. (b) Cyclic voltammogram of **DCV5T-Bu₄** in dichloromethane, TBAPF₆ (0.1 M) measured versus the ferrocene/ferrocenyl (Fc/Fc⁺) redox couple.

Table 1: Optical, electrochemical, and maximum solubility data for **DCV5T-Bu₄**, fullerene PC₆₁BM, and PC₇₁BM. Absorption spectra measured in CHCl₃, thin films spin-coated from chlorobenzene at 80 °C and electrochemical measurements in CH₂Cl₂/TBAPF₆ solutions (HOMO/LUMO vs Fc/Fc⁺$_{vac}$ = −5.1 eV).

compound	λ_{abs} (nm) solution	ε (L mol^{-1} cm^{-1}) solution	ΔE^{opt} (eV) solution	λ_{abs} (nm) film	ΔE^{opt} (eV) film	E^0_{ox1} (V)	E^0_{ox2} (V)
DCV5T-Bu₄	515	62 300	2.03	590,630	1.77	0.58	0.87
PC₆₁BM	329	40 100	3.08	—	—	—	—
PC₇₁BM	470	22 100	—	—	—	—	—

compound	E^0_{red} (V)	HOMO (eV)	LUMO (eV)	ΔE^{CV} (eV)	solubility CB (mg/mL)	solubility CN (mg/mL)	solubility ODCB (mg/mL)
DCV5T-Bu₄	−1.50	−5.6	−3.7	1.87	3	6	3
PC₆₁BM	—	−6.3 [34]	−4.0 [34]	—	31 [29]	31 [29]	—
PC₇₁BM	—	−6.3	−4.1	—	—	—	164

Figure 1b and summarized in Table 1. Measurements were performed in dichloromethane solutions containing tetrabutyl-ammonium hexafluorophosphate (TBAPF₆) and referenced against the internal ferrocene/ferrocenyl (Fc/Fc⁺) redox couple. The first and second reversible oxidation of **DCV5T-Bu₄** was observed at 0.58 and 0.87 V, respectively. Upon reduction of the molecule, an irreversible wave was observed at −1.50 V. The oxidation is attributed to the formation of stable radical cations and dications along the oligothiophene backbone, whereas the reduction corresponds to the more instable radical anions formed on the DCV groups. HOMO and LUMO energy levels were calculated to be −5.6 and −3.7 eV, respectively, from the onset of the first oxidation and reduction wave. The results are displayed in Figure 2 and compared to energy levels of three different electron-accepting fullerene derivatives used in the various experiments.

Solar cell devices were fabricated by spin-coating the **DCV5T-Bu₄**:PCBM blend from hot solutions at 80 °C on ITO|PEDOT:PSS-coated substrates, which were heated to
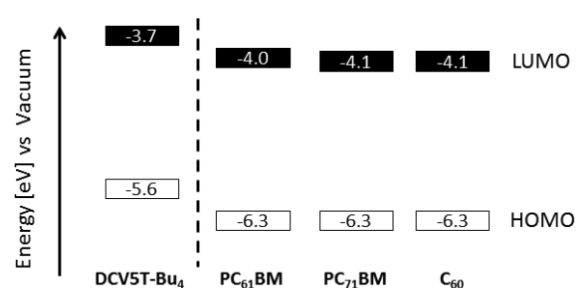

Figure 2: Diagram showing the HOMO and LUMO energy levels of **DCV5T-Bu₄**, PCBM derivatives [34,35], and C₆₀.

90 °C. Subsequently 1 nm LiF was deposited followed by 100 nm Al via thermal evaporation. *J–V* characteristics for blends of **DCV5T-Bu₄**/PC₆₁BM (1:1 wt. ratio) are displayed in Figure 3 and summarized in Table 2. When the active layer was deposited using only chlorobenzene (CB) as the solvent, a short-circuit current density (J_{sc}) of 5.2 mA/cm² , an open circuit potential (V_{oc}) of 1.09 V, a fill factor (FF) of 0.36, and a
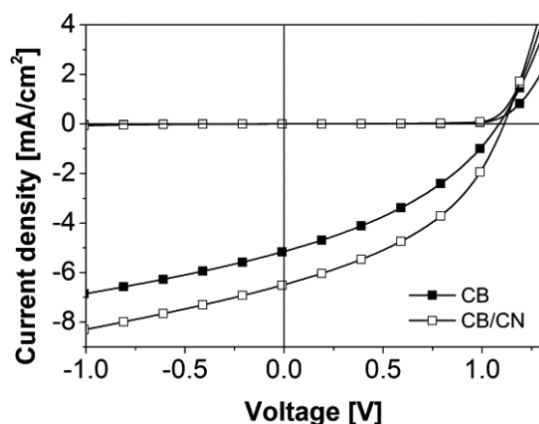
Figure 3: *J–V* curve of **DCV5T-Bu₄**:PC₆₁BM solution-processed solar cells made from 1:1 blends spin-coated from chlorobenzene solutions at 80 ˚C with (white squares) and without (black squares) the 1-chloronaphthalene additive.

saturation value of 1.33 that was calculated by dividing the current density measured at −1 V by J_{sc} at short-circuit conditions (sat. = $J(-1\ V)/J_{sc}(0\ V)$) [21].
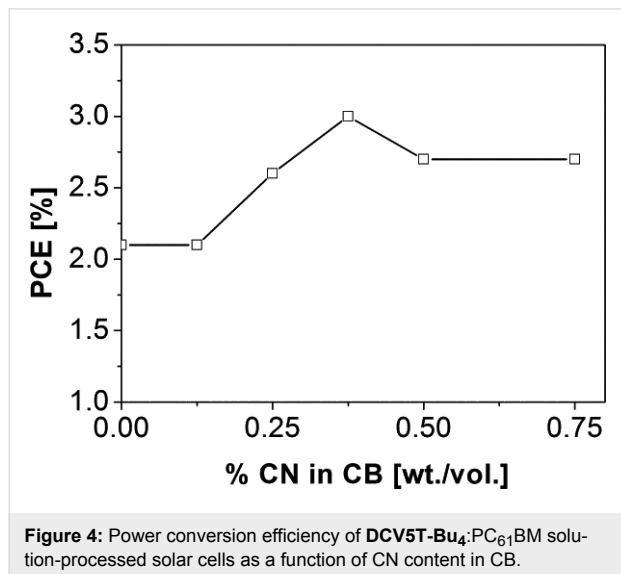
In order to investigate the effect of a solvent additive on the photovoltaic performance, a series of devices was made by varying the amount of 1-chloronaphthalene (CN) in CB from 0.125 to 0.75% wt./vol. All results are shown in Table 2 and the *J–V* curve for the best performing device (0.375% CN in CB) is compared to the device without solvent additive in Figure 3. Upon incorporation of 0.375% CN the J_{sc} is increased to 6.5 mA/cm², the V_{oc} remains similar at 1.11 V, and the FF increased to 0.41 resulting in a significant increase in PCE to 3.0%. The main reason for this improvement is believed to be the increase in charge generation, which is reflected in the higher J_{sc} (6.5 vs 5.2 mA/cm²), and an improved charge transport and collection, as evidenced by the higher fill factor (0.41 vs 0.37) and lower saturation value (1.28 vs 1.33), respectively. The EQE spectra shown in Figure 5b (vide infra) demonstrate that the **DCV5T-Bu₄**:PC₆₁BM devices generate a photocurrent in the range of 400 to 700 nm and display maximum conversion at 580 nm. The EQE at 580 nm was measured to 40% and 36% for solar cells made with and without solvent additives, respectively. Further information regarding the solar cell performance dependence on the donor–acceptor ratio is summarized in Table S2 in Supporting Information File 1.

Figure 4 demonstrates the dependence of the power conversion efficiency on the CN content in CB. From 0 to 0.375% CN, the PCE increased from 2.1% to a maximum value of 3.0%. Upon further increase of CN in CB to 0.50%, the device efficiency decreased to 2.7% and then leveled off. In order to investigate the solvent effect on the active layer formation, the maximum solubilities of **DCV5T-Bu₄** and PC₆₁BM were compared in both CB and CN (Table 1). PC₆₁BM displays an equally high solubility in both CB and CN (31 mg/mL) [29], whereas **DCV5T-Bu₄** is twice as soluble in CN as in CB (6 vs

PCE of 2.1% were determined. As shown in Figure 2, the LUMO level of **DCV5T-Bu₄** (−3.7 eV) was found to be about 0.3 eV higher in energy than that of PC₆₁BM (−4.0 eV), which should be sufficient to enable efficient electron transfer at the donor–acceptor interface in the photoactive blend layer [36,37]. Moreover, the deep HOMO level, which is typically observed for acceptor-substituted oligothiophenes [32], implied that the V_{oc} of the solar cell device should be quite high. Using the following empirical equation [37,38]:

$$V_{oc} \approx e^{-1} \cdot \left\{ E_{HOMO}\left(donor\right) - E_{LUMO}\left(acceptor\right) \right\} - 0.4V\ ,$$

the expected V_{oc} can be calculated to be 1.2 V, which is 0.11 V higher than the measured value (1.09 V). Despite the very high V_{oc}, a moderate PCE of 2.1% was obtained. The device made from CB displayed a relatively low fill factor (0.36), which is indicative of limited charge transport in the active layer. Furthermore, charge collection in the solar cell device may be limited by charge recombination, which is reflected in the high

Table 2: Photovoltaic parameters of solar cells fabricated using **DCV5T-Bu₄**:PCBM from chlorobenzene, chloronaphthalene as additive, and spin-coated at 80 °C. Device structure: ITO|PEDOT:PSS|**DCV5T-Bu₄**:PCBM (1:1)|LiF|Al.

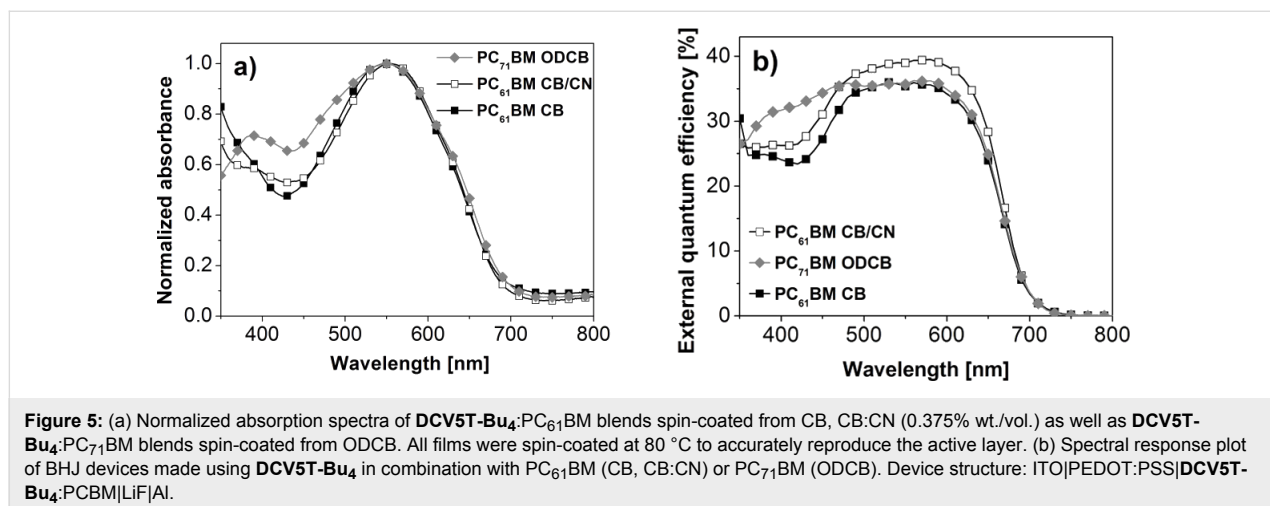| donor:acceptor	solvent	J_{sc} (mA/cm²)	V_{oc} (V)	FF	PCE (%)	$J(-1\ V)/J_{sc}(0\ V)$
DCV5T-Bu₄:PC₆₁BM	CB	5.2	1.09	0.36	2.1	1.33
DCV5T-Bu₄:PC₆₁BM	CB:CN (0.125%)	5.3	1.11	0.36	2.1	1.37
DCV5T-Bu₄:PC₆₁BM	CB:CN (0.25%)	5.9	1.10	0.39	2.6	1.29
DCV5T-Bu₄:PC₆₁BM	CB:CN (0.375%)	**6.5**	**1.11**	**0.41**	**3.0**	**1.28**
DCV5T-Bu₄:PC₆₁BM	CB:CN (0.50%)	5.9	1.10	0.41	2.7	1.28
DCV5T-Bu₄:PC₆₁BM	CB:CN (0.75%)	6.1	1.11	0.40	2.7	1.31
DCV5T-Bu₄:PC₇₁BM	ODCB	5.7	1.08	0.40	2.5	1.34

3 mg/mL). We reason that this difference in solubility influences the active layer film morphology, which will be discussed in greater detail in a later section.

Figure 4: Power conversion efficiency of **DCV5T-Bu₄**:PC₆₁BM solution-processed solar cells as a function of CN content in CB.

Further optimization of the **DCV5T-Bu₄**-based active layer was done by investigating the effect of replacing the PC₆₁BM electron acceptor with PC₇₁BM. As PC₇₁BM has a stronger absorption in the visible region of the solar spectrum than PC₆₁BM, it was expected that the J_{sc} values of the corresponding solar cells that contain PC₇₁BM would increase. The solar cells were fabricated in the exact same manner as those with PC₆₁BM, except the solvent was changed to *o*-dichlorobenzene (ODCB). If one now compares the short-circuit current densities and efficiencies of the **DCV5T-Bu₄**/PC₆₁BM/CB device with the **DCV5T-Bu₄**/PC₇₁BM/ODCB device then an increase is observed (5.2 vs 5.7 mA/cm² and 2.1 vs 2.5%, respectively). However an increase in the overall PCE for the optimized

PC₆₁BM (using a solvent additive) versus the optimized PC₇₁BM active layer was not observed. In fact, the **DCV5T-Bu₄**:PC₇₁BM blends showed lower J_{sc} values (5.7 vs 6.5 mA/cm²), similar V_{oc}, and FFs resulting in a lower PCE of 2.5% compared to the best **DCV5T-Bu₄**:PC₆₁BM device (3.0%). The stronger absorption of **DCV5T-Bu₄**:PC₇₁BM blends in the region from 400 to 500 nm is apparent in the normalized thin film absorption spectra shown in Figure 5a and in the photocurrent generated in the corresponding EQE spectrum (Figure 5b). However unfortunately, further attempts to improve the photovoltaic performance by using solvent additives in combination with PC₇₁BM were unsuccessful (see Table S1 in Supporting Information File 1).

The surface morphology of the D:A blend was investigated using atomic force microscopy (AFM). The samples were prepared in the same way as the photoactive layers for the solar cell devices; by spin-coating the **DCV5T-Bu₄**:PCBM blends from hot solutions at 80 °C on ITO|PEDOT:PSS-coated substrates heated to 90 °C. Figure 6 depicts the phase images of **DCV5T-Bu₄**:PC₆₁BM and **DCV5T-Bu₄**:PC₇₁BM spin-coated from CB, CB with 0.375% CN, or ODCB, respectively. It is possible to assign the lighter regions (higher phase shift) to areas with mostly donor material (**DCV5T-Bu₄**), whereas the darker regions (lower phase shift) contain mostly acceptor material (PCBM) [39]. The image shown in Figure 6a displays a relatively fine phase separation with domain sizes between 10–30 nm and a topography roughness averaged to be 0.4 ± 0.1 nm. Additionally, the film shown in Figure 6b, which was made with CN as solvent additive, displays similar domain sizes (10–30 nm) with a slightly lower topography roughness of 0.3 ± 0.1 nm. The histogram analysis taken over several images of different sizes gives a deeper insight into the corresponding D:A ratio (see Figure S3 in Supporting Information File 1). The surface of the photoactive layer deposited from the CB:CN mix-
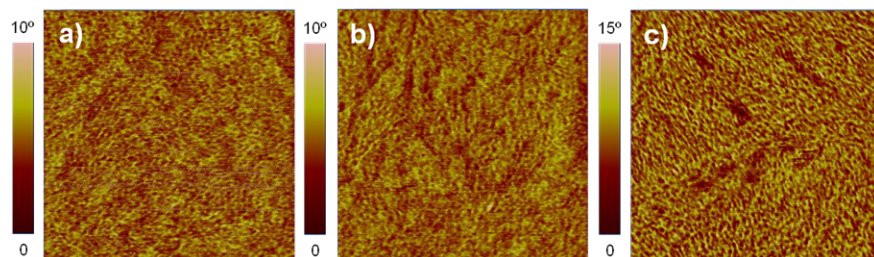

Figure 5: (a) Normalized absorption spectra of **DCV5T-Bu₄**:PC₆₁BM blends spin-coated from CB, CB:CN (0.375% wt./vol.) as well as **DCV5T-Bu₄**:PC₇₁BM blends spin-coated from ODCB. All films were spin-coated at 80 °C to accurately reproduce the active layer. (b) Spectral response plot of BHJ devices made using **DCV5T-Bu₄** in combination with PC₆₁BM (CB, CB:CN) or PC₇₁BM (ODCB). Device structure: ITO|PEDOT:PSS|**DCV5T-Bu₄**:PCBM|LiF|Al.

Figure 6: AFM phase images of samples spin-coated on ITO|PEDOT:PSS| with (a) **DCV5T-Bu$_4$**:PC$_{61}$BM from CB, (b) **DCV5T-Bu$_4$**:PC$_{61}$BM from CB:CN (0.375%), and (c) **DCV5T-Bu$_4$**:PC$_{71}$BM from ODCB. Image size: 1 × 1 μm.

ture revealed a 14% higher amount of PC$_{61}$BM than the film deposited from CB. The PCBM-rich regions are visible as dark depressions in the top left quadrant of the phase image shown in Figure 6b. Since the surface of the active layer under investigation contacts the cathode in the device, it would be reasonable to claim that the higher content of PCBM on the surface could lead to improved electron transport and collection in the photovoltaic device.

The observed changes in morphology between Figure 6a and 6b can be rationalized through the different solubility of **DCV5T-Bu$_4$** in CN versus CB (6 vs 3 mg/mL). Since CN has a higher boiling point than CB (259 vs 132 °C), upon evaporation of CB during the final spin-coating stage, the CN content near the substrate increases. Considering the higher solubility of the oligothiophene in CN, we suggest that **DCV5T-Bu$_4$**-richer domains are formed at the PEDOT:PSS interface. This hypothesis anticorrelates with the AFM results in which a PCBM-rich surface is found (vide supra), and both arguments explain the higher short-circuit current densities and fill factors observed in the solar cell devices made with the CN additive (see Table 2).

The **DCV5T-Bu$_4$**:PC$_{71}$BM blend depicted in Figure 6c shows large domains of PC$_{71}$BM up to 100 nm in size (darker regions) and a topography roughness averaged to be 0.4 ± 0.1 nm. Thus, implementation of PC$_{71}$BM led to large phase separation and consequently limited charge generation resulting in a reduction in short-circuit current densities (6.5 vs 5.7 mA/cm^2) and PCEs (3.0 vs 2.5%) in the solar cell device. The non-ideal phase separation of **DCV5T-Bu$_4$** and PC$_{71}$BM spin-coated from ODCB

can also be rationalized by using the relative maximum solubilities of the donor and acceptor in the casting solvent. The oligothiophene donor displays a maximum solubility in of 3 mg/mL versus the PC$_{71}$BM acceptor that shows a value of 164 mg/mL (see Table 1). We reason that it is this large difference in solubility of the electron donor and acceptor in ODCB that leads to a large phase separation and overall lower PCE (2.5 vs 3.0%) in the solar cell device containing PC$_{71}$BM and PC$_{61}$BM, respectively. This is in agreement with work done by Troshin et al., in which they correlated maximum solubilities of dozens of fullerene derivatives with maximum solar cell performances. In their study they proposed that novel donor polymers should be tested in organic solar cells with fullerene derivatives that have a similar solubility in the used solvent [40].

Acceptor-substituted oligothiophene **DCV5T-Bu$_4$** possesses the unique characteristic of being processable both in vacuum and from solution, which allows for a rare comparison of the two device types (Table 3). The previously published vacuum-deposited active layer generates a higher J_{sc} (7.9 vs 6.5 mA/cm^2), a lower V_{oc} (1.02 vs 1.11 V), and a similar FF (0.43 vs 0.41) compared to their solution-processed counterparts, which finally leads to an increase in the overall PCE (3.5 vs 3.0%) [21]. The lower open-circuit voltage found in the vacuum-processed device is attributed to the decreased LUMO energy of C$_{60}$ (−4.1 eV) versus PC$_{61}$BM (−4.0 eV) (Figure 2). The superior values for J_{sc} and FF of the vacuum-processed device can in part be explained by a better molecular packing in the photoactive layer. It is well known that during vacuum deposition the evaporation rate and substrate temperature can be

Table 3: Comparing vacuum [21] and solution-processed active layers of optimized solar cells fabricated from **DCV5T-Bu$_4$**. Solution-processed device structure: ITO|PEDOT:PSS|**DCV5T-Bu$_4$**:PC$_{61}$BM|LiF|Al.

donor:acceptor	solvent	D:A ratio	$T_{soln/sub}$ (°C)	J_{sc} (mA/cm^2)	V_{oc} (V)	FF	PCE (%)	J(−1 V)/J_{SC}(0 V)	EQE (%)
DCV5T-Bu$_4$:PC$_{61}$BM	CB:CN (0.375%)	1:1	80/90	6.5	1.11	0.41	3.0	1.28	40
DCV5T-Bu$_4$:C$_{60}$[21]	—	2:1	—/90	7.9	1.02	0.43	3.5	1.17	62

precisely controlled and may be optimized to create highly ordered domains of donor and acceptor material [41]. These crystalline domains allow for higher exciton diffusion lengths [42] and thus higher charge generation, and improve charge transport to the electrodes. The better photocurrent saturation values for the vacuum-deposited cells, 1.17 versus 1.28 for the solution-processed devices, indicate reduced recombination, resulting in increased charge collection. The relatively modest difference in solar cell efficiency (3.0 vs 3.5%) for the two fabrication methods demonstrates the versatility of our **DCV5T-Bu$_4$** material in contrast to, e.g., a merocyanine dye reported in literature (2.9 vs 4.9%) [43] or squaraine dye (2.7 vs 4.1%) [44].

Conclusion

We have demonstrated that the acceptor-substituted quin-quethiophene **DCV5T-Bu$_4$** can be applied in solution-processed bulk-heterojunction solar cells. Power conversion efficiencies were increased from 2.1% to 3.0% by using chloronaphthalene as a solvent additive. Atomic force microscopy experiments revealed that an excess of PC$_{61}$BM was present on the surface of the photoactive layer when the film was made with the additive. This finding was then correlated to the increased charge generation (J_{sc}), improved charge transport (J_{sc}, FF), and increased charge collection ($J(-1V)/J_{sc}(0\ V)$) observed in the *J–V* curve of the photovoltaic cells. Furthermore, a rare direct comparison of solution- and vacuum-processed solar cells was possible. The efficiency of the optimized **DCV5T-Bu$_4$**:PC$_{61}$BM device at 3.0% is approaching the value of the vacuum-deposited **DCV5T-Bu$_4$**:C$_{60}$ device, which has been previously reported to be 3.5%.

Supporting Information

Supporting Information File 1

Further measurement data.
[http://www.beilstein-journals.org/bjnano/content/supplementary/2190-4286-4-77-S1.pdf]

Acknowledgements

References

1. Spanggaard, H.; Krebs, F. C. *Sol. Energy Mater. Sol. Cells* **2004,** *83,* 125–146. doi:10.1016/j.solmat.2004.02.021
2. Günes, S.; Neugebauer, H.; Sariciftci, N. S. *Chem. Rev.* **2007,** *107,* 1324–1338. doi:10.1021/cr050149z
3. Boudreault, P.-L.; Najari, A.; Leclerc, M. *Chem. Mater.* **2011,** *23,* 456–469. doi:10.1021/cm1021855
4. Walker, B.; Kim, C.; Nguyen, T.-Q. *Chem. Mater.* **2010,** *23,* 470–482. doi:10.1021/cm102189g
5. Mishra, A.; Bäuerle, P. *Angew. Chem., Int. Ed.* **2012,** *51,* 2020–2067. doi:10.1002/anie.201102326
6. Bürckstümmer, H.; Tulyakova, E. V.; Deppisch, M.; Lenze, M. R.; Kronenberg, N. M.; Gsänger, M.; Stolte, M.; Meerholz, K.; Würthner, F. *Angew. Chem., Int. Ed.* **2011,** *50,* 11628–11632. doi:10.1002/anie.201105133
7. Xue, J.; Rand, B. P.; Uchida, S.; Forrest, S. R. *Adv. Mater.* **2005,** *17,* 66–71. doi:10.1002/adma.200400617
8. Chen, G.; Sasabe, H.; Wang, Z.; Wang, X.-F.; Hong, Z.; Yang, Y.; Kido, J. *Adv. Mater.* **2012,** *24,* 2768–2773. doi:10.1002/adma.201200234
9. Xiao, X.; Wei, G.; Wang, S.; Zimmerman, J. D.; Renshaw, C. K.; Thompson, M. E.; Forrest, S. R. *Adv. Mater.* **2012,** *24,* 1956–1960. doi:10.1002/adma.201104261
10. Fitzner, R.; Mena-Osteritz, E.; Mishra, A.; Schulz, G.; Reinold, E.; Weil, M.; Körner, C.; Ziehlke, H.; Elschner, C.; Leo, K.; Riede, M.; Pfeiffer, M.; Uhrich, C.; Bäuerle, P. *J. Am. Chem. Soc.* **2012,** *134,* 11064–11067. doi:10.1021/ja302320c
11. Wang, D. H.; Kyaw, A. K. K.; Gupta, V.; Bazan, G. C.; Heeger, A. J. *Adv. Energy Mater.* **2013,** *3,* 1161–1165. doi:10.1002/aenm.201300277
12. Yin, B.; Yang, L. Y.; Liu, Y. S.; Chen, Y. S.; Qi, Q. J.; Zhang, F. L.; Yin, S. G. *Appl. Phys. Lett.* **2010,** *97,* 023303. doi:10.1063/1.3460911
13. Li, Z.; He, G.; Wan, X.; Liu, Y.; Zhou, J.; Long, G.; Zuo, Y.; Zhang, M.; Chen, Y. *Adv. Energy Mater.* **2012,** *2,* 74–77. doi:10.1002/aenm.201100572
14. Zhou, J.; Zuo, Y.; Wan, X.; Long, G.; Zhang, Q.; Ni, W.; Liu, Y.; Li, Z.; He, G.; Li, C.; Kan, B.; Li, M.; Chen, Y. *J. Am. Chem. Soc.* **2013,** *135,* 8484–8487. doi:10.1021/ja403318y
15. Zhou, J.; Wan, X.; Liu, Y.; Zuo, Y.; Li, Z.; He, G.; Long, G.; Ni, W.; Li, C.; Su, X.; Chen, Y. *J. Am. Chem. Soc.* **2012,** *134,* 16345–16351. doi:10.1021/ja306865z
16. Sun, Y.; Welch, G. C.; Leong, W. L.; Takacs, C. J.; Bazan, G. C.; Heeger, A. J. *Nat. Mater.* **2012,** *11,* 44–48. doi:10.1038/nmat3160
17. van der Poll, T. S.; Love, J. A.; Nguyen, T.-Q.; Bazan, G. C. *Adv. Mater.* **2012,** *24,* 3646–3649. doi:10.1002/adma.201201127
18. Schulze, K.; Riede, M.; Brier, E.; Reinold, E.; Bäuerle, P.; Leo, K. *J. Appl. Phys.* **2008,** *104,* 074511. doi:10.1063/1.2990071
19. Ziehlke, H.; Burtone, L.; Koerner, C.; Fitzner, R.; Reinold, E.; Bäuerle, P.; Leo, K.; Riede, M. *Org. Electron.* **2011,** *12,* 2258–2267. doi:10.1016/j.orgel.2011.09.015
20. Schulze, K.; Uhrich, C.; Schüppel, R.; Leo, K.; Pfeiffer, M.; Brier, E.; Reinold, E.; Bäuerle, P. *Adv. Mater.* **2006,** *18,* 2872–2875. doi:10.1002/adma.200600658
21. Haid, S.; Mishra, A.; Uhrich, C.; Pfeiffer, M.; Bäuerle, P. *Chem. Mater.* **2011,** *23,* 4435–4444. doi:10.1021/cm201392c
22. Chu, T.-Y.; Lu, J.; Beaupré, S.; Zhang, Y.; Pouliot, J.-R.; Wakim, S.; Zhou, J.; Leclerc, M.; Li, Z.; Ding, J.; Tao, Y. *J. Am. Chem. Soc.* **2011,** *133,* 4250–4253. doi:10.1021/ja200314m
23. Chen, H.-Y.; Yang, H.; Yang, G.; Sista, S.; Zadoyan, R.; Li, G.; Yang, Y. *J. Phys. Chem. C* **2009,** *113,* 7946–7953. doi:10.1021/jp810798z

24. Yao, Y.; Hou, J.; Xu, Z.; Li, G.; Yang, Y. *Adv. Funct. Mater.* **2008**, *18*, 1783–1789. doi:10.1002/adfm.200701459

25. Salim, T.; Wong, L. H.; Bräuer, B.; Kukreja, R.; Foo, Y. L.; Bao, Z.; Lam, Y. M. *J. Mater. Chem.* **2011**, *21*, 242–250. doi:10.1039/c0jm01976c

26. Chen, F.-C.; Tseng, H.-C.; Ko, C.-J. *Appl. Phys. Lett.* **2008**, *92*, 103316. doi:10.1063/1.2898153

27. Lee, J. K.; Ma, W. L.; Brabec, C. J.; Yuen, J.; Moon, J. S.; Kim, J. Y.; Lee, K.; Bazan, G. C.; Heeger, A. J. *J. Am. Chem. Soc.* **2008**, *130*, 3619–3623. doi:10.1021/ja710079w

28. Peet, J.; Kim, J. Y.; Coates, N. E.; Ma, W. L.; Moses, D.; Heeger, A. J.; Bazan, G. C. *Nat. Mater.* **2007**, *6*, 497–500. doi:10.1038/nmat1928

29. Graham, K. R.; Wieruszewski, P. M.; Stalder, R.; Hartel, M. J.; Mei, J.; So, F.; Reynolds, J. R. *Adv. Funct. Mater.* **2012**, *22*, 4801–4813. doi:10.1002/adfm.201102456

30. Adamopoulos, G.; Heiser, T.; Giovanella, U.; Ould-Saad, S.; van de Wetering, K. I.; Brochon, C.; Zorba, T.; Paraskevopoulos, K. M.; Hadziioannou, G. *Thin Solid Films* **2006**, *511–512*, 371–376. doi:10.1016/j.tsf.2005.12.029

31. Fuhrmann, G.; Krömer, J.; Bäuerle, P. *Synth. Met.* **2001**, *119*, 125–126. doi:10.1016/s0379-6779(00)01173-5

32. Fitzner, R.; Reinold, E.; Mishra, A.; Mena-Osteritz, E.; Ziehlke, H.; Körner, C.; Leo, K.; Riede, M.; Weil, M.; Tsaryova, O.; Weiß, A.; Uhrich, C.; Pfeiffer, M.; Bäuerle, P. *Adv. Funct. Mater.* **2011**, *21*, 897–910. doi:10.1002/adfm.201001639

33. Schulz, G. L.; Mastalerz, M.; Ma, C.-Q.; Wienk, M.; Janssen, R.; Bäuerle, P. *Macromolecules* **2013**, *46*, 2141–2151. doi:10.1021/ma302404y

34. Lenes, M.; Wetzelaer, G.-J. A. H.; Kooistra, F. B.; Veenstra, S. C.; Hummelen, J. C.; Blom, P. W. M. *Adv. Mater.* **2008**, *20*, 2116–2119. doi:10.1002/adma.200702438

35. Hummelen, J. C.; Knight, B. W.; LePeq, F.; Wudl, F.; Yao, J.; Wilkins, C. L. *J. Org. Chem.* **1995**, *60*, 532–538. doi:10.1021/jo00108a012

36. Koster, L. J. A.; Mihailetchi, V. D.; Blom, P. W. M. *Appl. Phys. Lett.* **2006**, *88*, 052104. doi:10.1063/1.2170424

37. Scharber, M. C.; Mühlbacher, D.; Koppe, M.; Denk, P.; Waldauf, C.; Heeger, A. J.; Brabec, C. J. *Adv. Mater.* **2006**, *18*, 789–794. doi:10.1002/adma.200501717

38. Bijleveld, J. C.; Shahid, M.; Gilot, J.; Wienk, M. M.; Janssen, R. A. J. *Adv. Funct. Mater.* **2009**, *19*, 3262–3270. doi:10.1002/adfm.200900412

39. Shrotriya, V.; Yao, Y.; Li, G.; Yang, Y. *Appl. Phys. Lett.* **2006**, *89*, 063505. doi:10.1063/1.2335377

40. Troshin, P. A.; Hoppe, H.; Renz, J.; Egginger, M.; Mayorova, J. Y.; Goryachev, A. E.; Peregudov, A. S.; Lyubovskaya, R. N.; Gobsch, G.; Sariciftci, N. S.; Razumov, V. F. *Adv. Funct. Mater.* **2009**, *19*, 779–788. doi:10.1002/adfm.200801189

41. Wynands, D.; Levichkova, M.; Leo, K.; Uhrich, C.; Schwartz, G.; Hildebrandt, D.; Pfeiffer, M.; Riede, M. *Appl. Phys. Lett.* **2010**, *97*, 073503. doi:10.1063/1.3475766

42. Brabec, C. J.; Heeney, M.; McCulloch, I.; Nelson, J. *Chem. Soc. Rev.* **2011**, *40*, 1185–1199. doi:10.1039/c0cs00045k

43. Kronenberg, N. M.; Steinmann, V.; Bürckstümmer, H.; Hwang, J.; Hertel, D.; Würthner, F.; Meerholz, K. *Adv. Mater.* **2010**, *22*, 4193–4197. doi:10.1002/adma.201000800

44. Wei, G.; Wang, S.; Renshaw, K.; Thompson, M. E.; Forrest, S. R. *ACS Nano* **2010**, *4*, 1927–1934. doi:10.1021/nn100195j

A facile synthesis of a carbon-encapsulated Fe_3O_4 nanocomposite and its performance as anode in lithium-ion batteries

Raju Prakash[1,2], Katharina Fanselau[1], Shuhua Ren[1],
Tapan Kumar Mandal[1,3], Christian Kübel[4], Horst Hahn[1]
and Maximilian Fichtner[*1,5]

Letter

Address:
[1]Institute for Nanotechnology (INT), Karlsruhe Insititute of Technology (KIT), Hermann-von-Helmholtz-Platz 1, Karlsruhe, 76344, Germany, [2]current address: Centre for Automotive Energy Materials (CAEM), International Advanced Research Centre for Powder Metallurgy and New Materials (ARCI), Taramani, Chennai-600113, India, [3]Faculty of Science and Technology, ICFAI University, Selaqui, Dehradun-248197, India, [4]Karlsruhe Nano Micro Facility (KNMF), Karlsruhe Institute of Technology (KIT), Hermann-von-Helmholtz-Platz 1, Karlsruhe, 76344, Germany and [5]Helmholtz Institute Ulm (HIU), Albert-Einstein-Allee 11, Ulm, 89081, Germany

Email:
Maximilian Fichtner[*] - m.fichtner@kit.edu

* Corresponding author

Keywords:
electrochemistry; iron oxide; lithium-ion battery; nanoparticles; pyrolysis

Abstract

A carbon-encapsulated Fe_3O_4 nanocomposite was prepared by a simple one-step pyrolysis of iron pentacarbonyl without using any templates, solvents or surfactants. The structure and morphology of the nanocomposite was investigated by X-ray diffraction, scanning electron microscopy, transmission electron microscopy, Brunauer–Emmett–Teller analysis and Raman spectroscopy. Fe_3O_4 nanoparticles are dispersed intimately in a carbon framework. The nanocomposite exhibits well constructed core–shell and nanotube structures, with Fe_3O_4 cores and graphitic shells/tubes. The as-synthesized material could be used directly as anode in a lithium-ion cell and demonstrated a stable capacity, and good cyclic and rate performances.

Findings

Due to high energy density and excellent cyclic performance, lithium-ion batteries (LIBs) have become the leading energy storage device for portable electronic markets and for powering upcoming electric vehicles [1,2]. In order to obtain LIBs with superior performance, numerous strategies to find new materials are currently being explored [3]. Fe_3O_4 is widely regarded as one of the high energy-density anode materials for LIBs, and is based on the conversion mechanism

($Fe_3O_4 + 8 Li^+ + 8 e^- \leftrightarrow 3 Fe + 4 Li_2O$) [4-6]. The theoretical specific capacity of Fe_3O_4 is 926 mAh·g^{-1}, which is far beyond that of a graphite anode (372 mAh·g^{-1}). However, because of agglomerations and the significant volume change of active materials during the redox reaction, Fe_3O_4 anodes have suffered greatly from poor cyclic performances. A variety of strategies, such as carbon coatings [7], carbon core–shells [8], nanocomposites [9], nanostructures [10], or nano-encapsulation [11], have recently been explored to circumvent this problem. These strategies apply various synthetic methods [12] such as hydrothermal, coprecipitation, microemulsion, sol–gel, plasma synthesis, electro-spray, and laser pyrolysis techniques. Much improved electrochemical performances have been achieved with the modified materials [13].

However, all aforementioned methods need multi-step processes that include removing solvents, surfactants, or templates. Especially, the removal of solvents deposited on the nano-Fe_3O_4 surfaces is a major challenge, which restricts their practical applications [12]. Hence, it is crucial to develop a straightforward and solvent-free process for the synthesis of Fe_3O_4 nanocomposite.

Herein, we report a simple method that directly affords a carbon encapsulated Fe_3O_4 nanocomposite [Fe_3O_4–C] by employing $Fe(CO)_5$ precursor without any templates, solvents, or surfactants. This raw material acts not only as the source of iron and oxygen, but also of carbon, which gives rise to typical nanostructures. Fe_3O_4 nanoparticles are dispersed intimately in a carbon framework. The material could be used directly as anode and yielded a stable capacity.

In a typical synthesis, $Fe(CO)_5$ was sealed into a closed stainless steel Swagelok-type reactor under argon atmosphere as described previously [14]. The reactor was placed horizontally inside the home made rotating quartz-tube setup [15] in a furnace. The tube was rotated at 10 rpm during pyrolysis to obtain a homogeneous mixture. The reactor was heated at a rate of 5 °C·min^{-1} to 700 °C and kept at this temperature for 3 h. The reaction took place under autogenous pressure. After allowing the reactor to cool down to room temperature, the remaining pressure was released carefully. A dry fine black powder of [Fe_3O_4–C] produced was collected and used directly without any further treatment. The reaction precedes in two steps: in the first step, $Fe(CO)_5$ decomposes to form Fe and CO gas {$Fe(CO)_5(g) \rightarrow Fe(s) + 5CO(g)$} [16]. Subsequently, CO reacts with the active Fe nanoparticles to yield Fe_3O_4 nanoparticles and carbon {$Fe(s) + CO(g) \rightarrow Fe_3O_4–C_x(s) +$ gaseous material}. The iron nanoparticles catalyze the formation of nanotubes and shells from the in-situ generated carbon. Meanwhile, the Fe_3O_4 produced from the Fe nanoparticles is encapsulated within the nanotubes or carbon shells. Elemental analysis suggested that the composite consists of 70 wt % of Fe_3O_4 and 30 wt % of carbon. The energy dispersive X-ray spectroscopy (EDX) patterns by using SEM mode (Figure S1 in Supporting Information File 1) show that the as prepared [Fe_3O_4–C] is composed of C, Fe and O. The observed Fe/O mass ratio of the composite (ca. 2.7) is in close agreement with the nominal value of Fe_3O_4 (2.62).

The X-ray powder diffraction (XRD) pattern and the Raman spectrum of the as prepared nanocomposite are shown in Figure 1. All the diffraction peaks can be attributed to two well-
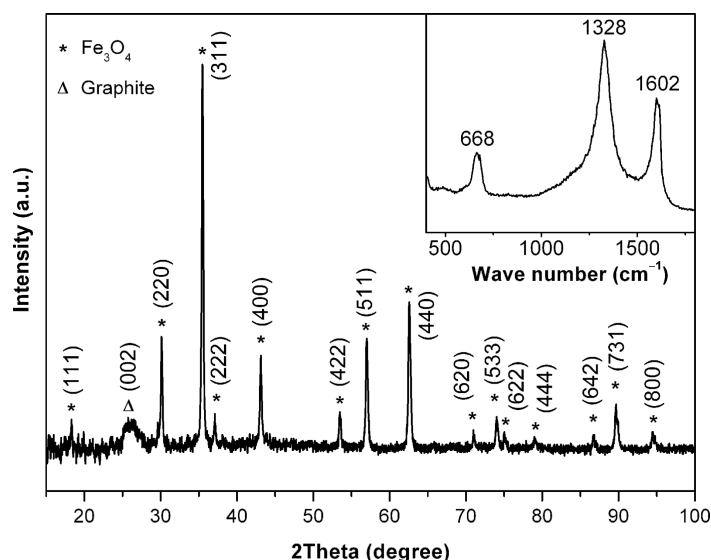

Figure 1: XRD pattern and Raman spectrum (inset) of [Fe_3O_4-C].

defined phases, which are hexagonal-phase graphitic carbon {26.4° (002); JCPDS-041-1487} and cubic-phase Fe_3O_4 {JCPDS-019-0629}. No signals for metallic iron or other oxides were detected in the XRD pattern, which indicates that the oxidation reaction was selective, and formed exclusively Fe_3O_4. Scherrer analysis was performed on high intensity Bragg peaks (220, 311, 400, 511 and 440) of Fe_3O_4, and the mean crystallite size was calculated to be 14 nm. The Raman spectrum of the composite showed two bands at 1328 and 1602 cm^{-1}, which are characteristic of the D (disorder-induced phonon mode [17]) and G (graphitic lattice mode E_{2g} [18]) bands of carbon, respectively. The intensity ratio I_G/I_D of 0.7 indicates that a significant quantity of disordered carbon is also present in the nanocomposite. In addition, the A_{1g} vibration mode of the Fe_3O_4 peak appeared at 668 cm^{-1}, which agrees well with the literature value for pure as well as for graphene encapsulated Fe_3O_4 [11,19]. The infrared spectrum of the nanocomposite exhibited a broad band at 560 cm^{-1}, which is typical for the Fe−O vibration of Fe_3O_4 [20].

The SEM image of [Fe_3O_4–C] (Figure 2) shows that the material consists of interlinked nanotubes and nanogranular structures. The diameters of the tubes were in the range between 10 and 100 nm and their lengths varied up to several micrometers.

A large number of tubes were encapsulated with Fe_3O_4 nanoparticles at their tips. However in some longer tubes, the particles were embedded in several places within the tube. TEM images of the nanogranular region of the composite confirmed the presence of a core–shell structure, containing Fe_3O_4 cores and graphitic onions shells. The interface between graphitic carbon and Fe_3O_4 with short-range disordered layers could be observed. The Fe_3O_4 particles were surrounded by roughly eight layers of graphite with an average carbon-coating thickness of about 3 nm. However, a few Fe_3O_4 particles were covered by several layers of carbon. In addition, a few incompletely/defectively carbon-coated as well as bare Fe_3O_4 nanoparticles could also be observed (Figure S2 in Supporting Information File 1). Fast Fourier transform (FFT) analysis of various HRTEM images (of crystallites located inside or outside of carbon shells, see Figure S3 in Supporting Information File 1) reveal that the observed lattice spacings fit very well to the cubic Fe_3O_4 (space group $Fd3m$) detected by XRD. The encapsulated Fe_3O_4 particles have diameters in the order of 30 nm. The lattice spacing of the adjacent graphitic layers is typically around 0.36 nm.

The nitrogen adsorption–desorption measurement shows type-IV isotherms with an H_3-type hysteresis loop (Figure 3), which
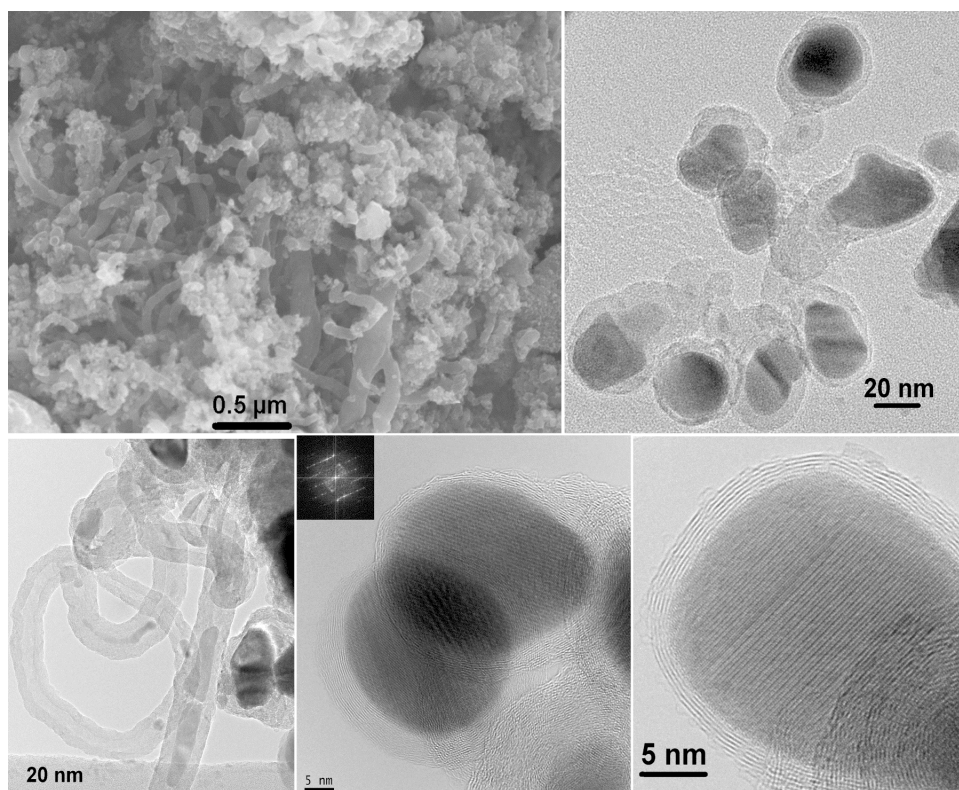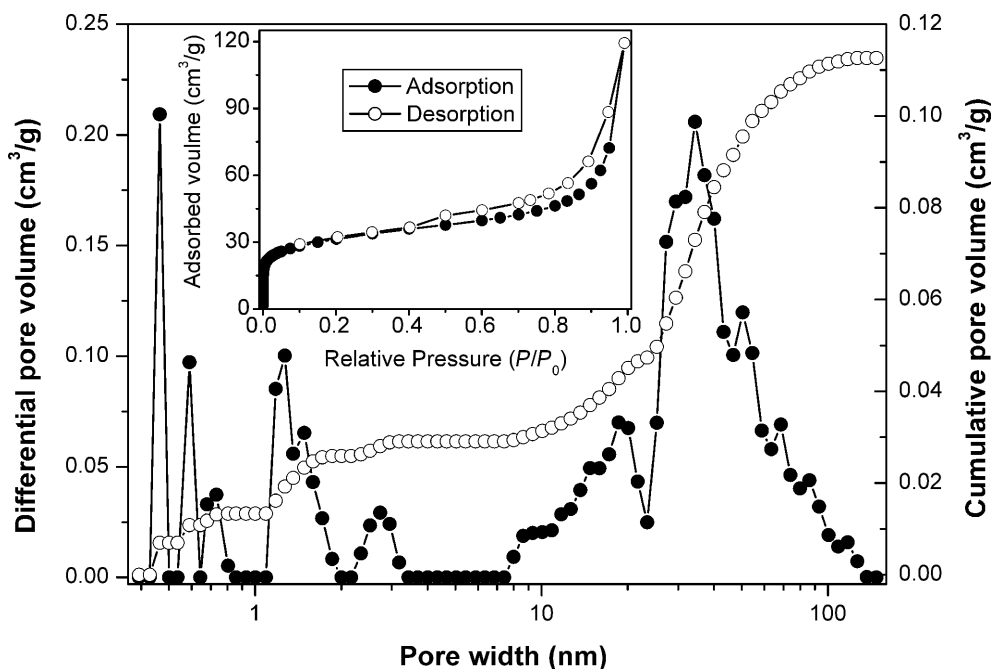

Figure 2: SEM (top left) and TEM images of [Fe_3O_4–C].

Figure 3: Nitrogen isotherm (inset) and pore width profile (cumulative: open circles, differential: filled circles) of [Fe_3O_4–C] measured at −196 °C.

indicates a mesoporous (pore width < 50 nm) nature of the material [21]. In addition, a sharp increase of the adsorbed gas at very low relative-pressures suggesting the presence of micropores (pore width < 2 nm). The micro- and mesoporous volumes were determined as 0.026 and 0.07 $cm^3 \cdot g^{-1}$, respectively. The differential pore volume estimated from the adsorption branch of isotherm by using the DFT model [22] suggests that the mesopore sizes were distributed between 10 and 35 nm. The BET specific surface area was calculated to be as high as 110.6 $m^2 \cdot g^{-1}$. It has been found that porous electrode materials can facilitate the diffusion of Li ions to active sites with less resistance and can also withstand the change of volume during the charge/discharge cycling [23]. Thus, the micro- and mesopores of [Fe_3O_4–C] could act as buffer for the volume change during redox cycle, which would lead to an enhanced cyclic performance as an anode material for LIBs.

The electrochemical performance of the [Fe_3O_4–C] anode has been evaluated with respect to Li metal. Figure 4a shows a typical galvanostatic profile for a [Fe_3O_4–C] cell cycled between 3.0 and 0.005 V at 93 $mA \cdot g^{-1}$. The obtained charge/discharge profiles are comparable to those of various Fe_3O_4 electrodes tested at similar current and voltage ranges [7-11]. During the first discharge the potential dropped abruptly down to about 0.8 V, which can be ascribed to the reaction of {$Fe_3O_4 + x$Li → Li$_x$Fe$_3$O$_4$} [24]. The long plateau corresponds to the conversion reaction and the sloping part of the discharge curve can be assigned to the formation of the solid electrolyte

interface (SEI) layer, as well as to the formation of a gel-like film through the reaction of Fe^0 and electrolyte [7-11]. The electrode exhibits a first-discharge capacity of 1480 $mAh \cdot g^{-1}$ (based on the composite weight) and a first-charge capacity of 960 $mAh \cdot g^{-1}$. The capacity decreases marginally over the first few cycles and then stabilizes at about 920 $mAh \cdot g^{-1}$ in the subsequent 50 cycles. The coulombic efficiency after the first cycle remained at nearly 100%. The cyclic voltammogram of [Fe_3O_4–C] is comparable to that of other Fe_3O_4 electrodes [9-11], and shows a cathodic wave at 0.56 V and an anodic wave at 1.78 V, which correspond to the Fe^{3+}/Fe^{2+}-to-Fe^0 redox couple. The irreversible wave at 0.4 V can be ascribed to the formation of the SEI. In the subsequent cycles, the reversible waves shifted slightly to more positive potentials. The CV curves of three successive scans almost overlap which reveals the good reversibility of the composite electrode.

Besides the cyclic stability, the electrode also exhibits a moderate rate capability performance. At current densities below 926 $mA \cdot g^{-1}$ the electrode exhibited good cyclic performances and an excellent capacity retention. When the electrode was cycled at 1852 and 2780 $mA \cdot g^{-1}$, respectively, the observed capacity retentions between the 3rd and the 50th cycles were about 72 and 63%, respectively. A similar trend has also been observed in other Fe_3O_4/C systems at high current rates [9,11], which could be ascribed to the slow conversion reaction kinetics. SEM images of the electrode cycled for 50 cycles at 93 $mA \cdot g^{-1}$ show a morphology similar to that of the

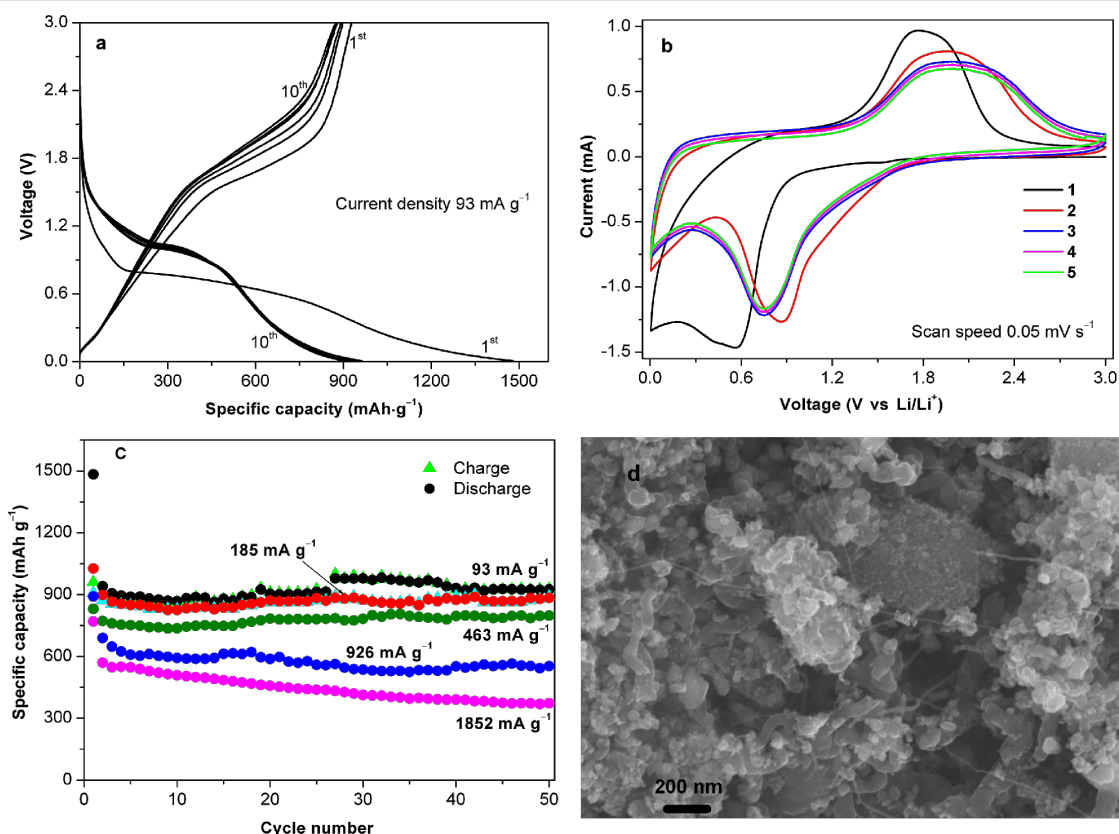**Figure 4:** Electrochemical properties of [Fe$_3$O$_4$–C]. (a) Charge/discharge curves, (b) cyclic voltammograms, (c) rate performance profile, and (d) SEM image of electrode after 50 cycles at 93 mA·g^{-1}.

original composite. This indicates that the active materials remain intact during cycling.

Both Fe$_3$O$_4$ and carbon are electrochemically active components for Li-ion storage and contribute to the overall capacity of the electrode. The good electrochemical performance of the composite can thus be attributed to its special morphology, porosity and also the synergistic effect by combining metal oxide and carbon nanotubes, which provides better electronic and ionic transport, as well as a tolerance toward the volume change during the reaction.

In summary, a new carbon encapsulated Fe$_3$O$_4$ nanocomposite was synthesized by a simple one-step pyrolysis of Fe(CO)$_5$. The nanocomposite exhibits well-constructed core–shell and nanotube structures with Fe$_3$O$_4$ cores and graphitic shells/tubes. The nanocomposite electrode exhibits a stable reversible capacity of 920 mAh·g^{-1} at 93 mA·g^{-1} in the subsequent 50 cycles. Further experiments are underway to check its extended stability and capacity retention behaviour. We believe that this method opens a simple way for producing carbon encapsulated metal oxide nanocomposites for energy storage, catalysis, and magnetic applications.

Supporting Information

Supporting Information File 1

General procedures and additional figures.
[http://www.beilstein-journals.org/bjnano/content/supplementary/2190-4286-4-79-S1.pdf]

Acknowledgements

References

1. Tarascon, J.-M.; Armand, M. *Nature* **2001,** *414,* 359–367. doi:10.1038/35104644
2. Brown, S.; Pyke, D.; Steenhof, P. *Energy Policy* **2010,** *38,* 3797–3806. doi:10.1016/j.enpol.2010.02.059
3. Guo, Y.-G.; Hu, J.-S.; Wan, L.-J. *Adv. Mater.* **2008,** *20,* 2878–2887. doi:10.1002/adma.200800627
4. Coey, J. M. D.; Berkiwitz, A. E.; Balcells, L.; Putris, F. F.; Parker, F. T. *Appl. Phys. Lett.* **1998,** *72,* 734–736. doi:10.1063/1.120859

5. Poizot, P.; Laruelle, S.; Grugeon, S.; Dupont, L.; Tarascon, J.-M.
    Nature **2000,** *407,* 496–499. doi:10.1038/35035045
6. Ren, S.; Prakash, R.; Wang, D.; Chakravadhanula, V. S. K.;
    Fichtner, M. *ChemSusChem* **2012,** *5,* 1397–1400.
    doi:10.1002/cssc.201200139
7. Muraliganth, T.; Murugan, A. V.; Manthiram, A. *Chem. Commun.* **2009,**
    7360–7362. doi:10.1039/b916376j
8. Wang, S.; Zhang, J.; Chen, C. *J. Power Sources* **2010,** *195,*
    5379–5381. doi:10.1016/j.jpowsour.2010.03.035
9. Ji, L.; Tan, Z.; Kuykendall, T. K.; Aloni, S.; Xun, S.; Lin, E.;
    Battaglia, V.; Zhang, Y. *Phys. Chem. Chem. Phys.* **2011,** *13,*
    7170–7177. doi:10.1039/c1cp20455f
10. Jin, S.; Deng, H.; Long, D.; Liu, X.; Zhan, L.; Liang, X.; Qiao, W.;
    Ling, L. *J. Power Sources* **2011,** *196,* 3887–3893.
    doi:10.1016/j.jpowsour.2010.12.078
11. Wang, J.-Z.; Zhong, C.; Wexler, D.; Idris, N. H.; Wang, Z.-X.;
    Chen, L.-Q.; Liu, H.-K. *Chem.–Eur. J.* **2011,** *17,* 661–667.
    doi:10.1002/chem.201001348
12. Mahmoudi, M.; Sant, S.; Wang, B.; Laurent, S.; Sen, T.
    Adv. Drug Delivery Rev. **2011,** *63,* 24–46.
    doi:10.1016/j.addr.2010.05.006
13. Laurent, S.; Forge, D.; Port, M.; Roch, A.; Robic, C.; Elst, L. V.;
    Muller, R. N. *Chem. Rev.* **2008,** *108,* 2064–2110.
    doi:10.1021/cr068445e
14. Prakash, R.; Mishra, A. K.; Roth, A.; Kübel, C.; Scherer, T.; Ghafari, M.;
    Hahn, H.; Fichtner, M. *J. Mater. Chem.* **2010,** *20,* 1871–1876.
    doi:10.1039/b919097j
15. Prakash, R.; Wall, C.; Mishra, A. K.; Kübel, C.; Ghafari, M.; Hahn, H.;
    Fichtner, M. *J. Power Sources* **2011,** *196,* 5936–5944.
    doi:10.1016/j.jpowsour.2011.03.007
16. Liu, S.; Tang, X.; Mastai, Y.; Felner, I.; Gedanken, A. *J. Mater. Chem.*
    2000, *10,* 2502–2506. doi:10.1039/b004901h
17. Yin, S.; Shen, P. K.; Song, S.; Jiang, S. P. *Electrochim. Acta* **2009,** *54,*
    6954–6958. doi:10.1016/j.electacta.2009.07.009
18. Lefrant, S.; Baltog, I.; Baibarac, M.; Schreiber, J.; Chauvet, O.
    Phys. Rev. B **2002,** *65,* 235401. doi:10.1103/PhysRevB.65.235401
19. de Faria, D. L. A.; Silva, S. V.; de Oliveira, M. T. *J. Raman Spectrosc.*
    1997, *28,* 873–878.
    doi:10.1002/(SICI)1097-4555(199711)28:11<873::AID-JRS177>3.0.CO
    ;2-B
20. Chen, L. Y.; Zhao, C. L.; Zhou, Y.; Peng, H.; Zheng, Y. Y.
    J. Alloys Compd. **2010,** *504,* L46–L50.
    doi:10.1016/j.jallcom.2010.05.165
21. Sing, K. S. W.; Everett, D. H.; Haul, R. A. W.; Moscou, L.;
    Pierotti, R. A.; Rouquérol, J.; Siemieniewska, T. *Pure Appl. Chem.*
    1985, *57,* 603–619. doi:10.1351/pac198557040603
22. Webb, P. A.; Orr, C. *Analytical Methods in Fine Particle Technology;*
    Micromeritics Instrument Corporation; Norcross: GA, USA, 1997.
23. Wang, D.-W.; Li, F.; Liu, M.; Lu, G. Q.; Cheng, H.-M.
    Angew. Chem., Int. Ed. **2007,** *47,* 373–376.
    doi:10.1002/anie.200702721
24. Wang, L.; Yu, Y.; Chen, P. C.; Zhang, D. W.; Chen, C. H.
    J. Power Sources **2008,** *183,* 717–723.
    doi:10.1016/j.jpowsour.2008.05.079

Influence of particle size and fluorination ratio of CF$_x$ precursor compounds on the electrochemical performance of C–FeF$_2$ nanocomposites for reversible lithium storage

Ben Breitung[*1], M. Anji Reddy[1], Venkata Sai Kiran Chakravadhanula[1,2], Michael Engel[1], Christian Kübel[1,2,3], Annie K. Powell[1,4], Horst Hahn[1,2] and Maximilian Fichtner[*1,2]

Full Research Paper

Address:
[1]Karlsruhe Insititute of Technology (KIT), Institute of Nanotechnology (INT), Hermann-von-Helmholtz-Platz 1, 76344 Eggenstein-Leopoldshafen, Germany, [2]Helmholtz Institute Ulm (HIU) Electrochemical Energy Storage, Albert-Einstein-Allee 11, 89081 Ulm, Germany, [3]Karlsruhe Insititute of Technology (KIT), Karlsruhe Nano Micro Facility (KNMF), Hermann-von-Helmholtz-Platz 1, 76344 Eggenstein-Leopoldshafen, Germany and [4]Karlsruhe Institute of Technology (KIT), Institute for Inorganic Chemistry, Engesserstrasse 15, D-76128 Karlsruhe, Germany

Email:
Ben Breitung[*] - ben.breitung@kit.edu; Maximilian Fichtner[*] - maximilian.fichtner@kit.edu

* Corresponding author

Keywords:
conducting carbon; conversion material; enregy-related; graphite fluoride; lithium battery; iron fluoride

Abstract

Systematical studies of the electrochemical performance of CF$_x$-derived carbon–FeF$_2$ nanocomposites for reversible lithium storage are presented. The conversion cathode materials were synthesized by a simple one-pot synthesis, which enables a reactive intercalation of nanoscale Fe particles in a CF$_x$ matrix, and the reaction of these components to an electrically conductive C–FeF$_2$ compound. The pretreatment and the structure of the utilized CF$_x$ precursors play a crucial role in the synthesis and influence the electrochemical behavior of the conversion cathode material. The particle size of the CF$_x$ precursor particles was varied by ball milling as well as by choosing different C/F ratios. The investigations led to optimized C–FeF$_2$ conversion cathode materials that showed specific capacities of 436 mAh/g at 40 °C after 25 cycles. The composites were characterized by Raman spectroscopy, X-Ray diffraction measurements, electron energy loss spectroscopy and TEM measurements. The electrochemical performances of the materials were tested by galvanostatic measurements.

Introduction

Lithium-ion batteries are key energy storage systems for portable and mobile electric devices. However, for applications that need high energy densities, current insertion-based lithium-ion batteries do not match the targets for such systems [1-4]. As a perspective, energy storage materials that are based on conversion reactions may offer high theoretical capacities and high theoretical energy densities for hydrogen storage and for electrochemical storage in batteries [5]. Compared to state-of-the-art insertion cathode materials with specific capacities of 150 mAh/g for $LiCoO_2$ [6] up to 170 mAh/g for $LiFePO_4$ [7] conversion cathode materials can theoretically provide more than three times higher theoretical specific capacities. The theoretical capacity of the herein investigated FeF_2/Li^+ conversion system amounts to 571 mAh/g [8]. This mainly results from a utilization of several oxidation states of the active metal that allows for a multi-electron process per redox step compared to only one-electron processes in the insertion materials [9-11].
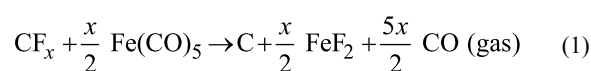
An early example for conversion reactions in batteries was demonstrated by Poizot et al. who used transition-metal oxides as anode materials [9]. Metal fluorides are also prominent examples as they reversibly react with lithium at relatively high voltages so that they can be used as cathode materials [5,8,12-16]. Fluorine is the lightest and smallest halogen in the periodic table of elements, which is a precondition to achieve a high gravimetric energy density in batteries. Iron fluorides are attractive as electrode materials because of their large abundance, low cost and low toxicity. However, because of the electrically insulating nature of metal fluorides, a well conducting nanoscale matrix is required to ensure the electron transport to the active material. Micrometer-sized metal fluoride particles are too big to accommodate the transfer of electric charge, and their capacity fades rapidly with cycling. Hence, a nanoscale dispersion of the material in the matrix is a precondition for its electrochemical activity [17,18]. In addition, volume changes that result from phase conversion of the active material during charging and discharging may lead to cracks in the particles and result in poor cyclic stabilities. For this reason, mostly carbon materials have been used as conducting matrix as well as to buffer the volume changes.

Various methods have been described in the literature to synthesize carbon–metal fluoride nanocomposites. For example, carbon–iron fluoride nanocomposites, which show superior electrochemical performance during the initial cycling, have been synthesized by high energy ball milling graphite and iron fluoride [17-19]. However, the major drawback of current conversion materials systems is their low cyclic stability during an extended number of cycles. Considerable efforts have been made to understand and optimize the electrochemical performance of the metal fluoride conversion systems [20-33].

Recently, conversion systems with excellent cyclic stabilities were synthesized through the pyrolysis of metallocenes with LiF, in which agglomerates of LiF and transition metal nanoparticles encapsulated in layers of graphitic carbon were formed. The agglomerates are interlinked by multiwall carbon nanotubes which are formed in situ [34-36]. Although these systems enhanced the cycling stability of the conversion reaction greatly because of the tight embedding of iron nanoparticles in the carbon matrix, their specific capacity was about 250 mAh/g, which is only one third of the theoretical value.

To improve the capacity and to still benefit from a stabilizing and tightly attached carbon matrix, a new solid-state chemical synthesis, which is based on a reaction between CF_x and $Fe(CO)_5$ to produce graphitic carbon–FeF_2 nanocomposites at 250 °C, was developed recently [37]. $Fe(CO)_5$ evaporates at 103 °C [38] and decomposes at temperatures above 120 °C [39]. In this way atomic sized Fe(0) nuclei are generated. These Fe(0) particles obviously react inside the CF_x matrix and produce FeF_2 nanoparticles by reducing the CF_x carbon backbone to graphitic carbon in a reactive intercalation process. The final material contains crystallites of FeF_2 with diameters of a few nanometers, which are closely packed and embedded between graphitic carbon sheets. The graphitic carbon enwraps the formed FeF_2 nanocrystallites and provides an electrical contact between the insulating FeF_2 particles and the collector. The overall reaction follows Equation 1:

$$CF_x + \frac{x}{2}\,Fe(CO)_5 \rightarrow C + \frac{x}{2}\,FeF_2 + \frac{5x}{2}\,CO\,(gas) \quad (1)$$

It was also shown that ball milling of CF_x as pretreatment significantly influences the electrochemical performance of the C–FeF_2 nanocomposites. The electrochemical properties of these nanocomposites likely depend on the amount and type of carbon present in the nanocomposites. In our previous studies we used only graphite fluoride with a fluorine to carbon ratio of 1.1. This resulted from the reaction with $Fe(CO)_5$ in 20 wt % of carbon related to the total mass of the composite. In the present work we focus on an optimization of properties by varying the CF_x pretreatment and by varying the amount of carbon in the nanocomposites using different precursors with a variable C to F ratio.

Experimental

Ball milling of the CF_x precursor was performed in a sealed tungsten carbide vial under inert conditions. The CF_x powder

was ball-milled for 2 h, with a ball to powder ratio of 24:1 and milling speeds of 200, 300, and 400 rpm.

To adjust the active material to carbon ratio in the products, different graphite fluoride samples were used with different fluorine to carbon ratios, which correspond to x in the reaction equation. The synthesis of the C–FeF_2 nanocomposites was performed in a tubular stainless steel reactor with metal fittings (VCR®). In a typical synthesis, 0.25 g graphite fluoride ($CF_{0.5}$, $CF_{0.7}$, $CF_{1.0}$, Alfa Aesar, 99%; $CF_{1.1}$, Sigma Aldrich, 99.9%) and the required amount of $Fe(CO)_5$ (Sigma Aldrich, 99%) were filled in the reaction vessel inside an argon-filled glove box. The amount of iron pentacarbonyl used for the synthesis was calculated for a complete reaction with the inserted CF_x to FeF_2. The vessel was closed and heated to 250 °C at a heating rate of 5 K/min and kept at this temperature for 24 h in a horizontal tube furnace. Afterwards, the reactor was let to cool down to room temperature. The pressure was released carefully and the remaining powder was collected under argon atmosphere. The black powder was used without further purification.

Transmission electron microscopy analysis was carried out on an image corrected Titan 80-300 (FEI) operated at 80 kV and equipped with a Tridiem 963 imaging filter (Gatan) for EEL spectroscopy with a nominal energy resolution of 0.8 eV. For the TEM analysis, the dry powders were distributed on holey carbon coated copper grids (Quantifoil).

Powder X-ray diffraction (XRD) patterns were recorded in a 2θ range of 10–40° by using a Philips X'pert diffractometer with Mo Kα radiation. Raman spectroscopy was performed with a confocal Raman microscope (CRM200, WITec). As excitation light source a HeNe gas laser from JDS Uniphase was used at a wavelength of 632.8 nm. The beam was focused through a 100× objective onto the sample. The Raman-scattered light was separated from the laser excitation light by using a holographic notch filter, and spectrally analyzed by using a grating spectrograph and a Peltier-cooled charge coupled device.

Electrochemical studies were performed in Swagelok® type cells. Each cathode material was tested 2–3 times, also at different temperatures and at different current densities. The variation of the obtained specific discharge capacities was always less than 30 mAh/g below or above the presented values for cathode materials cycled under the same conditions. The electrode fabrication and the building of electrochemical cells were done in an argon-filled glove box. The electrodes were fabricated by mixing the synthesized material and polyvinylidene fluoride (PVDF) in the mass ratio 90:10. A slurry containing the above mixture was prepared by using *N*-methyl-2-pyrrolidinone. It was spread on a stainless steel (SS) foil

(area: 1.13 cm^2) and dried on hot plate at 160 °C for 12 h. Typically, each electrode contained 3–4 mg of active material. Lithium foil (Goodfellow, 99.9 %) was used as the negative electrode, and a borosilicate glass fiber sheet was used as separator. The sheet was saturated with 1 M $LiPF_6$ in 1:1 ethylene carbonate (EC)/dimethyl carbonate (DMC) (LP30, Merck), which was used as electrolyte. The cells were placed in an incubator (Binder) to maintain a constant temperature of 25 ± 0.1 °C or 40 ± 0.1 °C. The electrochemical studies were carried out using an Arbin battery cycling unit.

Results and discussion
Optimization of ball milling conditions
It was shown that a pretreatment of the CF_x precursor directly influences the electrochemical performance of the resulting products [37]. When ball-milled CF_x was used for the reaction, a significant enhancement of the capacity of the cathode material was observed. To compare different ball-milled products of $CF_{1.1}$, the ball milling time of the graphite fluoride was set to 2 h for each sample, at rotation speeds which were 200 rpm, 300 rpm and 400 rpm. After the reaction with iron pentacarbonyl, these samples gave four different cathode materials hereafter named as $C(FeF_2)_{0.55}$, $C(FeF_2)_{0.55}\_200$, $C(FeF_2)_{0.55}\_300$, $C(FeF_2)_{0.55}\_400$ for unmilled $CF_{1.1}$, and $CF_{1.1}$ milled at 200, 300, and 400 rpm, respectively.

Figure 1 shows the cyclic capacity of the $C(FeF_2)_{0.55}$, $C(FeF_2)_{0.55}\_200$, $C(FeF_2)_{0.55}\_300$ and $C(FeF_2)_{0.55}\_400$ samples. The materials were cycled at a current density of 23 mA/g between 1.3 V and 4.3 V. The data reveals a big influence of the ball milling conditions of $CF_{1.1}$ on the cycling behavior of the nanocomposites. The samples with the $CF_{1.1}$ precursor ball-milled at 300 rpm showed the highest capacities
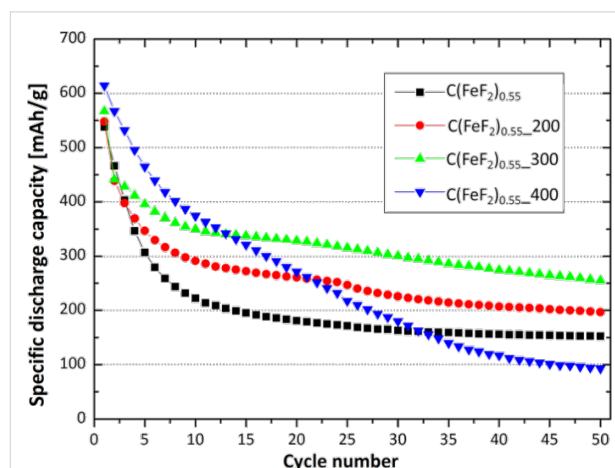

Figure 1: Cycling behavior of $C(FeF_2)_{0.55}$, $C(FeF_2)_{0.55}\_200$, $C(FeF_2)_{0.55}\_300$ and $C(FeF_2)_{0.55}\_400$. The materials were cycled with a current density of 23 mA/g between 1.3 V and 4.3 V.

upon cycling. The first discharge capacity increased with increasing ball milling speed of the used $CF_{1.1}$ precursor. The irreversible capacity loss (ICL) during cycling refers to the amount of capacity which cannot be retained in the following cycle. That means, a low or decreasing ICL is the precondition for a stable cycling of the material. For $C(FeF_2)_{0.55}\_400$ the ICL did not decrease during cycling, which leads to a decreasing cycling stability for this material, even if the first ICL only amounts to 47 mAh/g which is the lowest ICL for all investigated materials. For $C(FeF_2)_{0.55}$, $C(FeF_2)_{0.55}\_200$ and $C(FeF_2)_{0.55}\_300$ the capacity faded much more slowly after the first few cycles, and in the case of $C(FeF_2)_{0.55}\_300$ the capacity after 50 cycles (255 mAh/g) reached the highest value compared to the other materials.

Variation of carbon content

In order to investigate the influence of the carbon content on the electrochemical performance of the nanocomposite, different graphite fluorides ($CF_{0.5}$, $CF_{0.7}$, $CF_{1.0}$ and $CF_{1.1}$) were used as precursors. The materials were ball-milled at 300 rpm for 2 h as this was the best milling condition we could find with respect to the electrochemical performance. Other milling conditions were tested for all materials, but the obtained products showed the best cycling stability and specific capacity when ball-milled with 300 rpm. The ball-milled precursor was used to react with

a stoichiometric amount of $Fe(CO)_5$ at 250 °C for 24 h. The resulting products were named as $C(FeF_2)_{0.25}\_300$, $C(FeF_2)_{0.35}\_300$, $C(FeF_2)_{0.5}\_300$ and $C(FeF_2)_{0.55}\_300$, for $CF_{0.5}$, $CF_{0.7}$, $CF_{1.0}$ and $CF_{1.1}$ respectively. The calculated quantity of active material and carbon in each nanocomposite is presented in Table 1.

The X-ray diffraction patterns of the nanocomposites are shown in Figure 2a. All nanocomposites show diffraction peaks that correspond to the FeF_2 rutile structure. However, differences between the patterns can be noticed in the region around 20°. The XRD pattern of $C(FeF_2)_{0.25}\_300$ shows an increased intensity of the (210) peak and some additional peaks with lower intensities between 19° and 21°, which result from a graphitic type of carbon. The increase in intensity of the FeF_2(210) peak is the result of an overlapping FeF_2(210) signal, a graphite signal and different iron carbide signals. In the XRD patterns of nanocomposites synthesized from higher fluorinated CF_x, the graphite signal and the iron carbide signals decrease, which correspondingly leads to a decreased intensity at the FeF_2(210) peak. A change of the intensity ratio of the first two FeF_2 peaks ((110)/(101)) can be noticed as well. It is decreasing for materials with a higher content x of fluorine. Due to the overlap of the FeF_2(110) and the graphite peak, the signal at 12.2° has a higher intensity for composites with increasingly crystalline

Table 1: Graphite fluoride precursors and composition of the respective products.

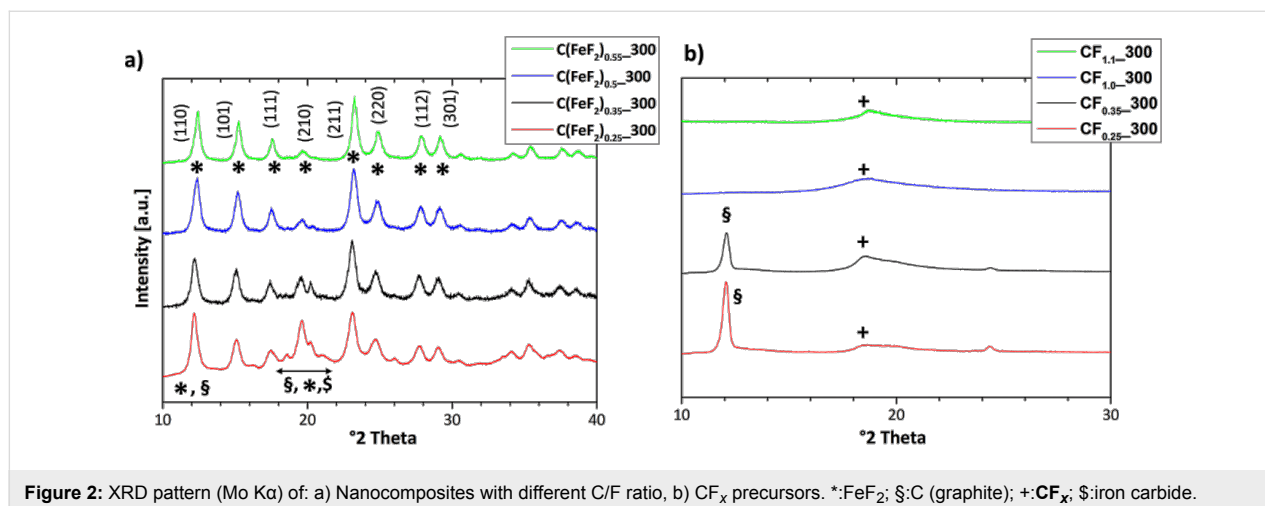| used graphite fluoride precursor	FeF_2 wt % in product	C wt % in product	designation of the related product
$CF_{0.5}\_300$	61	39	$C(FeF_2)_{0.25}\_300$
$CF_{0.7}\_300$	73	27	$C(FeF_2)_{0.35}\_300$
$CF_{1.0}\_300$	80	20	$C(FeF_2)_{0.5}\_300$
$CF_{1.1}\_300$	81	19	$C(FeF_2)_{0.55}\_300$

Figure 2: XRD pattern (Mo Kα) of: a) Nanocomposites with different C/F ratio, b) CF_x precursors. *:FeF_2; §:C (graphite); +:$\mathbf{CF_x}$; $:iron carbide.

graphitic domains, which leads to a higher ratio between the first two peaks. Hence, the ordered graphitic domains in the nanocomposites seem to decrease for higher x in the used CF_x precursors.

CF_x precursors with different x show different structures and types of bonding. Lower fluorinated graphite fluorides (lower x) lead to compounds, which contain carbon that is more graphitic in nature [40]. This tendency can also be seen in Figure 2b, in which XRD patterns (Mo Kα) are shown of the different types of CF_x. The data indicate that the structure of the CF_x precursors directly influences the nature of carbon in the synthesized nanocomposites.

The variation of the carbon structure in the nanocomposites was further investigated by Raman spectroscopy. Figure 3a shows the Raman spectra of the different nanocomposites, and Figure 3b shows the results of an analysis of the spectra. The position and the ratio of the D and G mode ($I(D)/I(G)$) in a Raman spectrum of carbon characterizes the structure and the order of the investigated carbon [41]. Ferrari et al. reported a model to characterize and classify different carbon structures [42,43]. According to this model two different types of carbon are present. Graphite shows a G-mode position of about 1580 cm^{-1} and a $I(D)/I(G)$ ratio of 0.25. Nanocrystalline graphite exhibits a G-mode position of about 1600 cm^{-1} and an increased $I(D)/I(G)$ ratio. For C(FeF$_2$)$_{0.25}$_300, a G-mode position of 1589 cm^{-1} and a $I(D)/I(G)$ ratio of 1.94 can be noticed. Thus, the nature of carbon in C(FeF$_2$)$_{0.25}$_300 does not fully match with the bulk graphite characteristics. The properties are shifted towards those of nanocrystalline graphite. With a G-mode position of 1595 cm^{-1} and a $I(D)/I(G)$ ratio of 2.36 the spectra of C(FeF$_2$)$_{0.35}$_300 matches with the description of nanocrystalline graphite. For C(FeF$_2$)$_{0.5}$_300 the same G-mode position was measured, but the $I(D)/I(G)$ ratio decreased to

1.73. During a transition from nanocrystalline graphite to amorphous carbon the VDOS (vibrational density of states) of graphite changes, the D-mode intensity decreases and the G mode retains its intensity, which results in a decreased $I(D)/I(G)$ ratio [42]. This tendency is continued with a further decrease of the $I(D)/I(G)$ ratio (1.63) for C(FeF$_2$)$_{0.55}$_300 which, in addition, shows a downshift of the G position to 1589 cm^{-1}.

In addition, EEL spectroscopy was performed to further elucidate on the carbon structure. The EEL spectra confirmed the data previously obtained with Raman spectroscopy about the characteristics of the carbon structure. The loss of the distinct sharp structure in the energy-loss near edge structure (ELNES) of the C K-edge (Figure 4) signifies a reduced order of the graphitic carbon matrix [44-46]. At the same time, the peaks, resulting from the transition of the electrons from the π to the π* or σ* band, increase for the products prepared with precursors with a lower C/F ratio. These peaks indicate the presence of a conjugated π system. That means, the choice of the CF_x precursor before the reaction with Fe(CO)$_5$ will determine the graphitic character of the carbon matrix.

The EEL spectra from the F K-edge, Fe L3-edge and Fe L2-edge (Figure 5) showed no difference between the various samples prepared with different CF_x precursors and are in good agreement with FeF$_2$ [47,48]. (See Supporting Information File 1 for L3/L2 intensity ratio data)

TEM and SAED measurements were made to investigate the microstructure and morphology of the nanocomposites.

Figure 6 shows TEM and SAED pictures of the nanocomposites. The material consists of graphitic carbon with embedded FeF$_2$ nanoparticles. Figure 6 a–c show images of the composites C(FeF$_2$)$_{0.5}$_300, C(FeF$_2$)$_{0.35}$_300 and C(FeF$_2$)$_{0.25}$_300, res-
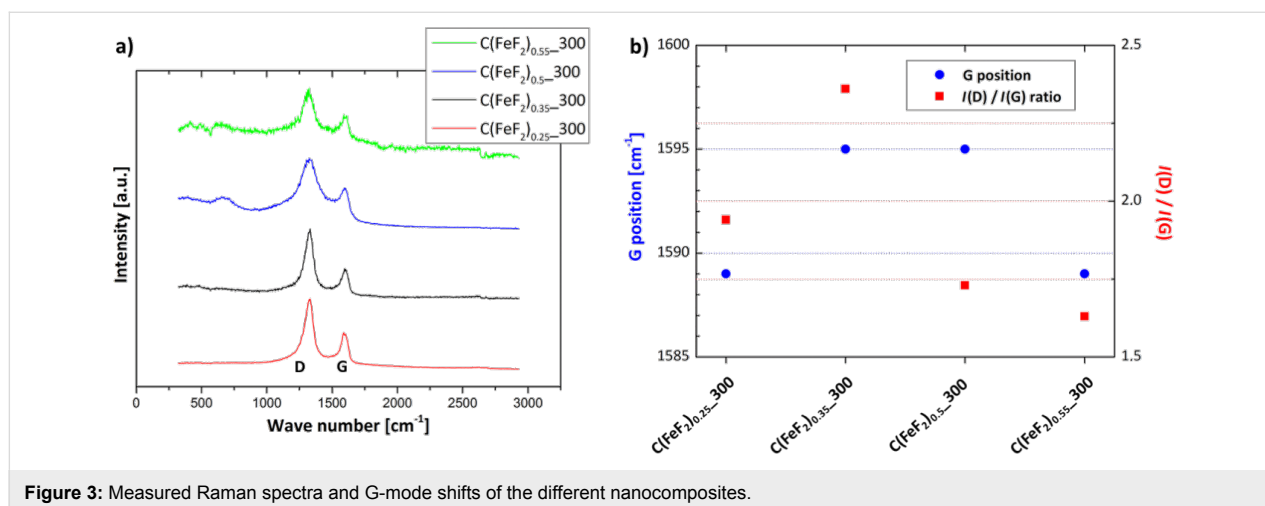

Figure 3: Measured Raman spectra and G-mode shifts of the different nanocomposites.

Figure 4: C K-edge EEL spectra of compounds with different carbon contents.

Figure 5: EEL spectra of $C(FeF_2)_{0.25}$_300. The spectrum shows the F K-edge and the Fe L3- and Fe L2-edges.

Figure 6: TEM and SAED pictures of a) $C(FeF_2)_{0.5}$_300, b) $C(FeF_2)_{0.35}$_300, c) $C(FeF_2)_{0.25}$_300 and d) one complete particle with SAED pattern of $C(FeF_2)_{0.25}$_300.

pectively. In comparison, in the $C(FeF_2)_{0.5}$_300 system, the FeF_2 particles are packed most densely. The FeF_2 particles in the $C(FeF_2)_{0.25}$_300 system have smaller diameters, mostly below 5 nm, and are more dispersed by the graphitic layers, which can be because of the higher atomic percentage of carbon. While the FeF_2 particle size increases slightly from $C(FeF_2)_{0.25}$_300 over $C(FeF_2)_{0.35}$_300 to $C(FeF_2)_{0.5}$_300 (below 5 nm at $C(FeF_2)_{0.25}$_300 to around 9 nm at $C(FeF_2)_{0.5}$_300) no visible size-changing effects between $C(FeF_2)_{0.5}$_300 and $C(FeF_2)_{0.55}$_300 could be found. Despite the absence of a change in the particle sizes the electrochemical behavior during cycling is very different between those samples. Therefore we attribute the different electrochemical behavior in all samples to the structural change of the carbon matrix and not to an effect which solely comes from the different FeF_2 particle size. The graphitic nature of the carbon was evident also in the SAED data. As can be seen in Figure 6d, a highly ordered crystalline structure of graphitic carbon, clearly indicated by the hexagonally arranged spots in the SAED, is shown, when the SAED pattern was taken from the particle surface. The diffraction rings in the picture can be assigned to the FeF_2 rutile structure.

In galvanostatic measurements, the nanocomposites were cycled at different temperatures with a current density of 25 mA/g between 1.3 V and 4.3 V (Figure 7). $C(FeF_2)_{0.5}$_300 showed the highest capacity and lowest ICL after a few cycles, which led to a high stability of the capacity for the first 40/30 cycles at 25/40 °C. At 40 °C no convergence to a stable capacity value was observed, instead the capacity faded almost linearly. The first discharge capacities also reached their maximum with $C(FeF_2)_{0.5}$_300 as cathode material, and faded for higher or lower contents of active material. The first discharge capacity of $C(FeF_2)_{0.5}$_300 at 40 °C reached a value of 635 mAh/g, which is beyond the theoretical value of an $FeF_2/$
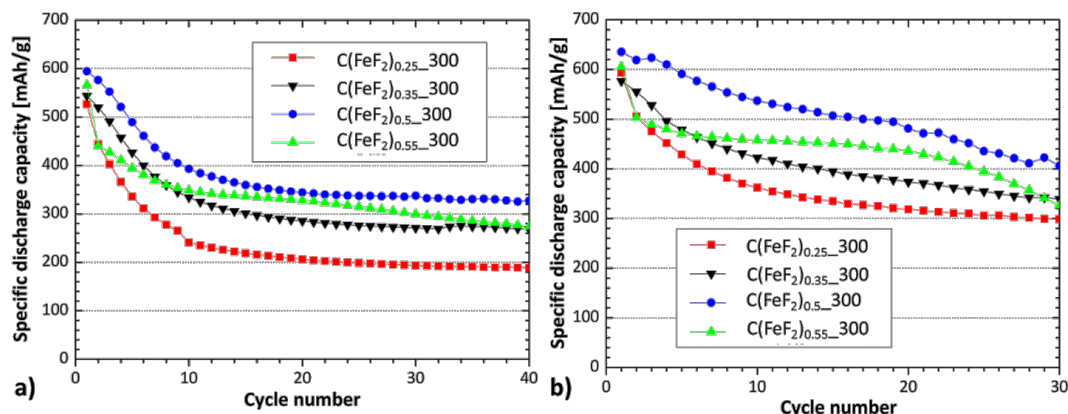
Figure 7: Discharge capacities at: a) 25 °C, b) 40 °C. The samples were cycled with a current density of 25 mA/g.

Li conversion system (571 mAh/g). This overcapacity is the consequence of an electrochemical reaction between unreacted $CF_{1.0}\_300$ and Li^+. Graphite fluoride is known to react with lithium to carbon and lithium fluoride between 2.0 V and 3.0 V [49]. This reaction can be seen in the discharge profile of the material (Figure 8). If the capacity that we attribute to the reac-

tion of graphite fluoride with lithium is subtracted from the first discharge capacity of 635 mAh/g, a capacity value is obtained that almost coincides with the theoretical value of the synthesized FeF_2. The discharge capacity which can be related to the reaction of CF_x, is indicated by a slope at the beginning of the first discharge cycle at the discharge profiles (Figure 8).

Figure 8: Charge/discharge profiles for the first 20 cycles of the nanocomposites at 25 °C. The samples were cycled with a current density of 25 mA/g.

Figure 9: Long time cycling of C(FeF$_2$)$_{0.25}$_300. a) Specific discharge capacity at different temperatures, b) Charge/discharge profile. The samples were cycled with a current density of 25 mA/g.

Cells with C(FeF$_2$)$_{0.5}$_300 as cathode material showed the highest capacity, but were lacking in cyclic stability. This capacity behavior was observed for the nanocomposites, which contain a more amorphous type of carbon (C(FeF$_2$)$_{0.5}$_300, C(FeF$_2$)$_{0.55}$_300). Contrary to that, the cyclic stability increased for nanocomposites with a higher graphitic carbon content and for lower temperatures (C(FeF$_2$)$_{0.25}$_300, C(FeF$_2$)$_{0.35}$_300). Figure 7 clearly shows that, in general, a higher working temperature increased the capacity but affected the cyclic stability of the test cells. Cells built with C(FeF$_2$)$_{0.25}$_300 as cathode material proved to be the most stable systems for long time measurements. Figure 9 shows the cells cycled at 25 °C and 40 °C for 200 cycles. The residence time of the electrode material in such a cell was around 80 days.

Conclusion

In conclusion, studies regarding the pretreatment and the C/F ratio of the CF$_x$ precursors for carbon–FeF$_2$ nanocomposites for reversible lithium storage as well as with respect to the electrochemical performance and the carbon structure of these nanocomposites were performed. The main reaction and processes during the first and the subsequent cycles were elucidated.

We have optimized the pretreatment and the C/F ratio of the CF$_x$ precursor. Galvanostatic tests of nanocomposites with a more amorphous type of carbon matrix (CF$_{1.1}$; 300 rpm ball-milling speed; 40 °C) showed a capacity of 436 mAh/g after 25 cycles while the nanocomposites with a more graphitic matrix (CF$_{0.5}$; 300 rpm ball-milling speed; 25 °C) showed a stable capacity between 150 mAh/g and 200 mAh/g for more than 150 cycles. The structure of the conducting carbon matrix seems to have a great influence on the electrochemical behavior. Raman measurements showed a transition from graphitic carbon, over nanocrystalline graphite to a more amorphous type of graphitic

carbon for the nanocomposites synthesized with different compositions CF$_x$. A higher graphitic character of the carbon matrix was found for materials produced with CF$_x$ precursors with of a lower F/C ratio). These results were confirmed by EELS and SAED measurements.

Supporting Information

Supporting Information File 1
Detailed experimental data.
[http://www.beilstein-journals.org/bjnano/content/
supplementary/2190-4286-4-80-S1.pdf]

References

1. Tarascon, J. M.; Armand, M. *Nature* **2001,** *414,* 359–367.
   doi:10.1038/35104644
2. Whittingham, M. S. *Chem. Rev.* **2004,** *104,* 4271–4301.
   doi:10.1021/cr020731c
3. Armand, M.; Tarascon, J.-M. *Nature* **2008,** *451,* 652–657.
   doi:10.1038/451652a
4. Goodenough, J. B.; Kim, Y. *Chem. Mater.* **2010,** *22,* 587–603.
   doi:10.1021/cm901452z
5. Fichtner, M. *J. Alloys Compd.* **2011,** *509,* S529–S534.
   doi:10.1016/j.jallcom.2010.12.179
6. Mizushima, K.; Jones, P. C.; Wiseman, P. J.; Goodenough, J. B.
   Solid State Ionics **1981,** *4,* 171–174.
   doi:10.1016/0167-2738(81)90077-1
7. Padhi, A. K.; Nanjundaswamy, K. S.; Goodenough, J. B.
   J. Electrochem. Soc. **1997,** *144,* 1188–1194. doi:10.1149/1.1837571
8. Li, H.; Balaya, P.; Maier, J. *J. Electrochem. Soc.* **2004,** *151,*
   A1878–A1885. doi:10.1149/1.1801451
9. Poizot, P.; Laruelle, S.; Grugeon, S.; Dupont, L.; Tarascon, J. M.
   Nature **2000,** *407,* 496–499. doi:10.1038/35035045
10. Laruelle, S.; Grugeon, S.; Poizot, P.; Dolle, M.; Dupont, L.;
    Tarascon, J.-M. *J. Electrochem. Soc.* **2002,** *149,* A627–A634.
    doi:10.1149/1.1467947

11. Pereira, N.; Klein, L. C.; Amatucci, G. G. *J. Electrochem. Soc.* **2002,** *149,* A262–A271. doi:10.1149/1.1446079
12. Arai, H.; Okada, S.; Sakurai, Y.; Yamaki, J. *J. Power Sources* **1996,** *68,* 716–719. doi:10.1016/S0378-7753(96)02580-3
13. Li, H.; Richter, G.; Maier, J. *Adv. Mater.* **2003,** *15,* 736–739. doi:10.1002/adma.200304574
14. Amatucci, G. G.; Pereira, N. *J. Fluorine Chem.* **2007,** *128,* 243–262. doi:10.1016/j.jfluchem.2006.11.016
15. Cabana, J.; Monconduit, L.; Larcher, D.; Palacín, M. R. *Adv. Mater.* **2010,** *22,* E170–E192. doi:10.1002/adma.201000717
16. Fichtner, M. *Phys. Chem. Chem. Phys.* **2011,** *13,* 21186–21195. doi:10.1039/c1cp22547b
17. Badway, F.; Pereira, N.; Cosandey, F.; Amatucci, G. G. *J. Electrochem. Soc.* **2003,** *150,* A1209–A1218. doi:10.1149/1.1596162
18. Plitz, I.; Badway, F.; Al-Sharab, J.; DuPasquier, A.; Cosandey, F.; Amatucci, G. G. *J. Electrochem. Soc.* **2005,** *152,* A307–A315. doi:10.1149/1.1842035
19. Amatucci, G. G.; Pereira, N.; Badway, F.; Sina, M.; Cosandey, F.; Ruotolo, M.; Cao, C. *J. Fluorine Chem.* **2011,** *132,* 1086–1094. doi:10.1016/j.jfluchem.2011.06.033
20. Liu, P.; Vajo, J. J.; Wang, J. S.; Li, W.; Liu, J. *J. Phys. Chem. C* **2012,** *116,* 6467–6473. doi:10.1021/jp211927g
21. Wang, F.; Robert, R.; Chernova, N. A.; Pereira, N.; Omenya, F.; Badway, F.; Hua, X.; Ruotolo, M.; Zhang, R.; Wu, L.; Volkov, V.; Su, D.; Key, B.; Whittingham, M. S.; Grey, C. P.; Amatucci, G. G.; Zhu, Y.; Graetz, J. *J. Am. Chem. Soc.* **2011,** *133,* 18828–18836. doi:10.1021/ja206268a
22. Li, C.; Gu, L.; Tsukimoto, S.; Van Aken, P. A.; Maier, J. *Adv. Mater.* **2010,** *22,* 3650–3654. doi:10.1002/adma.201000535
23. Li, T.; Li, L.; Cao, Y. L.; Ai, X. P.; Yang, H. X. *J. Phys. Chem. C* **2010,** *114,* 3190–3195. doi:10.1021/jp908741d
24. Basa, A.; Gonzalo, E.; Kuhn, A.; García-Alvarado, F. *J. Power Sources* **2012,** *197,* 260–266. doi:10.1016/j.jpowsour.2011.09.048
25. Gonzalo, E.; Kuhn, A. *J. Power Sources* **2010,** *195,* 4990–4996. doi:10.1016/j.jpowsour.2010.02.040
26. Liao, P.; Li, J.; Dahn, J. R. *J. Electrochem. Soc.* **2010,** *157,* A355–A361. doi:10.1149/1.3294788
27. Wu, W.; Wang, Y.; Wang, X.; Chen, Q.; Wang, X.; Yang, S.; Liu, X.; Guo, J.; Yang, Z. *J. Alloys Compd.* **2009,** *486,* 93–96. doi:10.1016/j.jallcom.2009.07.063
28. Wu, W.; Wang, X.; Wang, X.; Yang, S.; Liu, X.; Chen, Q. *Mater. Lett.* **2009,** *63,* 1788–1790. doi:10.1016/j.matlet.2009.05.041
29. Yamakawa, N.; Jiang, M.; Key, B.; Grey, C. P. *J. Am. Chem. Soc.* **2009,** *131,* 10525–10536. doi:10.1021/ja902639w
30. Doe, R. E.; Persson, K. A.; Meng, Y. S.; Ceder, G. *Chem. Mater.* **2008,** *20,* 5274–5283. doi:10.1021/cm801105p
31. Liao, P.; Macdonald, B. L.; Dunlap, R. A.; Dahn, J. R. *Chem. Mater.* **2008,** *20,* 454–461. doi:10.1021/cm702656k
32. Pereira, N.; Badway, F.; Wartelsky, M.; Gunn, S.; Amatucci, G. G. *J. Electrochem. Soc.* **2009,** *156,* A407–A416. doi:10.1149/1.3106132
33. Gocheva, I. D.; Tanaka, I.; Doi, T.; Okada, S.; Yamaki, J. *Electrochem. Commun.* **2009,** *11,* 1583–1585. doi:10.1016/j.elecom.2009.06.001
34. Prakash, R.; Wall, C.; Mishra, A. K.; Kübel, C.; Ghafari, M.; Hahn, H.; Fichtner, M. *J. Power Sources* **2011,** *196,* 5936–5944. doi:10.1016/j.jpowsour.2011.03.007
35. Prakash, R.; Mishra, A. K.; Roth, A.; Kübel, C.; Scherer, T.; Ghafari, M.; Hahn, H.; Fichtner, M. *J. Mater. Chem.* **2010,** *20,* 1871–1876. doi:10.1039/b919097j
36. Wall, C.; Prakash, R.; Kübel, C.; Hahn, H.; Fichtner, M. *J. Alloys Compd.* **2012,** *530,* 121–126. doi:10.1016/j.jallcom.2012.03.080
37. Reddy, M. A.; Breitung, B.; Chakravadhanula, V. S. K.; Wall, C.; Engel, M.; Kübel, C.; Powell, A. K.; Hahn, H.; Fichtner, M. *Adv. Energy Mater.* **2013,** *3,* 308–313. doi:10.1002/aenm.201200788
38. Barkley, T. K.; Vastano, J. E.; Applegate, J. R.; Bakrania, S. D. *Adv. Mater. Sci. Eng.* **2012,** *2012,* No. 685754. doi:10.1155/2012/685754
39. Liu, X.-Y.; Huang, B.-C.; Coville, N. J. *Carbon* **2002,** *40,* 2791–2799. doi:10.1016/S0008-6223(02)00193-8
40. Sato, Y.; Itoh, K.; Hagiwara, R.; Fukunaga, T.; Ito, Y. *Carbon* **2004,** *42,* 2897–2903. doi:10.1016/j.carbon.2004.06.042
41. Tuinstra, F.; Koenig, J. L. *J. Chem. Phys.* **1970,** *53,* 1126–1130. doi:10.1063/1.1674108
42. Ferrari, A.; Robertson, J. *Phys. Rev. B* **2000,** *61,* 14095–14107. doi:10.1103/PhysRevB.61.14095
43. Ferrari, A. C. *Solid State Commun.* **2007,** *143,* 47–57. doi:10.1016/j.ssc.2007.03.052
44. Kushita, K. N.; Hojou, K. *Ultramicroscopy* **1991,** *35,* 289–293. doi:10.1016/0304-3991(91)90081-G
45. Papagno, L.; Caputi, L. S. *Surf. Sci.* **1983,** *125,* 530–538. doi:10.1016/0039-6028(83)90583-6
46. Koma, A.; Miki, K. *Appl. Phys. A* **1984,** *34,* 35–39. doi:10.1007/BF00617572
47. El-Barbary, A. A.; Trasobares, S.; Ewels, C. P.; Stephan, O.; Okotrub, A. V.; Bulusheva, L. G.; Fall, C. J.; Heggie, M. I. *J. Phys.: Conf. Ser.* **2006,** *26,* 149–152. doi:10.1088/1742-6596/26/1/035
48. Cosandey, F.; Al-Sharab, J. F.; Badway, F.; Amatucci, G. G.; Stadelmann, P. *Microsc. Microanal.* **2007,** *13,* 87–95. doi:10.1017/S1431927607070183
49. Li, Y.; Chen, Y.; Feng, W.; Ding, F.; Liu, X. *J. Power Sources* **2011,** *196,* 2246–2250. doi:10.1016/j.jpowsour.2010.10.005

Lithium peroxide crystal clusters as a natural growth feature of discharge products in Li–O$_2$ cells

Tatiana K. Zakharchenko[‡1], Anna Y. Kozmenkova[‡1], Daniil M. Itkis[*1,2] and Eugene A. Goodilin[1,2]

Abstract

The often observed and still unexplained phenomenon of the growth of lithium peroxide crystal clusters during the discharge of Li–O$_2$ cells is likely to happen because of self-assembling Li$_2$O$_2$ platelets that nucleate homogeneously right after the intermediate formation of superoxide ions by a single-electron oxygen reduction reaction (ORR). This feature limits the rechargeability of Li–O$_2$ cells, but at the same time it can be beneficial for both capacity improvement and gain in recharge rate if a proper liquid phase mediator can be found.

Findings

The idea to utilize oxygen as an oxidizer in rechargeable batteries has been kept in mind for a long time because of the easy availability of O$_2$ in ambient air. Alkali metal negative electrodes were always attractive for metal–oxygen (metal–air) batteries as they show record parameters, which originate from the remarkably negative standard electrode potentials. Such cells have already been designed with lithium [1] or sodium [2] anodes and aprotic electrolytes. Unfortunately the practical specific energies are too far from theoretical values and, at the moment, the application of alkali-metal–air rechargeable batteries is impossible because of the very limited cycle life, which primarily arises from the low chemical stability of the

electrolytes [3] and the carbon positive electrodes [4]. The oyxgen reduction reaction, which occurs in the cathodes during the discharge of the batteries, leads to the formation of super-oxide anions O$_2^-$ that can survive in some aprotic solvents for a certain time [5] and participate in various side reactions. In the case of sodium–oxygen cells superoxide quickly associates with Na$^+$ ions and forms well-facetted cubic sodium superoxide (NaO$_2$) crystals, which are insoluble in the electrolytes and precipitate onto the electrode [2]. The situation is different for lithium–oxygen cells [6-8], in which LiO$_2$ cannot be formed, because it does not exist as a bulk phase at room temperature [9,10]. Instead, all the intermediates have to transform into

lithium peroxide (Li_2O_2) [11], which always demonstrates a very complex morphology [12] revealing sphere-, torroid- or rozette-like aggregates of plate-like particles. This repeated observation evidences a complex formation mechanism of lithium peroxide.

Here we report a new study of Li_2O_2 crystals growth upon the discharge of aprotic lithium–oxygen cells. We show that lithium peroxide plate-like crystals are likely to be formed in the liquid electrolyte phase rather than directly on the electrode surface. Li_2O_2 particles aggregate to produce finally submicron crystal clusters with different morphologies. To perform all the experiments, we utilized porous gold electrodes with an enhanced surface area and high stability with respect to all redox processes and interaction with peroxide and superoxide species (see Supporting Information File 1 for details). The porous gold electrodes that were utilized as the model electrodes (Figure 1a) were prepared from gold–silver alloy foils (see Supporting Information File 1 for experimental details). The mean pore size was estimated to be about 200 nm (see Figure S1 in Supporting Information File 1). This allowed us to observe changes in the morphology of lithium peroxide that are caused by the varying electrochemical experiment conditions. No side processes were expected for the chosen electrodes [13].

The galvanostatic discharge of the cells with such electrodes at different current densities (Figure 1b) in an oxygen-saturated 1 M solution of LiTFSI in dry DMSO resulted in the deposition of a porous Li_2O_2 layer on the gold surface (Figure 2a,b). The band at 790 cm^{-1} in the Raman spectra of the electrodes after the discharge (Figure 2c) is attributed to O–O stretch vibrations of lithium peroxide [14]. One of the most important experi-

mental conditions is the product generation rate that is being controlled predominantly by the discharge current density. Actually, this parameter determines a supersaturation level, which is required for nucleation and growth of solid phases. We found that the discharge at a lower current density (50 μA/cm^2) results in more dense Li_2O_2 films composed of small building blocks (Figure 2a) while separate stacks of Li_2O_2 plate-like crystals grew on the electrode operated at 200 μA/cm^2 (Figure 2b). The total amount of product formed on the electrodes is higher for low current density, which is in agreement with the area-specific capacities of the cathodes (Figure 1b). Both Li_2O_2 film and stacks comprise thin lithium peroxide plates with a diameter varing from 100 to 300 nm that corresponds to previously published data [15]. A typical TEM image of such platelets is presented in Figure 2d, their size of 30–50 nm seems to be natural for as-generated nuclei (embryo crystals) rather than for normally grown anisotropic crystals. The plate-like shape of the crystals can be expected as it is predicted by the Wulff rule [14,15].

The observation of the same building blocks that compose the complex morphologies of Li_2O_2 obtained in different electrochemical experiments allows to assume that the formation occurs more or less independently from the generation rate of superoxide ions. In the case of a heterogeneous nucleation of platelets on the surface of the gold electrode, a higher discharge current, and thus a higher concentration of the species being crystallized, would result in a denser layer of lithium peroxide, which is, obviously, opposite to our findings (Figure 1a,b). It seems plausible that the lithium peroxide forms aside of the electrode surface which plays the role of a generator for precursors that are subsequently converted to Li_2O_2.
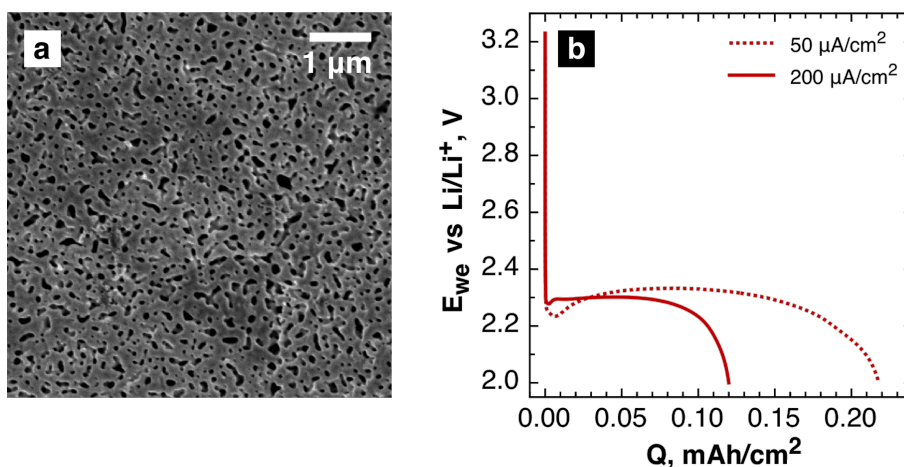

Figure 1: (a) Typical SEM image of the pristine porous gold electrodes. (b) Discharge voltage profiles recorded in a galvanostatic regime at current densities of 50 μA/cm^2 and 200 μA/cm^2.

Figure 2: SEM images of the porous gold electrode discharged at 50 µA/cm^2 (a) and 200 µA/cm^2 (b). (c) Raman spectra of the pristine and discharged electrodes. (d) TEM image of the porous gold electrode after discharge. Li$_2$O$_2$ plate edges are deformed by the electron beam.

To find out the most probable way for the generation of such building blocks, we performed a simple experiment purely based on the chemical generation of lithium peroxide in the ion exchange reaction $KO_2 + Li^+ \rightarrow K^+ + \frac{1}{2} Li_2O_2 + \frac{1}{2} O_2$.

Figure 3a demonstrates evidently that the morphology of lithium peroxide precipitated after the chemical reaction of KO$_2$ with Li$^+$ ions is quite similar to that of lithium peroxide produced in Li–O$_2$ cells (Figure 2). In the former case the
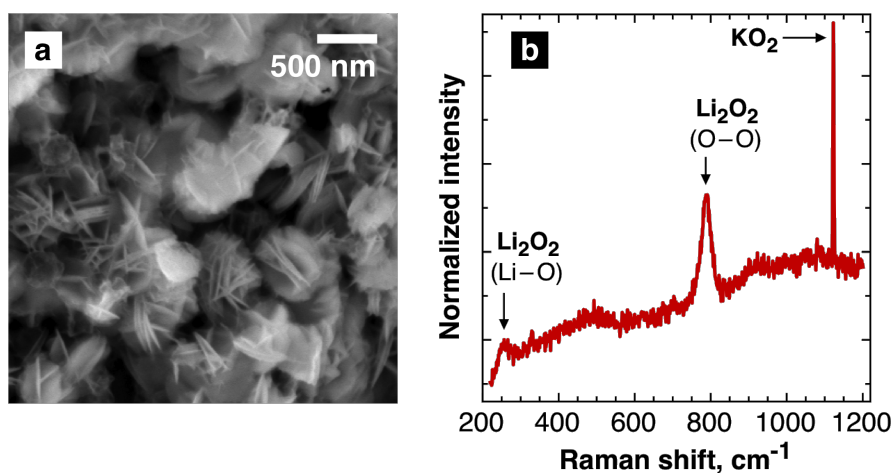

Figure 3: (a) SEM image of the Li$_2$O$_2$ precipitate obtained by the chemical reaction of KO$_2$ with a solution of LiTFSI. (b) Raman spectra of the precipitate.

precipitate, which was found to contain Li_2O_2 and residual KO_2 (Figure 3b), exhibited similar crystal clusters composed of thin platelets. This finding suggests that lithium peroxide particles can be formed right upon the formation of superoxide anions without the influence of the surface of the electrode. After being produced by either the electrochemical ORR or the chemical reaction with KO_2, the superoxide anions associate with Li^+ which leads to the unstable intermediate that is further converted to Li_2O_2. The growth of the lithium peroxide plate-like crystals and their further assembly can already occur in the liquid electrolyte.

Scheme 1 illustrates the suggested mechanism of the deposit growth during discharge. At first, molecular oxygen that is dissolved in the electrolyte is reduced to superoxide ions, $O_2 + e \rightarrow O_2^-$. These superoxide ions, which carry a negative charge, move away from the electrode surface driven by diffusion [16]. The subsequent disproportionation into a peroxide ion and oxygen, probably by intermolecular collisions as a rate limiting step, $O_2^- + O_2^- \rightarrow O_2^{2-} + O_2$, results in the generation of lithium peroxide that quickly exceeds a solubility threshold, which was estimated to be about 2.5 mM by (see Figure S3 in Supporting Information File 1). This means that the nucleation proceeds homogeneously and the phase formation is exhausted by the nucleation stage only without an intensive crystal growth because of the relatively high supersaturation that appeared as a result of the fast electrochemical generation of O_2^-. After that stage, Li_2O_2 platelets seem to be formed as observed recently for carbon electrodes [12]. The generated pristine platelets produce a colloidal system under the conditions of their continuous homogeneous nucleation. Most of the layered colloidal systems tend to aggregate if no sufficient electrostatic or steric stabilization is provided. In the particular case of lithium peroxide platelets, they gradually produce submicron crystal clusters with complex morphology.

Thus this study indicates that Li_2O_2 crystal clusters are deposited onto the electrode. This layer, however, remains porous, which allows a further mass transport between the electrode and the electrolyte. These deposits can then lose their electric contact with the electrode and thus additionally limit the rechargeablity of the Li–O_2 cell. On the other hand, the special morphology of Li_2O_2 provides a larger surface compared to well-facetted crystals or uniform films that might allow a faster recharge. This idea becomes highly interesting in view of recent findings of Chen et al. [17] who suggested a liquid phase mediator. Further work on this topic is in progress.

Supporting Information
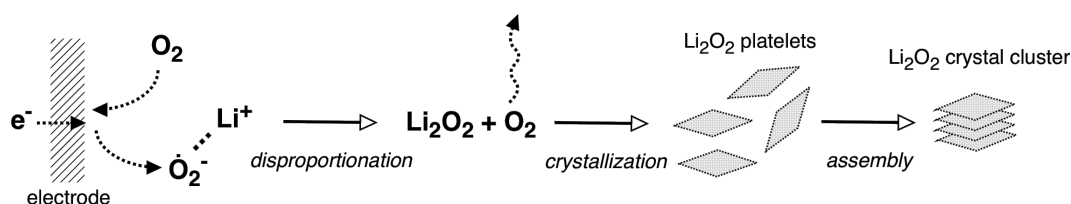
Supporting Information File 1
Experimental details.
[http://www.beilstein-journals.org/bjnano/content/supplementary/2190-4286-4-86-S1.pdf]

References

1. Abraham, K. M.; Jiang, Z. *J. Electrochem. Soc.* **1996,** *143,* 1–5. doi:10.1149/1.1836378
2. Hartmann, P.; Bender, C. L.; Vračar, M.; Dürr, A. K.; Garsuch, A.; Janek, J.; Adelhelm, P. *Nat. Mater.* **2013,** *12,* 228–232. doi:10.1038/nmat3486
3. Freunberger, S. A.; Chen, Y.; Peng, Z.; Griffin, J. M.; Hardwick, L. J.; Bardé, F.; Novák, P.; Bruce, P. G. *J. Am. Chem. Soc.* **2011,** *133,* 8040–8047. doi:10.1021/ja2021747
4. Itkis, D. M.; Semenenko, D. A.; Kataev, E. Yu.; Belova, A. I.; Neudachina, V. S.; Sirotina, A. P.; Hävecker, M.; Teschner, D.; Knop-Gericke, A.; Dudin, P.; Barinov, A.; Goodilin, E. A.; Shao-Horn, Y.; Yashina, L. V. *Nano Lett.* **2013,** *13,* 4697–4701. doi:10.1021/nl4021649
5. Laoire, C. O.; Mukerjee, S.; Abraham, K. M.; Plichta, E. J.; Hendrickson, M. A. *J. Phys. Chem. C* **2010,** *114,* 9178–9186. doi:10.1021/jp102019y
6. Lu, Y.-C.; Gallant, B. M.; Kwabi, D. G.; Harding, J. R.; Mitchell, R. R.; Whittingham, M. S.; Shao-Horn, Y. *Energy Environ. Sci.* **2013,** *6,* 750–768. doi:10.1039/C3EE23966G
7. Christensen, J.; Albertus, P.; Sánchez-Carrera, R. S.; Lohmann, T.; Kozinsky, B.; Liedtke, R.; Ahmed, J.; Kojic, A. *J. Electrochem. Soc.* **2012,** *159,* R1–R30. doi:10.1149/2.086202jes

Scheme 1: The suggested scheme for the formation of the Li_2O_2 precipitate during the discharge of a Li–O_2 cell.

8. Girishkumar, G.; McCloskey, B.; Luntz, A. C.; Swanson, S.; Wilcke, W. *J. Phys. Chem. Lett.* **2010,** *1,* 2193–2203. doi:10.1021/jz1005384

9. Lau, K. C.; Curtiss, L. A.; Greeley, J. *J. Phys. Chem. C* **2011,** *115,* 23625–23633. doi:10.1021/jp206796h

10. Bryantsev, V. S.; Blanco, M.; Faglioni, F. *J. Phys. Chem. A* **2010,** *114,* 8165–8169. doi:10.1021/jp1047584

11. Peng, Z.; Freunberger, S. A.; Hardwick, L. J.; Chen, Y.; Giordani, V.; Bardé, F.; Novak, P.; Graham, D.; Tarascon, J.-M.; Bruce, P. G. *Angew. Chem., Int. Ed.* **2011,** *50,* 6351–6355. doi:10.1002/anie.201100879

12. Mitchell, R. R.; Gallant, B. M.; Shao-Horn, Y.; Thompson, C. V. *J. Phys. Chem. Lett.* **2013,** *4,* 1060–1064. doi:10.1021/jz4003586

13. Peng, Z.; Freunberger, S. A.; Chen, Y.; Bruce, P. G. *Science* **2012,** *337,* 563–566. doi:10.1126/science.1223985

14. Radin, M. D.; Tian, F.; Siegel, D. J. *J. Mater. Sci.* **2012,** *47,* 7564–7570. doi:10.1007/s10853-012-6552-6

15. Mo, Y.; Ong, S. P.; Ceder, G. *Phys. Rev. B* **2011,** *84,* 205446. doi:10.1103/PhysRevB.84.205446

16. Herranz, J.; Garsuch, A.; Gasteiger, H. A. *J. Phys. Chem. C* **2012,** *116,* 19084–19094. doi:10.1021/jp304277z

17. Chen, Y.; Freunberger, S. A.; Peng, Z.; Fontaine, O.; Bruce, P. G. *Nat. Chem.* **2013,** *5,* 489–494. doi:10.1038/NCHEM.1646

License and Terms

Synthesis and electrochemical performance of $Li_2Co_{1−x}M_xPO_4F$ (M = Fe, Mn) cathode materials

Nellie R. Khasanova[*], Oleg A. Drozhzhin, Stanislav S. Fedotov,
Darya A. Storozhilova, Rodion V. Panin and Evgeny V. Antipov

Abstract

In the search for high-energy materials, novel 3D-fluorophosphates, $Li_2Co_{1−x}Fe_xPO_4F$ and $Li_2Co_{1−x}Mn_xPO_4F$, have been synthesized. X-ray diffraction and scanning electron microscopy have been applied to analyze the structural and morphological features of the prepared materials. Both systems, $Li_2Co_{1−x}Fe_xPO_4F$ and $Li_2Co_{1−x}Mn_xPO_4F$, exhibited narrow ranges of solid solutions: $x \leq 0.3$ and $x \leq 0.1$, respectively. The $Li_2Co_{0.9}Mn_{0.1}PO_4F$ material demonstrated a reversible electrochemical performance with an initial discharge capacity of 75 mA·h·g^{-1} (current rate of C/5) upon cycling between 2.5 and 5.5 V in 1 M $LiBF_4$/TMS electrolyte. Galvanostatic measurements along with cyclic voltammetry supported a single-phase de/intercalation mechanism in the $Li_2Co_{0.9}Mn_{0.1}PO_4F$ material.
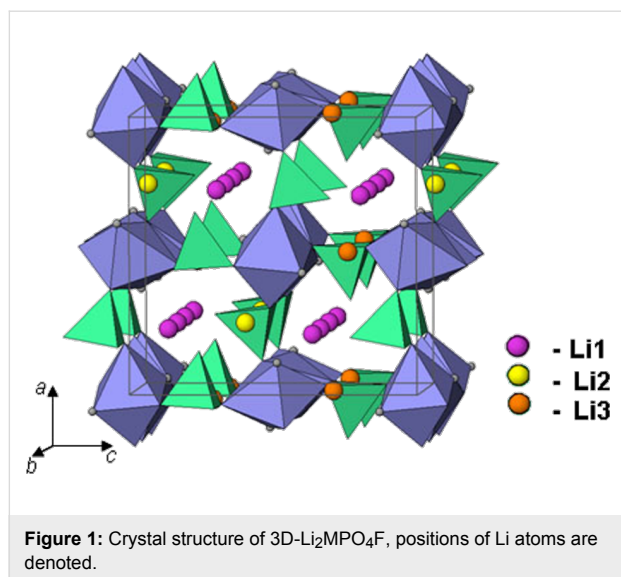
Introduction

In recent years the range of application of Li-ion batteries has been expanded from small-sized portable electronics to large-scale electric vehicles and stationary energy storage systems. Large-scale energy applications require batteries that are economically efficient, highly safe and that provide a high energy and power density. Today most of the cells in use have almost reached their intrinsic limits, and no significant improvements are expected. Therefore, current research in this field is directed towards the development of new high-performance ma-

terials. The specific energy of Li-ion batteries can be enhanced by applying cathode materials that operate at high voltages, and/or by increasing the specific capacity with materials that could cycle more than one Li atom per active transition metal atom. In this respect, fluorophosphates of the general formula A_2MPO_4F seem to be very attractive since they are expected to exhibit a high operating potential because of the increased ionicity of the M–F bond. Furthermore, A_2MPO_4F cathode materials may reach capacity values larger than 200 mA·h·g^{-1}, if more than

one lithium atom would participate in the reversible de/intercalation process.

Li$_2$CoPO$_4$F, which exhibits an electrochemical activity above 5 V vs Li/Li$^+$, is one of the attractive candidates in the fluorophosphate family [1]. This fluorophosphate possesses a three-dimensional (3D) tunnel structure and, by analogy to the olivine phase, is expected to demonstrate a good stability and reversibility upon cycling. It is built of edge-shared CoO$_4$F$_2$-octahedra interconnected with PO$_4$-tetrahedra, which generate a framework with channels through which alkali-ion diffusion can take place [2-4] (Figure 1). The reversible electrochemical activity of Li$_2$CoPO$_4$F has been studied by several groups [4-9]. Our previous investigation of this cathode material has revealed the de/intercalation of lithium occurs through a single-phase reaction mechanism. Moreover, according to the capacity–voltage dependence the extraction of more than one Li$^+$ ion should take place at potentials larger than 5.5 V [4], which is beyond the stability range of conventional electrolytes. An initial discharge capacity of 132 mA·h·g^{-1} that is delivered by Li$_2$CoPO$_4$F in a high-voltage electrolyte with fluorinated alkyl carbonates has been reported by S. Amaresh et al., however noticeable capacity fading has been observed upon prolonged cycling [8]. Therefore, the evaluation of the electrochemical performance of Li$_2$CoPO$_4$F and the other representative of this family such as Li$_2$NiPO$_4$F [2,10], is limited to conventional electrolytes. Hence, the development of new organic electrolytes with a wide range of application voltages and the investigation of high-voltage fluorophosphates using these new electrolyte systems are strongly required.

Figure 1: Crystal structure of 3D-Li$_2$MPO$_4$F, positions of Li atoms are denoted.

Another way to explore this fluorophosphate family is to adjust the operating voltage of these compounds to values that are sustained by conventional electrolytes. This might be achieved through a complete or a partial substitution of Co^{2+} by Fe^{2+} or Mn^{2+} with lower values of the of M^{2+}/M^{3+} redox potential. Here, we report on the synthesis and the investigation of Li$_2$Co$_{1-x}$M$_x$PO$_4$F (M = Fe, Mn) fluorophosphates, which have not been yet identified. Furthermore, different high-voltage electrolytes systems were tested and utilized to evaluate the electrochemical performance of the new synthesized compounds.
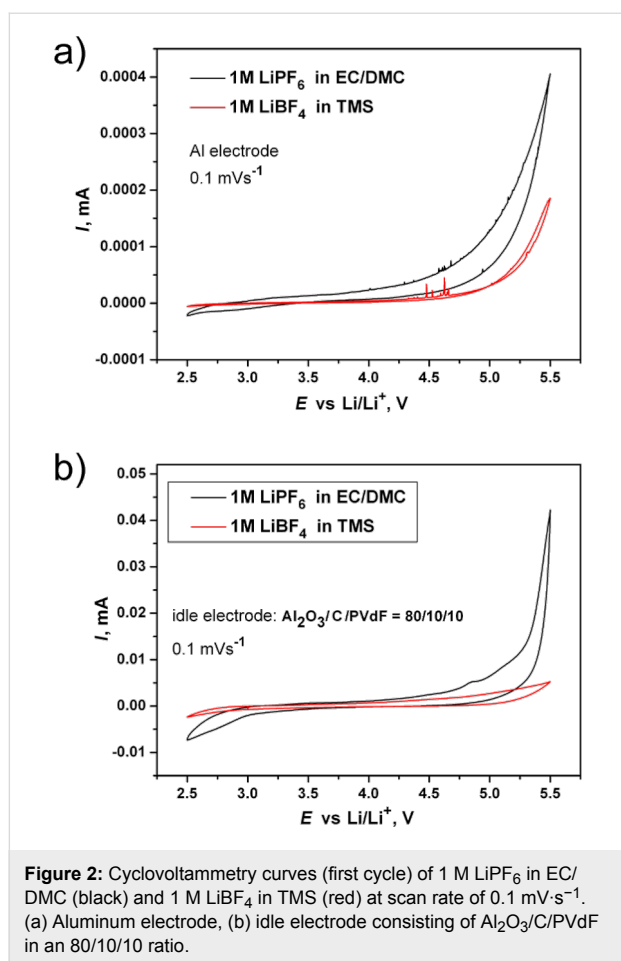
Results and Discussion
Testing of electrolytes
An electrochemical window that extends above 5.5 V (vs Li/Li$^+$) has been reported for several electrolytes systems based on sulfone or dinitrile solvents [10-14]. For instance, tetramethylene sulfone (TMS) in the presence of an imide salt (LiTFSI) demonstrated a resistance to electrochemical oxidation up to 6 V vs Li/Li$^+$ [11], while 1 M LiBF$_4$/(EC)/DMC/sebaconitrile was used to examine the high-voltage performance of the fluorophosphate Li$_2$NiPO$_4$F [10]. We chose 1 M LiBF$_4$/TMS to investigate the electrochemical activity of the fluorophosphate materials. LiBF$_4$ salt was chosen instead of LiTFSI, because the last one corrodes the aluminum current collector at high potentials.

Preliminarily, the stability of both electrolytes was investigated by cyclic voltammetry to further establish their compatibility with high-voltage cathode materials. Two types of working electrodes were used to evaluate the electrochemical window of the electrolytes: 1) Al-foil (since it is used as a current collector for the positive electrode); 2) an "idle electrode", which consisted of Al$_2$O$_3$/C/PVdF in a ratio of 80/10/10, in order to imitate the effect of the carbon- and binding electrode components at high potentials. Because the loading mass and the effective surface area of the active material on the electrodes that were used for electrolyte testing were similar in all experiments, the obtained current values were compared without normalization.

Both electrolytes exhibited an electrochemical stability up to 5.5 V (vs Li/Li$^+$) with aluminum as the working electrode (Figure 2a). For the first cycle the current detected at the highest potential did not exceed 0.4 μA, and it decreased (to 0.001 μA) upon subsequent cycling. It is clearly seen that the effect of the oxidation processes occurred at the Al electrode is negligible for both electrolytes when compared to a scanning with the idle electrode (Figure 2b). In the anodic sweep the commercial electrolyte showed a small increase in oxidation current at 4.8 V followed by drastic growth (up to 40 μA) around 5.2 V, while for the TMS electrolyte irreversible oxidation current peaks of 5 μA were detected. These results confirmed the reasonable

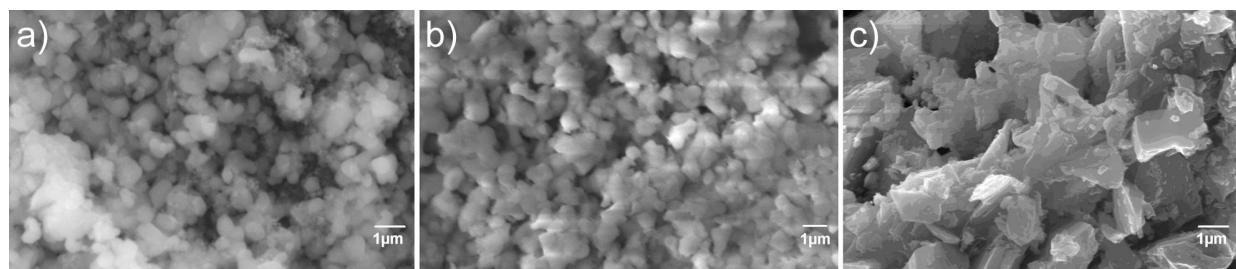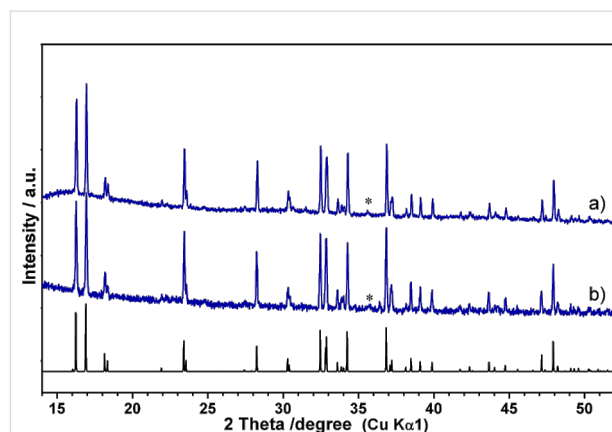stability of 1 M $LiBF_4$/TMS electrolyte up to 5.5 V, which agrees with data reported previously [12,13].

Figure 2: Cyclovoltammetry curves (first cycle) of 1 M $LiPF_6$ in EC/DMC (black) and 1 M $LiBF_4$ in TMS (red) at scan rate of 0.1 mV·s^{-1}. (a) Aluminum electrode, (b) idle electrode consisting of Al_2O_3/C/PVdF in an 80/10/10 ratio.

Investigation of $Li_2(Co,M)PO_4F$ (M = Mn, Fe)

Applied synthesis approaches were directed not only towards the investigation of $Li_2Co_{1-x}M_xPO_4F$ solid solutions, but also to the preparation of the corresponding electrode materials. Because of poor electronic and ionic conductivity that is inherent to polyanionic compounds, a carbon coating (for improving the electronic surface conductivity) and a down-sizing of the particles (in order to shorten the Li-ion transfer paths) were applied to enhance the electrochemical performance of the investigated materials. In order to reduce the particle size and to prevent grain coalescence the lowest temperatures usable for the formation of the pure olivine precursors and the fluorophosphates were always chosen.

The Li_2CoPO_4F/C composite for electrochemical measurements was synthesized according to a procedure that was optimized previously [4]. A mixture of $LiCoPO_4$/C with 1.05 equiv of LiF was annealed at 670 °C for 1 h under Ar-flow and subsequently quenched to room temperature. The XRD pattern confirmed the formation of Li_2CoPO_4F, though a small amount of WC (about 1%, from the ball-milling media) was also detected (Figure 3). The refined unit cell parameters of Li_2CoPO_4F/C (a = 10.444(3) Å, b = 6.374(2) Å, c = 10.868(3) Å, V = 723.6(5) Å^3) were in agreement with previously reported data [1,4]. The residual carbon in Li_2CoPO_4F/C was found to be 1.7%. According to the SEM images the synthesized material consisted of almost uniform particles with an average size of 0.7–0.9 μm (Figure 4).

Figure 3: Powder XRD patterns of Li_2CoPO_4F/C (a) and $Li_2Co_{0.9}Mn_{0.1}PO_4F$ (b). A theoretical pattern of Li_2CoPO_4F calculated by using PDF 56-149 is shown on the bottom. Reflections corresponding to WC are marked by an asterisk.

Figure 4: SEM images of fluorophosphate materials a) Li_2CoPO_4F/C, b) $Li_2Co_{0.9}Mn_{0.1}PO_4F$/C, c) $Li_2Co_{0.7}Fe_{0.3}PO_4F$.

In order to investigate the $Li_2Co_{1-x}Mn_xPO_4F$ solid solutions a combination of freeze-drying and solid-state techniques was applied. A mixture of $LiCo_{0.9}Mn_{0.1}PO_4$ obtained from cryo-granulate was annealed with 1.05 equiv of LiF in the temperature range of 650–700 °C for 1–2 h. Annealing at 680 °C for 1 h was found to be optimal for the preparation of the $Li_2Co_{0.9}Mn_{0.1}PO_4F$ phase. The XRD pattern of this sample (Figure 3) was indexed as an orthorhombic unit cell with parameters $a = 10.465(2)$ Å, $b = 6.3998(9)$ Å, $c = 10.898(2)$ Å and $V = 729.9(2)$ Å^3. No peaks of the olivine phase were observed, though a small amount of WC (about 1%, from the ball-milling media) was detected in the XRD pattern. Further attempts to increase the Mn content in $Li_2Co_{1-x}Mn_xPO_4F$ ($x = 0.2, 0.3$) by varying the annealing temperature and the heating duration ended up with multiphase samples that contained impurities of olivine and Li_3PO_4. Moreover, the unit cell parameters of the formed fluorophosphates were found to be close to those of $Li_2Co_{0.9}Mn_{0.1}PO_4F$. These results clearly indicated that $Li_2Co_{1-x}Mn_xPO_4F$ exhibited a very limited range for the solid solution ($x \leq 0.10$). For electrochemical testing $Li_2Co_{0.9}Mn_{0.1}PO_4F/C$ was synthesized by adding carbon black (5 wt %) to the olivine precursor at an intermediate step of preparation. The XRD pattern of the obtained sample confirmed the formation of pure fluorophosphate with cell parameters similar to those given above. EDX analysis of the prepared material found the Co/Mn ratio to be 0.89(1)/0.11(1), which agreed with the expected values from the chemical formula. The morphology of this sample was investigated by SEM and showed particles of submicron size (Figure 4). The residual carbon in the prepared composite was determined to be as 3.1% by TG analysis. This value was taken into account during the preparation of the electrode.

The synthesis of the iron-substituted fluorophosphates, $Li_2Co_{1-x}Fe_xPO_4F$, was performed by a two-step solid-state process. The optimization of the preparation conditions was done for the composition of $x = 0.3$. Figure 5a represents XRD patterns of the samples obtained by annealing mixtures of $LiCo_{0.7}Fe_{0.3}PO_4$ and LiF (with 10 wt % excess) at different temperatures. According to the XRD data, the fluorophosphate phase started to form above 700 °C, and further enhancement of the annealing temperature resulted in a decrease of the olivine impurities and in an increase of the fluorophosphate constituent. The formation of the almost pure $Li_2Co_{0.7}Fe_{0.3}PO_4F$ was observed upon heating at 740–750 °C. Above these temperatures (>760 °C) samples melted and were heavily contaminated by cobalt oxide. Thus, the annealing at 750 °C for 1 h in Ar was found to be optimum to yield $Li_2Co_{0.7}Fe_{0.3}PO_4F$. A tuning of the annealing temperature allowed us to synthesize pure fluorophosphates with different levels of substitution, $Li_2Co_{1-x}Fe_xPO_4F$ ($x = 0.1$–0.3) (Figure 5b). The XRD patterns

of obtained samples were indexed on the base of an orthorhombic structure with a *Pnma* space group and the unit cell parameters that are listed in Table 1. Careful inspection of the XRD data revealed negligible amounts of Li_3PO_4 and Co admixtures. It is evident from the obtained results that the synthesis of Fe-substituted compounds requires increased annealing temperatures that depend on the Fe-content in $Li_2Co_{1-x}Fe_xPO_4F$. For a higher Fe-substitution higher annealing temperatures are needed. The solid-state synthesis at elevated temperatures resulted in large micrometer-sized particles (2–4 μm) as observed by SEM (Figure 4). It should be noted that the presence of LiF, which is used as the reagent, promoted the coalescence of small particles and induced crystallite growth because of fluxing at elevated temperatures. In spite of varying the preparation conditions all attempts to increase the substitution level of Fe in $Li_2Co_{1-x}Fe_xPO_4F$ ($x = 0.4, 0.5$) led to multi-phase samples, with the fluorophosphate phases having cell parameters close to those of $Li_2Co_{0.7}Fe_{0.3}PO_4F$. Thus, it was concluded that the solid-solution range of $Li_2Co_{1-x}Fe_xPO_4F$ was limited to $x \leq 0.3$. Efforts to prepare a $Li_2Co_{0.7}Fe_{0.3}PO_4F/C$ composite by adding carbon black or glucose to the initial mixtures of reagents resulted in
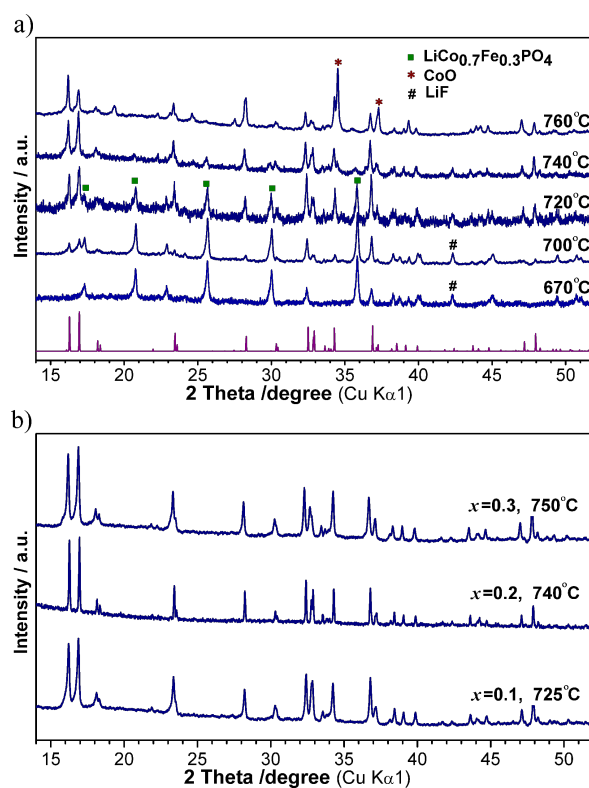

Figure 5: a) XRD patterns of a mixture of $LiCo_{0.7}Fe_{0.3}PO_4$ and LiF, annealed at different temperatures, starting from 670 °C. XRD peaks that correspond to impurities are marked. b) XRD patterns of $Li_2Co_{1-x}Fe_xPO_4F$ ($x = 0.1, 0.2, 0.3$), synthesized at the denoted temperatures.

Table 1: Unit cell parameters of fluorophosphates $Li_2Co_{1-x}M_xPO_4F$ (M = Mn, Fe).

x (M)	unit cell parameters of $Li_2Co_{1-x}M_xPO_4F$			
	a, Å	b, Å	c, Å	V, Å^3
0	10.439(2)	6.3731(12)	10.864(2)	722.8(2)
0.1 (Mn)	10.465(2)	6.3998(9)	10.898(2)	729.9(2)
0.1 (Fe)	10.440(2)	6.3862(13)	10.867(3)	724.5(4)
0.2 (Fe)	10.442(2)	6.4103(14)	10.884(2)	728.6(3)
0.3 (Fe)	10.453(1)	6.4096(8)	10.888(12)	729.5(2)

multiphase samples that contained large amounts of metallic Co (>10%), which can be explained by the strongly reductive conditions that appeared at elevated temperatures (>700 °C) because of the presence of C-containing additives. Therefore, for the electrochemical evaluation of the Fe-substituted fluorophosphates the electrodes were prepared from the carbon-free product $Li_2Co_{0.7}Fe_{0.3}PO_4F$ by thoroughly mixing it with Super-C carbon (10 wt %).

According to the obtained results $Li_2Co_{1-x}Fe_xPO_4F$ and $Li_2Co_{1-x}Mn_xPO_4F$ systems exhibit limited ranges of solid solution. This finding might be explained by differences in the sizes of transition metal ions: Apparently, the structure framework becomes unstable upon higher substitution of Co^{2+} (0.735 Å) by larger Fe^{2+} (0.780 Å) and Mn^{2+} (0.820 Å) [15]. Indeed, while Li_2MPO_4F (M = Co, Ni) can be obtained by direct synthesis, the preparation of 3D-Li_2FePO_4F requires the electrochemical ion-exchange of the Na-counterpart, and the corresponding Mn-based fluorophosphate has not been yet identified [16]. It is reasonable, that a substitution of Co^{2+} by Mn^{2+}, which has the largest ionic radius, only takes place in a smaller range ($x \leq 0.10$) than in the case of Fe^{2+} ($x \leq 0.30$). In both cases the substitution results in considerable expansion of the unit cell (ca. 7 Å^3) for the highest level of substitution (Table 1).

Electrochemical performance of $Li_2(Co,M)PO_4F$ (M = Mn, Fe)

According to galvanostatic measurements performed at a rate of C/5 (Figure 6) Li_2CoPO_4F starts to discharge at approx. 5 V, which agrees well with previous results. The Li/Li_2CoPO_4F cells delivered initial discharge capacities of ca. 90 and 85 mA·h·g^{-1} with the commercial and the sulfone-based electrolyte, respectively, and these values corresponded to a reversible de/intercalation of about 0.65 Li. During the initial cycles the charge capacity values were remarkably higher than the corresponding discharge capacities. This discrepancy in the capacities may result from a decomposition of the electrolyte on the conductive carbon and on the flurophosphate material at high potentials. For the TMS electrolyte this discrepancy disap-

peared upon subsequent cycling. During the 10th cycle the corresponding values became almost equal, with a coulombic efficiency of 98% (Figure 6). Moreover, there is less capacity fading when using the TMS electrolyte. During the 10th cycle the discharge capacity decreased to about 83% of the initial value in contrast to a decrease to about 45% found with the commercial electrolyte. The obtained results indicated a rather stable electrochemical performance of the Li_2CoPO_4F material at high voltages in the 1 M $LiBF_4$/TMS electrolyte. The

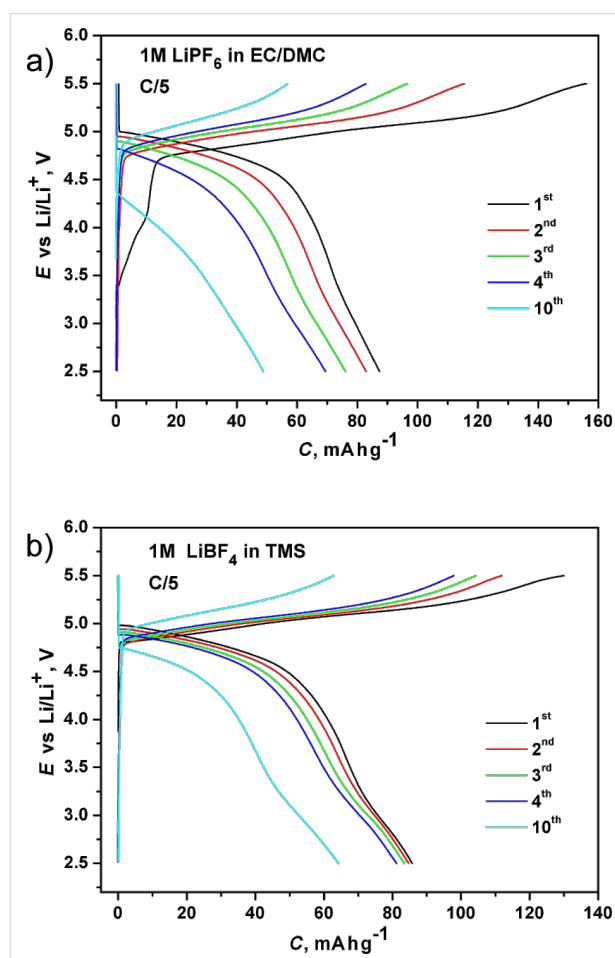**Figure 6:** Charge-discharge curves of Li_2CoPO_4F in the commercial (a) and in the sulfone-based electrolytes (b) measured at C/5.

decrease of the irreversible capacity, which leads to the high columbic efficiency, implies that this electrolyte forms a stable solid-electrolyte interface on the electrode surface, but this suggestion should be further investigated and confirmed.

A preliminary investigation of the electrochemical behavior of $Li_2Co_{0.7}Fe_{0.3}PO_4F$ was carried out with electrodes prepared from the well crystallized sample. Potentiodynamic measurements in both electrolytes resulted in broad peaks on the anodic and cathodic branches with the discharge capacity values being lower than 10 mA·h·g^{-1}. Because of the poor electrochemical activity, which is ascribed to the non-optimized morphology of the electrode material (particle size of 2–4 μm), any comparisons of $Li_2Co_{0.7}Fe_{0.3}PO_4F$ with the unsubstituted material were unreasonable.

Figure 7 shows the cyclovoltammetry (CV) curves of the Li/$Li_2Co_{0.9}Mn_{0.1}PO_4F$ cells cycled in both electrolytes. For the TMS electrolyte two oxidative peaks (at 4.9 V and 5.2 V) and a broad reductive peak (at 4.8 V) were observed in the first anodic and cathodic scans, respectively. During the second cycle the two oxidative peaks merged, and the broad peaks on the anodic (≈5.1 V) and cathodic (4.8 V) branches showed charge and discharge capacities of 135 and 70 mA·h·g^{-1}, respectively. The CV curves that were recorded in the commercial electrolyte were quite similar. The presence of two oxidative peaks in the first anodic scan (Figure 7) hints at the occurrence of at least two redox processes. We related them to the structure transformation upon deintercalation of Li, followed by a further removal of Li from the transformed structure. This irreversible structure transformation, which occurs upon first charging, was investigated by ex-situ XRD studies and described in detail in our previous paper. This transformation resulted in an expansion of the framework and a probable redistribution of Li ions within the framework [4]. Similar features were observed in CV curves of Li_2CoPO_4F by D. Wang et al. [5] and S. Amaresh et al. [8]. This indicates the intrinsic nature of this transformation.

Galvanostatic measurements on $Li_2Co_{0.9}Mn_{0.1}PO_4F$ (Figure 8) revealed the highest discharge capacities of 75 and 85 mA·h·g^{-1} in TMS and the commercial electrolytes, respectively. As in the

Figure 7: Cyclovoltammetry curves of the $Li_2Co_{0.9}Mn_{0.1}PO_4F$ electrodes in the commercial (a) and the sulfone-based (b) electrolytes recorded at 0.1 mV s^{-1}.

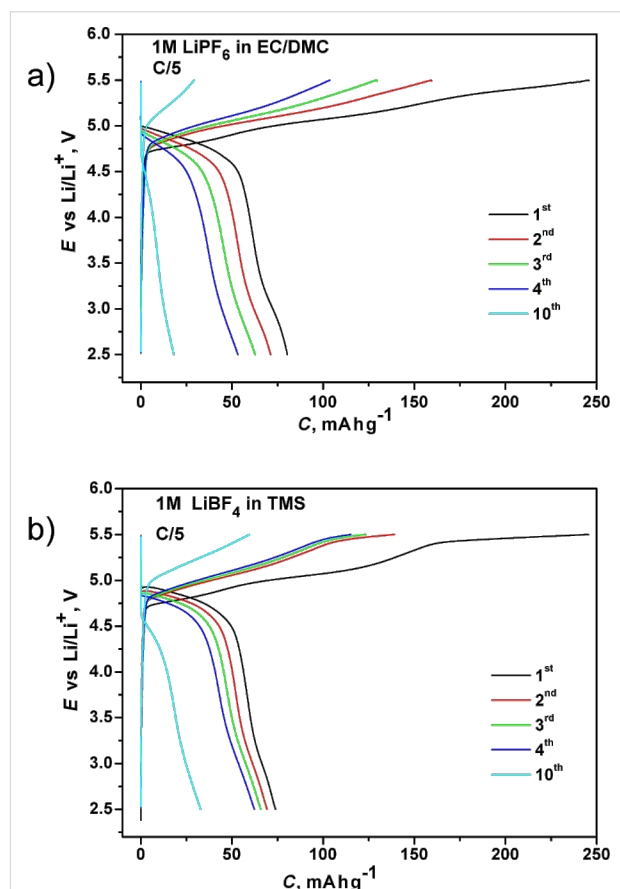**Figure 8:** Charge–discharge curves of $Li_2Co_{0.9}Mn_{0.1}PO_4/C$ in the commercial (a) and the sulfone-based (b) electrolytes measured at C/5.

case of Li_2CoPO_4F, the capacity fading of the Mn-substituted fluorophosphate was slower in the TMS electrolyte. Sloping charge–discharge profiles and broad CV peaks suggest a single-phase (solid-solution) reaction mechanism, similar to Li_2CoPO_4F [4,8]. There is no visible change in the operating potential of $Li_2Co_{0.9}Mn_{0.1}PO_4F$. Therefore it was difficult to draw a decisive conclusion on the effect of Mn-substitution on the electrochemical activity of the Li_2CoPO_4F system. A further optimization in synthesis and formulation of the cathode material (particle investigation and carbon coating) of Mn- and Fe-substituted fluorophosphates will improve their electrochemical performance and, thereby, answer the question about a possible fine tuning of the operating voltage of this fluorophosphate family through substitutions on the transition metal site.

Conclusion

New fluorophosphates, $Li_2Co_{1-x}Mn_xPO_4F$ and $Li_2Co_{1-x}Fe_xPO_4F$, were successfully synthesized and investigated. Both systems exhibited narrow ranges of solid solution that agreed well with the ionic sizes of the transition metals. Good cycling and capacity behavior was attained with the 1 M $LiBF_4$/TMS electrolyte. Galvanostatic measurements revealed a reversible electrochemical activity with discharge capacities as high as 90 and 75 $mA·h·g^{-1}$ for Li_2CoPO_4F and $Li_2Co_{0.9}Mn_{0.1}PO_4F$ respectively. A further investigation that includes the optimization of the electrode materials and the development of a high-voltage electrolyte is required to evaluate all potentials of this $Li_2Co_{1-x}M_xPO_4F$ (M = Mn, Fe) fluorophosphate family.

Experimental

The fluorophosphates, Li_2CoPO_4F and $Li_2Co_{1-x}M_xPO_4F$ (M = Fe, Mn) were synthesized in a two-steps process. In the first step $LiCo_{1-x}M_xPO_4$ olivine precursors were prepared through freeze-drying or ceramic techniques, depending on the transition metal. In the second step the obtained olivine samples were ball-milled with 1.05 equiv of LiF (5% excess), pelletized, annealed at 650–720 °C for 1–2 h under Ar flow and, subsequently, quenched to room temperature. As noticed above the technique applied to synthesize olivine precursors depended on the transition metal. Thus, $LiCoPO_4$ was prepared by a solid-state reaction from a stoichiometric mixture of Li_2CO_3 (99.1%), $(NH_4)H_2PO_4$ (99%), $Co(NO_3)_2·6H_2O$ (99.9%). It should be noted that the purity of initial reagents was checked by X-ray diffraction, the weight form of the crystallohydrates that were used for sample preparation was verified by thermogravimetric analysis. The initial reagents were mixed by planetary ball-milling, pelletized and then annealed in a tubular furnace (under steady Ar flow) at 380 °C for 10 h and at 600 °C for 15 h with intermediate regrinding. The Fe-substituted olivine precursors, $LiCo_{1-x}Fe_xPO_4$, were obtained from stoichiometric mixtures of

Li_2CO_3, $NH_4H_2PO_4$, $FeC_2O_4·2H_2O$ (99%) and $CoC_2O_4·2H_2O$ (99%). The annealing profile was similar to that described for $LiCoPO_4$. The oxalates, $FeC_2O_4·2H_2O$ and $CoC_2O_4·2H_2O$, were chosen as initial reagents because the mixture of CO and CO_2 released upon their decomposition suppressed the Fe^{2+} oxidation (in contrast to NO_2 evolved by nitrates) and, at the same time, did not reduce Co^{2+} to metallic Co.

The Mn-substituted olivine precursors, $LiCo_{1-x}Mn_xPO_4$, were prepared through the freeze spraying technique. The initial reagents $LiCH_3COO$ (99%), $NH_4H_2PO_4$, $Co(NO_3)_2·6H_2O$ and $Mn(CH_3COO)_2·3.2H_2O$ were dissolved in distilled water and combined to form a transparent solution with a pH value of 3.0–3.5, which was adjusted by adding 1 M CH_3COOH. This solution was exposed to freeze-spraying in liquid nitrogen, and the obtained product was subjected to vacuum sublimation in a Labconco sublimator (pressure 0.2 mbar, temperature range −40 to +30 °C) for 70 h. The prepared granulate was pressed into pellets and annealed at 350 °C for 10 h and at 550 °C for 15 h under Ar flow with intermediate regrinding.

The carbon-containing composites, $Li_2Co_{1-x}M_xPO_4F/C$, were prepared by adding carbon black (3–5 wt %) to the initial mixtures or, as in the case of M = Mn, to the products obtained from cryogranulates by annealing at 350 °C. The amount of residual carbon in the obtained composites was determined by thermal analysis and taken into account during the preparation of the electrodes.

Mechanical grindings (180–200 rpm for 2–3 h) were carried out in a Fritsch planetary micro-mill Pulverisette 7 while using a WC bowl, ZrO_2 balls and acetone media. Thermal analysis was performed in the temperature range of 20–750 °C (10 °C/min heating rate) by using a thermo-gravimetric differential scanning calorimetry (TG-DSC) apparatus STA-449 (Netzsch, Germany).

The samples were characterized by powder X-ray diffraction (XRD) using a Huber G670 Guinier camera (Cu Kα₁ radiation, Ge monochromator, image plate detector) and Bruker D8 Advance with a Lynxeye detector (Cu Kα radiation). The quantitative phase analysis for the selected samples was carried out by Rietveld refinement with the program JANA 2006 [17]. SEM investigation of powdered samples was performed with a JEOL JSM-6490LV scanning electron microscope equipped with an energy dispersive X-ray spectroscopy (EDX) attachment.

The electrochemical evaluation was performed in two-electrode-configuration cells with Li-metal foil acting both as the reference and counter electrodes, borosilicate glass was used as

a separator. The positive electrodes were prepared by thoroughly mixing the active material (80 wt %) with carbon Timcal Super C (10 wt %) and PVdF (10 wt %) dissolved in a minimal amount of *N*-methyl-pyrrolidone. This cathode slurry was cast on an Al-foil collector by using the doctor-blade technique with a typical loading of 1 mg·cm^{-2}. The prepared electrodes were dried, rolled and then dried again at 100 °C under vacuum for several hours. The electrochemical evaluation was carried out by using the following electrolytes: 1) 1 M LiPF$_6$ solution in ethylene carbonate (EC) and dimethylcarbonate (DMC) with a volume ratio of 1:1 (commercial electrolyte, Merck); 2) 1 M solution of LiBF$_4$ in tetramethylene sulfone (TMS). The latter electrolyte was prepared by dissolving an appropriate amount of LiBF$_4$ (99.99%, Aldrich) in TMS that was purified up to 99.8% before. The electrochemical cells were assembled in an Ar-filled glove box. All tested cells were left to relax before the measurements (10–20 h). A potentiostat/galvanostat Biologic VMP-3 was used for data collecting. The cyclic voltammetry scanning was performed in the voltage range of 2.5–5.5 V at a scan rate of 0.1 mV·s^{-1}. The galvanostatic charge–discharge cycling was conducted in the voltage range of 2.5–5.5 V at a rate of C/5 (the current required to deintercalate one Li ion from Li$_2$Co$_{1-x}$M$_x$PO$_4$F in 5 hours).

Acknowledgements

References

1. Okada, S.; Ueno, M.; Uebou, Y.; Yamaki, J.-i. *J. Power Sources* **2005,** *146,* 565–569. doi:10.1016/j.jpowsour.2005.03.149
2. Dutreilh, M.; Chevalier, C.; El-Ghozzi, M.; Avignant, D. *J. Solid State Chem.* **1999,** *142,* 1–5. doi:10.1006/jssc.1998.7908
3. Hadermann, J.; Abakumov, A. M.; Turner, S.; Hafideddine, Z.; Khasanova, N. R.; Antipov, E. V.; Van Tendeloo, G. *Chem. Mater.* **2011,** *23,* 3540–3545. doi:10.1021/cm201257b
4. Khasanova, N. R.; Gavrilov, A. N.; Antipov, E. V.; Bramnik, K. G.; Hibst, H. *J. Power Sources* **2011,** *196,* 355–360. doi:10.1016/j.jpowsour.2010.06.086
5. Wang, D.; Xiao, J.; Xua, W.; Nie, Z.; Wang, C.; Graff, G.; Zhang, J.-G. *J. Power Sources* **2011,** *196,* 2241–2245. doi:10.1016/j.jpowsour.2010.10.021
6. Dumont-Botto, E.; Bourbon, C.; Patoux, S.; Rozier, P.; Dolle, M. *J. Power Sources* **2011,** *196,* 2274–2278. doi:10.1016/j.jpowsour.2010.09.037
7. Wu, X.; Gong, Z.; Tan, S.; Yang, Y. *J. Power Sources* **2012,** *220,* 122–129. doi:10.1016/j.jpowsour.2012.07.099
8. Amaresh, S.; Kim, G. J.; Karthikeyan, K.; Aravindan, V.; Chung, K. Y.; Choc, B. W.; Lee, Y. S. *Phys. Chem. Chem. Phys.* **2012,** *14,* 11904–11909. doi:10.1039/c2cp41624g
9. Kosova, N. V.; Devyatkina, E. T.; Slobodyuk, A. B. *Solid State Ionics* **2012,** *225,* 570–574. doi:10.1016/j.ssi.2011.11.007
10. Nagahama, M.; Hasegawa, N.; Okada, S. *J. Electrochem. Soc.* **2010,** *157,* A748–A752. doi:10.1149/1.3417068
11. Xu, K. *Chem. Rev.* **2004,** *104,* 4303–4417. doi:10.1021/cr030203g
12. Abouimrane, A.; Whitfield, P. S.; Niketic, S.; Davidson, I. J. *J. Power Sources* **2007,** *174,* 883–888. doi:10.1016/j.jpowsour.2007.06.103
13. Watanabe, Y.; Kinoshita, S.-i.; Wada, S.; Hoshino, K.; Morimoto, H.; Tobishima, S.-i. *J. Power Sources* **2008,** *179,* 770–779. doi:10.1016/j.jpowsour.2008.01.006
14. Abu-Lebdeh, Y.; Davidson, I. *J. Electrochem. Soc.* **2009,** *156,* A60–A65. doi:10.1149/1.3023084
15. Shannon, R. D. *Acta Crystallogr., Sect. A* **1976,** *32,* 751–767. doi:10.1107/S0567739476001551
16. Khasanova, N. R.; Drozhzhin, O. A.; Storozhilova, D. A.; Delmas, C.; Antipov, E. V. *Chem. Mater.* **2012,** *24,* 4271–4273. doi:10.1021/cm302724a
17. Petricek, V.; Dusek, M.; Palatinus, L. *JANA 2006. The crystallographic computing system;* Institute of Physics: Praha, Czech Republic, 2006.

Adsorption of the ionic liquid [BMP][TFSA] on Au(111) and Ag(111): substrate effects on the structure formation investigated by STM

Benedikt Uhl[‡1,2], Florian Buchner[‡1,2], Dorothea Alwast[1,2], Nadja Wagner[1,2] and R. Jürgen Behm[*1,2]

Abstract

In order to resolve substrate effects on the adlayer structure and structure formation and on the substrate–adsorbate and adsorbate–adsorbate interactions, we investigated the adsorption of thin films of the ionic liquid (IL) 1-butyl-1-methylpyrrolidinium-bis(trifluoromethylsulfonyl)imide [BMP][TFSA] on the close-packed Ag(111) and Au(111) surfaces by scanning tunneling microscopy, under ultra high vacuum (UHV) conditions in the temperature range between about 100 K and 293 K. At room temperature, highly mobile 2D liquid adsorbate phases were observed on both surfaces. At low temperatures, around 100 K, different adsorbed IL phases were found to coexist on these surfaces, both on silver and gold: a long-range ordered ('2D crystalline') phase and a short-range ordered ('2D glass') phase. Both phases exhibit different characteristics on the two surfaces. On Au(111), the surface reconstruction plays a major role in the structure formation of the 2D crystalline phase. In combination with recent density functional theory calculations, the sub-molecularly resolved STM images allow to clearly discriminate between the $[BMP]^+$ cation and $[TFSA]^-$ anion.

Introduction

In the last 15 years ionic liquids (ILs) have attracted increasing attention due to their special physical and chemical properties such as a low volatility, high chemical stability, low flamma-bility, high intrinsic conductivity, high polarity, nearly vanishing vapour pressure and their wide electrochemical window [1-3]. Because of the enormous flexibility in varying

the combination and nature of cations and anions [4], e.g., by using different alkyl chain lengths at the cations [2,5-7] it is possible to systematically optimize ionic liquids for a specific application. Aside from many other applications, ionic liquids have been proposed as promising new solvents in electrochemical applications, e.g., in lithium ion batteries [8-10]. For the latter application, trifluoromethylsulfonyl imide [TFSA] based ionic liquids have turned out to be promising candidates; members of this group, e.g., alkylmethylpyrrolidinium-[TFSA] seem to suppress dendrite formation [11]. The underlying molecular processes, however, are not yet understood. Thus, a systematic and fundamental understanding of the interface between ionic liquids and the respective electrode surface (solid–liquid interface) is essential for developing improved future battery systems based on ILs. Correspondingly, the interaction between different ILs and various electrode materials was investigated by electrochemical methods, including, e.g., cyclovoltammetry, but also by other techniques such as in situ scanning tunnelling microscopy [12-14].

More detailed insight, on a molecular scale, may be gained in model studies investigating the interface between the respective solid surface and thin films of the IL under ultrahigh vacuum (UHV) conditions. These films can be deposited by physical vapour deposition, which allows to accurately control the film thickness (coverage) in the submono- to multilayer regime. Furthermore, applying proper cleaning procedures, high purity films can be obtained. This not only allows to use a wide variety of surface science tools for characterization of the IL adsorbates/adlayers, but also to vary the temperature over a wide range, down to cryogenic temperatures, where molecular motion is largely frozen. This way, the interaction between substrate and adsorbed ILs was investigated in a number of studies, applying both spectroscopic techniques such as ultraviolet photoelectron spectroscopy (UPS) [15,16], X-ray photoelectron spectroscopy (XPS) [17-21], or temperature programmed desorption (TPD) [22], as well as scanning probe microscopies (scanning tunnelling microscopy (STM) and atomic force microscopy (AFM)) [16,23,24]. These surface science techniques allow to gain detailed information on the electronic properties of the ILs and adsorption induced modifications therein, on the chemical nature of the adsorbed species, and on the structure and structure formation in the resulting adlayer. The latter in turn provides information on the molecule–substrate and molecule–molecule interactions in the respective adsorption system.

In the following, we will discuss these aspects for the adsorption of 1-butyl-1-methylpyrrolidinium-bis(trifluoromethylsulfonyl)imide [BMP][TFSA] (ball and stick models of the ions are shown in Figure 1a) comparing adsorption on the close-packed surfaces of Au and Ag. In that comparison, we will make use of new and recently published data [25,26]. In addition to their different chemical nature, these surfaces differ from each other in that the Au(111) surface is reconstructed, forming the well-known herringbone reconstruction [27], while the Ag(111) surface is not reconstructed. We will focus on questions related to structure and structure formation such as the nucleation and growth behavior and temperature effects thereon, the nature and stability of ordered phases, or the role of the substrate. First we will discuss the adsorption behavior for room temperature adsorption, then concentrate on the structure formation at low temperatures down to 100 K, and finally elucidate the thermal stability of the different adlayer phases.

Results and Discussion
Room temperature adsorption
Previous STM studies by Waldmann et al. and by Foulston et al. on the structure and structure formation of IL thin films on single crystal substrates, specifically for 1-butyl-1-methylpyrrolidinium-tris(pentafluoroethyl)trifluorophosphate [BMP][FAP] adsorption on Au(111) [24] and for 1-ethyl-3-methylimidazolium-[TFSA] ([EMIM][TFSA]) adsorption on Au(110) [16], respectively, indicated that at room temperature the thermal mobility of IL adsorbates is too high for resolving individual molecular entities by STM. Images recorded under these conditions resolved a characteristic noise in the tunnel current on the IL covered surfaces, which was not observed in the absence of the IL adlayer. The authors of those studies attributed this noise to the formation of a 2D gas or 2D liquid adlayer phase, where the IL adsorbates are mobile on the surface and cause a temporary modification in the tunnel current whenever a diffusing admolecule passes through the tunnel gap underneath the tip. (Note that the 2D gas and 2D liquid adlayer phase differ mainly by the adlayer density.) Similar effects were observed also for adsorption of [BMP][TFSA] on Au(111) [25] and on Ag(111) [26]. While this point shall be discussed in more detail later, it should be noted here already that the high mobility of the adsorbed species, which reflects a low lateral corrugation of the adsorption potential along the surface, is incompatible with the formation of localized covalent bonds between substrate and the adsorbed IL species.

Finally it should be noted that the STM images showed no indications of a restructuring of the Ag(111) or Au(111) surfaces upon interaction with [BMP][TFSA], as it was reported by Atkin et al. [23] for [BMP][TFSA] on Au(111) in electrochemical STM measurements, where bulk IL was in contact with the surface at potentials between −0.4 and −2.2 V vs the ferrocene/ferrocenium (Fc/Fc$^+$) redox couple [28]. Hence, the presence of the IL adsorbate alone is not sufficient to induce a restructuring of the substrate surface.

The information derived from STM imaging can be combined with results of spectroscopic measurements. XP spectra presented in [25] for submono- to multilayer [BMP][TFSA] films on Au(111) showed a similar dependence of the intensity of the different XPS signals (C(1s) and N(1s)) on the emission angle and an XPS based composition identical to the stoichiometric ratio, both in the submono- to monolayer regime and at higher coverages. Therefore, the authors of that study concluded that in average all atoms of the two ions are located in the same layer, with anions and cations placed side by side on the surface. Therefore, both ions in the first layer are in direct contact with the surface. This is also confirmed by the fact that for coverages up to 1 monolayer (ML) the C(1s) and N(1s) XPS signals show a shift of 1.1 eV to lower binding energy (BE), due to the interaction with the Au(111) surface. For Ag(111), where ARXPS measurements are not available, we expect a comparable adsorption behavior. This is supported also by the results of density functional theory (DFT) calculations discussed below.

These results can be compared with findings reported for other IL adsorption systems. For 1,3-dimethylimidazolium-[TFSA] ([MMIM][TFSA]) and 1-octyl-3-methylimidazolium-[TFSA] ([OMIM][TFSA]) adsorption on Au(111) [19], the same adsorption geometry with both the anion and cation in direct contact to the surface was concluded from ARXPS measurements at room temperature. The authors of that study deduced that the cation adsorbs with the imidazolium ring flat on the surface and that the anion adsorbs in a cis-conformation, with the SO_2-groups pointing to the surface and the CF_3-groups pointing towards the vacuum. The same adsorption geometry for the anion was also proposed by Sobota et al. [29] for [BMIM][TFSA] (B = butyl) adsorbed on a thin alumina film grown on NiAl(110) [30,31], utilizing a combination of infrared reflection absorption spectroscopy (IRAS) and density functional theory (DFT) calculations. [OMIM][TFSA], which differs from [MMIM][TFSA] only by its longer alkyl chain, showed a coverage dependent adsorption geometry on Au(111): at coverages below 0.6 ML, the octyl chain lies flat on the surface, while at higher coverages it sticks up from the surface, reducing the space requirement of the adsorbed ion pair. In contrast, for adsorption on other surfaces, also other adsorption geometries were reported: For [EMIM][TFSA] adsorption on a glass substrate, an adsorption geometry with the cations lying flat in direct contact with the surface and the anions placed on top of the cations was proposed based on ARXPS measurements [17]. For [MMIM][TFSA] adsorption on Ni(111) [20], a similar adsorption geometry was proposed for adlayers in the submonolayer coverage regime up to ≈0.8 ML. Finally, for coverages >0.8 ML, the ARXPS data did not show a vertical layering of the different ions, therefore under these conditions

both adsorbed cations and anions have to be in direct contact to the substrate. This behaviour was explained by an increasing repulsive electrostatic interaction between the ion pairs with increasing coverage, leaving the former configuration energetically less favourable at coverages above 0.8 ML compared to a structure with both species in direct contact with the surface.

Overall, though structural resolution of the IL adlayer was not possible at room temperature, the examples discussed above, with their very similar ILs (most of them contain the same anion and an imidazolium- or pyrrolidinium-based cation), demonstrate already that the structures resulting in ionic liquid adlayers depend sensitively on the substrate. This will become even more evident when comparing adlayer structures on the two different surfaces Ag(111) and Au(111) in the next section.

Low-temperature adsorption

The situation changes considerably when cooling the samples to lower temperatures. Under these conditions, molecular motion is frozen and the adsorbates can be resolved in STM measurements. Since cool-down was done very slowly (ca. 2 K min^{-1}), the system stays in thermal equilibrium until the adsorbates are immobilized and STM images show the surface at this freezing temperature. Although the resulting adlayer differs clearly from that in the solid–liquid interface at room temperature and above, e.g., by the much higher molecular mobility, these measurements provide sensitive information on the interactions between the adsorbed ions and on the variation in substrate–adsorbate interaction (adsorption potential) along the surface. These characteristic energies can be used as starting point also for the description of the solid–liquid interface at room temperature and above.

In their STM study on [BMP][FAP] adsorption on Au(111), Waldmann et al. resolved round shaped protrusions at temperatures below 210 K [24]. A direct assignment of these structures to adsorbed cations or anions and a clear identification of the adlayer structure in terms of co-planar adsorption of both types of ions or adsorption of one species on top of the other one, however, was not possible from these data. Likewise, in their STM study of [EMIM][TFSA] adsorption on Au(110), Foulston et al. identified round shaped protrusions at liquid nitrogen temperature, which were oriented along the missing row lines of the (1 × 2) reconstruction of the Au(110) surface, but without long-range ordering along the lines or strict correlations between neighbouring lines. These protrusions were proposed to represent the complete IL ion pair. Also in these images it was not possible to resolve and identify anions and cations [16]. Overall, these studies succeeded in resolving individual molecular entities, but were not able to derive the actual structure of the adlayer, or to identify anions and cations separately.

Going to the present system, [BMP][TFSA] adsorption on Ag(111) and Au(111), we find two types of structures, one type which similar to the above observations does not exhibit a long-range order but rather a short-range order, which we denote as '2D glass' phase, and a second one exhibiting a distinct long-range order [25,26]. This latter structure can be denoted as '2D crystalline' phase.

Examples for the '2D glass' adlayer structure are shown in Figure 1 for adsorption on Au(111) and later in Figure 2 for adsorption on Ag(111). STM images of the 2D crystalline structures are depicted in Figures 4–6 (see below).

We will first concentrate on the discussion of the '2D glass' structure. In Figure 1b, a Au(111) surface covered with

Figure 1: (a) Ball and stick model of 1-butyl-1-methylpyrrolidinium-bis(trifluoromethylsulfonyl)imide [BMP][TFSA] (grey: C, white: H, blue: N, red: O, green: S, yellow: F) (drawn with Chem3D). (b) STM image of a Au(111) surface covered with 0.7 ML of [BMP][TFSA] arranged in islands of the 2D glass phase. Inset: detail of the image in (b) with enhanced contrast between the adsorbate islands, resolving the Au(111) reconstruction pattern (T = 112 K, U_T = −1.9 V, I_T = −40 pA); (c) STM image of a Au(111) surface with a small amount (≈0.2 ML) of adsorbed [BMP][TFSA], resolving the preferential decoration of steps and the nucleation of small islands with 2D glass structure at the elbows of the Au(111) reconstruction, while islands with a 2D crystalline structure have grown larger. The Au(111) reconstruction pattern is visible on the uncovered parts of the surface (T = 111 K, U_T = −1.74 V, I_T = −0.020 nA). (d) High resolution image of the 2D glass phase on Au(111): longish protrusions with a lower height are visible between the round shaped protrusions (partly marked by white circles and ellipsoids) (T = 119 K, U_T = −1.06 V, I_T = 80 pA).

0.7 monolayers (ML) of [BMP][TFSA] adsorbates is shown (for a definition of 1 ML see Experimental section). In that image, the IL adsorbates appear as round shaped protrusions and form distinct islands on the surface. In between the islands, adsorbate free Au(111) surface areas appear, where the typical [27] zig-zag pattern of the Au(111) surface reconstruction is resolved (see inset with enhanced contrast in Figure 1b). The formation of islands demonstrates the presence of attractive interactions between the adsorbed IL species, which must be strong enough to cause island formation at the freezing temperature. Interestingly, the steps of the Au(111) surface are decorated with adsorbate species, hence these sites seem to be preferred adsorption sides. While this is true for both the ascending and descending side of the steps, on the lower and upper terrace side, respectively, the structural characteristics differ for both sites. On the upper terrace side, a single row of IL adsorbates follows the step, indicative of a stronger adsorption at these sites, similar to the frequent observation of stronger adsorption of atomic adsorbates and adsorbed small molecules [32]. At the lower terrace side, the IL adsorbates seem to condense at the ascending steps, forming large IL islands which grow over the Au(111) terraces. Interestingly, 2D condensation of IL adsorbates at the row of adsorbate species decorating the step edge on the upper terrace side is not possible. The physical reason for the different 2D condensation behavior on the upper and lower step edge is not yet clear.

In addition to the step edges, also the elbows of the Au(111) reconstruction act as nucleation sites for 2D island formation. A few examples are visible in Figure 1b. More clearly, this is observed in STM images recorded at low coverages, where only the steps and the elbows are covered with adsorbates, as illustrated in Figure 1c. This points to a higher adsorption energy at the elbow sites as compared to the other surface areas, similar to findings for metal epitaxy, e.g., Ni/Au(111) [33], or adsorption of large molecules such as porphyrin molecules [34].

The (short-range) ordering of the adsorbates in the islands was checked by calculating a Fourier transformation (FFT) in sections of STM images which show solely one island and the distribution of round shaped protrusions on it. The FFT always shows a broad circle (see [25]), as expected for a short-range ordered system. We found no evidence for a coverage effect on the density and structural characteristics of this phase in the submonolayer and monolayer regime.

On Ag(111), adsorption of [BMP][TFSA] leads to a similar '2D glass' structure. In this case, however, it is formed only on narrow terraces with a width of ≤10 nm, as can be seen exemplarily in the STM image in Figure 2, while on Au(111) there was no obvious influence of the terrace width discernible.
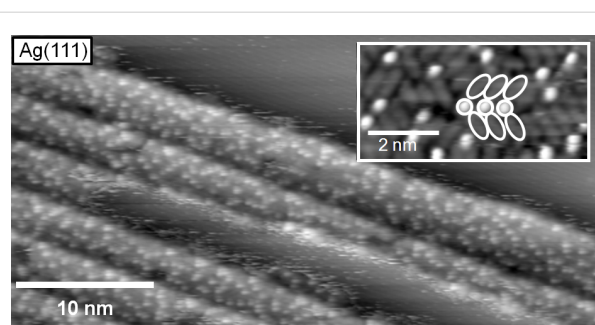

Figure 2: STM image of a submonolayer film of [BMP][TFSA] adsorbed on Ag(111); the narrow terraces of the surface are covered with IL islands in the 2D glass phase, the inset shows a high resolution image of the 2D glass structure resolving both the round shaped and the longish protrusions (marked with white circles and ellipsoids) (T = 135 K, U_T = −1.14 mV, I_T = 100 pA).

This difference is most easily explained by the presence/absence of the Au(111) reconstruction pattern, which seems to severely affect the ordering behavior. Keeping in mind that on Au(111) the elbows of the surface reconstruction act as nucleation sites for IL island formation, the larger tendency for disordered 2D structures on Au(111) can at least partly be ascribed to a mismatch between the lattice created by the elbow sites and the ordered lattices of IL adsorbates (see below). In that case, IL adsorbate islands created at neighbouring elbow sites are not in registry, and therefore can not coalesce easily. These effects are absent on the unreconstructed Ag(111) surface.

In the inset of Figure 2, we show a high resolution image of the 2D glass structure. It is recorded in the central area of an island with very little or no motion of the adsorbed molecules during imaging. Between the round shaped protrusions, longish protrusions with a lower apparent height are resolved. Some of these species are marked in the image by white circles and ovals for better identification. For Au(111), high resolution images of the disordered structure look exactly the same, with identical structures, mean distances between the protrusions etc. (see Figure 1d and inset in Figure 2). Therefore, the adsorption geometry, the structure formation and the molecule–molecule and molecule–substrate interactions in the 2D glass structure of [BMP][TFSA] should be identical on Au(111) and Ag(111) and they can be discussed for both substrates together. The first question relates to the origin of the different protrusions in the STM images. Most simply, the longish protrusions represent one ion type and the round shaped protrusions the other one. In that case, the adsorbed cations as well as the anions lie next to each other in direct contact to the surface, as it was already concluded from the XPS data for [BMP][TFSA] on Au(111) [25] and for the adsorption of the very similar ILs [MMIM][TFSA] and [OMIM][TFSA] on Au(111) [19]. A quantitative evaluation of the numbers of longish and round

shaped protrusions in several 2D glass domains and on several STM images yielded a ratio of 2:1. This leaves us with two different plausible explanations: either one ion type is represented by two parallel longish protrusions and the other one by the round shaped protrusion, or one type is represented by the round shaped protrusion plus one longish protrusion and the other one by the other longish protrusion. Though the first interpretation sounds more convincing, this question cannot be solved on the basis of the STM images alone. We will get back to this point after discussion of the 2D crystalline structure.

As evident in Figure 1d, the longish protrusions are aligned in rows of varying lengths (between 2 and 8 protrusions are typical), which are oriented at an angle of roughly 120° (or 240°) in between. The resulting threefold symmetry is probably due to an alignment to the closed packed directions of the Au(111) surface. So the structure is not completely random, even if there is no long-range order visible for the distribution of the round shaped protrusions in the FFT.

In addition to the differences in the structure formation processes between Au(111) and Ag(111), there seem to be differences also in the mobility of the IL adsorbates on these two surfaces. For the Ag(111) surface, apparently adsorbate free areas between IL adsorbate islands, e.g., on the central terrace in Figure 2 or in front of the topmost step in this image, show a significant noise. The noisy appearance resembles that obtained for imaging at room temperature, but in the latter case the noise is more pronounced and present on the entire terrace. On Au(111), this noise is visible also on similarly covered surfaces for STM imaging at 100 K, but is much less pronounced. This indicates that these areas are essentially free of mobile IL adsorbates. A higher mobility of IL adsorbates on Ag(111) compared to Au(111) is evident also from inspection of series of images from the same surface area, which reveal changes in the island boundaries with time. This is illustrated in Figure 3, which shows a time sequence of STM images (time between subsequent image starts: 11 s) recorded on a partly IL adsorbate covered Ag(111) surface. Beside the 2D glass phase, an apparently uncovered region is visible, which, as also described for the STM image in Figure 2, appears noisy. This sequence clearly demonstrates that the island edge (phase boundary) gradually changes with time (Figure 3a–r). While the major part of the round shaped protrusions persists on the same site from frame to frame, molecular jumps are detected for others. This is evident, e.g., in the areas marked with red ovals in Figure 3b and 3c. The two protrusions in the smaller oval are stable from image to image, while the protrusions in the larger oval collectively move to a lower position in the image. A red arrow is also included, pointing towards a single protrusion, which changed position. In Figure 3d and 3e, the arrows in the orange frame

mark a molecular jump between two consecutive images, while in subsequent images no motion at the same position takes place (Figure 3r). In Figure 3m and 3n, the blue circles label protrusions, which persist at the same positions, while for others at and close to the boundary between 2D glass structure and adsorbate free area significant changes are visible. Thus, both temporary changes directly at the phase boundary and also some limited motion inside the 2D glass phase is found on Ag(111). On Au(111), these processes were also observed, but less frequent. These structural changes can be explained either by a motion of IL adsorbates along the island edge or by a 2D adsorption–desorption equilibrium between the IL adsorbate islands and a 2D gas/liquid of IL adsorbates. As expected for this case, structural variations mainly take place at the island perimeter, while the inner part of the islands is essentially stable; with infrequent molecular jumps only in the vicinity of defects in the adlayer lattice.

Aside the 2D glass phase, also well ordered, 2D crystalline domains/islands are found on the surface. This is illustrated in the high resolution images of the 2D crystalline structure on Au(111) in Figure 4a and 4b. These images also reveal characteristic round shaped protrusions and in between longish, less pronounced protrusions. Similar to the findings in the 2D glass phase, the ratio between round and longish protrusions is 1:2. In the one lattice direction, the round shaped protrusions form a densely packed line of dimers, which are slightly rotated against the main direction of the line (in Figure 4a, the lines run roughly from the lower left to the upper right corner), which results in a zig-zag like appearance. Between two close-packed lines of round protrusions, there are always parallel lines with a lower density of these protrusions (50%). The resulting unit cell is marked yellow in Figure 4b. The longish protrusions are also aligned in row like structures, which run in the same direction as those formed by the round shaped protrusions (see second unit cell marked in Figure 4b, where the round and longish protrusions are marked by ovals and circles). Also in this case, there are two types of rows. In two neighboured rows the longish protrusions are oriented in the same direction. In the subsequent third row, they are rotated by ≈120°. In the latter row, the density of longish protrusions is only two thirds of that in the other two rows (4 instead of 6 longish protrusions per row and unit cell). The size of the unit cell seems to differ slightly, depending on whether the 2D crystalline domain is completely surrounded by a 2D glass domain, i.e., whether the surface is saturated with a monolayer of IL adsorbate, or whether there are adsorbate free surface areas around (= submonolayer coverage regime). The ordered domains in Figure 4a and 4b were recorded on a surface covered by a submonolayer film; in this case the unit cell has a size of 4.20 ± 0.04 nm × 3.37 ± 0.04 nm with an angle of 68 ± 2° in between. In the monolayer coverage

Figure 3: Sequence of STM images of [BMP][TFSA] adsorbed on Ag(111), acquired at 124 K, imaging the phase boundary between the 2D glass and 2D liquid phase (image-to-image time ≈11 s). Noisy features near the phase boundary and the successively changing phase boundary are indications for mobility at the phase boundary. A red frame in Figure 3b and 3c including two ovals marks two protrusions at stable positions (smaller oval), while the other protrusions in the larger oval shift to a lower position. The red arrow points out the changing position of a single protrusion. The orange boxes in Figure 3d and 3e highlight a molecular jump between two consecutive images. Subsequently, no motion is observed up to Figure 3r. The blue circles in Figure 3m and 3n show stable protrusions, while others at and close to the boundary between 2D glass structure and adsorbate free area clearly change positions (T = 124 K, U_T = −0.76 V mV, I_T = 50 pA).

Figure 4: High resolution STM images of the 2D crystalline structures on Au(111) (a, b) and Ag(111) (c). The unit cells are marked with yellow lines. Both structures are composed from round shaped and longish protrusions, which are marked with white circles and ellipsoids. In (a) the white line and in (b) the dashed lines mark the zig-zag lines of the Au(111) reconstruction, which are visible through the 2D crystalline structure of the IL adsorbates; the inset of (c) shows an enlarged part of image (c) with superimposed ball and stick models of [BMP][TFSA] (a: T = 139 K, U_T = −1.20 V, I_T = −0.060 nA; b: T = 116 K, U_T = −0.71 V, I_T = −0.10 nA; c: T = 134 K, U_T = −0.37 mV, I_T = 110 pA).
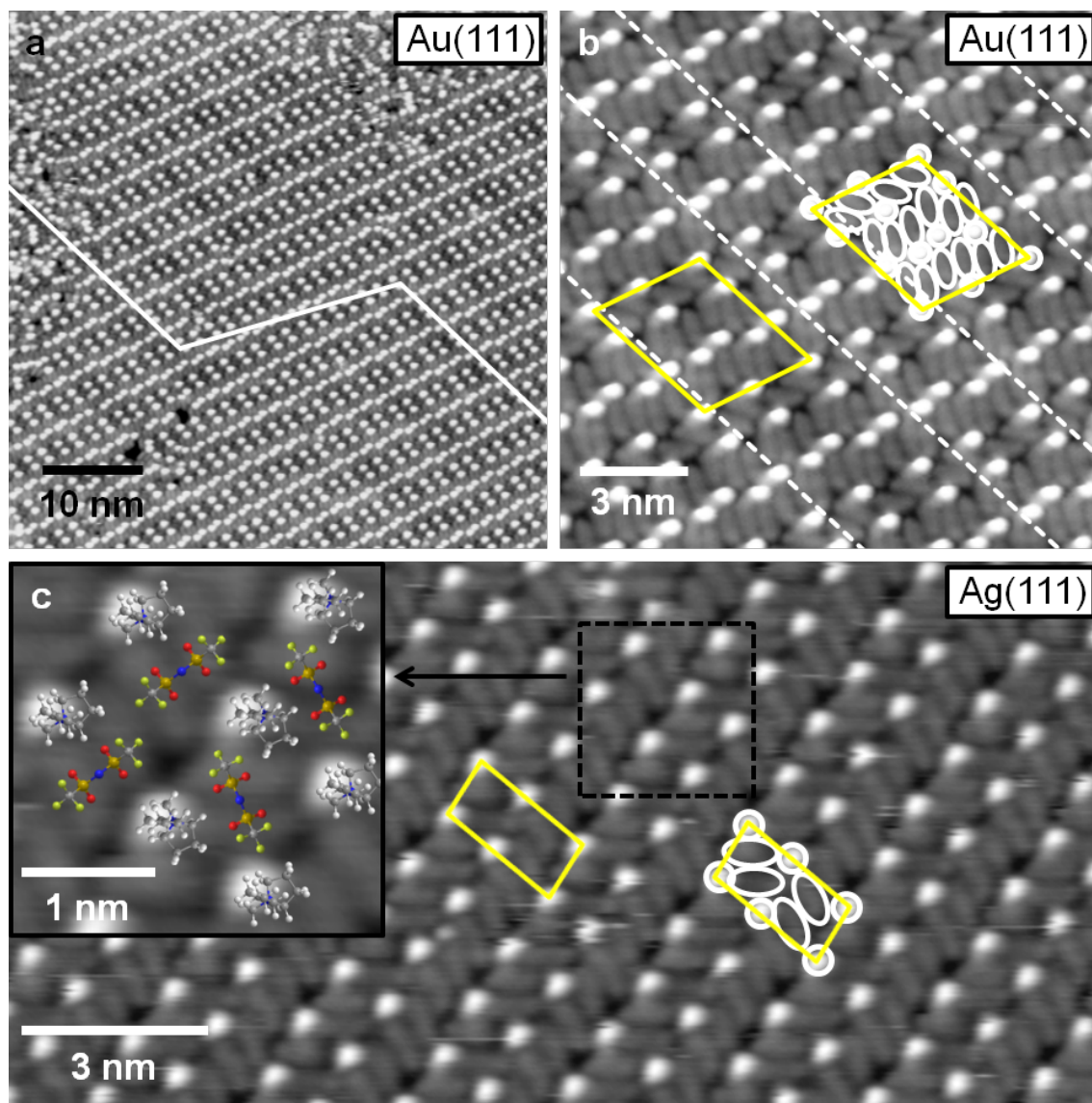
regime, the dimension of the unit cell shrunk to 3.79 ± 0.04 nm × 2.89 ± 0.04 nm, with an angle of 78 ± 2° in between, indicative of a certain flexibility in the structural arrangement of the adlayer. In both cases, the unit cell contains 8 round shaped and 16 longish protrusions, which most likely (see below) corresponds to 8 ion pairs of adsorbed [BMP][TFSA]. This gives a space requirement for one ion pair of 1.64 nm^2 in the submonolayer and 1.34 nm^2 in the monolayer coverage regime, equivalent to densities of 0.61 and 0.75 ion pairs per nm^2, respectively (see Table 1). The alignment of the unit cell with respect to the substrate lattice will be discussed below.

Atkin et al. [23] concluded from their AFM measurements that the first [BMP][TFSA] adlayer binds more strongly than the following layers, i.e., it binds more strongly to the metallic substrate than to itself. In that case, one may expect the saturation density in the first layer to be higher than in the bulk phase. For the present adsorption system this means that the bulk structure may be more similar to the ordered phase in the submonolayer coverage regime than to that at monolayer saturation.

The 2D crystalline structure of [BMP][TFSA] on Ag(111), shown in Figure 4c, is more simple than the one formed on

Table 1: Summary of the adsorbate densities and melting temperatures of the adlayer phases found on Ag(111) and Au(111).

IL adsorbate phase	density / nm^{-2}	2D melting temperature / K^{-1}
2D crystalline phase / Au(111), submonolayer coverage regime	0.61 ± 0.03	170 ± 5
2D crystalline phase / Au(111), monolayer coverage regime	0.75 ± 0.03	225 ± 5
2D glass phase / Au(111), submonolayer coverage regime	0.61 ± 0.03	113 ± 5
2D glass phase / Au(111), monolayer coverage regime	0.61 ± 0.03	173 ± 5
2D crystalline phase / Ag(111), submonolayer coverage regime	0.79 ± 0.03	180 ± 10
2D crystalline phase / Ag(111), monolayer coverage regime	0.79 ± 0.03	180 ± 10

Au(111). The round shaped protrusion are aligned in rows, running from the bottom left side to the top right side in Figure 4c. The spacing between these rows is slightly different, leading to the appearance of pairs of lines. In between these lines, the longish protrusions are also aligned in the same direction. The orientation of the long side of these protrusion changes by 120° between neighbouring rows (in the limits of the experimental accuracy), i.e, they are parallel to each other in every second row. In the row of longish protrusions that lies between the two more widely spaced rows of round shaped protrusion, the longish protrusions are aligned in a straight line (parallel to the row of round protrusions), in the neighbouring lines the longish protrusions are pairwise rotated away from the direction of the row, which allows a closer spacing between the neighbouring rows of round shaped protrusions. The unit cell of this structure is marked twice in Figure 4c with yellow lines; in one of these cases, the protrusions in the unit cell are marked by white circles and ovals. The size of the unit cell is 1.1 ± 0.1 nm × 2.3 ± 0.1 nm with an angle of 95 ± 3° in between the two lattice directions. For Ag(111), the size (2.5 nm^2) and geometry of the unit cell was found to be independent of the IL adsorbate coverage. The unit cell contains 2 round and 4 longish protrusions, which represent two [BMP][TFSA] ion pairs (see below). In that case, the space requirement per IL ion pair is 1.25 nm^2, the density of the adsorbed ion pairs is 0.79 nm^{-2}. This is very similar to the density of ion pairs on Au(111) in the monolayer regime, while in the submonolayer regime the ion pairs on Au(111) have a 30% lower density.

Next we will discuss additional aspects of the 2D crystalline phase, such as its alignment with respect to the substrate surface lattice, its distribution structure on the surface, etc. The orientation of the IL adlayer can be derived from larger scale images as shown in Figure 5a and 5b for Au(111). In the image in Figure 5a, the Au(111) surface was covered with 1 ML of [BMP][TFSA]. The image shows one island of the 2D crystalline structure, which is surrounded by the 2D glass structure, as typical for the monolayer regime. The amount of the 2D crystalline structure relative to that of the 2D glassy was found to vary between experiments. In most cases, the amount of the

2D glass structure is higher than that of the 2D crystalline phase, and islands of the latter phase are embedded in a surrounding 2D glass phase. In the submonolayer regime (Figure 5b) this is similar, but the amount of 2D crystalline structure relative to that of the 2D glass phase is typically higher. This is illustrated in Figure 1c: on samples with a low coverage of [BMP][TFSA] adsorbates we only observed small islands with 2D glass structure (which are mostly growing from the elbow sites of the Au(111) reconstruction pattern), while the islands of the 2D crystalline structure present in between are much larger. The physical reason for the higher fraction of 2D crystalline phase at lower coverages, which reflects an easier alignment of the adsorbate species during cool-down under theses conditions, may only be speculated upon. It may be related to more stable adsorption at the perimeter of islands of the 2D crystalline phase compared to (small islands of) the 2D glass phase, which allows preferential growth of the former ones during cool down at lower coverages, while at higher coverage such effects do not seem to play a significant role.

The STM image in Figure 5a reveals another phenomenon typical for [BMP][TFSA] on Au(111). The 2D crystalline structure is also severely affected by the reconstruction pattern of the Au(111) surface. In this image, the zig-zag line pairs of the herringbone reconstruction are clearly visible through the adlayer, they are marked in Figure 5a with white lines in the upper right part to guide the eye. Note that for the 2D glass phase the reconstruction could not be resolved. In Figure 4a and 4b, the reconstruction pattern is also visible, but less pronounced. It is marked by a white line in Figure 4a. The adlayer is usually aligned in such a way that the direction of the longer side of the unit cell (see Figure 4b) is parallel to the lines of the Au(111) reconstruction pattern. Accordingly, the 2D crystalline phase tends to grow in domains/islands which are limited by the domain boundaries of the herringbone reconstruction, i.e., by the bending points of the dislocation lines. This can be seen in Figure 5a, where the positions of the bending points of the Au(111) surface reconstruction are connected with white dashed lines. A large part of the 2D crystalline domain visible on this image, which extends diagonally
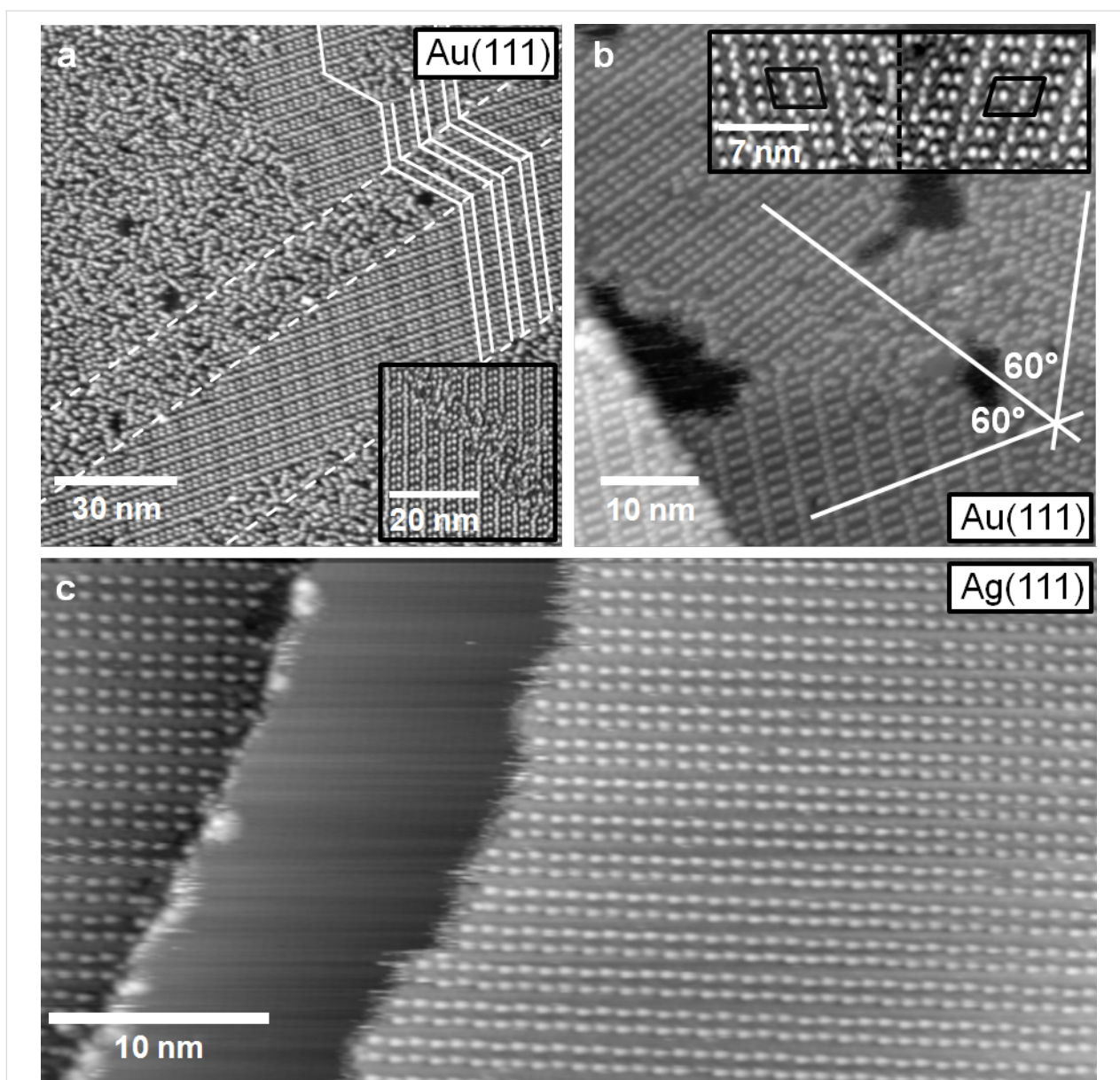
Figure 5: (a) STM image of a monolayer film of [BMP][TFSA] on Au(111), showing both 2D crystalline islands as well as 2D glass areas. The Au(111) reconstruction is visible in the 2D crystalline island (for better visibility it is marked with white lines in the upper right of the image). In the 2D glass domain, this is not resolved; dashed lines mark the domain boundaries of the Au(111) reconstruction pattern (T = 118 K, U_T = −1.25 V, I_T = −0.060 nA). (b) STM image of 2D crystalline domains of [BMP][TFSA] on a single Au(111) terrace in direct contact to each other. The domains are rotated by 60° to each other (T = 146 K, U_T = −1.20 V, I_T = 60 pA). (c) STM image of a submonolayer film of [BMP][TFSA] on Ag(111). The adlayer islands nearly completely consist of the 2D crystalline structure. The island boundary shows a frizzy appearance, which is associated with mobility of the adsorbed IL species, either along the island edge or in a 2D adsorption–desorption equilibrium between the 2D solid and the adjacent 2D gas phase (T = 130 K, U_T = −1.09 V, I_T = 80 pA).

across the image, grows on one domain of the Au(111) reconstruction and fills it nearly completely. As can be seen in the upper part of the image, it is also possible for the adlayer structure to grow across such kind of domain boundary in the Au(111) reconstruction pattern. This was only observed, however, when the adlayer domain spanned at least over three Au(111) reconstruction domains and the part with the 'wrong' orientation is in the middle. In this case we often observed a

narrow stripe of 2D glass phase directly at the elbows of the Au(111) reconstruction pattern (see inset in Figure 5a). Isolated 2D crystalline islands, which are limited to a single domain of the Au(111) reconstruction and where the rotational orientation of the adlayer island, as described above, does not fit to the orientation of the Au(111) reconstruction, have not been observed. It is interesting to note that the elbows of the Au(111) reconstruction act as nucleation sites for nucleation of 2D glass

phase islands, and on the other hand limit domains of the 2D crystalline phase, which seems to be in contrast to each other. A simple physical explanation is still missing.

Because of the threefold symmetry of the Au(111) surface and of the Au(111) reconstruction pattern there are only three different orientations for the 2D crystalline domain on the surface possible. In Figure 5b, three 2D crystalline domains are present which are rotated at angles of 120° relative to each other. Furthermore, because of the non-rectangular form of the adlayer unit cell, two different chiral forms of that unit cell (see Figure 4b) are possible along each direction, leading to 6 possible adlayer domains in total. An example for two islands with chiral structure is shown in the inset in Figure 5b.

On Ag(111), the situation is very different because of the absence of a surface reconstruction. In this case the domains of the 2D crystalline structure mostly extend across the entire terraces, i.e., the domains extend across hundreds of nanometers (if the surface is well prepared and the terraces are sufficiently large). This is equally true also for islands of the 2D crystalline phase in the submonolayer coverage regime, where these islands coexist with large areas of adsorbate free surface. At typical images sizes, most of the STM images show either a fully covered or an adsorbate free surface. Small terraces with a width ≤10 nm are covered with ILs adsorbed in the 2D glass structure as described above. The 2D crystalline structure is normally attached to an ascending Ag(111) step, mostly with a small amount of the 2D glass structure between step and ordered adlayer phase. In this case, the width of the 2D glass phase is between a few molecules to several nm. It seems as if the steps of the substrate surface disturb the formation of the 2D crystalline structure, rather than acting as nucleation sites. When comparing different domains (an example is shown in Figure 5c) of the 2D crystalline structure, they are all aligned in the same direction to each other (like in Figure 5c) or at angles of 60° or 120° to each other, even when they grow on different terraces of the substrate. This suggests that the adlayer structure also follows the threefold geometry of the Ag(111) surface. Due to experimental reasons (adlayer imaging requires a large tunnel resistance while atomic resolution require low tunnel resistances) it was not possible to achieve atomic resolution of the surface near a boundary of a 2D crystalline island, therefore it was not possible to correlate the adlayer orientation directly with the substrate lattice.

In addition to the different arrangements of [BMP][TFSA] on Au(111) and Ag(111), we also found differences in the mobility of the island edges of the 2D crystalline phase, evidenced by a frizzy appearance of the island edges (Figure 5b and 5c). The frizzyness of the island boundary is proportional to the displace-

ment of the boundary position between subsequent images, which arises from 2D adsorption/desorption of molecules at the island perimeter or diffusion of adsorbates along the island perimeter. The displacement can be quantified by determining the change in position of the island boundary in successive STM line scans. A quantitative evaluation revealed that the root mean square deviation of the position is more than double for Ag(111) (see Figure 5c) than for Au(111) (Figure 5b), indicative of a significantly higher mobility of the adsorbates at the island perimeters on the Ag(111) surface than on Au(111).

The mobility of the IL adsorbates at the edge of a 2D crystalline adlayer island on Ag(111) is resolved in more detail in the sequence of STM images shown in Figure 6. The images were acquired at the same position with a frame to frame time of 11 s. It is clearly visible that the island edge changes with time. Places, where the round shaped protrusions vanished from one image to the other, are labelled with red arrows. Those places, where a round shaped protrusion is added to the structure are labelled with green arrows. Similarly as discussed for the mobility of the 2D glass phase on Ag(111), we assume that these changes are due to sudden motion of IL adsorbates along the island edge, or, more plausible, to 2D adsorption–desorption equilibrium between the IL adsorbate islands and a 2D gas/liquid of IL adsorbates. Again those regions, which are apparently free of adsorbate appear with streaky features, which we attribute to highly mobile molecules in a 2D gas/liquid phase, which diffuse to fast to be resolved with STM. Round shaped protrusion in the inner parts of the islands remain stable over time. The difference compared to the 2D glass phase, where infrequent jumps of these protrusions were possible, is explained by a higher stability and the absence of defects in the 2D crystalline phase.

Despite of the considerable structural insight gained from these STM images it was not possible to unambiguously identify the adsorbed IL species, specifically the adsorbed cations and anions in these images. This is possible by combination with dispersion corrected density functional theory (DFT-D) calculations, performed recently for adsorption of individual [BMP][TFSA] ion pairs on Ag(111) [26]. Details on the calculations can be found elsewhere [26].

According to those calculations, the ring of the cation lies flat on the surface and the butyl group points upwards. The anion adsorbs in a cis-configuration (both SO_2-groups are positioned on the same side of the molecule, both CF_3 groups on the other side, as it is also shown in Figure 1a) on the Ag(111) surface and binds via its two oxygen atoms to the surface. The CF_3 groups point towards the vacuum. In this conformation both ion types of [BMP][TFSA] are in direct contact to the surface.
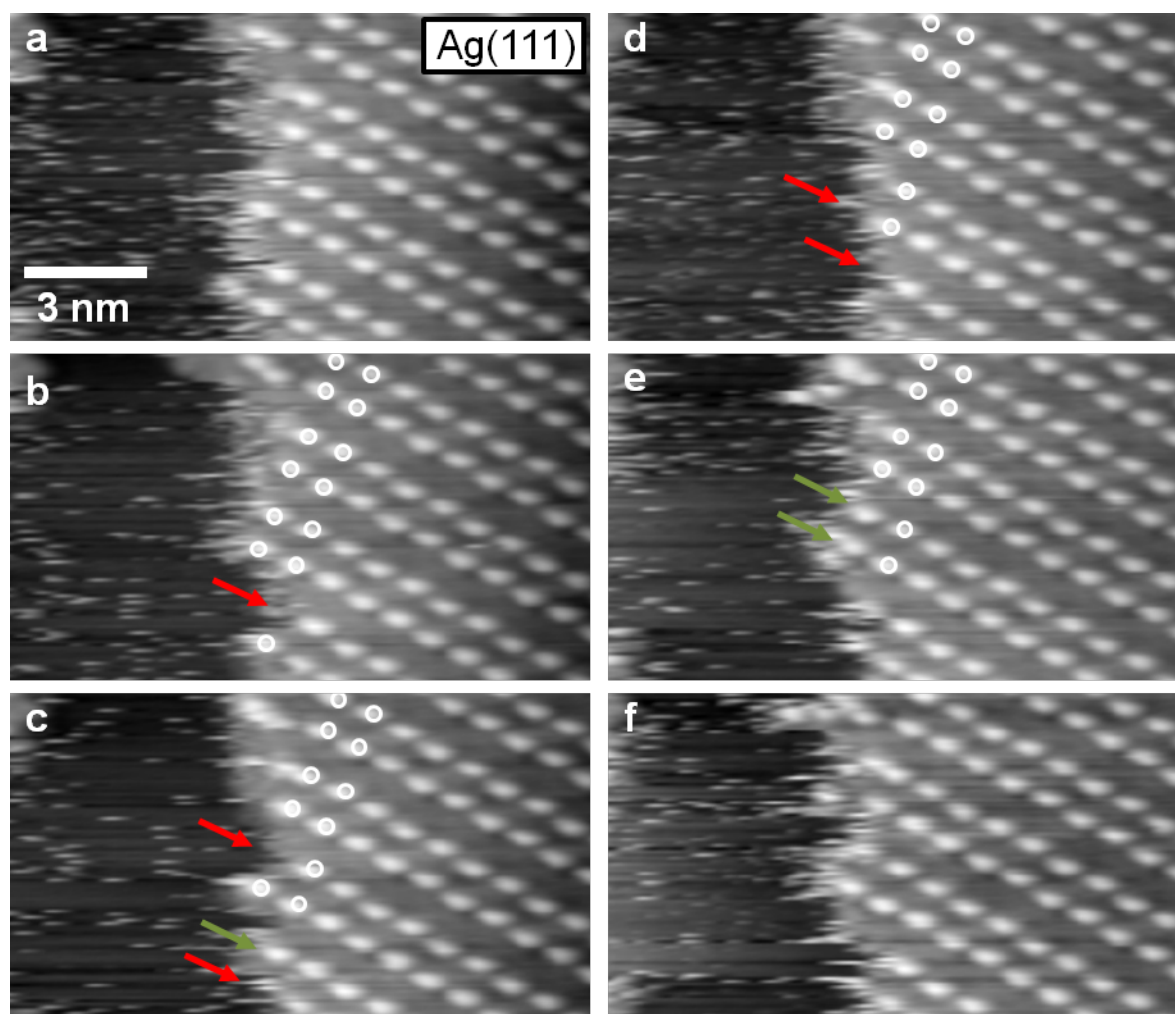
Figure 6: Time sequence of STM images at the phase boundary of the 2D crystalline phase of [BMP][TFSA] on Ag(111), recorded at 124 K (image to image time of ≈11 s) The images exhibit frizzy features directly at the 2D crystalline | 2D liquid interface, reflecting mobility of the adsorbed IL species, either along the island edge or in a 2D adsorption–desorption equilibrium. The red arrows in the images show places at the boundary, where round shaped protrusions vanish compared to the preceding image. The green arrows depict locations where a protrusion is attached to the boundary (T = 124 K, U_T = −0.76 V, I_T = 50 pA).

Simulated STM images using tunnelling conditions similar to the experimental ones (similar potential, comparable tip–surface separation) yield characteristic features very similar to those in the measured STM images. The upright standing butyl chain of the cation appears as round shaped protrusion. Right next to it an oval protrusion appears with lower height, which is due to the parts of the alkyl ring that are not directly lying below the butyl chain. In the measured STM images, only the round shaped protrusion is visible due to the limited resolution of the STM tip. The anion appears in the simulated images as two longish protrusions each of which is generated mainly by 2 fluorine atoms of the CF_3-groups, in perfect agreement with experimental findings. Similar to experimental data, also their height is significantly lower than that of the round shaped protrusion reflecting the butyl chain of the cation.

Although these calculations did not include interactions between neighboured adsorbed ion pairs, the good agreement between the characteristic features in the experimental and calculated STM images are strong evidence for the validity of this assignment. Further support comes from the qualitative agreement with the ARXPS measurements of [BMP][TFSA], [MMIM][TFSA] and [OMIM][TFSA] adsorbed on Au(111) [19,25]. A suggestion for the structure model for BMP-TFSA on Ag(111) based on these data is shown in the inset of Figure 4c, where ball and stick models of the [BMP$^+$] and [TFSA]$^-$ ions are superimposed to the STM-image.

Another interesting result from these calculations was that based on a Bader charge analysis of the adsorption complex, the charges of the cation and the anion hardly change upon adsorp-

tion, and that the adsorption bond is dominated by van der Waals interactions. We expect these results as characteristic also for adsorption on Au(111).

Thermal stability of the adlayer structure

Further information on adsorbate–adsorbate interactions can be derived from the thermal stability and the melting temperature of the structures on the surface. This was investigated by slowly heating up samples in the STM from 100 K to room temperature while recording STM images. Because of the very low heating rate (3 h for heating from 100 K to 300 K) the surface has enough time to maintain thermodynamic equilibrium during heating. Generally, the noise level in the STM images increased with rising temperature, implying a higher mobility of the 2D liquid on the surface. At certain temperatures it was finally not possible any more to resolve the adsorbate structures on the surface, which was interpreted as the temperature where the ion pairs, which before formed the island/domain started to move. This temperature is considered here as melting temperature (for the 2D glass structure it would be more correct to describe it as a glass transition when comparing to the notation in a bulk system, but for simplicity we use the term "melting temperature" for both adlayer structures). For the adlayer structures on the Au(111) surface, we could determine four different melting temperatures, which differ in a characteristic way: the 2D glass structure is stable up to a temperature of 113 ± 5 K in the submonolayer and up to 173 ± 5 K in the monolayer regime. The 2D crystalline structure is maintained up to 170 ± 5 K in the submonolayer and up to 225 ± 5 K in the monolayer regime. Hence, islands are thermally less stable than closed layers and the 2D glass structure is less stable than the 2D crystalline one.

On Ag(111), the melting temperature could only be determined for the 2D crystalline phase, where it was found to be 180 ± 10 K, both in the submonolayer and monolayer coverage regime. Because of the small amount of the 2D glass structure on the surface it was not possible to determine a defined melting point for the 2D glass structure, it definitely decays at lower temperatures than the 2D crystalline structure.

The thermal stability of the island is mainly determined by two parameters, by the surface diffusion barrier, i.e., the activation barrier for the motion of individual adsorbed species between two adjacent adsorption sides, and the interactions between adjacent adsorbates (adsorbate–adsorbate interactions). The fact that the IL adsorbates form islands at low temperatures is a clear proof for the existence of attractive adsorbate–adsorbate interactions between the adsorbed IL species. Furthermore it shows that the adsorbate–adsorbate interactions exceed the strength of the surface diffusion barrier, since otherwise the IL adsorbates would be trapped on their adsorption sites before

they are able to undergo a 2D nucleation and growth process during cool-down to 100 K. Sufficient mobility of individual molecules is indicated also by the mobility at the island edges. Therefore, the temperature for 2D melting is dominated by the strength of the attractive adsorbate–adsorbate interactions. Interestingly, the trend in melting temperatures of the 2D crystalline phases on Ag(111) and Au(111) does not correlate with that of the adlayer density (see Table 1). While the 2D melting temperature on Ag(111) is only little higher than that of the 2D crystalline adlayer on Au(111) in the submonolayer regime, the density is comparable with that of the monolayer coverage adlayer on Au(111). This indicates that the adlayer stability is affected by the nature of the substrate, not only by purely distance (and thus density) dependent adsorbate–adsorbate interactions.

Since the structures in the 2D glass phase are similar for both substrates, we would expect the same melting temperature in both cases. It was not possible, however, to reliably determine the melting temperature of the 2D glass phase on Ag(111) (see above). For adsorption on Au(111), the lower melting temperature in the 2D glass phase compared to that in the 2D crystalline phase arises from the fact that the 2D glass phase is most likely a kinetically hindered structure and therefore not in thermodynamic equilibrium, which is less stable than the equilibrium phase. Interestingly, though the monolayer and the submonolayer coverage 2D glass adlayer have the same local density, the melting temperature of the latter is significantly lower. On the other hand, the melting temperature of the 2D glass phase at monolayer coverage and the 2D crystalline phase at submonolayer coverage, which also have similar densities, are essentially identical. In that case, the higher amount of defects in the former structure does not seem to play an important role.

Conclusion

We have investigated substrate effects on the structure and structure formation, and thus on the substrate–adsorbate and adsorbate–adsorbate interactions, for the adsorption of [BMP][TFSA] by STM, by comparing their adsorption on the close-packed Au(111) and Ag(111) surfaces under UHV conditions in the temperature region between 100 K and 293 K. In combination also with previous data, these measurements lead to the following conclusions and adsorption characteristics:

1) Upon adsorption at room temperature, the [BMP][TFSA] adsorbates form a 2D gas/2D liquid phase with highly mobile adsorbed species on the surface. The integrity of the ions is maintained and both ions are in direct contact with the substrate surface. Interaction with the surface results in modifications of the electronic structure compared to that in condensed

thicker layers. While XPS data exist only for adsorption on Au(111), we expect similar behavior also for adsorption on Ag(111).

2) Upon cooling the sample to 100 K, molecular motion in the adlayer is frozen and the adsorbates form islands/domains on the surface with 2D crystalline and 2D glass structures. In the submonolayer coverage regime, these coexist with (essentially) adsorbate free surface areas (2D gas). On Ag(111), the adsorbates form large islands consisting of a single domain of the 2D crystalline structure on terraces wider than ≈10 nm, while small terraces are (partly) covered with a 2D glass structure, and this phase dominates also in regions directly in front of ascending substrate steps. On Au(111), both structures are formed in small islands on the surface in the submonolayer regime. In the monolayer regime islands of the 2D crystalline phase are surrounded by the 2D glass phase. The 2D crystalline adlayer structure on Ag(111) is oriented along Ag surface lattice, with 3 different adlayer lattice orientations at angles of 120° to each other reflects the threefold symmetry of the Ag(111) substrate.

3) The 2D solid adlayer phases exhibit characteristic patterns consisting of round protrusions and longish protrusions in a ratio of 1:2. Based on comparison with results of previous DFT calculations [26], the round protrusion are identified as cations, with their ring lying flat on the surface and the butyl group pointing upwards, while the [TFSA] anions are represented by pairs of parallel longish protrusions. These mainly arise from the CF_3 groups which are pointing upwards, while the anions bind to the surface with their O-atoms. Based on the similar structural characteristics in the STM images, we expect a similar adsorption geometry also for Au(111), where no DFT calculations exist.

4) Structure formation and adlayer structure/adlayer order are strongly affected by the reconstruction of the Au(111) substrate. Furthermore, they are also affected by the chemical nature of the substrate. The latter is reflected by the slightly different geometry (and IL adsorbate density) of the adlayer unit cell on the two surfaces, while the general appearance of the adlayer structure is identical on both substrate surfaces. The comparable density achieved on Au(111) in the monolayer coverage regime points to similar size substrate–adsorbate interactions on both surfaces. The influence of the reconstruction of the Au(111) surface is indicated in several ways: In addition to steps, the elbows of the Au(111) reconstruction act as preferential nucleation sites, starting island growth at these sites. Furthermore, they tend to induce narrow stripes of 2D glass phase in the adlayer when overgrown by an 2D crystalline adsorbate island/domain. The orientation of the 2D crystalline structure is also influenced by the Au(111) reconstruction

pattern, it prefers to be oriented with the longer side of its unit cell along the Au(111) dislocation lines. Therefore domain boundaries of the adlayer structure often coincide with the connection line of adjacent elbows, where the Au(111) reconstruction pattern bends.

5) The (2D) melting temperature of the 2D solid phases is affected by substrate effects, by the adlayer coverage and by the order in the adlayer/domain. The melting temperature is significantly higher for the 2D crystalline phase on Au(111) than for the 2D glass phase, and it is higher in the (more closely packed) adlayer in the monolayer coverage regime than in the submonolayer coverage regime on the same substrate. For adsorption on Ag(111), where the density of the 2D crystalline phase does not depend on the overall coverage and where the size of the 2D crystalline islands is generally very large, we found no effects of the overall IL adsorbate coverage. The 2D melting temperature on Ag(111) resembles that on Au(111) in the submonolayer coverage regime, despite of the significantly lower density in the latter case. On the other hand, despite of similar densities on Ag(111) and Au(111) in the monolayer coverage regime (2D crystalline phase), the melting is significantly higher in the latter case, indicative of stronger (effective) adsorbate–adsorbate interactions on Au(111) than on Ag(111).

Experimental

The measurements were performed in an UHV system with a base pressure of $<4 \times 10^{-10}$ mbar, equipped with an Aarhus type STM (SPECS; Aarhus STM 150), which allows measurements in the temperature range between 90 and 400 K, and standard facilities for surface preparation and surface characterization.

The Au(111) and Ag(111) samples were purchased from Mateck GmbH and cleaned by repeated sputtering with Ar^+ (0.5 keV, 4 µA, 30 min) and heating to 770 K for 30 min, until atomically flat surfaces with mean terrace sizes of >100 nm were obtained (checked by STM). The Au(111) surface exhibited the typical reconstruction pattern with its characteristic regular zig-zag pattern [27]. Between two measurements, only a single cleaning cycle was sufficient to obtain a clean surface again.

The ionic liquid [BMP][TFSA] was purchased from Merck in ultrapure quality. It was mounted in a quartz crucible in a Knudsen effusion cell (Ventiotec, OVD-3) in the UHV chamber. It was degassed for more than one week in UHV at room temperature, followed by several hours degassing at 360 K. The crucible itself was also baked at 870 K in UHV before filling it with the IL. Prior to the experiments, the evaporation behaviour of [BMP][TFSA] was tested with a quartz

micro balance. Based on these preliminary measurements, an evaporation temperature of 375 K was used in the experiments, which resulted in a pressure of 5×10^{-10} mbar. At this flow, a deposition time of 3 min resulted in a coverage of ca. 1 ML, as verified by STM. The cleanliness of the IL vapour was tested with a quadrupole mass spectrometer.

One monolayer is defined as one closed layer of ions in direct contact to the surface. In other publications [19,21], one closed layer of IL was defined as a layer of IL molecules with the cation and anion on top of each other, which gives 50% smaller values compared to our definition. These values were corrected to fit our definition in the present discussion.

Acknowledgements

References

1. Welton, T. *Chem. Rev.* **1999,** *99,* 2071. doi:10.1021/cr980032t
2. Wasserscheid, P.; Keim, W. *Angew. Chem., Int. Ed.* **2000,** *39,* 3772. doi:10.1002/1521-3773(20001103)39:21<3772::AID-ANIE3772>3.0.CO;2-5
3. Silvester, D. S. *Analyst* **2011,** *136,* 4871. doi:10.1039/c1an15699c
4. Endres, F.; Zein El Abedin, S. *Phys. Chem. Chem. Phys.* **2006,** *8,* 2101. doi:10.1039/b600519p
5. Slattery, J. M.; Daguenet, C.; Dyson, P. J.; Schubert, T. J. S.; Krossing, I. *Angew. Chem.* **2007,** *119,* 5480. doi:10.1002/ange.200700941
6. Appetecchi, G. B.; Montanino, M.; Zane, D.; Carewska, M.; Alessandrini, F.; Passerini, S. *Electrochim. Acta* **2009,** *54,* 1325. doi:10.1016/j.electacta.2008.09.011
7. Ueno, K.; Tokuda, H.; Watanabe, M. *Phys. Chem. Chem. Phys.* **2010,** *12,* 1649. doi:10.1039/b921462n
8. Armand, M.; Tarascon, J.-M. *Nature* **2008,** *451,* 652. doi:10.1038/451652a
9. Scrosati, B.; Garche, J. *J. Power Sources* **2010,** *195,* 2419. doi:10.1016/j.jpowsour.2009.11.048
10. Yabuuchi, N.; Shimomura, K.; Shimbe, Y.; Ozeki, T.; Son, J.-Y.; Oji, H.; Katayama, Y.; Miura, T.; Komaba, S. *Adv. Energy Mater.* **2011,** *1,* 759. doi:10.1002/aenm.201100236
11. MacFarlane, D. R.; Forsyth, M.; Howlett, P. C.; Pringle, J. M.; Sun, J.; Annat, G.; Neil, W.; Izgorodina, E. I. *Acc. Chem. Res.* **2007,** *40,* 1165. doi:10.1021/ar7000952
12. Endres, F. *ChemPhysChem* **2002,** *3,* 144. doi:10.1002/1439-7641(20020215)3:2<144::AID-CPHC144>3.0.CO;2-#
13. Borisenko, N.; Zein El Abedin, S.; Endres, F. *J. Phys. Chem. B* **2006,** *110,* 6250. doi:10.1021/jp057337d
14. Moustafa, E. M.; Zein El Abedin, S.; Shkurankov, A.; Zschippang, E.; Saad, A. Y.; Bund, A.; Endres, F. *J. Phys. Chem. B* **2007,** *111,* 4693. doi:10.1021/jp0670687
15. Ikari, T.; Keppler, A.; Reinmöller, M.; Beenken, W. J. D.; Krischok, S.; Marschewski, M.; Maus-Friedrichs, W.; Höfft, O.; Endres, F. *e-J. Surf. Sci. Nanotechnol.* **2010,** *8,* 241. doi:10.1380/ejssnt.2010.241
16. Foulston, R.; Gangopadhyay, S.; Chiutu, C.; Moriarty, P.; Jones, R. G. *Phys. Chem. Chem. Phys.* **2012,** *14,* 6054. doi:10.1039/c2cp23901a
17. Cremer, T.; Killian, M.; Gottfried, J. M.; Paape, N.; Wasserscheid, P.; Maier, F.; Steinrück, H.-P. *ChemPhysChem* **2008,** *9,* 2185. doi:10.1002/cphc.200800300
18. Kolbeck, C.; Cremer, T.; Lovelock, K. R. J.; Paape, N.; Schulz, P. S.; Wasserscheid, P.; Maier, F.; Steinrück, H.-P. *J. Phys. Chem. B* **2009,** *113,* 8682. doi:10.1021/jp902978r
19. Cremer, T.; Stark, M.; Deyko, A.; Steinrück, H.-P.; Maier, F. *Langmuir* **2011,** *27,* 3662. doi:10.1021/la105007c
20. Cremer, T.; Wibmer, L.; Calderón, S. K.; Deyko, A.; Maier, F.; Steinrück, H.-P. *Phys. Chem. Chem. Phys.* **2012,** *14,* 5153. doi:10.1039/c2cp40278e
21. Steinrück, H.-P. *Phys. Chem. Chem. Phys.* **2012,** *14,* 5010. doi:10.1039/c2cp24087d
22. Armstrong, J. P.; Hurst, C.; Jones, R. G.; Licence, P.; Lovelock, K. R. J.; Satterley, C. J.; Villar-Garcia, I. J. *Phys. Chem. Chem. Phys.* **2007,** *9,* 982. doi:10.1039/b615137j
23. Atkin, R.; Zein El Abedin, S.; Hayes, R.; Gasparotto, L. H. S.; Borisenko, N.; Endres, F. *J. Phys. Chem. C* **2009,** *113,* 13266. doi:10.1021/jp9026755
24. Waldmann, T.; Huang, H.-H.; Hoster, H. E.; Höfft, O.; Endres, F.; Behm, R. J. *ChemPhysChem* **2011,** *12,* 2565. doi:10.1002/cphc.201100413
25. Uhl, B.; Cremer, T.; Roos, M.; Maier, F.; Steinrück, H.-P.; Behm, R. J. *Phys. Chem. Chem. Phys.* **2013,** *15,* 17295. doi:10.1039/c3cp52184b
26. Buchner, F.; Forster-Tonigold, K.; Uhl, B.; Alwast, D.; Wagner, N.; Farkhondeh, H.; Groß, A.; Behm, R. J. *ACS Nano* **2013,** *7,* 7773. doi:10.1021/nn4026417
27. Barth, J. V.; Brune, H.; Ertl, G.; Behm, R. J. *Phys. Rev. B* **1990,** *42,* 9307. doi:10.1103/PhysRevB.42.9307
28. Rogers, E. I.; Silvester, D. S.; Poole, D. L.; Aldous, L.; Hardacre, C.; Compton, R. G. *J. Phys. Chem. C* **2008,** *112,* 2729. doi:10.1021/jp710134e
29. Sobota, M.; Nikiforidis, I.; Hieringer, W.; Paape, N.; Happel, M.; Steinrück, H.-P.; Görling, A.; Wasserscheid, P.; Laurin, M.; Libuda, J. *Langmuir* **2010,** *26,* 7199. doi:10.1021/la904319h
30. Jaeger, R. M.; Kuhlenbeck, H.; Freund, H.-J.; Wuttig, M.; Hoffmann, W.; Franchy, R.; Ibach, H. *Surf. Sci.* **1991,** *259,* 235. doi:10.1016/0039-6028(91)90555-7
31. Libuda, J.; Bäumer, M.; Freund, H.-J. *J. Vac. Sci. Technol., A* **1994,** *12,* 2259. doi:10.1116/1.579126
32. Hammer, B.; Nielsen, O. H.; Nørskov, J. K. *Catal. Lett.* **1997,** *46,* 31. doi:10.1023/A:1019073208575
33. Chambliss, D. D.; Wilson, R. J.; Chiang, S. *Phys. Rev. Lett.* **1991,** *66,* 1721. doi:10.1103/PhysRevLett.66.1721
34. Yokoyama, T.; Yokoyama, S.; Kamikado, T.; Okuno, Y.; Mashiko, S. *Nature* **2001,** *413,* 619. doi:10.1038/35098059

Many-body effects in semiconducting single-wall silicon nanotubes

Wei Wei and Timo Jacob[*]

Full Research Paper

Address:
Institute of Electrochemistry, Ulm University, Albert-Einstein-Allee 47, D-89081 Ulm, Germany

Email:
Timo Jacob[*] - timo.jacob@uni-ulm.de

* Corresponding author

Abstract

The electronic and optical properties of semiconducting silicon nanotubes (SiNTs) are studied by means of the many-body Green's function method, i.e., *GW* approximation and Bethe–Salpeter equation. In these studied structures, i.e., (4,4), (6,6) and (10,0) SiNTs, self-energy effects are enhanced giving rise to large quasi-particle (QP) band gaps due to the confinement effect. The strong electron−electron ($e−e$) correlations broaden the band gaps of the studied SiNTs from 0.65, 0.28 and 0.05 eV at DFT level to 1.9, 1.22 and 0.79 eV at *GW* level. The Coulomb electron−hole ($e−h$) interactions significantly modify optical absorption properties obtained at noninteracting-particle level with the formation of bound excitons with considerable binding energies (of the order of 1 eV) assigned: the binding energies of the armchair (4,4), (6,6) and zigzag (10,0) SiNTs are 0.92, 1.1 and 0.6 eV, respectively. Results in this work are useful for understanding the physics and applications in silicon-based nanoscale device components.
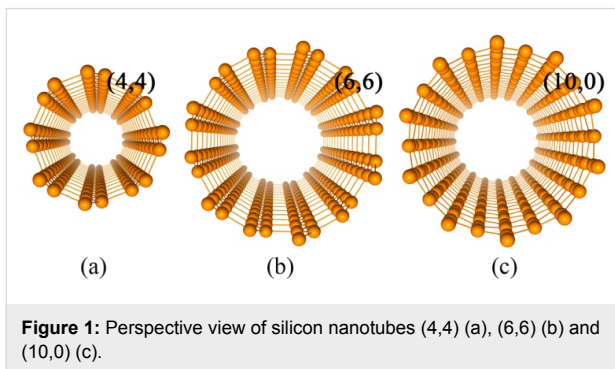
Introduction

Silicon nanotubes [1-5] (SiNTs) have been demonstrated to be emerging materials with exclusive applications in micro- and nanoelectronics [6-12]. An extra advantage of SiNTs lies in the natural compatibility with current silicon-based technology. Their noncytotoxic nature, further, makes them promising candidates for a large variety of biotechnological applications as well. In addition, due to the quantum confinement effect, SiNTs have great potential for photoemission applications directly on silicon substrates that in turn could lead to the integration of photonics and microelectronic devices on a single chip [13].

One-dimensional SiNTs have been viewed as potential basic building blocks for future applications. SiNTs exhibit, for instance, excellent electrochemical performances when being used as anodes for lithium rechargeable batteries [10-12]. Although the ground-state geometric and electronic properties of SiNTs have been studied [14-17], properties of excited states, for example optical absorption of SiNTs, are still in need. It is of high importance to correctly understand the optical properties of SiNTs due to fundamental applications in electro-optical fields.

In structures with reduced dimensionality, higher quasi-particle (QP) excitation energies can be reached by confinement effects, which enhance electron−electron (*e*−*e*) self-energy effects. In addition, reduced electronic screening leads to the formation of excitonic resonances or strongly bound excitons with considerable binding energies. Therefore, many-body effects [18-31] are required to understand this kind of systems sufficiently, especially their single-particle excitation and optical absorption properties.

It is well-known that density functional theory (DFT) often fails in describing the properties of light absorption. This process requires a description of two-particle properties, which certainly goes beyond single-electron excitations that can be described at the purely electronic level. Fortunately it is possible to make quantitative predictions of the absorption spectra and the band structures of a wide class of systems by combining the *GW* approximation and the Bethe−Salpeter equation (BSE) [32-37], i.e., many-body Green's function perturbation theory. The *GW*+BSE scheme properly includes the *e*−*e* correlations and *e*−*h* interactions and its results frequently match experimental results in an excellent manner [38-41].

In the present work, many-body effects in semiconducting single-wall (4,4), (6,6) and (10,0) SiNTs, as shown in Figure 1, are studied. It has been identified that the self-energy effects are evident in the studied SiNTs, giving rise to large QP band gaps, and the excitonic effects distinctly modify optical absorption properties, resulting in the formation of bound excitons with considerable binding energies. The results shed some light on understanding the physical properties of SiNTs and potential applications in silicon-based nanoscale device components. It should be pointed out that many-body effects have also been highlighted in silicon nanowires [24,42] and carbon nanotubes due to the reduced dimensionality [43-45].

Figure 1: Perspective view of silicon nanotubes (4,4) (a), (6,6) (b) and (10,0) (c).

Computational details

On the basis of DFT-calculated ground-state wave functions, obtained with the plane wave packge QUANTUM ESPRESSO

[46], QP calculations have been performed. For these calculations we used a plane-wave basis set with a cutoff energy of 50 Ry and the local density approximation (LDA) for the exchange−correlation energy in conjunction with the norm-conserving pseudopotentials for treating the core-electrons. A Monkhorst−Pack *k*-mesh of 20 integration points is used along the SiNTs tubes. A sufficiently large vacuum spacing of 13 Å surrounding the tube is imposed to separate periodic images and to avoid spurious interactions. Geometry optimization has been done with an energy convergence criterion of 5.0×10^{-6} eV and a force convergence criterion of 0.01 eV/Å.

As already summarized in [47], starting from the LDA wave functions and Coulomb screening, QP energies (within the *GW* approximation for the electron self-energy operator Σ) are obtained by solving the Dyson equation [48]:

$$G_{n\mathbf{k}}(\omega) = \left[\left(G_{n\mathbf{k}}^{0}(\omega) \right)^{-1} - \Sigma_{n\mathbf{k}}(\omega) + V_{n\mathbf{k}}^{\mathrm{XC}} \right]^{-1}$$

with the non-interacting Green's function

$$G_{0}^{n\mathbf{k}}(\omega) = \frac{f_{n\mathbf{k}}}{\omega - \varepsilon_{n\mathbf{k}} - i0^{+}} + \frac{1 - f_{n\mathbf{k}}}{\omega - \varepsilon_{n\mathbf{k}} + i0^{+}},$$

and $f_{n\mathbf{k}}$ being the occupation factor and $\varepsilon_{n\mathbf{k}}$ the Kohn−Sham energies. The Dyson equation is solved non-self-consistently, i.e., within the $G_{0}W_{0}$ approximation, leading to $\Sigma = iG_{0}W_{0}$. Though a fully self-consistent *GW* calculation often improves the accuracy, in some cases it can even overestimate the band gap. As the $G_{0}W_{0}$ approximation gives a band gap for bulk Si in excellent agreement with experiment, no self-consistent *GW*-treatment was necessary in the present work. Afterwards the random-phase approximation (RPA) was employed to obtain the reducible response function, while the generalized plasmon−pole model served as basis for treating dynamical screening effects in the self-energy.

The optical absorption spectrum, which is directly associated with the imaginary part of the macroscopic dielectric function, is defined in terms of the microscopic inverse dielectric function as

$$\varepsilon_{\mathrm{M}}(\omega) \equiv \lim_{\mathbf{q} \to 0} \frac{1}{\left[\varepsilon(\mathbf{q}, \omega)^{-1} \right]_{\mathbf{G}=0, \mathbf{G}'=0}}.$$

The coupled excitonic effects and absorption spectra are calculated by solving the BSE in terms of two-particle Green's function of quasi-electron and quasi-hole states, which is obtained by performing a second iteration of Hedin's equation:

$$\overline{L}_{\substack{nn'\mathbf{k} \\ mm'\mathbf{k}'}}(\omega) = L^0_{nn'\mathbf{k}}(\omega)[\delta_{nm}\delta_{n'm'}\delta_{\mathbf{kk}'} + i\sum_{\substack{ss'\mathbf{k}_1}} \Xi_{\substack{nn'\mathbf{k} \\ ss'\mathbf{k}_1}} \overline{L}_{\substack{ss'\mathbf{k}_1 \\ mm'\mathbf{k}'}}(\omega)],$$

where $\Xi_{\substack{nn'\mathbf{k} \\ ss'\mathbf{k}_1}}$ is the kernel describing tow-particle screened inter-actions. $\overline{L}$ satisfies the following relation:

$$\lim_{\mathbf{q}\to 0}\chi^0_{\mathbf{GG}'}(\mathbf{q},\omega) =$$

$$-i\sum_{nn'\mathbf{k}}\sum_{mm'\mathbf{k}'}\lim_{\mathbf{q}\to 0}\left[\rho^*_{n'n\mathbf{k}}(\mathbf{q},\omega)\rho_{m'm\mathbf{k}'}(\mathbf{q},\mathbf{G}')\right]\overline{L}_{\substack{nn'\mathbf{k} \\ mm'\mathbf{k}'}}(\omega).$$

Finally, the macroscopic dielectric function can be expressed as

$$\varepsilon_{\mathrm{M}}(\omega) \equiv 1 - \lim_{\mathbf{q}\to 0}\frac{8\pi}{|\mathbf{q}|^2 \Omega N_{\mathrm{q}}}$$

$$\cdot\sum_{nn'\mathbf{k}}\sum_{mm'\mathbf{k}'}\rho^*_{n'n\mathbf{k}}(\mathbf{q},\mathbf{G})\rho_{m'm\mathbf{k}'}(\mathbf{q},\mathbf{G}')\times\sum_{\lambda}\frac{A^{\lambda}_{n'n\mathbf{k}}\left(A^{\lambda}_{m'm\mathbf{k}'}\right)^*}{\omega - E_{\lambda}}$$

The standard Tamm−Dancoff approximation is adopted, in which only the positive *e−h* interactions are considered and, in addition, the non-Hermitian BSE reduces to a Hermitian one that can be solved with efficient and stable iterative methods [49]. For studying excitations in nanostructures [50] and in molecular systems [51] solving the BSE within the Tamm−Dancoff approximation is successively becoming a standard tool. For both the *GW* and BSE calculations, a box-shaped truncation of 13 Å is applied to screen the Coulomb interactions. Calculations including many-body effects are performed by using the YAMBO program suite [48].

Results and Discussion

On the DFT-LDA level, the band gap of Si is calculated to be 0.61 eV, while at the *GW* level it turns out to be 1.17 eV, in good accordance to the band gap obtained from experiment [52]. As demonstrated in previous theoretical works [25,33], we reproduce the optical absorption spectrum of bulk Si with excitonic effects emphasized. The analogue of graphene but with Si instead of C is two-dimensional silicene, for which many efforts have been made to synthesize this material [53,54]. In silicene, massless Dirac fermions, as in graphene, have been demonstrated, and thus silicene holds a substantial promise for future applications in nanoelectronics. Because of the presence of two-dimensional silicene, the synthesis of one-dimensional SiNTs is waiting for its realization. It has been discussed that the extra cost to produce SiNTs from silicene is of the same order of the equivalent cost in carbon [1]. In silicene, the optical responses are characterized by resonant excitations [54].

Figure 2 shows the band structures of (4,4), (6,6) and (10,0) SiNTs, which indicate semiconducting character as band gaps

appear. In case of armchair (4,4) SiNT, the band structure indicates an indirect band gap of 0.32 eV at Z point and a direct band gap of 0.65 eV at the *k* point on two-thirds way from Γ to Z in the one-dimensional Brillouin zone along the tube (2π/3a). However, it has been indicated that (*n,n*) armchair SiNTs are not stable for *n* < 6 [14]. In the case of a more stable armchair (6,6) and zigzag (10,0) SiNTs, as-calculated band structures show direct band gaps of 0.28 and 0.05 eV (50 meV), respectively. In (10,0) SiNT, the vanishingly narrow gap appears at the Γ point. However, there are still controversies with respect to the dependence of the conductance (semiconducting or metallic) on the chirality and/or diameter of SiNTs [1,14,15]. This discrepancy can be attributed, for instance, to the different symmetries of the initial structures from where SiNTs are constructed [15]. In the current work, after geometry relaxation, SiNTs prefer to be in a gear-like configuration.
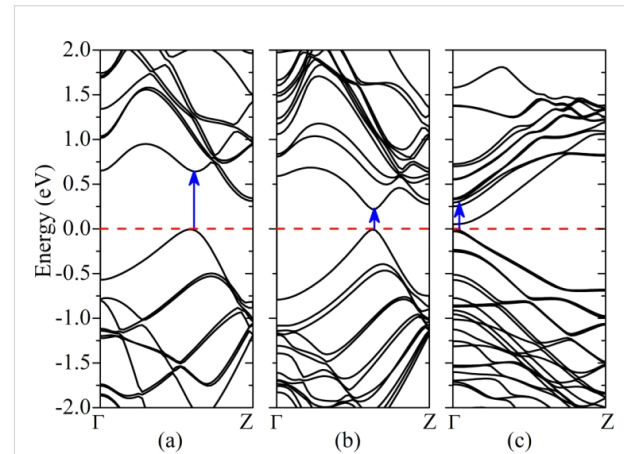

Figure 2: Band structures of silicon nanotubes (4,4) (a), (6,6) (b) and (10,0) (c). The Fermi level is set at the top of valence band, and the arrows indicate the *k* point where the inter band transitions occur.
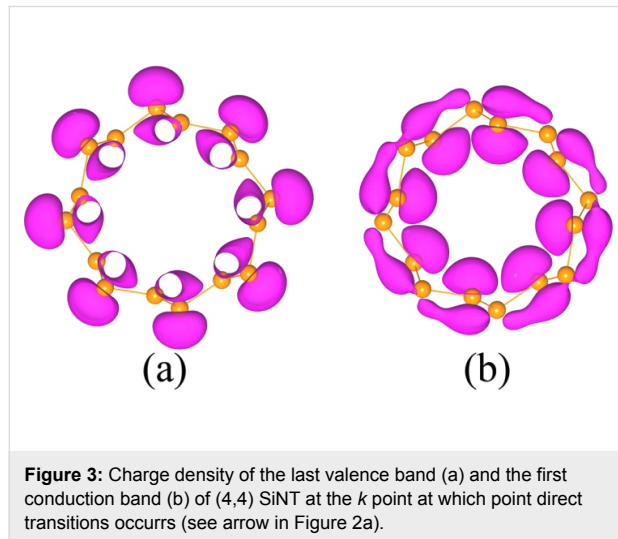
However, the standard DFT-based method generally underestimates band gaps because the independent particle picture breaks down. When including the *e−e* self-energy effects within the *GW* approximation, band gaps of the selected SiNTs are significantly broadened to be 1.9 (1.43 for indirect gap), 1.22 and 0.79 eV for the different SiNTs, respectively. In Table 1, all the relevant values are summarized. In the framework of *GW* approximation, such enormous modifications on the Kohn−Sham LDA values originate from enhanced *e−e* correlations due to the confinement effect in SiNTs with reduced dimensionality. A simple "scissor rule" is inapplicable due to the fact that the screening behavior determines the QP corrections [55]. For example, the QP self-energy effects give electron and hole masses smaller than the values predicted by DFT [56]. The nonlocal character of the self-energy operator in the *GW* framework is responsible for such a behavior [57]. As illus-

trated later, the exciton binding energy compensates the discrepancy between the electronic band gap calculated by DFT and the optical gap observed experimentally.

Table 1: Band gap at DFT-LDA and *GW* levels ($E_{g\text{-DFT}}$ and $E_{g\text{-}GW}$), QP corrections to the DFT-LDA gaps (QPC), excitation energy (E^I) and binding energy (E^b) of the first bound exciton of silicon nanotubes. All values are in eV.

	$E_{g\text{-DFT}}$	$E_{g\text{-}GW}$	QPC	E^I	E^b
(4,4)	0.65	1.9	1.25	0.98	0.92
(6,6)	0.28	1.22	0.94	0.12	1.1
(10,0)	0.05	0.79	0.74	0.19	0.6

As a representation, electronic wave functions of the last valence band and the first conduction band of (4,4) SiNT at the *k* point at which the direct transition occurrs are shown in Figure 3. As can be seen from the wave function of the last valence band, the weak π bonds are predominating with p_z states floating above Si atoms due to the fact that sp^3 hybridization in silicon is stable, which is in accordance with the mixed sp^2–sp^3 hybridization in silicene. In Figure 3b, a strong mixture of the π* states and σ* states exists in the tubes forming a ring-like distribution due to the curvature effects. In addition, one can see where the electrons are excited (with holes left).

Figure 3: Charge density of the last valence band (a) and the first conduction band (b) of (4,4) SiNT at the *k* point at which point direct transitions occurrs (see arrow in Figure 2a).

In Figure 4, optical absorption spectra of studied SiNTs for light propagation along the tube are presented. In case of SiNTs, the quasi-one-dimensional nature causes optical transitions to obey well-defined selection rules across the entire bands. In comparison with the spectra at independent-particle level (LDA-RPA, not shown), self-energy effects generally blue-shift the oscillator strength (*GW*+RPA). When considering *e*−*h* interactions

(*GW*+BSE), optical absorption properties of SiNTs are characterized by strong excitonic effects. In comparison with the single-particle spectrum, as can be seen from Figure 4, this prominent variation in weight redistribution of the oscillator strength reveals a global red-shift of the whole spectrum. In particular, optically active excitons (bound) below the onset of the single-particle transition continuum turns up with considerably large binding energies. The excitation energies E^I of the first bound excitons (the first sharp peaks in Figure 4) of (4,4), (6,6) and (10,0) SiNTs are 0.98, 0.12 and 0.19 eV, respectively. Binding energies, defined as the differences between the excitonic energy and the one-particle continuum onset and can be considered as a sign of *e*−*h* interactions, of these bound excitons are 0.92, 1.1 and 0.6 eV for (4,4), (6,6) and (10,0) SiNTs, respectively. The optically allowed transitions are mainly ascribed to the direct transitions between the last valence band and the first conduction band in (4,4) and (6,6) SiNTs, and between the last valence band and the third conduction band in the case of (10,0) SiNT. The smaller binding energy of the bright exciton in (10,0) SiNT is probably a consequence of the smaller quasi-electron effective mass. Since the interband transitions between the last valence band and the first conduction band are dipole-forbidden, there are several dark (optically inactive) excitons below the bound exciton in (10,0) SiNT. Compared with two-dimensional silicene, excitonic effects in SiNTs are stronger due to the lower dimensionality.
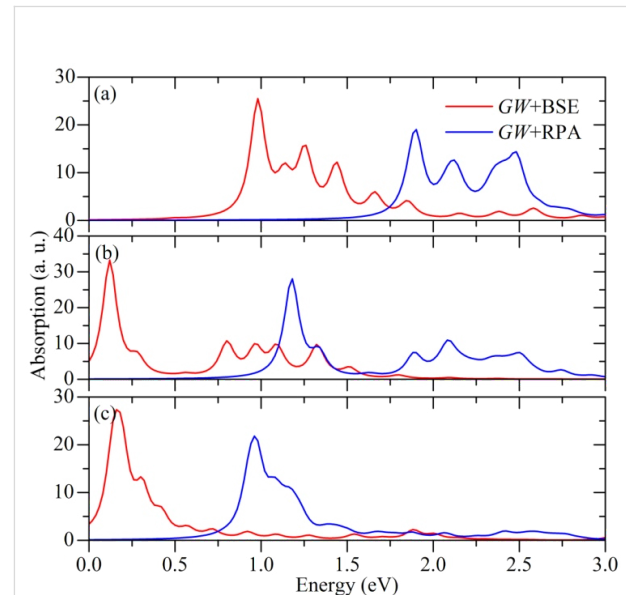

Figure 4: Absorption spectra of silicon nanotubes for light polarization along the tube calculated with and without the inclusion of *e*−*h* Coulomb interactions, i.e., *GW*+BSE and *GW*+RPA, respectively: (4,4) (a), (6,6) (b) and (10,0) (c). For the *GW*+BSE calculation, five occupied and five empty bands and a Lorentzian broadening of 0.05 eV are used.

The BS two-particle's Hamiltonian was diagonalized to obtain the *e−h* wave functions (quantum amplitudes) to show the correlation between excited electrons and holes in real space. Figure 5 shows the resulting three-dimensional electron probability distribution $|\psi(r_e;r_h)|^2$ of the bound excitons of selected SiNTs. As shown in Figure 5a, the bound exciton of (4,4) SiNT has a relatively small distribution radius featured by a damping nature, which is an indication of a strong binding between excited electrons and holes with large binding energy. In the case of (6,6) and (10,0) SiNTs, the wave functions of the first bound excitons extend far away along the tubes, similar to a nature of resonant excitons. The reduced electronic screening governs the strong binding of excitons in SiNTs, which is revealed by the huge overlap of exciton wave functions. In all studied SiNTs structures, exciton wave functions are strongly cylindrically asymmetric.
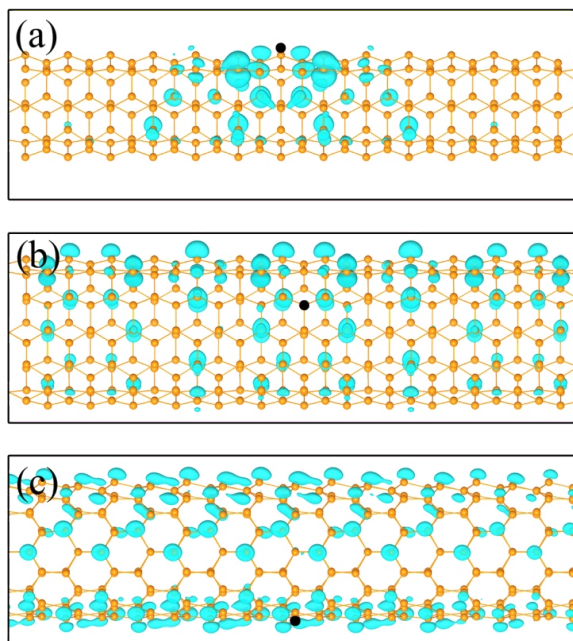

Figure 5: Electron probability distribution $|\psi(r_e;r_h)|^2$ for finding the electrons r_e with the hole position r_h (black dot) fixed slightly above a Si atom for the bound excitonic state of silicon nanotubes (4,4) (a); (6,6) (b) and (10,0) (c).

Quantitative representations of the electron distribution of the first excitons of studied SiNTs are demonstrated in Figure 6. In agreement with the exciton wave functions shown in Figure 5, the first bound exciton of (4,4) SiNTs is mainly localized within a radius of 20 Å. In the case of (6,6) and (10,0) SiNTs, the exciton radii extend over 60 Å. However, we also can see the damping nature, and the envelope function in the case of (10,0) SiNT.
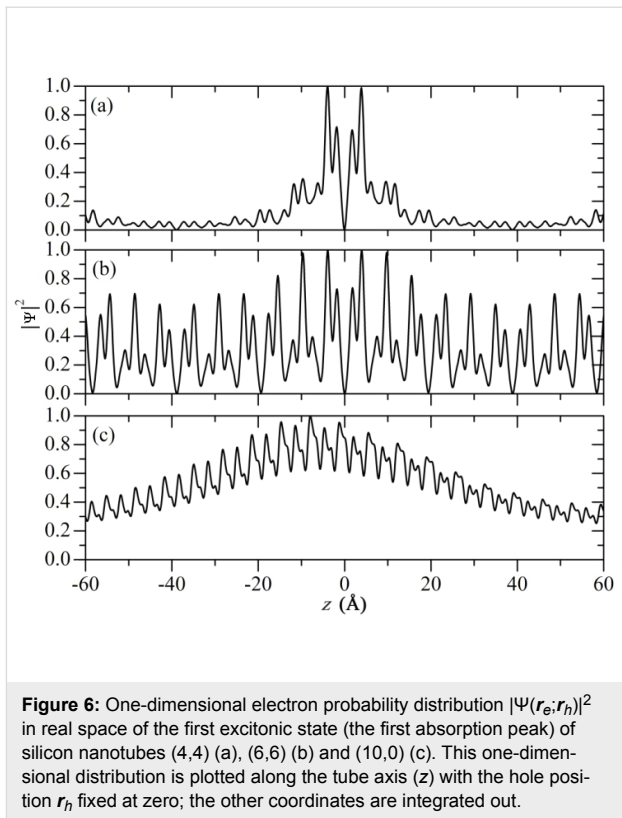

Figure 6: One-dimensional electron probability distribution $|\Psi(r_e;r_h)|^2$ in real space of the first excitonic state (the first absorption peak) of silicon nanotubes (4,4) (a), (6,6) (b) and (10,0) (c). This one-dimensional distribution is plotted along the tube axis (*z*) with the hole position r_h fixed at zero; the other coordinates are integrated out.

Conclusion

In summary, electronic and optical properties of single-wall semiconducting SiNTs have been studied by means of first-principles many-body perturbation theory. It has been elucidated that many-body effects strongly depend on the dimensionality of the system, and the quasi-one-dimensional features can be reflected in band structures and optical responses. One-dimensional structures, armchair (4,4) and (6,6), and zigzag (10,0) SiNTs, have been proven to be characterized by strong many-body effects due to the quantum confinement effect. The self-energy effects increase the single-particle excitation energy resulting in large QP band gaps in the studied SiNTs. The absorption properties are dominated by excitonic effects due to the reduced electronic screening giving rise to the formation of bound excitons with considerable binding energy. Since SiNTs are of great interest for basic scientific studies as well as potential applications, results in this work are of importance for a good understanding such systems.

Acknowledgements

References

1. Fagan, S. B.; Baierle, R. J.; Mota, R.; da Silva, A. J. R.; Fazzio, A. *Phys. Rev. B* **2000,** *61,* 9994–9996. doi:10.1103/PhysRevB.61.9994

2. Singh, A. K.; Briere, T. M.; Kumar, V.; Kawazoe, Y. *Phys. Rev. Lett.* **2003,** *91,* 146802. doi:10.1103/PhysRevLett.91.146802

3. Sha, J.; Niu, J.; Ma, X.; Xu, J.; Zhang, X.; Yang, Q.; Yang, D. *Adv. Mater.* **2002,** *14,* 1219–1221. doi:10.1002/1521-4095(20020903)14:17<1219::AID-ADMA1219>3.0.CO;2-T

4. Chen, B.; Xu, Q.; Zhao, X.; Zhu, X.; Kong, M.; Meng, G. *Adv. Funct. Mater.* **2010,** *20,* 3791–3796. doi:10.1002/adfm.201001190

5. Perepichka, D. F.; Rosei, F. *Small* **2006,** *2,* 22–25. doi:10.1002/smll.200500276

6. Yoo, J.-K.; Kim, J.; Jung, Y. S.; Kang, K. *Adv. Mater.* **2012,** *24,* 5452–5456. doi:10.1002/adma.201201601

7. Ben-Ishai, M.; Patolsky, F. *Angew. Chem., Int. Ed.* **2009,** *48,* 8699–8702. doi:10.1002/anie.200903583

8. Ben-Ishai, M.; Patolsky, F. *J. Am. Chem. Soc.* **2011,** *133,* 1545–1552. doi:10.1021/ja109197u

9. Gao, R.; Strehle, S.; Tian, B.; Cohen-Karni, T.; Xie, P.; Duan, X.; Qing, Q.; Lieber, C. M. *Nano Lett.* **2012,** *12,* 3329–3333. doi:10.1021/nl301623p

10. Song, T.; Xia, J.; Lee, J.-H.; Lee, D. H.; Kwon, M.-S.; Choi, J.-M.; Wu, J.; Doo, S. K.; Chang, H.; Park, W. I.; Zang, D. S.; Kim, H.; Huang, Y.; Hwang, K.-C.; Rogers, J. A.; Paik, U. *Nano Lett.* **2010,** *10,* 1710–1716. doi:10.1021/nl100086e

11. Park, M.-H.; Kim, M. G.; Joo, J.; Kim, K.; Kim, J.; Ahn, S.; Cui, Y.; Cho, J. *Nano Lett.* **2009,** *9,* 3844–3847. doi:10.1021/nl902058c

12. Wu, H.; Chan, G.; Choi, J. W.; Ryu, Y., III; ao, Y.; McDowell, M. T.; Lee, S. W.; Jackson, A.; Yang, Y.; Hu, L.; Cui, Y. *Nat. Nanotechnol.* **2012,** *7,* 310–315. doi:10.1038/NNANO.2012.35

13. Taghinejad, M.; Taghinejad, H.; Abdolahad, M.; Mohajerzadeh, S. *Nano Lett.* **2013,** *13,* 889–897. doi:10.1021/nl303558f

14. Durgun, E.; Tongay, S.; Ciraci, S. *Phys. Rev. B* **2005,** *72,* 075420. doi:10.1103/PhysRevB.72.075420

15. Yang, X.; Ni, J. *Phys. Rev. B* **2005,** *72,* 195426. doi:10.1103/PhysRevB.72.195426

16. Palaria, A.; Klimech, G.; Strachan, A. *Phys. Rev. B* **2008,** *78,* 205315. doi:10.1103/PhysRevB.78.205315

17. Bunder, J. E.; Hill, J. M. *Phys. Rev. B* **2009,** *79,* 233401. doi:10.1103/PhysRevB.79.233401

18. Yang, L.; Deslippe, J.; Park, C.-H.; Cohen, M. L.; Louie, S. G. *Phys. Rev. Lett.* **2009,** *103,* 186802. doi:10.1103/PhysRevLett.103.186802

19. Wei, W.; Jacob, T. *Phys. Rev. B* **2012,** *86,* 165444. doi:10.1103/PhysRevB.86.165444

20. Wei, W.; Jacob, T. *Phys. Rev. B* **2013,** *87,* 085202. doi:10.1103/PhysRevB.87.085202

21. Cudazzo, P.; Attaccalite, C.; Tokatly, I. V.; Rubio, A. *Phys. Rev. Lett.* **2010,** *104,* 226804. doi:10.1103/PhysRevLett.104.226804

22. Bockstedte, M.; Marini, A.; Pankratov, O.; Rubio, A. *Phys. Rev. Lett.* **2010,** *105,* 026401. doi:10.1103/PhysRevLett.105.026401

23. Wirtz, L.; Marini, A.; Rubio, A. *Phys. Rev. Lett.* **2006,** *96,* 126104. doi:10.1103/PhysRevLett.96.126104

24. Bruno, M.; Palummo, M.; Marini, A.; Del Sole, R.; Ossicini, S. *Phys. Rev. Lett.* **2007,** *98,* 036807. doi:10.1103/PhysRevLett.98.036807

25. Marini, A.; Del Sole, R. *Phys. Rev. Lett.* **2003,** *91,* 176402. doi:10.1103/PhysRevLett.91.176402

26. Bernardi, M.; Palummo, M.; Grossman, J. C. *Phys. Rev. Lett.* **2003,** *108,* 226805. doi:10.1103/PhysRevLett.108.226805

27. Yang, L. *Nano Lett.* **2011,** *11,* 3844–3847. doi:10.1021/nl201928g

28. Chen, Z.; Wang, X.-Q. *Phys. Rev. B* **2011,** *83,* 081405. doi:10.1103/PhysRevB.83.081405

29. Trevisanutto, P. E.; Holzmann, M.; Côté, M.; Olevano, V. *Phys. Rev. B* **2010,** *81,* 121405. doi:10.1103/PhysRevB.81.121405

30. Yang, L. *Phys. Rev. B* **2011,** *83,* 085405. doi:10.1103/PhysRevB.83.085405

31. Marinopoulos, A. G.; Reining, L.; Rubio, A.; Vast, N. *Phys. Rev. Lett.* **2003,** *91,* 046402. doi:10.1103/PhysRevLett.91.046402

32. Onida, G.; Reining, L.; Rubio, A. *Rev. Mod. Phys.* **2002,** *74,* 601–659. doi:10.1103/RevModPhys.74.601

33. Rohlfing, M.; Louie, S. G. *Phys. Rev. B* **2000,** *62,* 4927–4944. doi:10.1103/PhysRevB.62.4927

34. Hedin, L. *Phys. Rev.* **1965,** *139,* A796–A823. doi:10.1103/PhysRev.139.A796

35. Sham, L. J.; Rice, T. M. *Phys. Rev.* **1966,** *144,* 708–714. doi:10.1103/PhysRev.144.708

36. Hanke, W.; Sham, L. J. *Phys. Rev. Lett.* **1979,** *43,* 387–390. doi:10.1103/PhysRevLett.43.387

37. Hanke, W.; Sham, L. J. *Phys. Rev. B* **1980,** *21,* 4656–4673. doi:10.1103/PhysRevB.21.4656

38. Rohlfing, M.; Louie, S. G. *Phys. Rev. Lett.* **1999,** *82,* 1959–1962. doi:10.1103/PhysRevLett.82.1959

39. Rohlfing, M.; Louie, S. G. *Phys. Rev. Lett.* **1998,** *80,* 3320–3323. doi:10.1103/PhysRevLett.80.3320

40. Rohlfing, M.; Louie, S. G. *Phys. Rev. Lett.* **1998,** *81,* 2312–2315. doi:10.1103/PhysRevLett.81.2312

41. Rohlfing, M.; Louie, S. G. *Phys. Rev. Lett.* **1999,** *83,* 856–859. doi:10.1103/PhysRevLett.83.856

42. Yang, L.; Spataru, C. D.; Louie, S. G.; Chou, M. Y. *Phys. Rev. B* **2007,** *75,* 201304. doi:10.1103/PhysRevB.75.201304

43. Spataru, C. D.; Ismail-Beigi, S.; Benedict, L. X.; Louie, S. G. *Phys. Rev. Lett.* **2004,** *92,* 077402. doi:10.1103/PhysRevLett.92.077402

44. Deslippe, J.; Spataru, C. D.; Prendergast, D.; Louie, S. G. *Nano Lett.* **2007,** *7,* 1626–1630. doi:10.1021/nl070577f

45. Maultzsch, J.; Pomraenke, R.; Reich, S.; Chang, E.; Prezzi, D.; Ruini, A.; Molinari, E.; Strano, M. S.; Thomsen, C.; Lienau, C. *Phys. Rev. B* **2005,** *72,* 241402. doi:10.1103/PhysRevB.72.241402

46. Giannozzi, P.; Baroni, S.; Bonini, N.; Calandra, M.; Car, R.; Cavazzoni, C.; Ceresoli, C.; Chiarotti, G. L.; Cococcioni, M.; Dabo, I.; Corso, A. D.; de Gironcoli, S.; Fabris, S.; Fratesi, G.; Gebauer, R.; Gerstmann, U.; Gougoussis, C.; Kokalj, A.; Lazzeri, M.; Martin-Samos, L.; Marzari, N.; Mauri, F.; Mazzarello, R.; Paolini, S.; Pasquarello, A.; Paulatto, L.; Sbraccia, C.; Scandolo, S.; Sclauzero, G.; Seitsonen, A. P.; Smogunov, A.; Umari, P.; Wentzcovitch, R. M. *J. Phys.: Condens. Matter* **2009,** *21,* 395502. doi:10.1088/0953-8984/21/39/395502

47. Wei, W.; Jacob, T. *Phys. Rev. B* **2013,** *88,* 045203. doi:10.1103/PhysRevB.88.045203

48. Marini, A.; Hogan, C.; Grüning, M.; Varsano, D. *Comput. Phys. Commun.* **2009,** *180,* 1392–1403. doi:10.1016/j.cpc.2009.02.003

49. Grüning, M.; Marini, A.; Gonze, X. *Nano Lett.* **2009,** *9,* 2820–2824. doi:10.1021/nl803717g

50. del Puerto, M. L.; Tiago, M. L.; Chelikowsky, J. R. *Phys. Rev. Lett.* **2006,** *97,* 096401. doi:10.1103/PhysRevLett.97.096401

51. Hirata, S.; Head-Gordon, M. *Chem. Phys. Lett.* **1999,** *314,* 291–299.
doi:10.1016/S0009-2614(99)01149-5

52. Gryko, J.; McMillan, P. F.; Marzke, R. F.; Ramachandran, G. K.;
Patton, D.; Deb, S. K.; Sankey, O. F. *Phys. Rev. B* **2000,** *62,*
R7707–R7710. doi:10.1103/PhysRevB.62.R7707

53. Chen, L.; Liu, C.-C.; Feng, B.; He, X.; Cheng, P.; Ding, Z.; Meng, S.;
Yao, Y.; Wu, K. *Phys. Rev. Lett.* **2012,** *109,* 056804.
doi:10.1103/PhysRevLett.109.056804

54. Fleurence, A.; Friedlein, R.; Ozaki, T.; Kawai, H.; Wang, Y.;
Yamada-Takamura, Y. *Phys. Rev. Lett.* **2012,** *108,* 245501.
doi:10.1103/PhysRevLett.108.245501

55. Yang, L.; Cohen, M. L.; Louie, S. G. *Nano Lett.* **2007,** *7,* 3112–3115.
doi:10.1021/nl0716404

56. Spataru, C. D.; Ismail-Beigi, S.; Capaz, R. B.; Louie, S. G.
Phys. Rev. Lett. **2005,** *95,* 247402.
doi:10.1103/PhysRevLett.95.247402

57. Prezzi, D.; Varsano, D.; Ruini, A.; Marini, A.; Molinari, E. *Phys. Rev. B*
2008, *77,* 041404. doi:10.1103/PhysRevB.77.041404